APPLICATION OF THOMSON SCATTERING AT 1.06μm AS A DIAGNOSTIC FOR SPATIAL PROFILE MEASUREMENTS OF ELECTRON TEMPERATURE AND DENSITY ON THE TCV TOKAMAK

THÈSE N^{O} 1654 (1997)

PRÉSENTÉE AU DÉPARTEMENT DE PHYSIQUE

ÉCOLE POLYTECHNIQUE FÉDÉRALE DE LAUSANNE

POUR L'OBTENTION DU GRADE DE DOCTEUR ÈS SCIENCES

PAR

Stefan FRANKE
Diplom-Physiker, Universität Fridericiana, Karlsruhe, Allemagne
de nationalité allemande

acceptée sur proposition du jury:

Dr R. Behn, directeur de thèse
Prof. Dr H.F. Döbele, corapporteur
Dr P.D. Morgan, corapporteur
Dr M.R. Siegrist, corapporteur
Dr H. Weisen, corapporteur

Lausanne, EPFL
1997

Zusammenfassung

Der Tokamak TCV (eine Abkürzung für den Ausdruck 'Tokamak mit variablem Querschnitt') ist seit Ende 1991 am Forschungszentrum für Plasmaphysik in Lausanne (CRPP) in Betrieb und nimmt eine besondere Stellung unter den experimentellen Fusionsreaktoren ein, die das Einschlußverhalten von Tokamakplasmen mit nicht-zirkularem Querschnitt erforschen. Seine Einzigartigkeit in Bezug auf die Untersuchung magnetischer Gleichgewichte, die an anderen modernen, zum Teil größeren Fusionsreaktoren nicht realisiert werden können, stellt den Experimentator vor gewisse Probleme. Messungen werden häufig an Plasmakonfigurationen durchgeführt, die sich von einer zur nächsten Entladung ändern. Die reduzierte Symmetrie in Plasmen mit hoher Elongation oder Triangularität schränkt die Anwendungsmöglichkeiten von Inversionsalgorithmen deutlich ein, die aus linienintegrierten Messungen von Plasmaparametern deren Profile errechnen.

Ein Fusionsreaktor wie TCV, der speziell für Untersuchungen des Einflußes der Plasmaform auf das Einschluß- und Stabilitätsverhalten ausgelegt wurde, muß in jedem Fall über Diagnostiken verfügen, die die zur Charakterisierung des Einschlußverhaltens wichtigen Elektronentemperatur- und -dichteprofile liefern. Für TCV wurde aus diesem Grund eine leistungsfähige Thomsonstreudiagnostik konzipiert, die sowohl räumlich als auch zeitlich aufgelöste Elektronentemperatur- und -dichtemessungen durchführen kann. Details über den Aufbau des an TCV installierten Systems als auch die entsprechenden Resultate sind der Hauptgegenstand dieser Arbeit.

Eine Basisversion der Thomsonstreudiagnostik war mit nur 10 Beobachtungsvolumina ausgerüstet. In diesem Fall ist eine ausreichende Auflösung für Profilmessungen nur dann gewährleistet, wenn sich diese auf Entladungen im oberen Teil des gestreckten Vakuumgefäßes beschränken. Die Diagnostik wurde deswegen durch 15 zusätzliche, auf insgesamt 25 Beobachtungsvolumina erweitert, wobei gleichzeitig wesentliche technische Änderungen des Detektionssystems aller räumlichen Kanäle vorgenommen wurden. Diese stark modifizierte Version gestattet Messungen an beliebigen TCV-Plasmen, sowohl Entladungen im unteren und oberen Teil des Vakuumgefäßes als auch Entladungen mit hochelongiertem Querschnitt, die seit wenigen Monaten im Routinebetrieb erzeugt werden können (eine Elongation von $\kappa=2.47$ stellt den bis dato erreichten Höchstwert dar). Neben einer Beschreibung des modifizierten Detektionssystems sowie einiger exemplarischer Messungen, beschränkt sich die vorliegende Arbeit jedoch primär auf die Präsentation der Ausstattung und die Analyse von Meßergebnissen, die mit der ursprünglichen Version erzielt wurden.

Der Komplexität der Thomsonstreudiagnostik an TCV wird nur eine ausführliche Beschreibung gerecht, die sich in den Anfangskapiteln dieser Arbeit wiederfindet. Aufgrund des diskreten Charakters der Meßpunkte, aus denen sich die Profile zusammensetzen, werden diese im gesamten Bereich an TCV möglicher Profilformen gefittet. Zu diesem Zweck wurde eine Reihe von Programmen entwickelt, welche zur Profilanalyse ein Mindestmaß an Eingriffen von Benutzerseite erfordern. Diese Fitroutinen benutzen aus kubischen B-Splines abgeleitete Basisfunktionen zur Profilinterpolation in normierten Flußkoordinaten, wodurch die Profildarstellung vereinheitlicht und vergleichende Analysen mit Daten anderer Diagnostiken erleichtert werden.

Unabhängig von der Komplexität einer Tokamakdiagnostik bleibt deren primäre Aufgabe, Meßergebnisse zu liefern, die zum Verständnis der Fragestellungen verschiedener Experimentierkampagnen beitragen. Da Einrichtungen zur Zusatzheizung während der für diese Arbeit relevanten Meßkampagnen nicht zur Verfügung standen, beschränkt sich die Bandbreite der Messungen auf Plasmen mit Ohmscher Heizung. Zur Charakterisierung der Temperaturprofile wurde deswegen untersucht, in wieweit der Effekt der Profilkonsistenz an TCV beobachtet werden kann. Wenn der für das Phänomen maßgebliche Sicherheitsfaktor am Plasmarand in der für nicht-zirkulare Plasmen geeigneten Form beschrieben wird, läßt sich der Effekt eindeutig beobachten, zumindest für Werte der Plasmaelongation bis zu $\kappa=1.9$ und der Plasmatriangularität im Bereich $-0.4<\delta<0.7$.

Einen hohen Rang im Forschungsprogramm an TCV nehmen Experimente ein, die Auswirkungen der Plasmaform auf den Energieeinschluß untersuchen. In diesem Fall kommt den Profildaten der Thomsonstreudiagnostik eine zentrale Bedeutung zu, da augenblicklich nicht verfügbare Daten über Ionentemperatur- und -dichteprofile nur glaubwürdige Angaben über die Elektronenenenergieeinschlußzeit zulassen. Speziell die Analyse der Elektronentemperaturgradienten nahe des Plasmarandes als Funktion der Triangularität zeigt, daß die beobachtete Abnahme der Energieeinschlußzeit mit zunehmendem δ durch das Zusammenspiel geometrischer Effekte und einer Verschlechterung des Energieeinschlußes mit steigendem Ohmschen Heizfluß erklärt werden kann.

Schließlich wird die wichtige Frage angegangen, wie die Integration von Elektronendruckprofilen in das Programm zur Rekonstruktion der Plasmagleichgewichte an TCV (LIUQE) dessen Resultate beeinflußt bzw. verbessert. Im Routinebetrieb benutzt LIUQE nämlich einzig die Ergebnisse magnetischer Diagnostiken, was oftmals zu Plasmadruckprofilen (und folglich zu Energieeinschlußzeiten) führt, die in krassem Widerspruch zu gemessenen Elektronendruckprofilen stehen. Aufgrund nicht verfügbarer Ionenprofildaten, kann diese Analyse nur durchgeführt werden, wenn die gemessenen Elektronendruckprofile mit modellisierten Ionendruckprofilen kombiniert werden. Die den Modellen zugrundeliegenden Ionentransportmechanismen werden erläutert, bevor die Resultate der mit den verschiedenen Modellen gerechneten Gleichgewichtsrekonstruktionen diese Arbeit abrunden.

Abstract

The variable configuration tokamak, TCV, in operation at CRPP since the end of 1991, is a particularly challenging machine with regard to the experimental systems that must provide essential information regarding properties of confined plasmas with strongly shaped, non-circular cross-sections. Although TCV is unique in its capacity for the study of magnetic equilibria not previously examined in modern, large tokamaks, this flexibility poses serious problems for the experimentalist who may be required, for example, to make measurements in completely different configurations from one discharge to the next. Highly shaped plasmas also render more complex, or even impossible, the application of inversion techniques for the recovery of plasma profiles based on chordal measurements which necessarily yield line averaged quantities.

The importance of the energy confinement issue in a machine designed specifically for the investigation of the effect of plasma shape on confinement and stability is self-evident, as is the necessity for a diagnostic capable of providing the profiles of electron temperature and density required for evaluation of this confinement. For TCV, a comprehensive Thomson Scattering (TS) diagnostic was the natural choice, specifically owing to the resulting spatially localized and time resolved measurement. The details of the system installed on TCV, together with the results obtained from the diagnostic comprise the subject matter of this thesis.

A first version of the diagnostic was equipped with only ten observation volumes. In this case, adequate spatial resolution can only be maintained if measurements are limited to plasmas located in the upper half of the highly elongated TCV vacuum vessel. The system has recently been upgraded through the addition of a further fifteen observation volumes, together with major technical improvements in the scattered light detection system. This new version now permits TS observations in all TCV plasma configurations, including equilibria produced in the lower and upper halves of the vacuum vessel and the highly elongated plasmas now routinely created (κ=2.47 is the maximum elongation achieved at the time of writing). Whilst a description of the new detection system along with some results obtained using the extended set of observation volumes are included, this thesis reports principally on the hardware details of and the interpretation of data from the original, ten observation volume system.

The complexity of the TCV Thomson Scattering system can only be effectively conveyed through considerable descriptive effort and such details can be found in the earlier chapters of this work. Effort is also required if the set of discrete data points constituting the profile is to be effectively fitted over the wide range of profile shapes encountered in TCV. For this purpose, a number of analysis routines have been developed during the course of this research with which TS profile data can be reliably fitted with a minimum of user intervention. These routines are based on cubic spline interpolation within a normalized poloidal flux coordinate system facilitating the comparison of TS data with the results of other TCV diagnostics.

However complex a given tokamak diagnostic may be, its primary purpose is, of course, to provide relevant data for use in understanding the results obtained from any particular experimental campaign. The hardware descriptions and data analysis techniques of the earlier chapters thus give way, in the second half of this thesis, to a series of studies dedicated to the use of TS data for physics understanding. The absence of an additional heating system on TCV throughout the duration of this research, necessarily limits the scope of such studies to the case of ohmic plasmas only.

Some effort is devoted to an investigation of the extent to which the phenomena of profile consistency in ohmically heated discharges is observed in TCV. In general, if a form for the edge safety factor appropriate to shaped plasmas is adopted, the effect does appear to prevail, at least for elongations up to $\kappa=1.9$ and for plasma triangularities in the range $-0.4<\delta<0.7$.

An area constituting high priority in the TCV experimental programme is the study of the effect of plasma shape on energy confinement. In this case, TS profiles are of the utmost importance since the current absence of experimental information regarding the ion temperature and density in TCV precludes a reliable estimate of anything but the electron energy confinement time. Analysis of changes in the electron temperature gradient near the plasma edge as a function, in particular, of plasma triangularity, shows that the observed decrease in energy confinement time with increasing δ can be explained in terms of a combination of geometrical effects and heat flux degradation.

The important question of how the inclusion of TS electron pressure profiles may modify or improve the results of the TCV equilibrium reconstruction algorithm, LIUQE, is also addressed. Such reconstructions are presently computed solely on the basis of magnetic measurements, but often lead to reconstituted total pressure profiles (and hence energy confinement times) in clear contradiction with the TS electron pressure profiles. Since ion pressure profile measurements are unavailable, the use of TS data as input to LIUQE can only be performed if the Thomson profiles are combined with assumed ion pressure profiles. These theoretical profiles depend, in turn, on the assumed mechanism of ion transport. An attempt to model this transport, together with a presentation of the effect of additional experimental constraints on the results of equilibrium reconstructions constitute the material of the final chapter of this thesis.

Ce qui embellit le desert, dit le petit prince,
c'est qu'il cache un puits quelque part

Antoine de Saint-Exupéry

C'est en essayant que les grecs ont pris Troie

Théocrite

Table of Contents

Zusammenfassung 1

Abstract 3

1 Introduction. 13

1.1 Thermonuclear Fusion 13
1.2 Tokamak Principle 15
1.3 Purpose of Thomson Scattering. 17
1.4 Outline of this Thesis 18

2 Basic Theory of Incoherent Thomson Scattering. 19

2.1 Introduction 19
2.2 Scattering from a Single Non-Relativistic Electron. 19
2.3 Scattering from Many Electrons 24
2.4 Relativistic Effects and the Spectral Density Function. 26

3 The Thomson Scattering System on TCV 29

3.1 The Tokamak TCV 29
  3.1.1 Design Parameters and Performance 29
  3.1.2 Relevant Diagnostics on TCV 32
    3.1.2.1 Magnetic Diagnostics. 32
    3.1.2.2 Far Infrared Interferometer (FIR) 33
    3.1.2.3 Soft X-ray Tomography 34
    3.1.2.4 Ultra Soft X-ray Spectroscopy .34
    3.1.2.5 X-ray Monitor Diodes. 35

3.1.2.6 Bolometry 35
3.1.2.7 Neutral Particle Analyser (NPA) 35
3.1.2.8 Visible Spectroscopy 35
3.2 The Thomson Scattering Experiment on TCV 36
3.2.1 General Design Aspects 36
3.2.2 Layout of the System 38
3.2.2.1 Laser System 38
3.2.2.2 Optical Beam Path 39
3.2.3 Detection Optics 40
3.2.4 Filter Polychromators 42
3.2.4.1 The "3-channel" filter polychromators 42
3.2.4.1.1 Optical Layout 43
3.2.4.1.2 Detectors 44
3.2.4.1.3 Signal Amplification 45
3.2.4.2 The "4-channel" Filter Polychromators 45
3.2.4.2.1 Optical Layout 45
3.2.4.2.2 Detectors 47
3.2.4.2.3 Signal Amplification 48
3.2.5 Laser Operation and Control 48
3.2.6 Optical Alignment 49
3.2.7 Data Acquisition 49
3.2.7.1 Introduction 49
3.2.7.2 Components and Triggering 49
3.2.7.3 Acquisition Cycle during a Discharge 51
3.3 Analysis of Scattered Signals 53
3.3.1 Evaluation of T_e and n_e 53
3.4 Calibration methods 56
3.4.1 Laboratory Calibrations 57
3.4.1.1 Spectral Calibration 57
3.4.1.2 Identification of Systematic Errors 59
3.4.1.3 Broad-band Calibration 60
3.4.2 Calibration In-situ 63
3.4.2.1 Introductory Remarks 63
3.4.2.2 Example of a Raman Calibration in N_2 63
3.5 The Data Analysis Program, TSA 67
3.5.1 Computation of the Weighted Average Electron Temperature 69
3.5.2 Computation of the Electron Density 70

4 Profile Analysis in Normalized Flux Coordinates 73

4.1 Introduction 73
4.2 Explanation of the Profile Analysis 75
4.2.1 The Interpolation Scheme 75
4.2.2 Location of the Knots 79
4.2.3 Error Analysis of the Profile Fits 81

4.2.4 Application of the Profile Analysis 84
4.2.5 Limits and Possibilities for Improvement 84

5 T_e and n_e Profiles in Different Discharge Conditions on TCV 89

5.1 Sawtooth Signatures on T_e Profiles 89
5.2 Comparison of Density Measurements from Interferometry and Thomson Scattering 93
5.3 T_e and n_e Profiles in ELM-free, Ohmic H-modes 96
5.4 Performance of the Vertical System Equipped with 25 Polychromators 97
  5.4.1 T_e and n_e Profiles in Highly Elongated Plasmas 98
  5.4.2 T_e and n_e Profiles in Plasmas with “Exotic” Shapes 99

6 Influence of Plasma Shaping on T_e and n_e Profiles in Ohmically Heated Plasmas 103

6.1 Conditions of the Experimental Study 103
6.2 Variation of Profile Shapes with Plasma Parameters 105
  6.2.1 Interpolation of T_e and n_e Profiles 105
  6.2.2 Characterisation of Profile Shapes - The Peaking Factor 106
  6.2.3 Scaling Laws for the Peaking Factors 108
  6.2.4 Profile Consistency 112
6.3 Summary 115

7 Influence of Plasma Shape on Confinement and Transport . 117

7.1 Introduction 117
7.2 The Electron Energy Confinement Time and its Dependence on Shape Parameters 117
7.3 Degradation of Confinement with Heat Flux 124
7.4 The "Shape Enhancement Factor" 129
7.5 The Possible Role of the Ions in the Heat Transport 132
7.6 Conclusions 133

8 Influence of Constraints from Measured Pressure Profiles on the Equilibrium Reconstruction 135

8.1 The Equilibrium Reconstruction Code LIUQE 135
8.1.1 The Standard Version ("Magnetic" LIUQE) 135
8.1.2 The Version with Additional Constraints, in particular Pressure Profiles ("Kinetic" LIUQE) 139
8.1.3 Using LIUQE with Additional Constraints. 142
8.2 Evaluation of Total Plasma Pressure Profiles. 143
8.2.1 Motivation 143
8.2.2 Selection of a Data Base. 144
8.2.3 Models for Total Plasma Pressure Profiles. 146
8.2.3.1 Ion Pressure Proportional to the Electron Pressure 146
8.2.3.2 Deriving the Ion Pressure Profile from a Transport Model. 146
8.2.3.2.1 Evaluation of the T_i Profile from the Ion Heat Diffusion Equation 147
8.2.3.2.2 Solving the Differential Equation; The Numerical Scheme (Crank-Nicholson). 150
8.2.3.2.3 Estimation of the Ion Heat Diffusivity 151
8.2.3.2.4 Determination of the Ion Concentrations. 155
8.3 Results from Equilibrium Reconstructions with Kinetic Constraints 155
8.3.1 Influence of the Selection of Base Functions. 156
8.3.1.1 Role of the Pressure Profiles. 156
8.3.1.2 Effect on W_t. 158
8.3.1.3 Effect on q_0 159
8.3.1.4 Effect on Flux Surface Geometry 160
8.3.2 Model Influence on p_i. 163
8.4 Conclusions 166

9 Final Conclusions 169

9.1 Experimental Arrangement. 169
9.2 Data Analysis and Results 170

References 173

Appendix A) Rotational Raman Scattering. 179

Appendix B) Distribution of Spectral Channels 183

Appendix C) Parameters for the Neoclassical Calculation
of the Ion Heat Diffusivity. 187

Appendix D) Summary of Symbols and Expressions 188

Acknowledgements. 189

Curriculum vitae 191

1 Introduction

1.1 Thermonuclear Fusion

Maintenance of prosperity and welfare in highly industrialized countries and their development in threshold or third world countries is based on sufficient and secure availability of energy resources. In the early 1990's, the total energy consumption of the Earth's population (4.5 billion people) came to approximately $3.5 \cdot 10^{20}$ J/year. The remaining fossil fuel energy resource is estimated at a few 10^{23}J, the solar energy reaching the Earth attains some $5 \cdot 10^{24}$J/year and nuclear fission technology, including advanced schemes such as breeder reactors, has a potential of several 10^{23}J. Unfortunately, the production of CO_2 and its subsequent environmental impact via global warming are serious obstacles in the path of the long term continuation of energy supply though the burning of fossil fuels. Moreover, the combustion of coal and oil as a chemical process is wasteful in comparison with the more efficient nuclear reactions. Exploitation of the latter by large scale breeder technology suffers from lack of acceptance due to public fear of accident and the generation of long-lived radioactive waste. At present, economic arguments would appear to handicap the massive use of solar energy.

If it proves to be technologically feasible, the process of nuclear fusion is an attractive alternative to the energy resource dilemma. Fusion based on Deuterium-Tritium (D-T) reactions could provide around $5 \cdot 10^{27}$J (limited global resources of Lithium), whilst Deuterium-Deuterium (D-D) reactions could potentially supply a total of 10^{31}J as a consequence of the huge natural Deuterium resources (Deuterium is present to 0.015 Mol-% of natural Hydrogen). Although a plethora of technological problems remain to be solved, the enormous available resource and relatively limited environmental impact are important advantages of fusion as a means for future energy production [47], [53].

As a consequence of its very favourable rate coefficient ($\langle\sigma(v)\cdot v\rangle \approx 10^{-22}\mathrm{m}^3/\mathrm{s}$ at temperatures around 10 keV), the fusion of a Deuterium nucleus and with a Tritium nucleus to yield an alpha-particle and an energetic neutron is the preferred candidate amongst a number of energy releasing fusion reactions:

$$D + T \rightarrow {}^{4}He(3.52MeV) + n(14.06MeV)$$

(1.1)

At the temperatures required for fusion to occur, all atoms taking part in the reactions are fully ionized and the resulting ensemble of ions and electrons constitutes a completely ionized plasma. In general, the nuclei sustain a large number of Coulomb collisions before tunnelling through the repelling barrier of the interaction potential. The charged particles and their associated energy must therefore be confined over a time interval long enough to allow a sufficient number of Coulomb collisions to occur. Since there will be a continuous loss of energy and particles from the plasma in any thermonuclear reactor, it is appropriate to define the characteristic confinement times, τ_E and τ_p, over which energy and particles would be lost from the system if the energy and particle sources were removed.

In 1957, John D. Lawson derived a fusion reactor power balance criterion for the specific case of energy input from a source outside the plasma and assuming an idealized cyclic process in which the thermonuclear power output and the energy losses can be converted to electrical energy and regained as useful heat [28]. If the efficiency of this conversion process is to be at least 33%, the Lawson criterion imposes a condition on the product of the particle density and the energy confinement time for plasma temperatures in the range 20→30keV:

$$n\tau_E \geq 6 \cdot 10^{19} m^{-3} s$$

(1.2)

International research effort aimed at satisfying this requirement is currently directed along two principal routes:

a) *Inertial Confinement*: In this approach, characterized by very high particle densities ($n \approx 10^{30} m^{-3}$) and very short energy confinement times ($\tau_E \approx 0.1 ns$), D-T pellets are isotropically heated by ultra-short, high energy laser pulses or particle beams in order to evaporate the outer layers and compress the inner regions by the propagation of shock waves.

b) *Magnetic confinement*: Charged particles in a magnetic field perform helical gyrations around the field lines due to the Lorentz force. If the Larmor-radius, ρ_L of this gyration for a deuterium ion, ($\rho_L \approx 2$ mm in a magnetic field, B=1.4T and a plasma temperature, T≈500eV) is small compared with typical device dimensions, the particles essentially follow the magnetic field lines ('guiding centre approximation'). Different methods have been employed in an effort to produce this magnetic confinement in large scale experiments, including so-called mirror machines, stellarators and tokamaks. Of these, the tokamak concept is currently favoured as a future energy producing reactor. Confinement times of around 1s have already been achieved on the largest operating experimental machines (JET [24]).

1.2 Tokamak Principle

A tokamak (from the Russian 'Toroidalnaya Kamera Magnitnaya Katuschka' meaning toroidal magnetic chamber) is an axisymmetric structure in which the plasma is confined by a toroidal magnetic field configuration (fig. 1.1). In steady-state, the Lorentz forces acting on the plasma particles (electrons and ions) must balance their pressure gradients:

$$\vec{j} \times \vec{B} = \vec{\nabla} p = \vec{\nabla}(p_i + p_e) \tag{1.3}$$

where $\vec{j}$ denotes the plasma current density and p_i and p_e are respectively the ion and the electron pressures. Scalar multiplication of eqn. 1.3 by $\vec{j}$ or $\vec{B}$ shows that $\vec{j}$ and $\vec{B}$ must lie on surfaces of constant pressure. It can also be shown that these surfaces are surfaces of constant poloidal flux, Ψ, where Ψ denotes the magnetic flux through a circular disc perpendicular to the tokamak axis.

A purely toroidal magnetic field, B_ϕ cannot, by itself, confine the tokamak plasma. The toroidal curvature of the field lines, coupled with the radial decrease of B_ϕ, $B_\phi \approx B_{\phi_0} R_0 / R$ (where R denotes the major plasma radius and B_{ϕ_0} the vacuum magnetic field on the magnetic axis) lead to particle drifts which displace electrons and ions in opposite directions. The resulting space charge generates an electric field perpendicular to the toroidal magnetic field and the resulting $\vec{E} \times \vec{B}$ force drives the plasma particles outward in major radius [74].

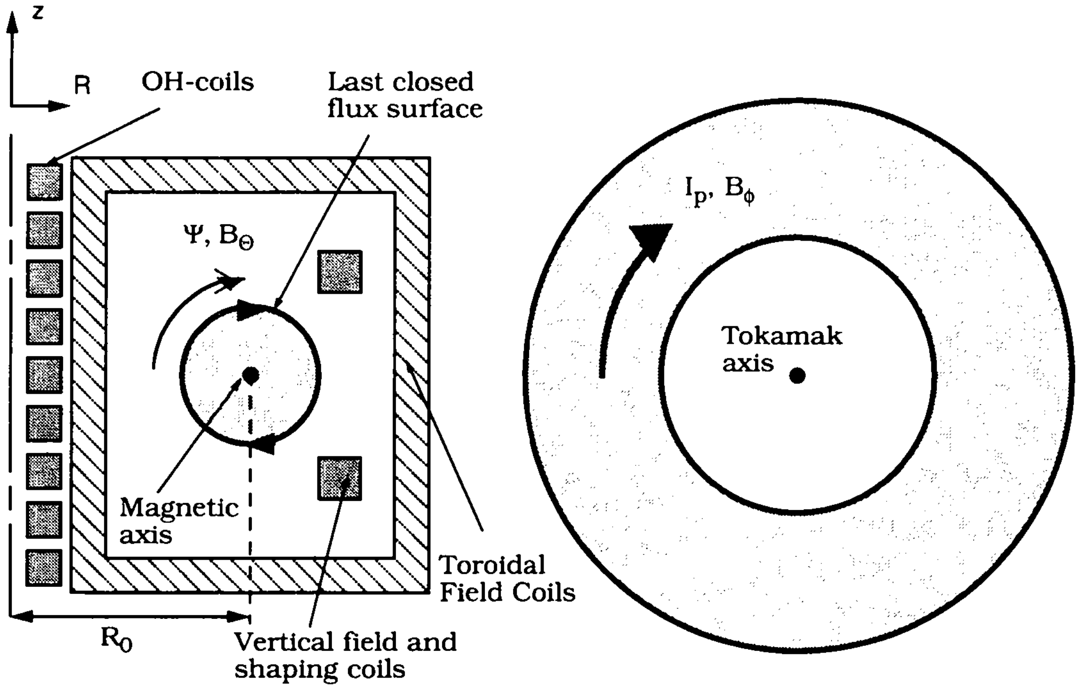

Figure 1.1: Poloidal and toroidal sections through a schematic tokamak

In a tokamak, the problem of space charge is overcome by "twisting" the field lines such that particles move periodically between the inner and outer plasma regions. The "twist" is produced by generating a poloidal magnetic field component, B_Θ, resulting from a toroidal current, I_p induced in the plasma using the windings of a large central solenoid as primary turns and the plasma as a single, secondary turn of a transformer. This toroidal current is carried essentially by the electrons owing to their large mobility (small mass) in comparison with the ions. In addition to the toroidal and poloidal magnetic field components, a vertical field produced by external coils or image currents in a conducting shell is also required to counteract hoop forces arising from the radial decrease of the magnetic field pressure and tending to expand the plasma ring.

The "twist" of the total magnetic field is characterized by the safety factor, q, describing the pitch of the helical field lines. In the circular cross-section, large aspect ratio approximation ($a/R \ll 1$, where a is the plasma minor radius), it is given by

$$q = \frac{aB_\phi}{RB_\Theta} \propto \frac{1}{I_p} \qquad (1.4)$$

The safety factor specifies the number of complete toroidal circuits a field line must make before completing a single poloidal circuit. The name originates from the requirement that $q > 1$ (known as the Kruskal-Shafranov limit [74]) everywhere for reasons of MHD stability against the lowest order kink mode.

The principal plasma heating mechanism in a tokamak is ohmic heating by means of the inductively driven plasma current. Since the ohmic power density, $p_{oh} = \eta j^2$ depends on the plasma resistivity, η and since η is a function of the electron temperature, $\eta \sim T_e^{-3/2}$, the maximum attainable temperatures are limited by the maximum attainable current density for which the above safety factor criterion is satisfied. For example, in a tokamak with $B_\phi = 1.5T$, the maximum central electron temperature that can be reached with ohmic heating alone lies in the range 1→1.5keV.

1.3 Purpose of Thomson Scattering

Of equal importance to the machine itself are the diagnostic systems required to characterize the tokamak plasma. Measurements in high-temperature tokamak plasmas, where central ion and electron temperatures of respectively $T_i(0)$ =35keV and $T_e(0)$=12keV can be reached [33], are clearly rather difficult, since methods involving physical contact with plasma particles can only be employed at the very edge where particle temperatures and densities are the lowest. Remote measurements, based on analysis of particles or radiation interacting with or emitted from the plasma, are therefore necessary to diagnose the plasma core.

The tokamak plasma may be characterized by a variety of global parameters such as plasma current, energy content and confinement time and by local parameters such as emissivity and particle temperature and density. In general, these quantities are ideally measured throughout the discharge duration with a temporal resolution short compared with the typical timescales of changes within the plasma, e.g. transitions to different confinement regimes, MHD activity. The required resolution should therefore not exceed several 10's of ms. In addition, the spatial distribution of local quantities must be resolved on a scale small compared with the overall device dimensions.

Despite their relative complexity, Thomson scattering systems have become standard tokamak diagnostics for measurements of plasma electron temperature and density profiles. Indeed, the technique was successfully applied by

Peacock et al., to confirm the high electron temperatures reported in the late 1960's by the group working on the Russian tokamak, T3 [42]. The basic process behind the technique is light scattering by free electrons, a process generally characterized by a fairly low cross-section: $\sigma = 6.65 \cdot 10^{-29} m^2$. However, the use of short-pulsed, high-power lasers together with fast and sensitive detection optics permit the measurement of T_e and n_e from ≈10eV and $\approx 10^{18}m^{-3}$ respectively. The required spatial resolution depends on the particular device dimensions. Systems currently installed on tokamaks cover the range from 2mm (RTP [11]) to 10cm (JET [39]).

1.4 Outline of this Thesis

This thesis may be divided into two major sections. The first section includes a short review of the theory of incoherent Thomson scattering (Chapter 2) whilst Chapter 3 describes in detail the Thomson scattering diagnostic installed on the TCV tokamak. Chapter 3 also contains a short introduction to TCV, the plasma performance to date and some brief notes concerning the complementary diagnostic systems whose results have been employed in this thesis.

The second section, comprising Chapters 4→8, encompasses the experimental results obtained with the TS system. Chapter 4 describes the data processing technique applied to T_e and n_e profile analysis. In Chapter 5, the performance of the TCV Thomson scattering diagnostic, both with the initial and the upgraded versions of the detection system, is presented for a variety of discharge conditions. Chapters 6 and 7 describe efforts to quantify the phenomenon of the profile consistency on TCV and to improve understanding of the influence of plasma shape on energy confinement in ohmic plasmas. In Chapter 8, a first attempt at improving the quality of plasma magnetic equilibrium reconstructions on TCV by means of plasma pressure profiles measured by the TS system brings the experimental section to a close.

2 Basic Theory of Incoherent Thomson Scattering

2.1 Introduction

The theory of light scattering in a plasma can be found in a number of standard texts ([22], [59]). An important result of the theory of Thomson scattering is the so-called scattering form factor (or spectral density function), $S(\vec{k},\omega)$, which is proportional to the spectral distribution of the scattered power. A detailed description of the theory is beyond the scope of this thesis, but in the following sections, an expression for the scattered power, P_s will be derived in terms both of $S(\vec{k},\omega)$ and $S(\Theta,\lambda)$, where Θ is the scattering angle and λ the detected wavelength in the reference frame of the observer. Once these parameters are known, the plasma electron temperature, T_e and density, n_e may be deduced.

2.2 Scattering from a Single Non-Relativistic Electron

Under the influence of the field, $\vec{E}_i$ of an incident electromagnetic wave of angular frequency, ω_i free electrons will oscillate at the same frequency. They will therefore emit radiation which forms a dipole pattern in the non-relativistic limit. Since the radiation is also emitted in directions different from that of the incident wave, the event is called scattering. If the radiation energy can be neglected with respect to the electron rest energy $(h\omega_i/2\pi \ll m_e c^2)$, the effect is known as Thomson scattering.

If $\vec{r}(t)$ denotes the spatial position of a single electron, the acceleration due to the local electric field of a plane monochromatic wave can be written as:

$$\frac{d^2\vec{r}}{dt^2} = -\frac{e}{m_e}\vec{E}_i e^{i(\vec{k}_i\vec{r}(t) - \omega_i t)} \tag{2.1}$$

where k_i is the wave vector of the incident wave. The acceleration depends explicitly on time through the phase factor, $\omega_i t$ and implicitly via the vector, $\vec{r}(t)$. The Fourier spectrum of the acceleration will therefore contain frequency components which depend on the electron motion in the absence of an electric field. This fact is at the basis of applications using the scattering process for plasma diagnostic purposes.

To compute the power scattered by an accelerated electron, the electromagnetic potentials $\vec{A}$ and Φ satisfying Maxwell's equations in the Lorentz-gauge must be calculated:

$$\vec{E} = -\vec{\nabla}\Phi - \frac{\partial \vec{A}}{\partial t} \qquad \vec{B} = \vec{\nabla} \times \vec{A} \tag{2.2}$$

The Liénard-Wiechert potentials describe an electron moving with the velocity $\vec{v}_e$ [23]:

$$\Phi = \frac{e}{4\pi\varepsilon_0}\frac{1}{R(1-\vec{\beta}(t')\hat{e}_s(t'))} \qquad \vec{A} = \frac{e\mu_0}{4\pi}\frac{\vec{v}_e}{R(1-\vec{\beta}(t')\hat{e}_s(t'))} \tag{2.3}$$

where $R = |\vec{R}| = |\vec{x}-\vec{r}|$ denotes the distance between the scattering electron and the observer, $\hat{e}_s = \vec{R}/R$, $\vec{\beta}(t') = \vec{v}_e(t')/c$ and t' is the retarded time, $t' = t - R(t')/c$ (figure 2.1). In the far field, $|\vec{R}| \gg |\vec{r}|$, we can set $R = x - \hat{e}_s\vec{r}$ so that $t' = t - (x - \hat{e}_s\vec{r}(t'))/c$.

The amplitude of the scattered wave at the observer is then to a good approximation independent of the electron location with respect to the origin so that for $\beta \ll 1$, eqn. 2.2 and 2.3 yield:

$$\vec{E}_s(\vec{x},t) = \frac{e}{4\pi\varepsilon_0 c^2}\frac{1}{R}\left[\hat{e}_s \times \left[\hat{e}_s \times \frac{d}{dt}\vec{v}\right]\right] \qquad \vec{B}(\vec{x},t) = \frac{1}{c}\hat{e}_s \times \vec{E}_s \tag{2.4}$$

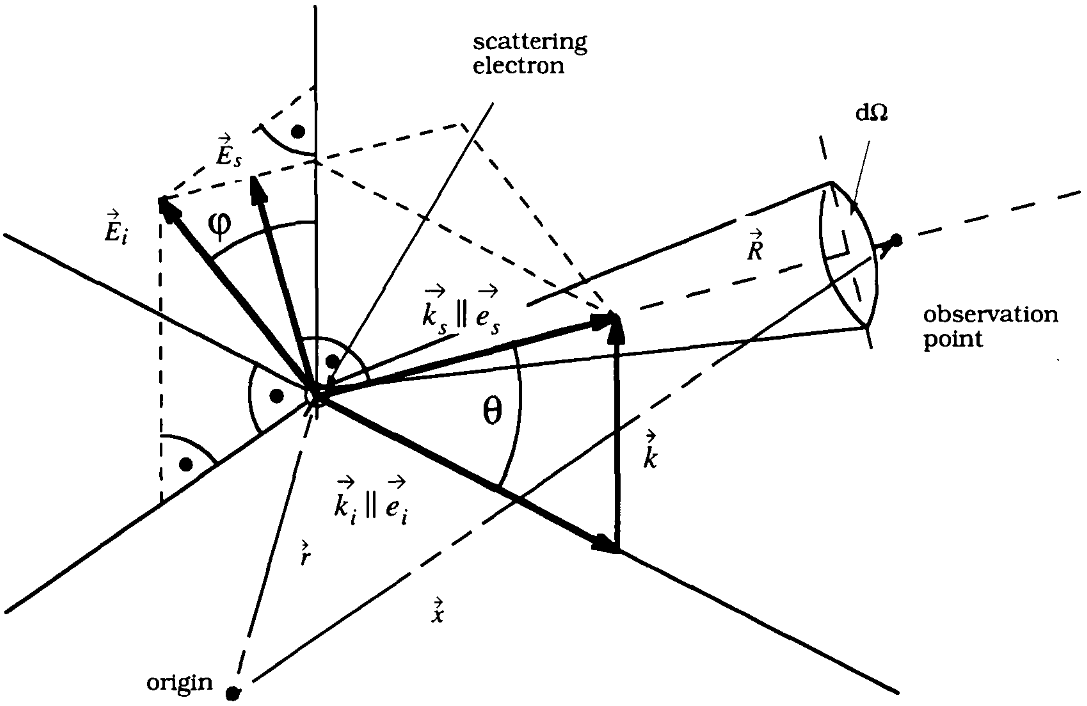
scattering electron
dΩ
$\vec{E}_s$
$\vec{E}_i$
φ
$\vec{R}$
$\vec{k}_s \parallel \vec{e}_s$
θ
$\vec{k}$
observation point
$\vec{k}_i \parallel \vec{e}_i$
$\vec{r}$
$\vec{x}$
origin

Figure 2.1: Scattering geometry for a single moving electron.

The electric field, $\vec{E}_s$, of the wave scattered from a moving electron may now be obtained using eqn. 2.1:

$$\vec{E}_s = \frac{e^2}{4\pi\varepsilon_0 m_e c^2 R}[\vec{\Pi}\times\vec{E}_i]e^{i(\omega_i t' - \vec{k}_i\vec{r}(t'))} \tag{2.5}$$

where '$\vec{\Pi}\times_{\rightarrow}$' replaces the polarization operator, '$\hat{e}_s \times_{\rightarrow} [\hat{e}_s \times\ ]$'. The vector $\vec{E}_s$ lies in the (E_i,k_s)-plane, but remains perpendicular to e_s. Due to the electron motion, the force acting on it must be evaluated at the retarded time, t'. Assuming the incident wave to be linearly polarized, the time-averaged power which an electron radiates into a solid angle $d\Omega$ is given by:

$$\frac{dP_s}{d\Omega} = \langle S_s \rangle R^2 = \left(\frac{e^2}{4\pi\varepsilon_0 m_e c^2}\right)^2 \frac{1}{2}\varepsilon_0 c \left|\vec{E}_i\right|^2 (1 - (\sin\Theta\cos\varphi)^2) \tag{2.6}$$

where $\langle S_s \rangle$ denotes the time-averaged absolute value of the Poynting vector of the scattered radiation, Θ the scattering angle between the vectors $\vec{k}_i$ and $\vec{k}_s$, φ the angle between $\vec{E}_i$ and the plane $(\hat{e}_i, \hat{e}_s)$ and

$$r_e = \frac{e^2}{4\pi\varepsilon_0 m_e c^2} = 2.82 \cdot 10^{-15} m \tag{2.7}$$

the classical electron radius. Since $\langle S_i \rangle = (1/2)\varepsilon_0 c \left|\vec{E}_i\right|^2$, eqn. 2.6 describes a linear relationship between $dP_s/d\Omega$ and $\langle S_i \rangle$. The proportionality factor

$$\frac{d\sigma}{d\Omega} = r_e^2 (1 - (\sin\Theta\cos\varphi)^2) \tag{2.8}$$

is known as the differential cross-section. The total scattering cross-section for Thomson scattering of a single free electron may be obtained by integration of this proportionality factor over Θ and φ:

$$\sigma_{TH} = \frac{8}{3}\pi r_e^2 = 6.65 \cdot 10^{-29} m^2 \tag{2.9}$$

For a time interval, T_s, long compared with the oscillation period ($T_S \gg 2\pi/\omega_i$), the frequency spectrum of the scattered electric field at the observer may be obtained by Fourier transformation:

$$\vec{E}_s(\vec{x}, \omega_s) = \int_{T_s} \vec{E}_s(\vec{x}, t) e^{i\omega_s t} dt = \frac{r_e}{R} \int_{T_{s'}} (\vec{\Pi} \times \vec{E}_i) e^{i[\vec{k}_i \vec{r}(t') - \omega_i t' + \omega_s (t' + (x - \vec{e}_s \vec{r}(t'))/c)]} \kappa' dt' \tag{2.10}$$

where $\kappa' = 1 - \hat{e}_s\vec{\beta}'$. Defining $\vec{k}_s = \omega_s\hat{e}_s/c$ and neglecting for now the electron cyclotron motion, eqn. 2.10 is integrable and yields, for constant electron velocity:

$$\vec{E}_s(\vec{x},\omega_s) = 2\pi\kappa\frac{r_e}{R}e^{i\vec{k}_s\vec{x}}(\vec{\Pi}\times\vec{E}_i)\delta(\vec{k}\vec{v}_e-\omega)$$

(2.11)

where $\omega = \omega_s - \omega_i$ and $\vec{k} = \vec{k}_s - \vec{k}_i$. The scattered field from a single electron therefore occurs at a unique frequency given by:

$$\omega_s = \omega_i + \vec{k}\vec{v}_e = \omega_i\frac{(1-\hat{e}_i\vec{\beta})}{(1-\hat{e}_s\vec{\beta})} = \omega_d$$

(2.12)

where this last expression is the Doppler shifted angular frequency, ω_d, of the incident wave arising from a combined shift due to the electron motion both towards the source and the observer. The shift is directly proportional to the particle velocity in one dimension along the scattering vector, $\vec{k}$. Based on this fact, Thomson scattering can be used as a means of deriving the velocity distribution function of a large number of particles from a measurement of the scattered power spectrum.

Since the magnitude of the Poynting vector can be written as $\langle S_s\rangle = 1/2\varepsilon_0 c|\vec{E}_s(\vec{x},t)|^2$, where $\vec{E}_s(\vec{x},t)$ is the Fourier transform of eqn. 2.11, the mean power per unit solid angle and unit frequency radiated by a single electron is (eqn. 2.6):

$$\frac{d^2P_s}{d\Omega d\omega_s} = r_e^2|\vec{\Pi}\times\vec{e}_i|^2\langle S_i\rangle\delta(\omega_s-\omega_d)$$

(2.13)

2.3 Scattering from Many Electrons

Since the scattered field of a single electron satisfies Maxwell's equations which are linear in $\vec{E}$, the scattered field of a large number of electrons can be computed by superposition of single electron contributions. When calculating the total radiation field, phase relations amongst individual electrons in the scattering volume must be considered.

Since every individual charged plasma particle (electrons and ions) is surrounded by a large number of other charged particles, the phase relations can only be properly assessed when the phase contributions of both the individual particles and the surrounding charge cloud are accounted for. The charge cloud ensures that the particle's electric potential will be shielded within a typical distance, the Debye-length λ_D,

$$\lambda_D = \sqrt{\frac{\varepsilon_0 e T_e}{n_e e^2}} \tag{2.14}$$

where T_e is given in energy units (eV). For comparable temperatures, electrons move much faster than ions so that the latter cannot follow and remain present as immobile, positive background charges. By analogy with the electron-hole model in semiconductor physics, the shielding cloud of a test electron can be imagined as an assembly of randomly distributed "absent electrons" (referred to as holes with an attributed charge equal to +e).

A parameter allowing correlations between the phases of test electrons and the shielding cloud to be assessed, is the scattering parameter, α where $\alpha = 1/(|\vec{k}|\lambda_D)$. Assuming that the scattering induces only a small change in the wavelength, $|\vec{k_s}| \approx |\vec{k_i}|$ (figure 2.2) this parameter can be written as:

$$\alpha = \frac{\lambda_i}{2\pi\lambda_D 2\sin(\Theta/2)} \tag{2.15}$$

Observing the motion of charged particles on a microscopic scale compared with the Debye-length (equivalent to the requirement $\alpha \ll 1$) only thermal motions of electrons and "holes" are identifiable. The random distribution of the “holes” in the shielding cloud will therefore ensure that the scattered fields of the electrons and the shielding cloud are incoherent. In this case, known as incoherent Thomson scattering, the total scattered power is then the sum of individual electron powers. For the TCV Thomson scattering system (scattering angles $60° \leq \Theta \leq 120°$), the condition of incoherent scattering is well satisfied at the chosen wavelength of $\lambda_i = 1.064\mu m$: $1/14 \leq \alpha \leq 1/27$ (T_e=10eV, n_e=10^{20}m^{-3}).

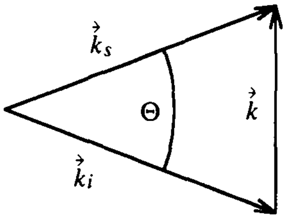

Figure 2.2: *Relation between $\vec{k}_i$, $\vec{k}_s$ and $\vec{k}$.*

In order to compute the total incoherent scattered power from a large number of electrons within a volume element, $d\vec{x}d\vec{v}$ at the point, $(\vec{x},\vec{v})$ in phase space, the location and velocity of each electron must be known for every time, t during the interval T_S. If the electrons are in thermal equilibrium, the number of electrons within the volume element is given by $fd\vec{v}d\vec{x}$, where $f = f(\vec{x}, \vec{v})$ is the Maxwellian distribution function at temperature T_e. In this case, the total incoherent scattered power spectrum can be written as:

$$\frac{d^2 P_s}{d\Omega d\omega_s} = r_e^2 \langle S_i \rangle \iint \left| \vec{\Pi} \times \vec{e}_i \right|^2 \kappa f(\vec{v}) \kappa \delta(\vec{k}\vec{v} - \omega) d\vec{v} d\vec{x} \tag{2.16}$$

where $\langle S_i \rangle$ is assumed to be constant in space.

2.4 *Relativistic Effects and the Spectral Density Function*

At values of T_e>100eV, characteristic of confined plasmas on TCV, the scattering process must be treated relativistically. In this case, the polarisation of the scattered radiation and the scattered spectrum are modified:

a) The polarisation operator '$\vec{\Pi} \times$ ' (defined in its non-relativistic form in eqn. 2.6) becomes dependent on $\vec{\beta}$ when the relativistic equations of motion are introduced. As a consequence, the electron sees a change in the orientation of the incident field vector which results in a fraction, ~β^2 of the scattered light being polarised in a direction orthogonal to the incident polarisation. For T_e≈1keV, however, the depolarisation attains values of only around 1% and can thus be neglected for ohmically heated plasmas on TCV.

b) Since approaching electrons scatter more light in the direction of the observer than those which are receding, the scattering spectrum is blue-shifted due to the forward bias in the radiation pattern of a relativistic electron. At T_e≈100eV, the asymmetry in the spectrum leads to an overestimation of T_e by 5% for Θ=90° if the spectrum is analysed only on the short wavelength side and assumed to be symmetric.

For all configurations of the TS system on TCV, both $\vec{E}_i$ and, to a good approximation, $\vec{E}_s$ are polarized perpendicularly to the scattering plane. In this case, Selden [57] derives an expression equivalent to eqn. 2.13 for the scattered power of relativistic electrons:

$$\frac{d^2P_s}{d\omega_s d\Omega} = P_i n_e L r_e^2 \frac{\omega_s^2}{\omega_i^3} \int \frac{1-\beta^2}{1-\vec{\beta}\vec{e}_s} f^*(\beta) u(\vec{\beta}) \delta\left(\frac{\omega_s}{\omega_i} - \frac{1-\vec{\beta}\vec{e}_i}{1-\vec{\beta}\vec{e}_s}\right) d\vec{\beta} \tag{2.17}$$

where $f^*(\beta)$ denotes the velocity-dependent part of the distribution function, P_i the incident laser power, L the length of the scattering volume, V, $\langle S_i \rangle / L = P_i L / V$ and

$$u(\vec{\beta}) = \left(1 - \frac{(1-\cos\Theta)}{(1-\vec{\beta}\vec{e}_i)(1-\vec{\beta}\vec{e}_s)} (\vec{\beta}\vec{E}_i)^2\right)^2 \tag{2.18}$$

Dividing the RHS of eqn. 2.18 by $(P_i n_e L r_e^2)$ yields the definition of the spectral density function, $S(\vec{k},\omega_s)$. For $100\text{eV} \le T_e \le 100\text{keV}$, Selden [56] gives a straightforward algebraic expression in which $\vec{k}$ and ω are replaced by the equivalent variables, Θ and λ_s:

$$S(\varepsilon,\Theta) = \frac{1}{\lambda_i} a(\zeta) \frac{e^{-2\zeta B(\varepsilon,\Theta)}}{A(\varepsilon,\Theta)}, \tag{2.19}$$

where

$$\varepsilon = \frac{\lambda_s}{\lambda_i} - 1, \quad \zeta = \frac{m_e c^2}{2eT_e},$$

$$A(\varepsilon,\Theta) = (1+\varepsilon^3)[2(1-\cos\Theta)(1+\varepsilon)+\varepsilon^2]^{1/2},$$

$$B(\varepsilon,\Theta) = \left[1 + \frac{\varepsilon^2}{2(1-\cos\Theta)(1+\varepsilon)}\right]^{1/2} - 1,$$

and

$$a(\zeta) = \left(\frac{\zeta}{\pi}\right)^{1/2}\left(1 - \frac{15}{16\zeta} + \frac{345}{512\zeta^2} + \dots\right).$$

The scattered spectral power can then be written in a form which will be used later in Section 3.3.1 for analysis of the scattered spectrum:

$$\frac{d^2 P_s}{d\lambda_s d\Omega} = P_i n_e L r_e^2 S(T_e,\varepsilon,\Theta) \tag{2.20}$$

Measurement of the spectral density function thus yields the electron temperature, whilst the total scattered power gives the electron density.

The small total Thomson scattering cross-section (eqn. 2.9) leads us to expect a low value for the incoherent scattering signal. Taking, as a typical example, a scattering volume of L=40mm near the tokamak plasma centre with $n_e \approx 10^{20} m^{-3}$ and assuming the scattered photons to be collected within a solid angle of $\Delta\Omega \approx 1.5 \cdot 10^{-2}$sr, only a fraction of the order of $3 \cdot 10^{-13}$ of the incident photons will reach the detection system. This crude estimate serves to illustrate the major source of difficulty when planning the installation of a Thomson scattering system. Since the detectable signal level depends on the number of incident photons and since the scattered photons must be discriminated from those due to plasma radiation (the number of which increases with the period of the measurement), a very powerful radiation source is needed. Finally, the investigation of time-dependent phenomena requires a continuous, or at the very least a repetitively emitting source. To satisfy all these requirements, modern systems use repetitively pulsed lasers emitting at wavelengths in the visible or near-infrared spectral range, sufficiently short to ensure incoherent scattering at typical tokamak plasma electron densities. The available laser energy per pulse, the desired minimum detectable electron density and the optical throughput of the detection system determine the size of the scattering volumes and hence the spatial resolution of the system.

3 *The Thomson Scattering System on TCV*

3.1 *The Tokamak TCV*

3.1.1 *Design Parameters and Performance*

The TCV tokamak ('Tokamak à Configuration Variable') has been designed explicitly for the study of the effect of plasma shape on confinement and stability [20]. Plasma currents exceeding 1MA have already been produced [21] and the maximum design elongation of κ=3 should soon be achieved. The flexibility of TCV is such that limited or diverted configurations with varying triangularity and elongation can readily be formed, even from one discharge to the next. This flexibility is due in part to the provision of 16 independently driven poloidal field shaping coils mounted in two vertical stacks of 8 on each side of the vacuum vessel.

The vacuum vessel itself is of almost rectangular cross-section (fig. 3.1). The internal surface area ($\approx 23m^2$) is presently covered to 64% by graphite protection tiles (top and bottom, inner wall, belt limiter on the outer wall). Vessel bakeout to $200^{\circ\circ}$C and "boronization" by plasma chemical vapour deposition in a $10\%B_2D_6/90\%He$ gas mixture are standard vessel conditioning techniques. During operation, the typical base vacuum level resides at $p \approx 5 \cdot 10^{-9}$mbar. Depending on the operational campaign (limited or diverted plasmas, H-mode operation etc.) He glow discharge cleaning is used extensively as a means of controlling the short term recycling.

Since the beginning of operation in November 1992, TCV has produced a wide range of limited discharges, in most cases with the Last Closed Flux Surface (LCFS) defined by the central column tiles and a host of diverted configurations including single (Single Null Upper and Lower, SNU/SNL) and double null (Double Null Diverted discharge, DND) equilibria. To date, limited ohmic L-modes (Low energy confinement) and H-modes (High energy confinement) together with diverted ELMy (Edge Localized Mode) and ELM-free H-modes have been achieved. The following discharge parameters have been attained:

I_p>=1MA, -0.77<=δ<=0.86, 1<=κ<2.47, $<n_e>_L$<=$2.25 \cdot 10^{20}m^{-3}$ (fig. 3.2). A pair of fast internal stabilization coils, recently successfully commissioned, together with modifications to part of the graphite first wall armour should soon allow the parameter range to be extended to the design limits (Table 3-1).

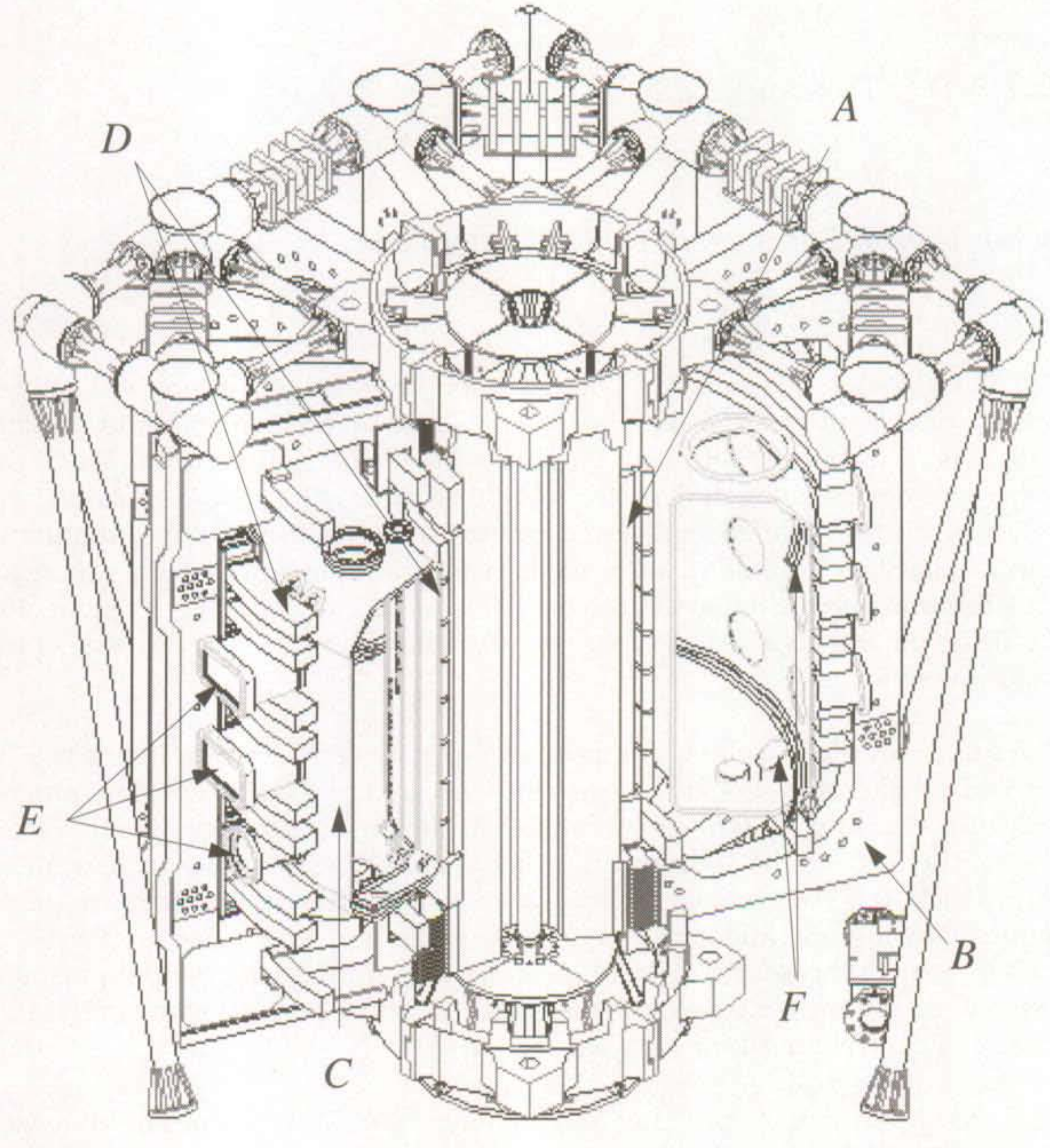

Figure 3.1: Schematic view of TCV. (A): OH-transformer coils, (B): Toroidal field coils, (C): Vacuum vessel, (D): Shaping coils, (E): Observation ports, (F): Internal shaping coils

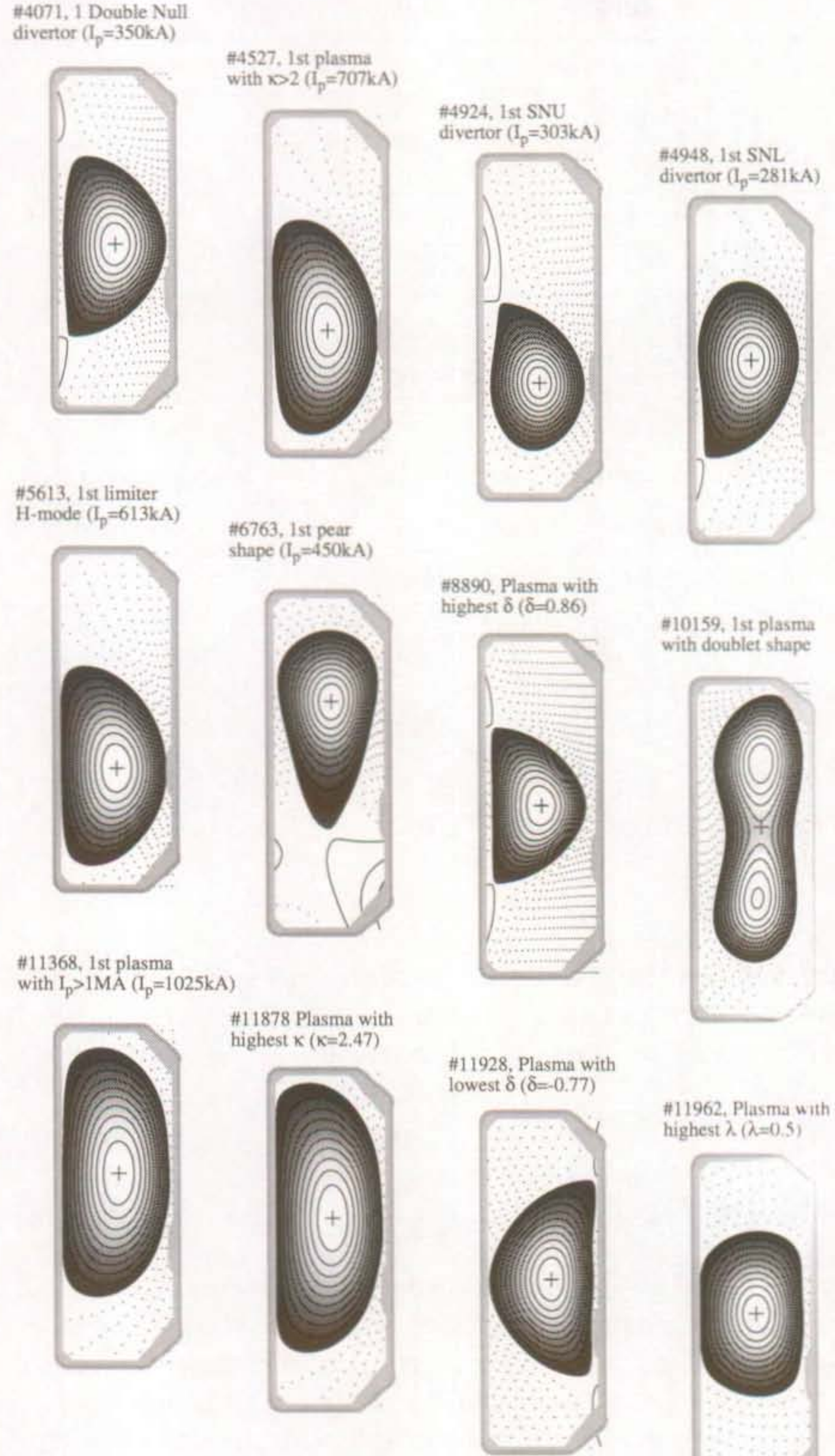
#4071, 1 Double Null divertor (I_p=350kA)
#4527, 1st plasma with κ>2 (I_p=707kA)
#4924, 1st SNU divertor (I_p=303kA)
#4948, 1st SNL divertor (I_p=281kA)
#5613, 1st limiter H-mode (I_p=613kA)
#6763, 1st pear shape (I_p=450kA)
#8890, Plasma with highest δ (δ=0.86)
#10159, 1st plasma with doublet shape
#11368, 1st plasma with I_p>1MA (I_p=1025kA)
#11878 Plasma with highest κ (κ=2.47)
#11928, Plasma with lowest δ (δ=-0.77)
#11962, Plasma with highest λ (λ=0.5)

Figure 3.2: Various discharge configurations produced in the TCV tokamak

Table 3-1: TCV Design Parameters

Major Radius	0.875 m
Vessel Internal Full Width	0.56 m
Vessel Internal Full Height	1.54 m
Nominal Aspect Ratio	3.66
Maximum Plasma Elongation	3.0
Plasma Triangularity	-0.77 -> 0.86
Maximum Toroidal Field on Magnetic Axis	1.43 T
Maximum Plasma Current	1.2 MA
Flux Swing From Air Core Transformer	3.4 Vsec (+/-1.7 V)
Maximum Loop Voltage	10 V/turn
Wall resistance of vacuum vessel	55 mΩ
Average Wall Thickness	1.8 cm, stainless steel

3.1.2 Relevant Diagnostics on TCV

Table 3-2 summarizes the diagnostic set currently available on TCV. The following sections will present in more detail those diagnostics of particular importance to the results presented in this thesis.

3.1.2.1 Magnetic Diagnostics

Magnetic probes and flux loops are required for plasma control and equilibrium reconstruction. The unique flexibility of TCV for shape control renders the magnetic diagnostic set extremely important and extensive. At four separate toroidal locations, arrays of 38 probes are placed in poloidal bands around the inside of the vacuum vessel behind the graphite protection tiles. These probes measure the component of the poloidal field tangential to the vessel wall. Further, identical probes have been added on the low (total of 4) and the high (total of 8) field side midplanes to form toroidal bands which are used to determine the toroidal mode numbers (n<=8) of observed MHD-activity. A set of 38 full or partial poloidal flux loops and 25 saddle coils are wound on the outside of the vacuum vessel. The entire set of magnetic measurements is used for evaluation of the plasma equilibrium in the equilibrium inversion code, LIUQE (Chapter 8, [19]).

Table 3-2: Diagnostics on TCV

Type of Diagnostic	Measured Parameter
Magnetics: Pick-up coils, flux loops and diamagnetic loop	Plasma equilibrium and shape control, equilibrium reconstruction, plasma stored energy
Far infrared Interferometer (FIR)	Line integrated electron density
Soft X-ray tomography	Plasma emissivity
Ultrasoft X-ray spectroscopy	Helium and Hydrogen like light impurities
X-ray monitor diodes	Central electron temperature, toroidal mode numbers
Bolometry	Plasma radiated power distribution
Neutral Particle Analyzer (NPA)	Central ion temperature
Visible spectroscopy	Impurity lines, Bremsstrahlung, edge ion temperature
Visible light monitors	D_α and impurity lines
Soft X-ray pulse height analyser	Metallic impurities, suprathermal electrons
Infrared camera	Divertor target temperature, power load
Langmuir probe array	T_e and n_e at divertor targets
Hard X-ray monitor	Suprathermal electrons
Visible camera (tangential)	Plasma position and boundary shape

3.1.2.2 *Far Infrared Interferometer (FIR)*

The FIR installed on TCV is of the Mach-Zehnder type and provides line integrated measurements of the electron density, $\bar{n}_e$ along a maximum of 6 vertical chords in a single poloidal plane. This line density is proportional to the phase shift, at the beat frequency, between a beam passing through the plasma and a frequency shifted reference beam. At the chosen wavelength of 214.6μm, only minor refraction effects may be observed even at very high line averaged densities ($<n_e>_L \approx 2.2 \cdot 10^{20} m^{-3}$) and measurements are typically made at a precision of about $5 \cdot 10^{17} m^{-2}$. At present, pyroelectric detectors and collection optics limit the temporal resolution to about 6kHz and the chord diameter to approximately 20mm. During TCV operation, real time processing of the central chord signal at R=0.9 m is used for feedback control of the plasma electron density.

3.1.2.3 Soft X-ray Tomography

This diagnostic measures the line integrated plasma X-ray emissivity in the energy range 1→10 keV. Since impurity line emission from the plasma edge in the visible and VUV-range is filtered by Beryllium absorption foils of 47 μm thickness, the X-ray signal originates essentially from bremsstrahlung and recombination radiation. The system consists of 10 linear detector arrays, each comprising one strip of 20 Silicon pin diodes. The arrays are distributed in 9 ports of a single poloidal sector to give full poloidal coverage. The resulting 200 lines-of-sight are used to perform a tomographic reconstruction [1] of the local X-ray emissivity for all plasma configurations on TCV (typical resolution: 30-40 mm).

Since the local X-ray emissivity is a strong function of T_e and n_e, the measured signals are sensitive, for example, to the presence of MHD-instabilities. In the particular case of sawtooth oscillations, analysis of the emissivities by the method of singular value decomposition yields the geometric location of the sawtooth inversion radius or, equivalently, the q=1 surface [25]. Additional information regarding the concentrations of main impurity ions is required for evaluation of the local radiated power and effective ion charge from the soft X-ray measurements [70].

3.1.2.4 Ultra Soft X-ray Spectroscopy

A calibrated polychromator based on a set of synthetic, multilayer mirrors permits the selective measurement of line emission in the spectral range 200→800eV. In the case of TCV, the diagnostic is most often used to obtain the radiation level from Hydrogen and Helium like states of highly ionized light impurities such as Boron, Carbon, Oxygen and Nitrogen. The instrument is mounted vertically above the vacuum vessel so that its viewing chords cross the plasma typically at 40% of the minor radius. In most cases (but depending on the T_e profile), the largest fraction of the line radiation originates from the outer regions of the plasma. Under certain simplifying assumptions, the relative impurity concentrations derived from the measurement can be used to compute a value for the plasma effective ion charge, Z_{eff} [71].

3.1.2.5 X-ray Monitor Diodes

An ensemble of 4 Silicon diodes collect the X-ray emission along a slightly off-centre vertical line-of-sight (R=0.84 m). The detection bands are individually limited by Beryllium high-pass filters of various cut-off energies, E_c. Since the local emissivity for a given detection band is proportional to the product, $n_e^2 Z_{eff} e^{-E_c/T_e}$, T_e can be determined from the ratio between the detected power in two different channels. This strong dependence on the central T_e makes the temporal evolution of the X-ray temperature, T_e^X, very sensitive to sawtooth oscillations. Combination of this temperature with $\bar{n}_e$ measurements from the FIR-interferometer gives readily available, but not always very accurate estimation of the central Z_{eff}.

3.1.2.6 Bolometry

Bolometer sensors using Au-foils measure the total incident radiation power in a wide spectral range, 1eV→10keV. A total of 64 detectors are distributed in a poloidal plane in an arrangement similar to that for the soft X-ray cameras. The relatively low number of lines-of-sight and high fluctuations in the radiated power level (e.g. from line radiation near plasma/surface interaction zones) makes accuracy in tomographic inversion more difficult to achieve than for the soft X-ray range. The measurement nevertheless gives a good estimate of the total radiated power.

3.1.2.7 Neutral Particle Analyser (NPA)

An electrostatic analyser with a time resolution of 20ms is used to deduce the ion temperature from energy distribution measurements of the neutral particle charge-exchange flux along a vertical line-of-sight (R=0.9m). By an appropriate selection of the energy range, an ion temperature characteristic of the plasma centre can be deduced, but the measurement is strongly influenced by the neutral source distribution at the plasma edge.

3.1.2.8 Visible Spectroscopy

The system consists of a high resolution Czerny-Turner spectrometer and an optical multi-channel analyser. The plasma radiation is collected along a vertical chord at R=1.05m and transmitted to the spectrometer via an optical fibre. The system measures line spectra with a typical resolution of 2.5ms, from which the impurity species, plasma bulk motion and the ion temperature can be deduced. Using a CX transition of Boron (BV, n=8-7), the system can be used to provide ion temperature measurements in the outer plasma regions.

3.2 The Thomson Scattering Experiment on TCV

3.2.1 General Design Aspects

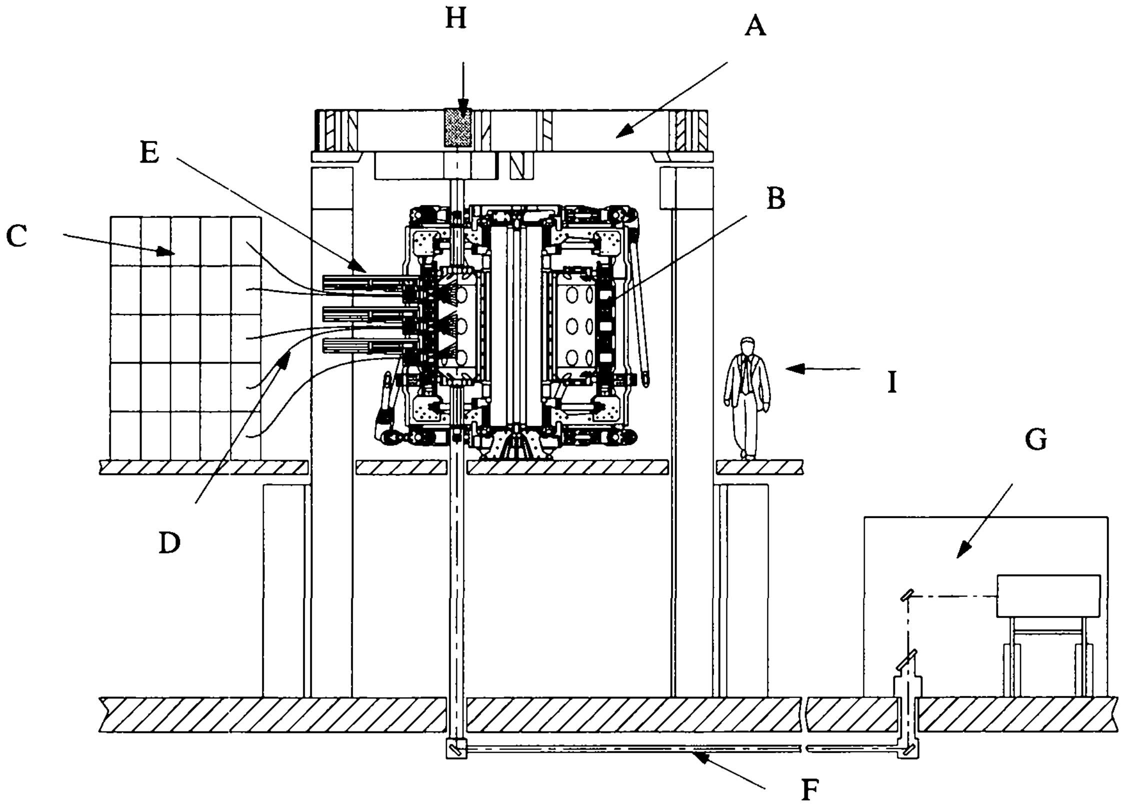

Figure 3.3: Overview of the Thomson Scattering System on TCV, (A): Support structure, (B): Vacuum vessel, (C): Polychromator rack, (D): Glass fibres, (E): Precision slides and objectives, (F): Closed beam duct, (G): Laser room, (H): Beam dump, (I): Standard physicist

To account for the wide variety of possible plasma equilibria, the TCV Thomson scattering system has been designed to collect the scattered radiation along a vertical chord across almost the entire poloidal vessel cross-section (fig. 3.3, 3.4). To ensure both good coverage of the vertical chord by the scattering volumes and permanent access to the vacuum vessel, low f-number optics mounted in three horizontal ports project the scattered radiation onto highly transmissive fibre bundles. For spectral analysis, the radiation is transported to interference filter polychromators whose f-number is adapted to the numerical aperture of the fibres. An appropriate choice of the filter bandwidth, permits the measurement of electron temperatures in the range 50eV→2.5keV for electron densities greater than $5\cdot10^{18}\text{m}^{-3}$ (see appendix B). As a first step, a system comprising only 10 spatial channels has been implemented, using polychromators with three filter channels. The major part of the results presented in this thesis has been obtained with this system. Recently, it has been upgraded to 25 spatial channels permitting full coverage of the vertical extent of highly elongated plasmas (fig. 3.4b).

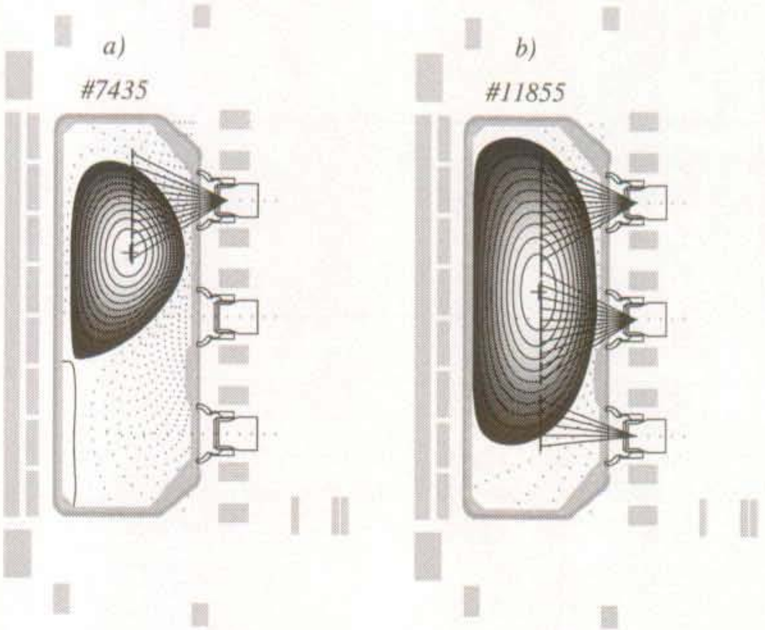

Figure 3.4: Schematic view of the two scattering configurations used with respectively 10 and 25 observation volumes: a) Discharges #7109-10213, b) #10214 onwards. The configuration with 10 observation volumes was equipped with "3-channel" polychromators, whilst the upgraded configuration with 25 observation volumes uses "4-channel" polychromators.

Fig. 3.5 illustrates schematically the order in which the various aspects of the TCV Thomson scattering system will be described in the remainder of this chapter.

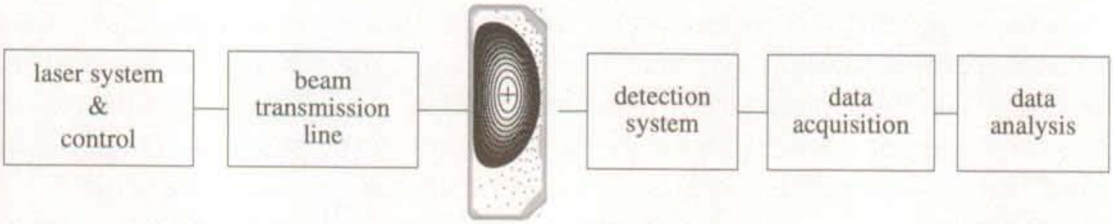

Figure 3.5: Flow chart illustrating the order in which elements of the TS system will be described in the following sections.

3.2.2 Layout of the System

3.2.2.1 Laser System

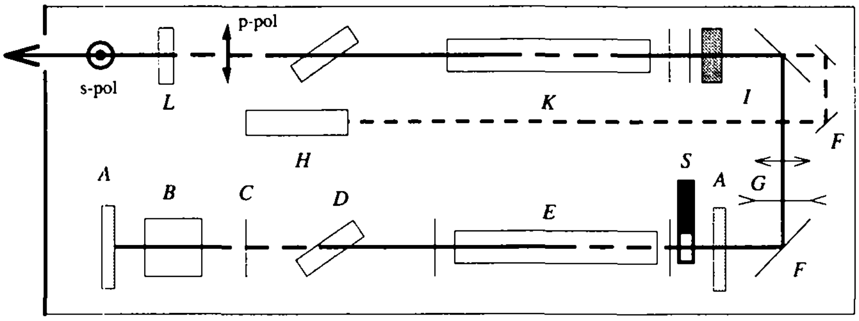

Figure 3.6: Schematic top view of the Nd:YAG-laser. (A): Cavity Mirror, (B): Pockels Cell, (C): Quarter-wave plate, (D): Dielectric polarizer, (E): Laser oscillator, (F): Bending mirror, (G): Telescope, (H): Alignment laser, (I): Quartz-plate, (K): Laser amplifier, (L): Half-wave plate, (S): Intra-Cavity Shutter

We have chosen a commercially available, high power, Q-switched Nd:YAG-laser (Continuum, model YG-681-C), consisting of a combined oscillator-amplifier unit emitting at λ=1.064 μm and operating at repetition frequencies of up to 20Hz. The internal structure of the laser unit (fig. 3.6) has been adapted to optimize the output energy in the horizontally polarized direction. The thermally induced birefringence due to the photoelastic effect of thermal strains in the laser rod causes a depolarization of radiation from the oscillator. Turning both polarization directions of the oscillator beam by 90° using an optically active quartz-plate between the oscillator and the amplifier, allows this depolarization to be partially compensated, when the beam passes through the laser amplifier. A dielectric polarizer at the Brewster angle after the laser amplifier rejects the vertical polarization direction. The output energy attainable per pulse for an optimized internal Q-switch delay is between 1.0→1.1J, with a typical pulse width of 10→15ns. The beam diameter at the laser unit output is approximately 10mm with a measured half-beam divergence of 0.5 mrad. To allow permanent access to the laser system (even during TCV operation) and to protect against interference from tokamak stray fields, the laser unit has been placed in a separate area.

3.2.2.2 Optical Beam Path

Table 3-3: Parameters of Focusing Optics

Location of telescope	distance of 2nd lens to final combination focal point [m]	f(Lens 1) [mm]	f(Lens 2) [mm]	Distance between Lens 1 and 2 [mm]	Effective focal length [m]
Laser room	33.7→45.6	-300	475	180→182	20.5→28.5
Beam duct below tokamak	6.1→6.5	-380	620	305→310	3.3→3.6

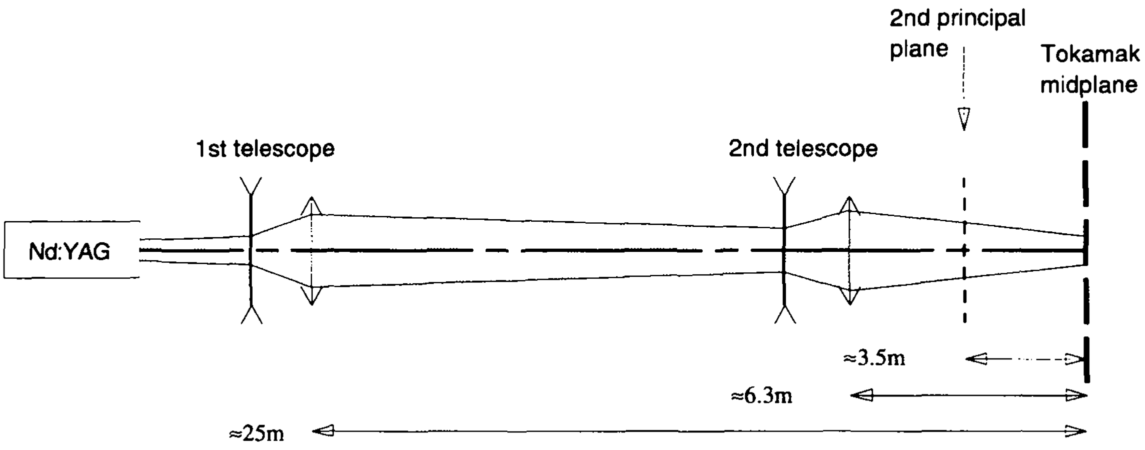

Figure 3.7: Focusing optics for Nd:YAG beam path

By means of 10 steering mirrors, the laser beam is guided to the vacuum vessel, passing through it from bottom to top. The arrangement keeps the linear polarization of the beam such that the E-field vector is parallel to the toroidal B-field in the plasma midplane. The mirrors are treated with a special high reflection coating, which although optimized for $\lambda=1.064\mu m$, still permits the use of a He-Ne laser for alignment purposes. The simultaneous requirements of a homogeneous laser power deposition profile along the vertical chord and a power load on the entrance and exit windows below the damage threshold ($\approx 1GW/cm^2$) makes further beam shaping necessary. Adaptation of the beam divergence by a telescope in the laser room and its focusing by a second telescope 6m away from the tokamak midplane (Table 3-3, fig. 3.7), leads to a beam spatial profile along the vertical chord, increasing from Ø≈2mm at the vessel midplane to Ø≈4mm for the outermost observation volumes. To avoid breakdown of the air in between the two lenses, both telescopes are a combination of a negative and a positive lens (in direction of the laser beam). The entrance and exit Brewster windows are mounted on long extension flanges to limit the power load there ($\approx$250MW/cm^2), whilst the level of stray light from the windows is reduced by a set of diaphragm baffles inside the flanges. In fact, the almost complete coverage of the inner vessel walls by carbon tiles provides an effective viewing dump for the detection optics and stray light levels have been found to be negligible.

After passing through the vacuum vessel, the beam is collected in a beam dump (fig. 3.8), which completely absorbs the laser power. Careful design of the beam guide optics ensures that between 0.8→0.9 J of the laser energy arrives at the tokamak midplane, giving an overall energy loss for the system of only 25-30%.

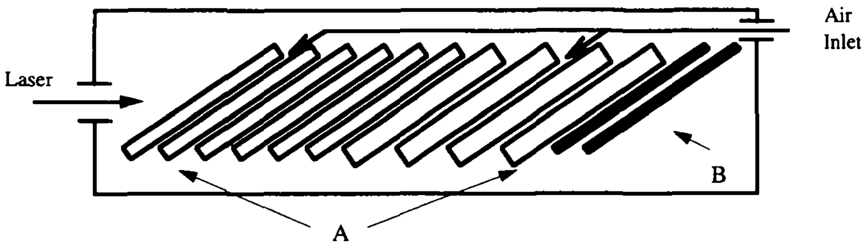

Figure 3.8: Schematic view of the beam dump, (A): window glass plate, (B): Cobalt glass absorbers

3.2.3 Detection Optics

The radiation scattered from the vertical beam is collected by wide angle camera lenses [51] inserted into three horizontal ports at z=-460mm, 2.5mm and 455mm relative to the TCV equatorial plane and positioned directly behind reentrant vacuum windows giving a distance of 350mm from the laser chord to the front end of the lens. Safety shutters close automatically to protect the observation windows from coating during boronization or glow discharges. The optical axes of the camera lenses and the laser chord are arranged such that the scattering plane is perpendicular to the toroidal magnetic field.

The wide angle camera lenses (f=95mm, front lens: Ø=80mm) have been specially designed for this application [51]. The f-number (f#=2.2), is adapted to the numerical aperture of the fibres (N.A.=0.22) and each lens projects a 50cm long section of the plasma with a magnification of m=0.3 onto the front ends of at most 11 fibres in the image plane. The vignetting losses out to 0.8 of the relative field are below 10% and could be kept below 30% at maximum field (30° off axis). Each camera lens and associated fibres may be remotely or manually inserted into, or retracted from, the torus observation port using a pneumatically driven precision slide onto which also the fibre front ends are fixed (fig. 3.9).

The optical fibre bundles (CeramOptec, Optran WF 1000/1100) consist of 9 single quartz glass, large core fibres (Ø=1mm). Mounted in line, their front ends define the scattering volume dimensions (35-40 mm). At the polychromator end, fibre bundles with rectangular and circular sections respectively are used with the *"3-channel"* and *"4-channel"* versions.

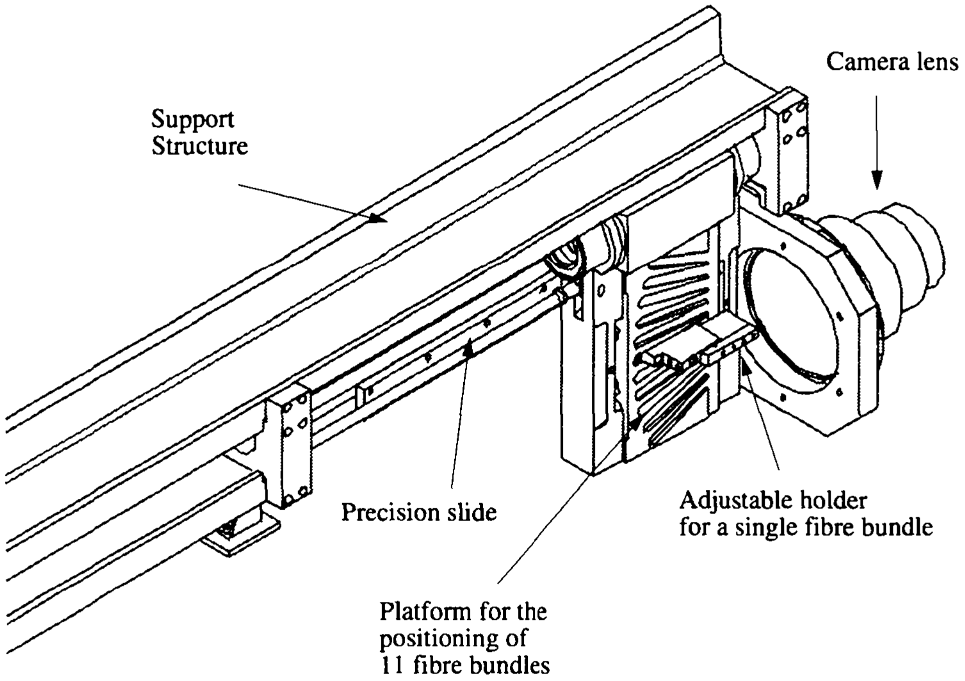
Support Structure
Camera lens
Precision slide
Adjustable holder for a single fibre bundle
Platform for the positioning of 11 fibre bundles

Figure 3.9: Support structure for the optical fibres and camera lens

3.2.4 Filter Polychromators

Different kinds of spectrometers can be used as dispersive elements for analysis of the scattering spectrum, although grating spectrometers or filter polychromators are most commonly employed. Grating spectrometers in combination with CCD-cameras (so-called TV-Thomson scattering systems) are capable of spatial resolutions as low as 2mm [11]. However, to achieve high sensitivity at high spatial resolution requires higher laser power, which is only available from single pulse systems (e.g. single pulse ruby lasers). Therefore, TV systems presently operate at very low sampling frequencies (a few Hz). Grating spectrometers may also be used in repetitively pulsed systems, but the generally higher f-number compared with filter polychromators means that the latter are preferred when seeking the highest sensitivity for a given spatial resolution. Filter polychromators with low f-numbers are, moreover, better adapted to the large numerical aperture of the fibre bundles. Repetitively pulsed Thomson scattering systems based on Nd:YAG or Nd:YLF lasers thus generally make use of filter polychromators. Several examples can be found on other modern tokamaks (DIII-D [7], ASDEX-Upgrade [38], FTU [40]).

The filter polychromators used on TCV divide the scattered radiation into a maximum of 4 spectral channels on the short wavelength side of the laser line. Each spectral channel comprises a wide-band interference filter and a low-pass edge filter, used as a blocking filter. As a consequence of their high quantum-efficiency in the visible and near infra-red regions of the spectrum, Silicon-avalanche photodiodes are used as detectors.

As mentioned earlier, the TCV Thomson scattering detection system has recently been modified with regard to the filter polychromator number, layout and electronic design. We distinguish, therefore, between a *"3-channel"* and a *"4-channel"* version. Since the main physical results contained in this thesis (Chapters 6, 7 and 8) have been obtained with the *"3-channel"* version, we first describe its technical layout, before detailing the modifications leading to the *"4-channel"* version.

3.2.4.1 The "3-channel" filter polychromators

For this first version of the TS system, the 10 polychromators attributed to the 10 observation volumes are stacked inside a welded structure located at about 7m radially distant from the tokamak axis. To shield electronic and optical components, each polychromator casing consists of a closed, black aluminium box (dimensions: $32 \cdot 12 \cdot 101$ cm^3).

3.2.4.1.1 Optical Layout

Fig. 3.10 illustrates schematically the optical imaging in a single *"3-channel"* filter polychromator. At its entrance slit, the fibre bundle carrying the scattered signal is fixed in a holder, adjustable in both the horizontal and vertical directions. High quality camera lenses (ISCO Kiptaron, f=50 mm, f#=1.2) are used as entrance and detector objectives and produce a reduced image (magnification m≈0.7) of the fibre bundle on the sensitive area of the detectors ($0.8 \cdot 7\text{mm}^2$). A field lens (f=175mm) placed in the intermediate image plane projects the pupil of the entrance objective onto that of the detector objective. An aperture for stray light rejection is placed close to the intermediate image plane.

Three wide-band interference filters are integrated into the optical path as beam splitters and can be tilted about horizontal and vertical axes. Blocking filters are placed in front of the detector objectives. Whilst the optical paths of the second and the third channel (from the aperture for stray light rejection to the detector lenses) are equivalent, the path of the first channel is significantly longer. As a consequence, the beam diameter in this channel becomes larger before reaching the focusing lens in comparison with the channels two and three and gets closer to the limiting aperture (lens diameter, filter diameter, see fig. 3.10). For off-axis beams, the spectral channel 1 and 2 will suffer to a larger amount of vignetting when the polychromator is illuminated within the full numerical aperture of the fibre bundle. The consequences of this vignetting effect for calibration measurements are discussed in Section 3.4.1.2. Table 3-4 lists the combination of wide band filters which has been chosen to cover a range of T_e from 50eV→2.5keV with an acceptable signal-to-noise ratio, S/N>=10 (see appendix B). Stray light rejection at the laser line is better than 10^{-6}.

Table 3-4: Interference Filter Characteristics

Spectral Channel	λ_{centre} (nm)	FWHM (nm)
F1	1045	20
F2	1012	45
F3	960	60

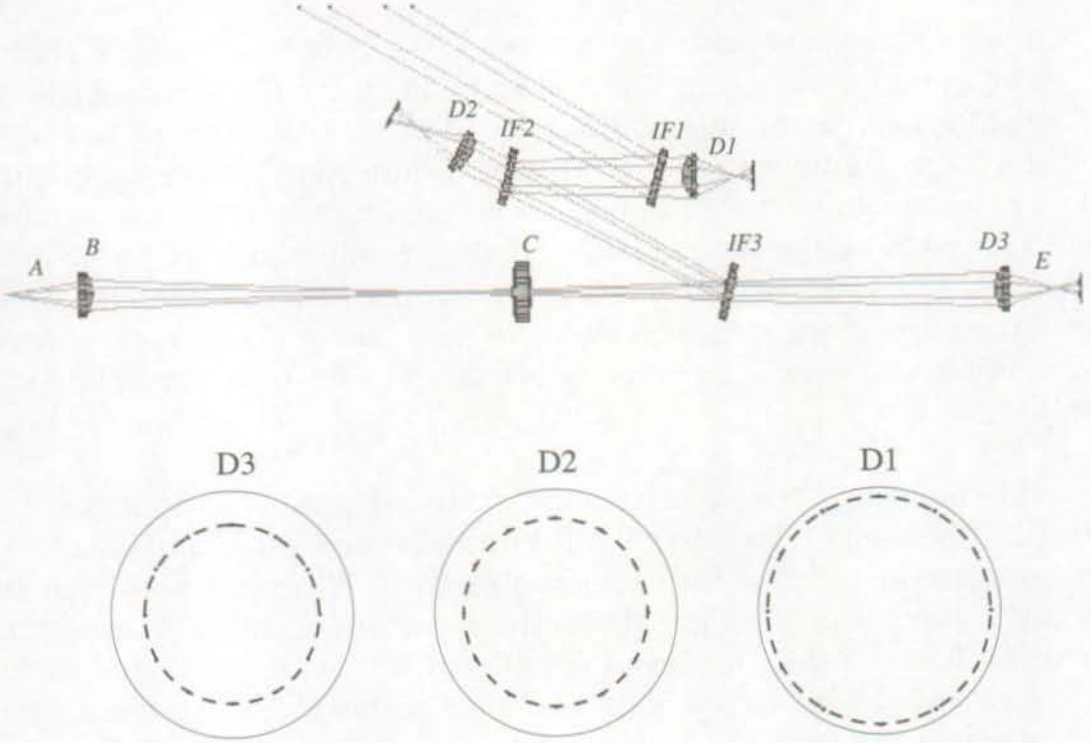

Figure 3.10: Result of ray tracing analysis for on-axis rays with an angular field of view of 20° in a "3-channel" filter polychromator; 'A': Object plane, 'B': Relay lens, 'C': Field lens, 'Dx': Focusing lens and low-pass filter, 'IFx': Wide band interference filter where x denotes the spectral channel (Table 3-4), 'E': Image plane. The bottom picture shows the calculated beam diameter at the position of the focusing lenses relative to their effective diameter. The enlargement of the beam diameter in the first spectral channel compared with channels 2 and 3 is clearly shown.

3.2.4.1.2 Detectors

The small Thomson scattering cross-section together with the short-pulse operation of the Nd:YAG-laser require fast and sensitive detectors in the near infra-red spectral range. Silicon avalanche photodiodes have become a widely used detector type due both to their favourable quantum efficiency of between $\rho=0.8$ at $\lambda=960$nm and $\rho=0.2$ at $\lambda=1060$nm and to their high internal gain factors ($M\approx100$) at a NEP of the order of $10^{-13} W/Hz^{1/2}$. The sharp drop in their efficiency for longer wavelengths limits the domain of application to the short wavelength side of the laser line. The *"3-channel"* polychromators use avalanche diodes (RCA, model C30974E) with a system bandwidth of 20MHz as detectors. Each detector module incorporates a preamplifier, such that responses of up to $3.7\cdot10^5$V/W are achieved when the diodes are operated close to their maximum bias voltages (typically between 340V and 380V at room temperature). A stabilised, external HV-power supply provides a reference bias voltage of U_B=400V, which is then adapted by individual voltage dividers. Varying the response of each diode by modifying U_B permits adjustment of the output signal to match the dynamic range of the subsequent high-frequency amplifiers.

A disadvantage of avalanche photodiodes is the temperature dependence of the avalanche gain due to the temperature dependence of the charge carrier ionization rates. Heat dissipation in the preamplifiers leads to a gradual rise in the detector temperature and a consequent decrease in its response. This degradation stabilizes after approximately one hour. To monitor the detector response each one is irradiated with short pulses (Δt=5µs) from a single stable LED reference diode (λ_l=940nm), coupled to each detector element via optical fibres. Variations in sensitivity are measured by comparing the signal from a given detector with that from a reference detector. This normalization is also used following any variation in the applied bias voltage.

3.2.4.1.3 Signal Amplification

The preamplifier output signals are divided into a high and a low frequency branch, of which only the HF-branch will be considered here. The inverting HF-amplifiers (773CM, bandwidth 50 MHz) have individually adjustable gains of $g_{HF} \leq 50$. The gain factors must be selected and measured for all channels before each experimental campaign. The maximum signal amplitude of -1V in the linear regime limits the dynamic range of the system.

3.2.4.2 The "4-channel" Filter Polychromators

In upgrading the vertical TS system to 25 observation volumes, a new version of the polychromator was designed which is equipped with four spectral channels (fig. 3.11). A new type of detector-preamplifier modules is used (EG&G, LLAM 1787) which comprises a circuit for active temperature stabilization. In order to obtain a modular system, the generation and transmission of reference light pulses has been incorporated into each polychromator. The new design also features improved detection electronics equipped with remotely controllable HF-amplifiers.

3.2.4.2.1 Optical Layout

In the previous version the input slit of the polychromator was formed by the rectangular pattern of the fibres at the end of the bundle. This slit was then imaged onto detectors with a rectangular sensitive area (detector type available at that time). With regard to vignetting it is more advantageous to arrange the fibres in a circular pattern of the same area, thus reducing the required field of view. This choice imposes naturally detectors with circular sensitive areas. F-number of input and focusing optics could be kept low by using aspherical lenses (Table 3-5, fig. 3.12). At present, only 3 spectral channels in each polychromator are fully equipped. Two sets of interference filters are used to cover the temperature ranges of 50eV$\leq T_e \leq$2.5keV and 100eV$\leq T_e \leq$5keV (Table 3-6).

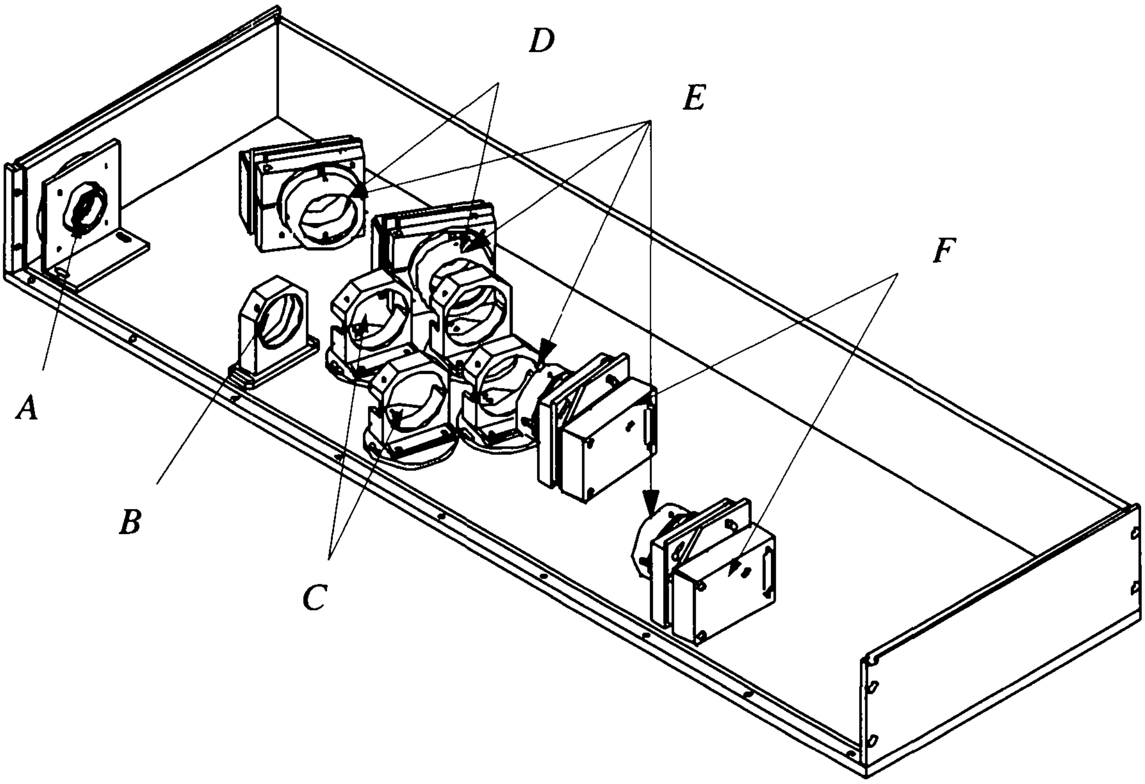

Figure 3.11: Isometric view of the "4-channel" filter polychromator, (A): Relay lens, (B): Field lens, (C): Wide band interference filters, (D): Low pass blocking filters, (E): Focusing lens, (F): Detector and amplifier modules.

Table 3-5: Optical Components of the "4-channel" Polychromators

	Shape	Focal Length [mm]	Diameter [mm]
Relay lens	plano-aspheric	28	31.5
Field lens	bi-convex	140	40
Focusing lens	plano-aspheric	42	50

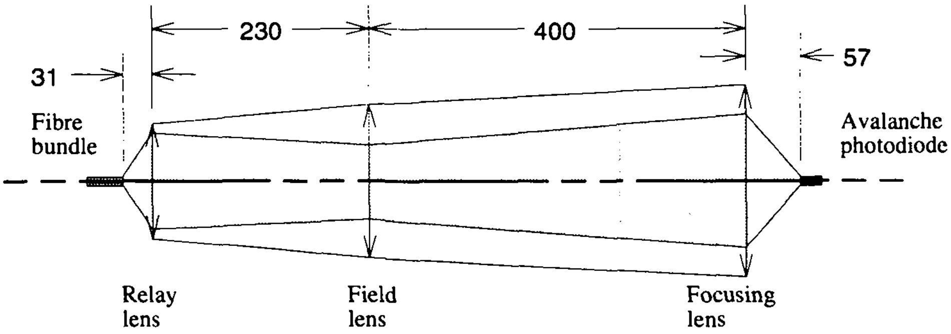

Figure 3.12: Imaging geometry for a single spectral channel

Table 3-6: Interference Filter Combinations for the "4-channel" Polychromators

	T_e-range $50eV \leq T_e \leq 2500eV$		T_e-range $100eV \leq T_e \leq 5000eV$	
Spectral Channel	λ_{centre} (nm)	FWHM (nm)	λ_{centre} (nm)	FWHM (nm)
F1	1041	20		
F2	1012	38	1012	38
F3	950	85	950	85
F4			830	160

3.2.4.2.2 Detectors

In this four channel version, the detector element (RCA, model CD1787) is mounted onto a Peltier thermo-electric circuit. A feedback circuit controls the current through the Peltier cooler and stabilizes the temperature of the avalanche diode to ±0.1°C around the preselected value of 13.2°C for optimized signal-to-noise performance. The high voltage power supplies for the detectors in this upgraded version are now placed inside the polychromator housing so that, although the avalanche voltages can still be individually adjusted, this can no longer be performed from outside the polychromator casing.

3.2.4.2.3 Signal Amplification

The output of the detector-preamplifier modules is connected to a set of three HF-amplifiers (Burr-Brown OPA-603, bandwidth 50Mhz). Each stage can be addressed via remote control (using local BITBUS links). The HF-gain factors may be increased from $g_{HF}{\approx}0.5$ to $g_{HF}{\approx}100$ in 8 steps, allowing the signal amplitudes to be matched to the dynamic range of the subsequent digitizers on a shot to shot basis.

3.2.5 Laser Operation and Control

During a TCV-shot cycle, laser operation (ignition of the flashlamps, activation of the Q-switch, action on intra-cavity shutters) is fully remotely controlled. The required trigger signals are generated by local slave units [29] and synchronized to the 1MHz TCV master clock pulses. The temporal resolution is sufficient to optimize the flashlamp and Q-switch triggers for maximum energy output performance (delay≈300μs), but is not precise enough for synchronization of the data acquisition units. Before each shot operation cycle, the trigger and timer parameters can be interactively modified via graphical VSYSTEM interfaces linked to live VSYSTEM databases residing on the VAX-computers.

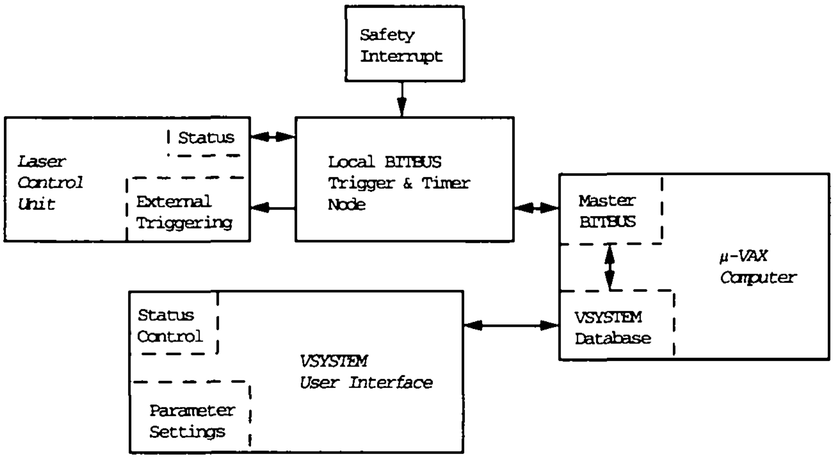
Safety Interrupt
Laser Control Unit
Status
External Triggering
Local BITBUS Trigger & Timer Node
Master BITBUS
VSYSTEM Database
μ-VAX Computer
Status Control
Parameter Settings
VSYSTEM User Interface

Figure 3.13: Laser Control Scheme

For safety reasons, the stray light intensity from the torus entrance and exit vacuum windows is continuously monitored by optical fibres. An unusually high amount of stray light indicates possible damage to the window surfaces. Since further illumination by the high power laser may, in this case, lead to catastrophic loss of vacuum, the intra-cavity safety shutter is immediately triggered to terminate the emission.

A fraction of the laser output energy is recorded by a fast pin-photodiode which detects the radiation transmitted by one of the steering mirrors. The rising edge of the laser energy monitor signal serves as trigger for the data acquisition system, thus providing precise synchronization with low jitter.

3.2.6 Optical Alignment

Only during TCV vacuum openings are direct measurements of the scattering angles, the size and the vertical positions of the scattering volumes possible. To obtain such measurements, a ruler is placed inside the vacuum vessel and precisely aligned along the laser beam direction. The optical fibres are then illuminated by a source at the polychromator end of the bundle, and adjusted such that a sharp image of their front end is projected onto the ruler. Further, fine adjustment is performed later by maximising the signals obtained during Raman scattering experiments in Nitrogen (Section 3.4.2.2).

3.2.7 Data Acquisition

3.2.7.1 Introduction

A complete description of every TCV discharge in terms of system parameters and measured data is provided by the model driven data acquisition system, MDS+ [14]. Each shot is associated with a *"tree"* structure defined by the model and containing *"subtrees"* carrying, for example, the description of a given diagnostic. The TS system experimental interface is CAMAC based, with the principal components described below.

3.2.7.2 Components and Triggering

A measurement of the number of photons scattered into a given spectral channel corresponds to integration of the detector current during a time period synchronised with the laser pulse. This may be accomplished using fast gated, charge-sensitive analog-to-digital converters (ADC's). We have chosen 16-

channel fast encoding and read-out ADC-modules (LeCroy Fera 4300B) with 11bit conversion range and a sensitivity of 0.25pC/count. After digitization, the data are immediately transferred into buffer memories (LeCroy Fera 4301B), with data acquisition and transfer being controlled by a separate driver module (Fera 4301). Table 3-7 compiles the configuration of data acquisition modules for the *"3 and 4 channel"* versions of the detection system.

Table 3-7: Configuration of Data Acquisition Modules and Signal Attribution

	10 Observation volumes ("3-channel" polychromators)		*25 Observation volumes ("4-channel" polychromators)*	
	Number			
ADC-modules (Fera 4300B)	2		9	
Driver modules (Fera 4301)	1		1	
Memory modules (Fera 4302)	1		3	
	Attribution of Signal Channels			
	ADC ch.	*Connected Signal*	*ADC ch.*	*Connected Signal*
	1-3	Spectral Channels 1-3, polychromator #1	1-3	Spectral channels 1-3, polychromator #1
	...	...	4	n.c.
	28-30	Spectral Channels 1-3, polychromator #10	...	...
	31	Laser energy monitor	97-99	Spectral channels 1-3, polychromator #25
	32	LED reference detector	100	n.c.
			101	Laser energy monitor
			102-112	n.c.
			113-137	LED reference detectors, Polychromator #1-#25
			138-144	n.c.

Synchronization of the data acquisition modules with the scattered signals is achieved by a gate pulse triggered by the laser pulse itself. For this purpose, the signal from a laser monitor diode is fed into a fast discriminator followed by an adjustable delay line. When only the detector response to the LED-reference pulses is measured, a BITBUS-timer module generates separate trigger pulses (fig. 3.14). The integration time (GATE≈150ns) is adapted to the bandwidth limited FWHM (≈50ns) of the scattering signal and to the electronic jitter (≈10ns).

Since the ADC accepts only signals of single, negative polarity, typical noise fluctuations in the output signal must be compensated by an internally generated, adjustable offset ('pedestal') which must be larger than the expected noise amplitude. Double pulse measurements with and without laser (delay ≈100μs) are therefore required to subtract the pedestal and to estimate the signal fluctuations caused by noise and plasma radiation.

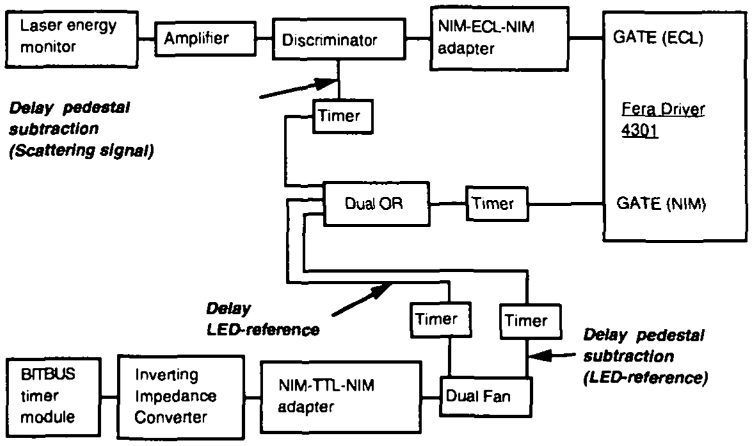
Laser energy monitor
Amplifier
Discriminator
NIM-ECL-NIM adapter
GATE (ECL)
Delay pedestal subtraction (Scattering signal)
Timer
Fera Driver 4301
Dual OR
Timer
GATE (NIM)
Delay LED-reference
Timer
Timer
Delay pedestal subtraction (LED-reference)
BITBUS timer module
Inverting Impedance Converter
NIM-TTL-NIM adapter
Dual Fan

Figure 3.14: Schematic overview of the electronic components used for generation of the data acquisition triggers (GATE). With the exception of the laser energy monitor, the amplifier, the BITBUS timer module and the impedance converter, all components are available as compact NIM modules (C.A.E.N.).

3.2.7.3 Acquisition Cycle during a Discharge

Before, during and after a tokamak discharge, the data acquisition must measure different signal types: LED-reference, stray light, scattered signal and noise. In order to obtain measurements of the detector response without perturbation by plasma radiation, the LED-reference signals are generated before and after a discharge. Stray light signals are acquired before plasma breakdown, followed by the scattered signals during the discharge. Within a period of 100μs following acquisition of each scattering signal, the pedestal and noise contributions are measured (fig. 3.15). Table 3-8 compiles the sampling frequency and the time windows for the different signals.

Table 3-8: Acquired Signals During a Thomson Scattering Experiment

Type of signal	Sampling frequency [Hz]	Time period [sec]
LED-reference (1)	50	$-2.5 \le t < -2.0$ $3.0 \le t < 3.5$
Stray light (2)	20	$-0.95 \le t \le 0$
Scattering (3)	20	$0.05 \le t \le 2.0$
Pedestal subtraction, fluctuations (noise)	Delay of 100µs to signals 1) to 3)	

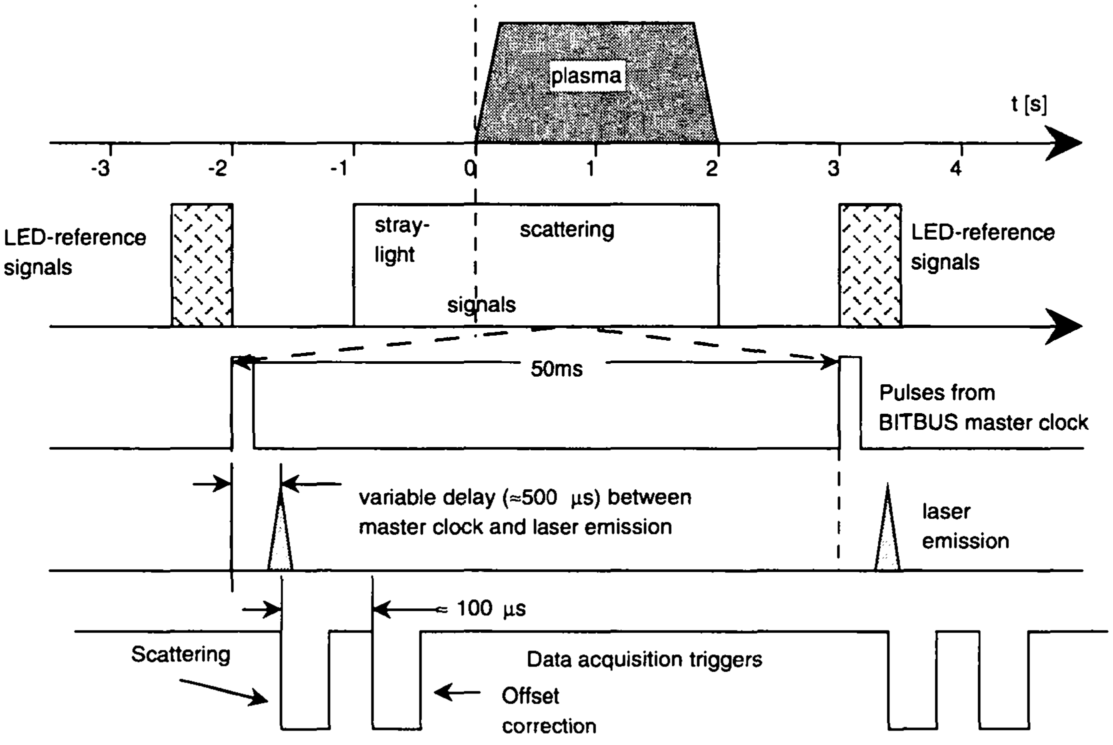
plasma
t [s]
-3
-2
-1
0
1
2
3
4
LED-reference signals
stray-light
scattering
signals
LED-reference signals
50ms
Pulses from BITBUS master clock
variable delay (≈500 µs) between master clock and laser emission
laser emission
≈ 100 µs
Scattering
Data acquisition triggers
Offset correction

Figure 3.15: Overview of the Thomson scattering timing sequence during a TCV-discharge

Following each discharge, the data are read out from the buffer memory and stored in attributed MDS+ nodes in the form of matrices of size (320·32) for the 10 observation volume system) and (320·144) for the upgraded system with 25 observation volumes.

3.3 Analysis of Scattered Signals

Analysis of the scattered signals requires that the shape and amplitude of the scattered light spectrum are determined. When a large number of narrow spectral detection channels lies within the expected width of the scattering spectrum, this can be performed by non-linear fitting with T_e and n_e as free parameters. Such a procedure cannot be applied when few spectral channels with large bandwidth are used. It turns out, however, that the ratio of the scattered signals in different spectral channels is an unambiguous and monotonic function of T_e. Once T_e is known, n_e can be determined from the recorded signal in a particular channel.

3.3.1 Evaluation of T_e and n_e

According to eqn. 2.20, we can calculate the scattered power, P_{jm}^{TH} collected by the detectors, j in the (presently 3) different channels of a polychromator, m:

$$P_{jm}^{TH} = P_i^{TH} r_e^2 L_m \Delta\Omega_m n_{e,m} \int_{-\infty}^{\infty} \tau_{jm}(\lambda) S(T_{e,m}, \Theta_m, \lambda) d\lambda \tag{3.1}$$

where m is equivalent to the labelling of observation volumes. In eqn. 3.1, P_i^{TH} is the incident laser power, $\Delta\Omega_m$ denotes the solid angle subtended by the observation volume, m, at the camera lens and $\tau_{jm}(\lambda)$ the absolute spectral transmission between the observation volumes and the detector elements. This includes the observation window, the camera lens, the fibre bundles, the imaging optics inside the polychromator and the interference and blocking filters.

When we want to convert the power incident on a particular detector into an electronic signal, we must account for the fact that each detector element has a spectral response, $R_{b,jm}^{TH} = r_{jm}(\lambda) \cdot u_{b,jm}^{TH}$ [V/W], where $r_{jm}(\lambda)$ denotes the spectral response at the reference bias voltage, U_b^{ref}. The factor $u_{b,jm}^{TH}$ describes the bias voltage dependent part of $R_{b,jm}^{TH}$, with the index b representing the actual bias voltage, U_b. The factor $u_{b,jm}^{TH}$ is determined by measuring the detector response to LED-reference pulses for various bias voltages, U_b. Inserting the '*Spectral response function*' (a measurable quantity - see Section 3.4.1.1):

$$\tau_{jm}^{*}(\lambda) = \frac{\tau_{jm}(\lambda) \cdot r_{jm}(\lambda)}{\tau_m},$$

(3.2)

into eqn. 3.1, we obtain:

$$V_{jm}^{TH} = P_i^{TH} r_e^2 L_m n_{e,m} \Delta\Omega_m u_{b,jm}^{TH} \tau_m \int_{-\infty}^{\infty} \tau_{jm}^{*}(\lambda) S(T_{e,m}, \Theta_m, \lambda) d\lambda = P_i^{TH} Q_{jm}^{TH}$$

(3.3)

where the normalization factor τ_m is dimensionless and can be regarded as a transmission coefficient. Passing the HF-amplifier with a gain factor g_{jm}^{TH}, the current driven through the ADC input impedance, Z_{jm}=50 Ω, is integrated while the GATE is open and converted (A_{jm} = 4 counts/pC):

$$S_{jm}^{TH} = \frac{g_{jm}^{TH} Q_{jm}^{TH} A_{jm}}{Z_{jm}} \int_{GATE} P_i^{TH} dt = \frac{g_{jm}^{TH} Q_{jm}^{TH} A_{jm}}{Z_{jm}} M S_{MON}^{TH}$$

(3.4)

S_{jm}^{TH} is the measured scattered and S_{MON}^{TH} the measured laser energy monitor signal, in units of "counts". Since the power collected by the laser energy monitor, P_{MON}^{TH} is assumed to be proportional to the incident laser power inside the scattering volume, $P_{MON}^{TH} \sim P_i^{TH}$, we can write:

$$\int_{GATE} P_i^{TH} dt = M \cdot S_{MON}^{TH}.$$

(3.5)

The number of signal counts, S_{jm}^{TH} normalized by g_{jm}^{TH} and $u_{b,j}^{TH}$ then corresponds to the total energy, E_{jm} of all photons scattered into channel j during the gate pulse. The ratio of the scattered energies in two neighbouring channels can be written as:

$$\frac{u_{b,k}^{TH} g_{km}^{TH} S_{jm}^{TH}}{u_{b,j}^{TH} g_{jm}^{TH} S_{km}^{TH}} = \frac{E_{jm}}{E_{km}} = \frac{\int \tau_{jm}^{*}(\lambda) S(T_{e,m}, \Theta_m, \lambda) d\lambda}{\int \tau_{km}^{*}(\lambda) S(T_{e,m}, \Theta_m, \lambda) d\lambda} \tag{3.6}$$

Since the spectral response functions can be measured, the ratios E_{jm}/E_{km}, named conversion functions, are functions of $T_{e,m}$ only and can be calculated in advance. For use with the Thomson scattering analysis program (Section 3.5) the results of these calculations are stored in look-up tables. Four different ratios are used for the analysis: $R_q=E_{2m}/E_{1m}$; E_{3m}/E_{1m}; $(E_{3m}+E_{2m})/E_{1m}$; E_{3m}/E_{2m} (for the spectral channel notation see Tables 3-4 and 3-6). Figure 3.16 illustrates the behaviour of T_e as a function of these ratios.

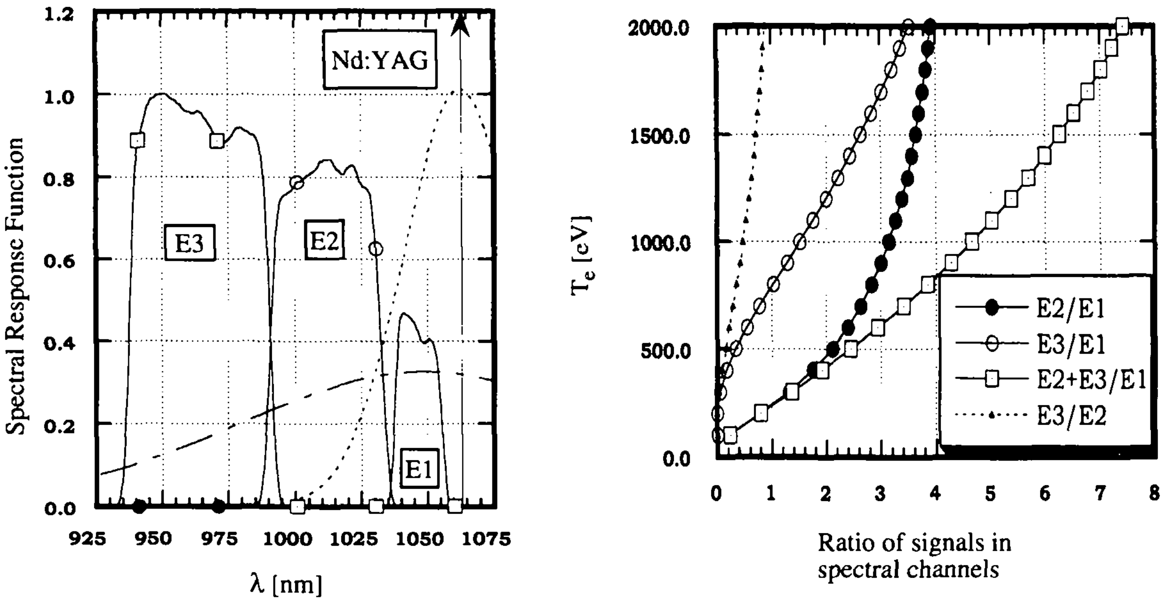

Figure 3.16: On the left: 3 typical, measured Spectral Response Functions for a given polychromator together with the scattering form factor $S(T_{e,m}, \Theta_m=90°, \lambda)$ for $T_e=100eV$ (dashed line) and $T_e=1keV$ (dash-dotted line). On the right: conversion functions according to eqn. 3.6. The weights of T_e from the different conversion functions are inversely proportional to the local derivative of the conversion function.

When $T_{e,m}$ is known, a factor, $c_{j,m}$ (fig. 3.17) can be used to relate the scattered energy in the spectral channels to the total scattered energy:

$$c_{j,m} = \frac{\int_{-\infty}^{\infty} \tau_{jm}^{*}(\lambda) S(T_{e,m}, \Theta_m, \lambda) d\lambda}{\int_{-\infty}^{\infty} S(T_{e,m}, \Theta_m, \lambda) d\lambda} = (1+\alpha^2) \int_{-\infty}^{\infty} \tau_{jm}^{*}(\lambda) S(T_{e,m}, \Theta_m, \lambda) d\lambda \,, \tag{3.7}$$

where $1 + \alpha^2 \approx 1$. Knowledge of the absolute sensitivity of each spectral channel thus allows n_e to be determined (Section 3.4.2).

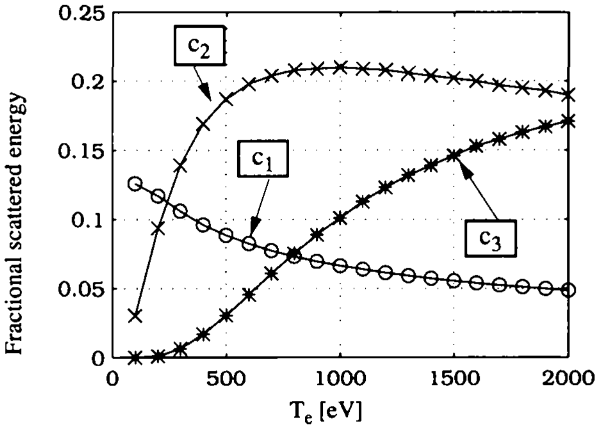

Figure 3.17: Fraction of scattered energy in 3 spectral channels of a given polychromator as a function of T_e. The curves have been computed on the basis of the measured 'Spectral Response Functions' presented in fig. 3.16.

3.4 Calibration methods

Analysis of the scattered signals relies on calibration of the detection system at different levels. These calibrations must provide:

a) the relative spectral response function of the polychromator channels

b) the absolute sensitivity of the complete detection system.

Whilst the relative spectral response functions can be separately measured in the laboratory, the absolute calibration can only be performed once the complete system has been installed on TCV.

3.4.1 Laboratory Calibrations

3.4.1.1 Spectral Calibration

The *'Spectral Response Function'* describes the response of the detection system to a radiation source of constant spectral emissivity. According to eqn. 3.2 all wavelength dependent optical elements from the scattering volume to the detector must be included in this response. In practice, response functions are measured by illuminating the polychromator input (including the fibre bundle) with a radiation source of known spectral emissivity and recording the detector output as a function of wavelength. The spectral transmissions of the camera lens and observation windows are accounted for separately once the calibration measurements are complete. Finally, the response functions are normalized such that the maximum value of the three functions for a given polychromator is equal to unity.

The experimental arrangement is shown in fig. 3.18. As spectral source we use a Czerny-Turner monochromator (f=200mm, f#=4) illuminated by a tungsten ribbon lamp ($P \approx 150W$). The light source is modulated by a chopper (f=120Hz) in order to use the lock-in technique for recording of the detector output signals. A condenser lens (f=125mm, m=1.5) with low f-number (f#=2), is used to project an image of the tungsten filament ($\approx 2 \cdot 20mm^2$) on the entrance slit. This ensures that the full length of the monochromator entrance slit (width d=100μm, height h=20mm) is illuminated for all acceptance angles. Before beginning a series of spectral calibration measurements, the monochromator wavelength scale is calibrated using a cesium spectral lamp. The monochromator exit slit is imaged onto the input end of the fibre bundle (using a camera lens, f=125mm, f#=1.6, m=1) such that all 9 fibres forming the linear array are illuminated. The chosen slit width of 100μm is a compromise between intensity (signal amplitude $\approx 100mV$) and the achievable spectral resolution ($\Delta\lambda \approx 1.4nm$). A typical spectral scan has a step size of $\Delta\lambda = 0.25nm$ and begins once the detector response at a fixed avalanche voltage has stabilized. Analog lock-in amplifiers (FEMTO, LIA-MV-140) are used to track the detector output signals which are then digitized by slow A/D-converters (NB-MIO 16). Data read-out and storage is performed using LabVIEW on a MacIntosh computer.

Although lacking a calibration in terms of absolute emissivity, the experimental arrangement is essentially a spectro-radiometer. A relative spectral emissivity is obtained by using a calibrated Germanium detector as reference and inserting this detector in place of the fibre bundle to determine a source function. This source function is then used to renormalize the polychromator channel measurements.

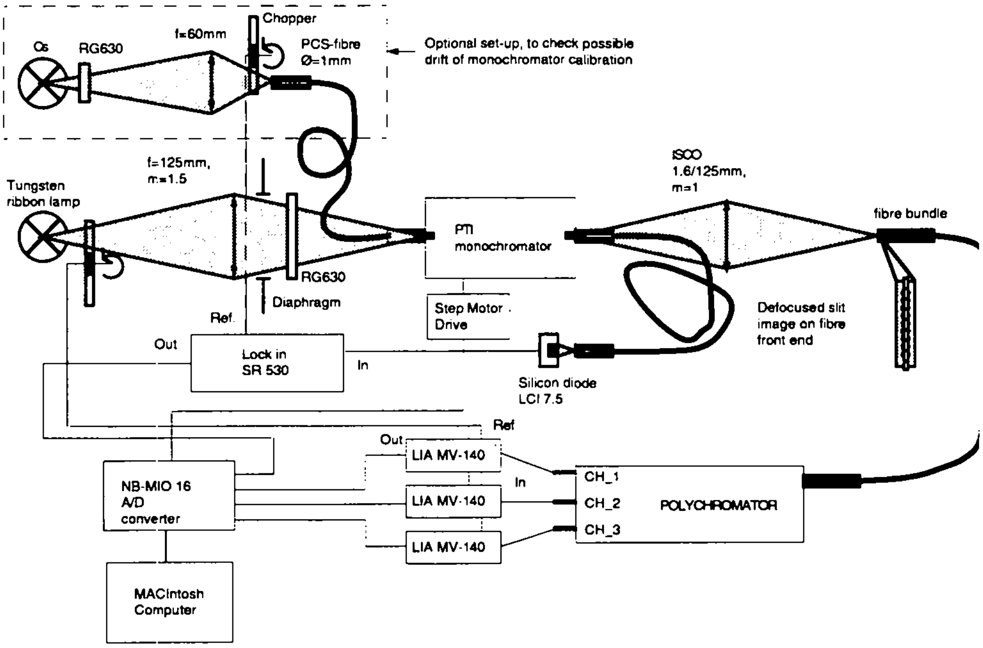
Chopper
Cs
RG630
f=60mm
PCS-fibre
Ø=1mm
Optional set-up, to check possible drift of monochromator calibration
f=125mm,
m=1.5
Tungsten ribbon lamp
RG630
Diaphragm
Ref.
Out
Lock in
SR 530
In
PTI
monochromator
Step Motor
Drive
ISCO
1.6/125mm,
m=1
fibre bundle
Defocused slit image on fibre front end
Silicon diode
LCI 7.5
Ref
Out
LIA MV-140
LIA MV-140
LIA MV-140
In
CH_1
CH_2
CH_3
POLYCHROMATOR
NB-MIO 16
A/D
converter
MACIntosh
Computer

Figure 3.18: Experimental arrangement for measurement of the 'Spectral Response Function'

The spectral accuracy of the spectral response functions depends principally on the stability of the monochromator calibration together with a precise and reproducible initial setting of the grating before each wavelength scan. Monochromator calibrations before and after a series of spectral calibrations have shown that the accuracy on the measured position of different Cs lines in the infrared spectral range [52] is within the step size ($\Delta\lambda$=0.25nm) of the monochromator scan. The reproducibility of the initial grating setting has also been verified by coupling the emission of the cesium lamp via optical fibres to the monochromator. An analysis of 15 Cs-spectra obtained in this way shows that imperfect reproducibility in the initial grating setting leads to inaccuracies in the monochromator calibration not exceeding $\Delta\lambda$=+/-0.8nm.

Within the accuracy of the spectral calibration, a possible long-term drift in the spectral filter transmission and consequently the *'Spectral response functions'* could not be observed in our case. Slight variations in response function amplitudes following a period of several months in between two measurements are due to inaccuracies in the experimental parameters, in particular the temperature dependent response of those avalanche detectors comprising the 3 channel polychromators for which active temperature stabilization is not installed (Section 3.2.4.1).

3.4.1.2 Identification of Systematic Errors

The accuracy of the T_e values provided by the TS system depends to a large extent on the precision of the spectral response function (Section 3.4.1.1). To minimize systematic errors during the calibration, the polychromators must be illuminated under conditions which closely resemble those experienced on TCV. A spectral calibration should therefore respect the following conditions:

1) Fixed attribution of a single fibre bundle to each polychromator

2) Fixed orientation of a fibre bundle in its support

3) Precise adjustment of the avalanche bias voltage

4) Irradiation of the fibre bundle front ends across the entire acceptance angle (N.A.=0.22, α=12.7 ^{0})

Conditions 1)-3) are satisfied by the procedure described here. With respect to condition 4), the maximum angle of α=7.2^0 achievable with the monochromator (f#=4) is insufficient to reproduce the angular field of view characteristic of the 'real' TS measurements on TCV. In a separate experiment we have demonstrated that the radiation cone leaving the fibre bundle at one end depends strongly on that used to illuminate the other end. As a consequence, the illumination of spectral channels during a spectral calibration is different from that prevailing during a measurement on TCV. Figure 3.19 shows the collected power leaving the fibre as a function of the observation solid angle for varying solid angle subtended by the source irradiating the fibre entrance. Clearly, the lower the solid angle subtended by the incident radiation, the more restricted is the angular spread of the radiation leaving the fibre at the other end.

We have also established that the relative responses of the spectral channels in each polychromator change both when the spectral source is replaced by a broad-band source and when the solid angle subtended at the front end of the fibre is varied. In particular, when comparing the channel ratios (used to compute T_e - Section 3.3.1), those involving the first spectral channel (in particular the first channels of the '3-channel' filter polychromators) are most sensitive to variations in the solid angle. This leads to a systematic error in the calculated T_e as a result of vignetting inside the polychromator. In fact, the optical paths for the three spectral channels are not fully equivalent and a detector at the end of the chain (in particular the last one, i.e. spectral channel #1), will not receive radiation from the full cone emitted by the fibre. The differences in the beam paths are sufficiently large that the field lens cannot form an image of the entrance pupil (first lens) onto each of the focusing lenses. Since the solid angle is reduced during spectral calibration measurements, vignetting may not be important in this case. During Thomson scattering measurements on TCV, however, irradiation occurs over all fibre acceptance angles and we must account for vignetting.

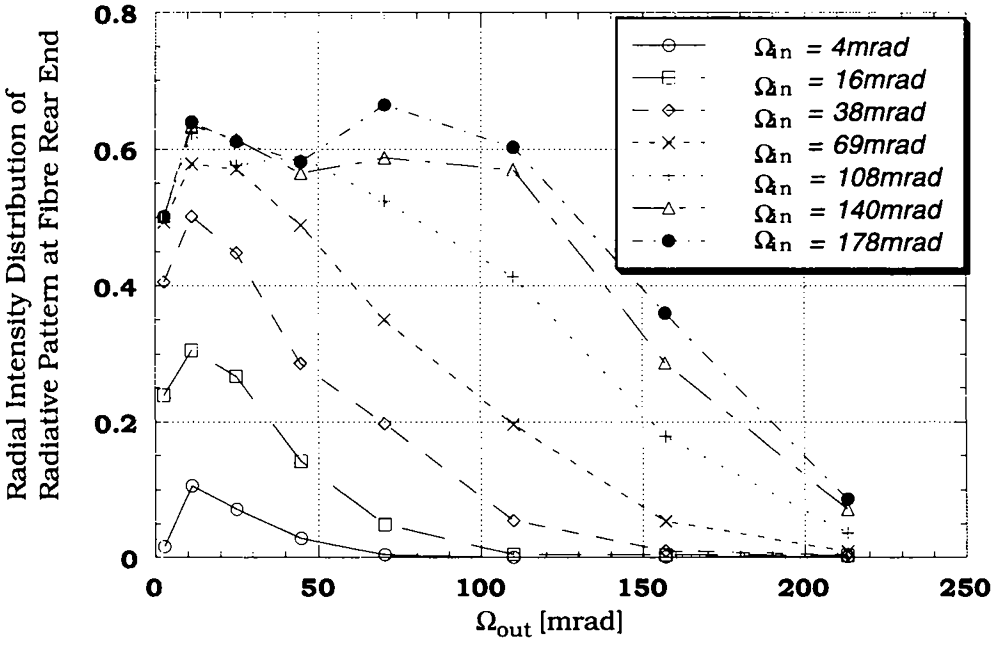

Figure 3.19: Collected radiative power at the exit end of a fibre bundle as a function of the observation solid angle. The curves for different solid angles of the incident radiation show that the radiation pattern at the exit end is influenced by that at the front end

3.4.1.3 Broad-band Calibration

In order to verify the first calibration and to quantify the effect of the vignetting errors described above, we have performed a second, broad-band calibration, in which the illumination conditions are essentially those experienced during the real scattering experiment. A broad-band calibration measures the response, V_{jm}, of a spectral channel to the irradiation by a standard calibration source of known spectral radiance:

$$V_{jm} = A\tau_m \Delta\Omega_m u_{b,jm}^{TH} \int_{-\infty}^{\infty} \tau_{jm}{}^*(\lambda) \cdot L(\lambda) d\lambda \qquad (3.8)$$

where $L(\lambda)$ denotes the spectral radiance of the source (W/m^2·sr·nm) and A the emitting surface. The remaining parameters have already been defined in eqn. 3.1.

Fig. 3.20 illustrates the experimental arrangement. The geometry and magnification reproduce the actual conditions on TCV for a scattering angle of $\theta=90^0$. The part of the source which homogeneously illuminates the fibre bundle front end is equal to the projection of the scattering volume perpendicular to the scattering plane. Within the bandwidth of the spectral channels, the spectral radiance of the standard calibration source is known with an accuracy of 1%. The response in each channel is determined with an analogue oscilloscope triggered by the mechanical chopper.

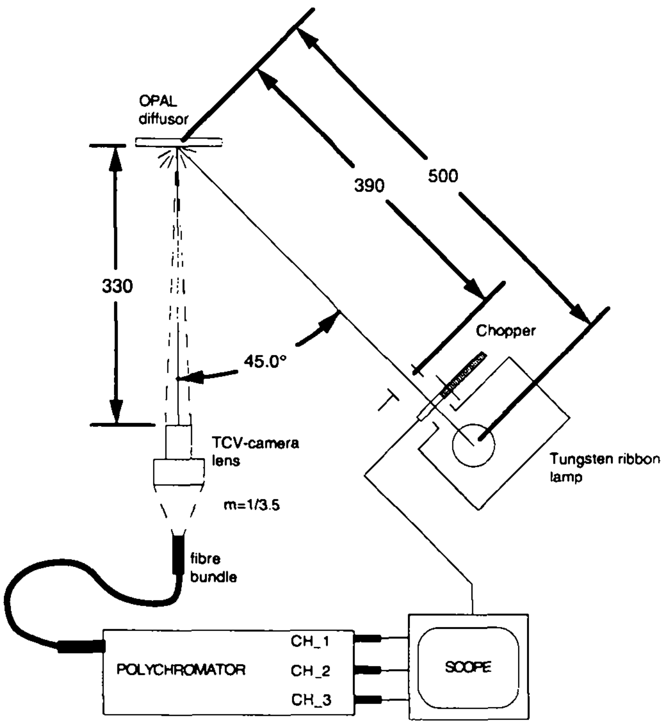

Figure 3.20: Experimental arrangement for the broad-band calibration. The standard calibration source consists of a large OPAL-diffusor illuminated by a tungsten filament lamp at a fixed and stabilized current (I=6.5 A), at a fixed distance (d=500 mm) between the filament and the diffusor and positioned at 45 ^{0} with respect to the optical axis of the collection lens.

Since the spectral radiance of the calibration source is known, we can compare the ratios of the measured responses, V_{jm}/V_{km} (j,k=1,2,3; j≥k) to the expected values, $V_{jm}^{calc}/V_{km}^{calc}$, e.g.:

$$\frac{V_{jm}}{V_{km}} \leftrightarrow \frac{V_{jm}^{calc}}{V_{km}^{calc}} = \frac{\int_{-\infty}^{\infty} \tau_{jm}^{MS*}(\lambda) \cdot L(\lambda) d\lambda}{\int_{-\infty}^{\infty} \tau_{km}^{MS*}(\lambda) \cdot L(\lambda) d\lambda} \tag{3.9}$$

where $\tau_{jm}^{MS*}(\lambda)$, $\tau_{km}^{MS*}(\lambda)$ represent the measured spectral response functions. Differences between the calculated and the measured ratios indicate systematic errors which can then be accounted for quantitatively in the form of a correction factor, F_{jm}:

$$\frac{V_{jm}}{V_{km}} = \frac{F_{jm} V_{jm}^{calc}}{F_{km} V_{km}^{calc}} \tag{3.10}$$

Fig. 3.21 shows the ratios, F_{jm}/F_{km} resulting from both a spectral and a broad-band calibration using ten '3-channel' polychromators. Channels 2 and 3 are in general less affected than channel 1. We therefore set $F_{3m} = 1$ and derive the correction factors for the other channels from the ratios. This choice may appear somewhat arbitrary, but this is of no importance since it is only the ratios which must be corrected in the calculation of T_e.

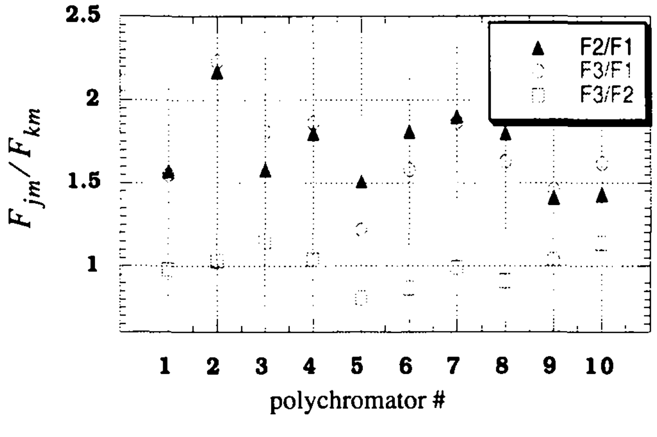

Figure 3.21: Ratios of correction factors, F_{jm}/F_{km}, for all ten '3-channel' filter polychromators. Ratios involving the first spectral channel indicate systematic errors of more than 40% in the spectral calibration.

3.4.2 Calibration In-situ

3.4.2.1 Introductory Remarks

As shown in Section 3.4.1.1, T_e measurements are based on signal ratios and therefore require only a relative calibration. For measurements of n_e, however, the absolute sensitivity of the detection system (optics, spectrometers, amplifiers, data acquisition) must be known. An absolute calibration of this nature can only be performed under conditions identical to those of a Thomson scattering measurement. Rayleigh and Rotational Raman scattering (RRS) from neutral, molecular gases are two examples of methods that are routinely used for such purposes.

Rayleigh scattering is elastic scattering and frequently used, despite the stray light pollution, when the spectrometer (e.g. the combination of a grating and a CCD-camera [11]) has a channel on the laser line, λ_l. In contrast, the inelastic process of Rotational Raman scattering results in a multitude of spectral lines on both sides of λ_l (Stokes-, anti-Stokes branch). If H_2, D_2 and N_2 ([15], [40], [75]) could be used as working gases, absolute calibration of each polychromator channel would be possible.

3.4.2.2 Example of a Raman Calibration in N_2

Even though the anti-Stokes Raman transitions cover only the spectral channel closest to the laser line (fig. 3.22, appendix A), the TCV TS system is calibrated using Raman scattering in N_2. This choice is mainly driven by the danger of strong exothermal reactions between oxygen and hydrogenic gases such as H_2 and D_2.

In a similar fashion to eqn. 3.1, the response of the first spectral channel to a Raman scattering signal can be written as follows:

$$V_{1m}^{RAM} = P_i^{RAM} n_G L_m \Delta\Omega_m \tau_m u_{b,1m}^{RAM}\left(\frac{7}{4}\sum_{n=1}^{N}\tau_{1m}{}^*(\lambda_n)\sigma_G^{RAM}(\lambda_n)\right) \tag{3.11}$$

where n_G denotes the density of the scattering gas, determined from the measured gas pressure at room temperature using the ideal gas equation, $p_G = k_B n_G T_G$. Since the typical linewidth of Raman transitions in gases at low pressure is of the order of a few Angstrøm, it is negligible compared to the width of the spectral response functions. The weighted integral of the continuous scattering spectrum is therefore replaced by the weighted and discrete sum over the RRS scattering cross-sections, $\sigma_G^{RAM}(\lambda_n)$. The summation applies to the cross-sections of all transitions lying within the spectral range of the spectral response functions. Systematic errors in $\tau_{jm}*(\lambda_n)$ are compensated by the absolute calibration. The factor 7/4 in eqn. 3.11 accounts for the scattering geometry and for the polarization insensitivity of the collection and detection optics (Appendix A). In what follows, we will use the abbreviation:

$$\frac{7}{4}\sigma_{G,m}^{RAM} = \frac{7}{4}\sum_{n=1}^{N}\tau_{1m}*(\lambda_n)\sigma_G^{RAM}(\lambda_n) \tag{3.12}$$

where $\sigma_{G,m}^{RAM}$ denotes the calculated RRS cross-section of the first spectral channel.

During a series of RRS measurements, Raman scattering, $s_{jm,r}^{RAM}$ and offset correction signals, $s_{jm,r}^{OFFS}$ are acquired. The acquisition timing scheme is modified with respect to that during a TCV discharge (fig. 3.15) so that the full available buffer memory can be used exclusively for intermediate storage of the scattered radiation and offset correction signals. After averaging over many samples, this approach leads to an excellent relative error of less than 5%.

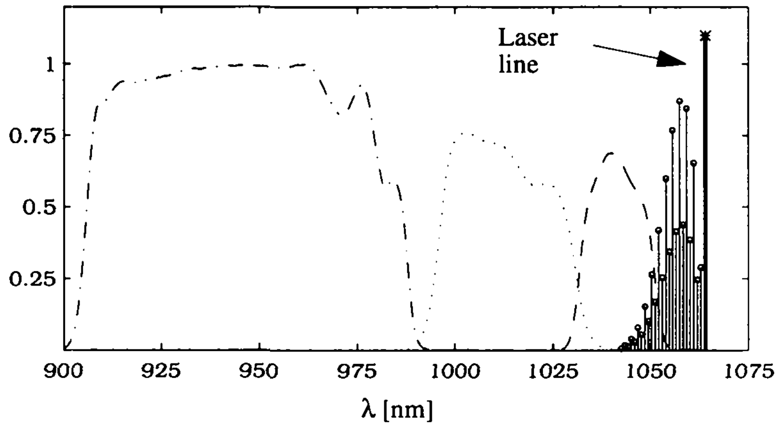

Figure 3.22: Spectral response functions of three polychromator channels together with the anti-Stokes Raman lines. The relative amplitude of the Raman lines indicates the strength of the scattering cross-sections on a logarithmic scale.

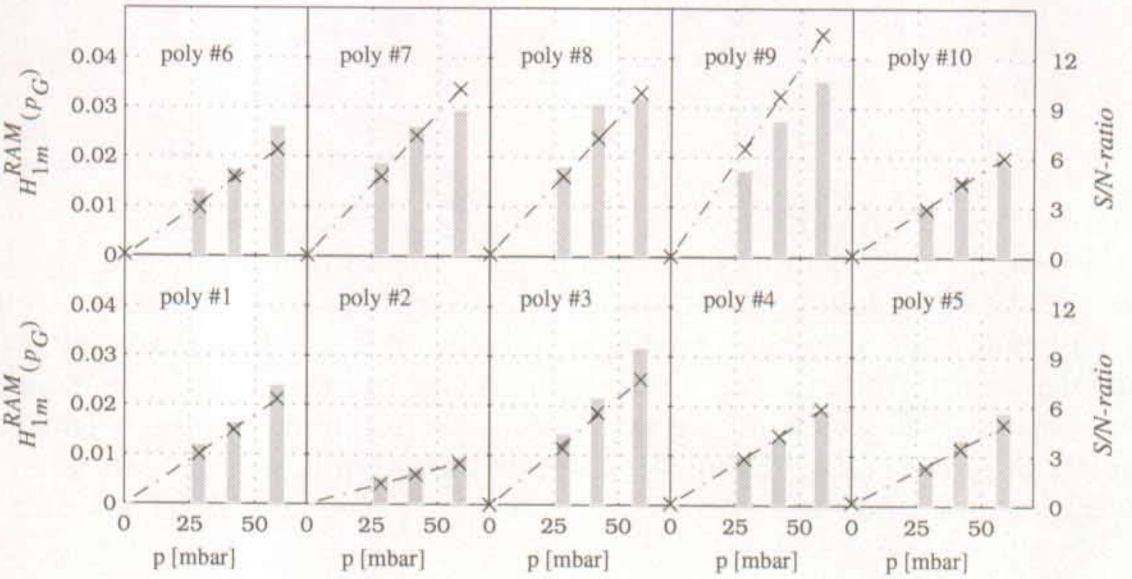

Figure 3.23: The curves show the results of a Raman calibration in terms of the 'normalised Raman response' (axis captions on the left, 'x' symbols) and the measured S/N-ratio (axis captions on the right, histograms) as a function of the filling pressure. The good correlation of the response data samples with a linear fit in all the spectral channels yields a statistical error on the slope which remains below 3%.

The full Raman scan comprises measurements at 4 scattering gas pressures in the interval 0→60mbar. For each pressure, the averaged number of net signal counts is calculated:

$$S_{1m}^{RAM}(p_G) = \frac{1}{256}\left(\sum_{n=1}^{256}\left[s_{1m}^{RAM}(p_G) - \frac{1}{256}\sum_{n=1}^{256} s_{1m}^{BACK}(p_G)\right]\right) \tag{3.13}$$

Normalizing $S_{1m}^{RAM}(p_G)$ to the offset corrected laser energy monitor signal $S_{MON}^{RAM}(p)$ and g_{1m}^{RAM}, we obtain the *normalised Raman response* of the spectral channels:

$$H_{1m}^{RAM}(p_G) = \frac{S_{1m}^{RAM}(p_G)}{g_{1m}^{RAM} S_{MON}^{RAM}(p_G)} \tag{3.14}$$

The spectral channel sensitivity is finally determined by a linear regression [4], which takes account of the statistical error on $S_{1m}^{RAM}(p)$:

$$H_{1m}^{RAM}(p_G) = h_{1m}^{RAM} p_G + \delta_{1m} \tag{3.15}$$

The coefficient δ_{1m} is a measure of the stray light level in the particular spectral channel. The Raman measurements have shown that δ_{1m} is close to zero and that the stray light level can thus be neglected (fig. 3.23). A suitable quantity describing the absolute sensitivity of calibrated spectral channels is the equivalent electron density, n_e^{eqv}. This parameter represents the plasma electron density which yields, for a given plasma electron temperature, a TS signal of equal amplitude under identical experimental conditions (incident radiation power, parameter settings of detection system). This value may be obtained by combining eqn. 3.3 and 3.11:

$$n_{e,1m}^{eqv} = \frac{n_{N2}}{r_e^2} \frac{\frac{7}{4}\sigma_{G,m}^{RAM}}{\int \tau_{1m}*(\lambda) \cdot S(T_{e,m}, \Theta_m, \lambda) d\lambda} \tag{3.16}$$

Inserting the slope, h_{1m}^{RAM} into eqn. 3.16 we obtain:

$$n_{e,1m}^{eqv}(T_{e,m}) = \frac{S_{1m}^{RAM}}{S_{MON}^{RAM} g_{1m}^{RAM} h_{1m}^{RAM} k_B T_{N2} r_e^2} \frac{\frac{7}{4}\sigma_{G,m}^{RAM}}{\int \tau_{1m}*(\lambda) \cdot S(T_e, \Theta_m, \lambda) d\lambda} \tag{3.17}$$

Eqn. 3.17 shows that n_e^{eqv} is a function of the electron temperature (via the scattering form factor) and is directly proportional to the measured Raman scattering signal.

As reference value for the spectral channel sensitivity we use the equivalent electron density of a Raman scattering signal which yields a minimum signal-to-noise ratio of 10 at T_e=500eV. The n_e^{eqv} values plotted in fig. 3.24 illustrate that this parameter shows large variations amongst different spectral channels. This variations may be due to poor alignment (compare also fig. 3.21) or variations in detector NEP. We note, that electron temperatures lower than 500eV yield better spectral channel sensitivities, since the fraction of radiation scattered into the 1st spectral channel increases when the electron temperature decreases. Measurements of the electron density near the plasma edge, where n_e is usually the lowest, can therefore be performed with better density resolution.

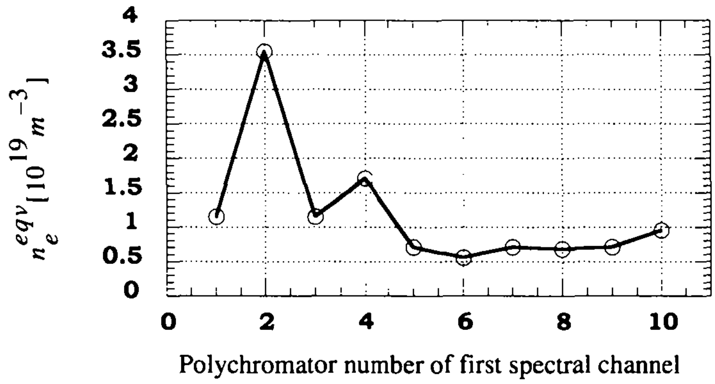

Figure 3.24: Equivalent electron densities at T_e =100eV for absolutely calibrated spectral channels as obtained from Raman scattering in N_2 (see fig. 3.23), when a signal-to-noise ratio of 10 is assumed.

3.5 The Data Analysis Program, TSA

The Thomson Scattering Analysis program, TSA begins with the matrix of acquired scattering signals (Table 3-8) obtained after a completed Thomson scattering cycle (Section 3.2.7.3), computes the T_e and n_e profiles and stores the results in the 'MDS+' data structure for further analysis. The main steps of the program are illustrated by the flow chart in fig. 3.25, in which the different points at which the results of the various absolute and relative calibrations (Section 3.4) are accounted for are emphasized.

The quantity "*best* T_e" appearing in the flow chart refers to the weighted average electron temperature, T_e*. Details of how this quantity and the estimated uncertainty, ΔT_e* are obtained from the measured spectral channel signal ratios (Section 3.3.1) are given below.

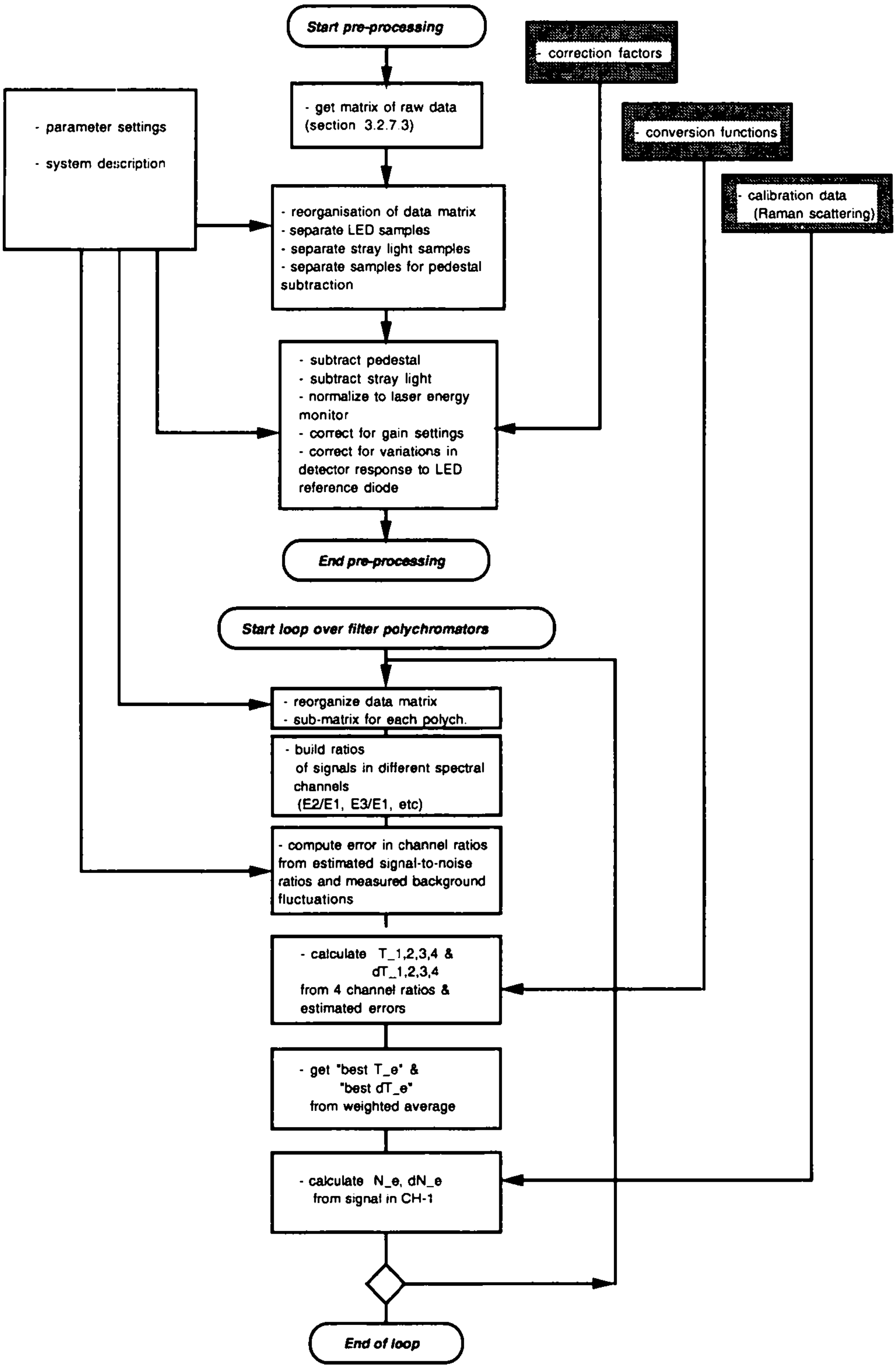
Start pre-processing
- correction factors
- get matrix of raw data (section 3.2.7.3)
- conversion functions
- parameter settings
- system description
- calibration data (Raman scattering)
- reorganisation of data matrix
- separate LED samples
- separate stray light samples
- separate samples for pedestal subtraction
- subtract pedestal
- subtract stray light
- normalize to laser energy monitor
- correct for gain settings
- correct for variations in detector response to LED reference diode
End pre-processing
Start loop over filter polychromators
- reorganize data matrix
- sub-matrix for each polych.
- build ratios of signals in different spectral channels (E2/E1, E3/E1, etc)
- compute error in channel ratios from estimated signal-to-noise ratios and measured background fluctuations
- calculate T_1,2,3,4 & dT_1,2,3,4 from 4 channel ratios & estimated errors
- get "best T_e" & "best dT_e" from weighted average
- calculate N_e, dN_e from signal in CH-1
End of loop

Figure 3.25: Flow chart for the Thomson scattering data analysis program.

3.5.1 Computation of the Weighted Average Electron Temperature

The weighted average electron temperature is based on the following expression:

$$T_e{}^* = \frac{1}{\sum (1/\Delta T_{e,q})^2} \sum_{q=1}^{4} \frac{T_{e,q}}{(\Delta T_{e,q})^2} \tag{3.18}$$

where $T_{e,q}$ denotes the electron temperature derived from the different spectral channel signal ratios. The uncertainty on $T_e{}^*$ is composed of statistical, $\Delta T_{e,stat}{}^*$ and systematic, $\Delta T_{e,syst}{}^*$ contributions in the proportion:

$$\Delta T_e{}^* = 0.4\Delta T_{e,stat}{}^* + 0.6\Delta T_{e,syst}{}^* \tag{3.19}$$

where

$$\frac{1}{\Delta T_{e,stat}{}^*} = \left(\sum_{q=1}^{4} \left(\frac{1}{\Delta T_{e,q}} \right)^2 \right)^{1/2} \qquad \Delta T_{e,syst}{}^* = \left(\frac{1}{N} \sum_{q} (T_{e,q} - T_e{}^*)^2 \right)^{1/2} \tag{3.20}$$

The uncertainties of $T_{e,q}$, $\Delta T_{e,q}$ are evaluated using the following scheme:

a) Estimation of the signal-to-noise ratio:

$$\Delta S_{sc,j} = \frac{S_j^{TH}}{C\sqrt{S_j^{TH}} + D} \tag{3.21}$$

This expression using two dimensionless constants (C, D) includes the noise contributions from the detector and its preamplifier. It is assumed that the noise from the following HF amplifiers does not affect the signal-to-noise ratio. The two parameters C and D are computed by non-linear least-square fits of the signal-to-noise ratios which can be measured during a Raman scattering experiment. At present, the same values for C an D are used for all spectral channels: C=1.1, D=350.

b) Computation of the uncertainty on scattered signals in the spectral channels:

$$\Delta S_j^{TH} = (\sigma_{bg,j}^2 + \Delta S_{sc,j}^2 + \sigma_{stray,j}^2)^{1/2} = \Delta E_j \tag{3.22}$$

where $\sigma_{bg,j}$ and $\sigma_{stray,j}$ represent the measured standard deviations due to fluctuations in stray light and plasma background radiation.

c) Estimation of the upper and lower limits of spectral channel signal ratios:

$$R_q^{MAX,MIN} = \frac{E_2 \pm \Delta E_2}{E_1 \mp \Delta E_1}, \frac{E_3 \pm \Delta E_3}{E_1 \mp \Delta E_1}, \ldots \tag{3.23}$$

d) Computation of electron temperatures associated with the limits in c) to obtain finally:

$$\Delta T_{e,q} = \frac{1}{2}(T_e(R_q^{MAX}) - T_e(R_q^{MIN})) \tag{3.24}$$

3.5.2 Computation of the Electron Density

After some algebraic transformations of eqn. 3.4, 3.11 and 3.15 we obtain for the weighted average electron density, n_e^* :

$$n_e^* = \frac{u_{b,1}^{RAM} S_1^{TH} \frac{7}{4} \sigma_G^{RAM}}{g_1^{TH} S_{MON}^{TH} u_{b,1}^{RAM} r_e^2 k_B T_{N2} c_1(T_e^*) h_1^{RAM}} = \zeta \frac{S_1^{TH} \frac{7}{4} \sigma_G^{RAM}}{c_1(T_e^*) h_1^{RAM}} \tag{3.25}$$

where the polychromator index is omitted and the spectral channel index, j is set to 1 in order to emphasize that only the first spectral channels can be absolutely calibrated and thus be used for the computation of n_e^*. The factor ζ comprises all those parameters with negligible error contributions. By analogy with the calculation of T_e^*, the uncertainty on n_e^* is an estimate of statistical and systematic contributions:

$$\Delta n_e^* = \Delta n_{e,syst}^* + \Delta n_{e,stat}^* \tag{3.26}$$

where

$$\Delta n_{e,syst}^* = 0.05 n_e^* \qquad \Delta n_{e,stat}^* = min[|n_e^{MAX} - n_e^*|, |n_e^{MIN} - n_e^*|] \tag{3.27}$$

and

$$n_e^{MAX,\,MIN} = \xi \frac{(S_1^{TH} \pm \Delta S_1^{TH})\frac{7}{4}\sigma_G^{RAM}}{(h_1^{RAM} \mp \sigma_{h_1^{RAM}})c_1(T_e^* \pm \Delta T_e^*)} \tag{3.28}$$

The statistical uncertainty of the absolute sensitivity appears in the slope obtained from Raman scattering measurements (eqn. 3.15), $\sigma_{h_1^{RAM}}$.

To explain the systematic error of 5% (eqn. 3.27), we refer to eqn. 3.12 (definition of σ_G^{RAM}) and to Section 3.4.1.1 in which the error in the wavelength scale of the spectral response functions was given ($\Delta\lambda \approx \pm 0.8 nm$). Fig. 3.26 shows that the computation of σ_G^{RAM} must be sensitive to errors in the wavelength scale since strong lines of the anti-Stokes Raman transitions appear in the wings of the spectral response function. Computations of σ_G^{RAM} using spectral response functions shifted to shorter/longer wavelengths show, in fact, a decrease/increase in σ_G^{RAM} of the order of 5%. This value clearly depends on the precise shape of the first spectral channel response function, but is nevertheless a reasonable estimate which can be applied to all polychromators.

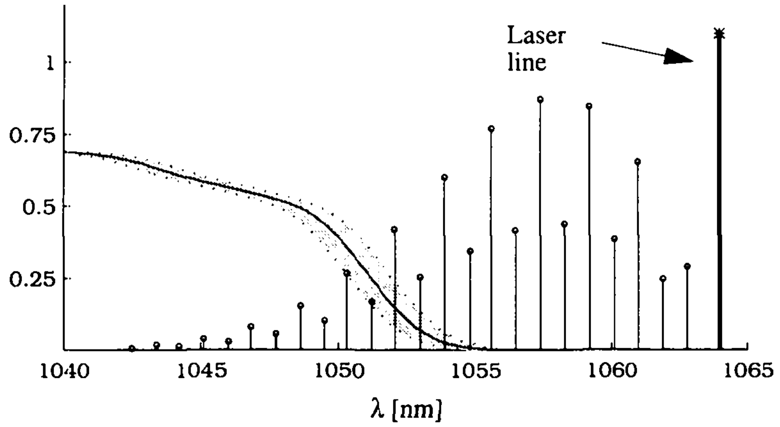

Figure 3.26: Measured spectral response function (see also fig. 3.22) of first polychromator channel (patched surface) together with the anti-Stokes Raman lines. The hatched surface represents the response functions shifted to shorter/longer wavelengths by Δλ≈0.8nm. The spread of the response function values at fixed λ illustrates the uncertainties when the weighted cross-section of a Raman transition is computed.

4 Profile Analysis in Normalized Flux Coordinates

4.1 Introduction

The Thomson scattering system measures T_e and n_e profiles along a vertical chord at a number of observation volumes (10 respectively 25) with fixed spatial coordinates. This profile description depends on the plasma position and is particularly difficult to use on TCV where the plasma shape can change radically and in which the profile information must be incorporated into data analysis employing the results of other diagnostics with different geometries. This difficulty can be overcome by considering quantities like T_e and n_e to be constant on magnetic flux surfaces, so that the original spatial coordinates can be mapped onto a normalised flux coordinate, ρ which may be obtained from the poloidal flux, $\Psi(r, z)$ by the simple transformation:

$$\rho = \sqrt{1 - \Psi(r, z)/\Psi(r_0, z_0)} \tag{4.1}$$

where $\Psi(r_0, z_0)$ denotes the flux on the magnetic axis. For Thomson scattering measurements with a limited number of observation volumes, coverage of only half of the poloidal cross-section is sufficient for profile representation in the entire ρ-space. Parameters such as the total energy, W_e and the total number of plasma electrons, N_e can then be obtained by integration of the profiles (Table 4-1).

The use of normalised flux coordinates is appropriate when the transport coefficients along the field lines are large enough to ensure negligible parallel T_e and n_e gradients and thus to make T_e and n_e constant on magnetic surfaces. Within the neoclassical transport description, this is a good approximation provided that the mean-free-path of the electrons along the field lines is large compared with the poloidal larmor radius, or, alternatively, that the collision frequency ($\nu_{ee}{\approx}10^7$Hz, $\nu_{ei}{\approx}10^4$Hz for $n_e{\approx}10^{19}$m^{-3} and $T_e{\approx}100$eV) is small compared with the ratio between the electron cyclotron frequency and the safety factor ($\omega_{ce}/q \approx 4 \cdot 10^9Hz/q$). Even though neoclassical transport coefficients fail by about two orders of magnitude to describe the typical measured values, the approximation of constant T_e and n_e on flux surfaces remains valid down to the lower limit of T_e accessible with the Thomson scattering system on TCV (several 10's of eV near the LCFS).

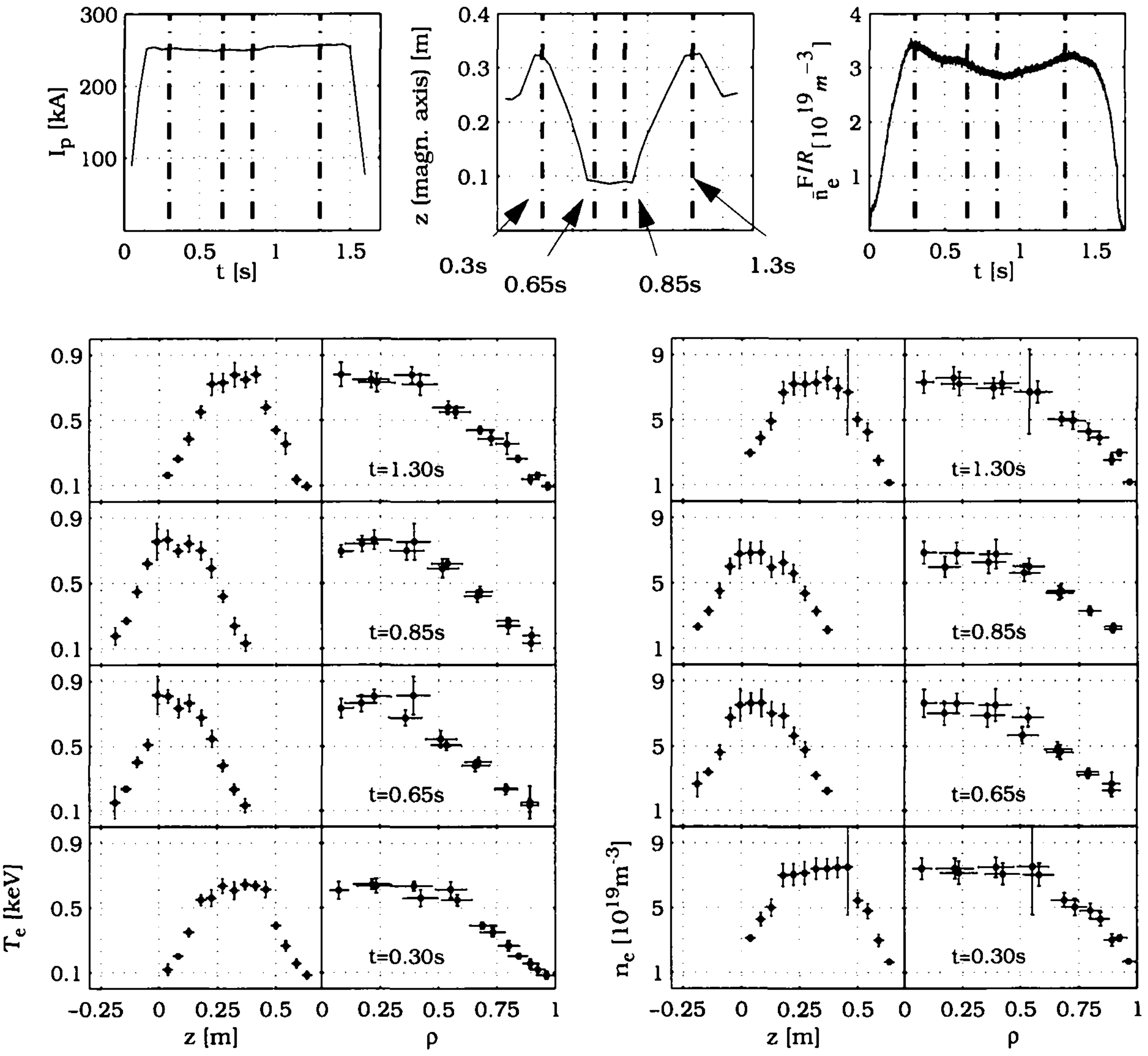

Figure 4.1: Vertical shift of the magnetic axis by more than 20 cm during the stationary phase of a discharge with moderate plasma current (I_p≈250kA, $\bar{n}_e^{FIR}$≈$3\cdot 10^{19} m^{-3}$). The T_e and n_e profiles are displayed at 4 different times, in order to illustrate the influence of the shift on the profiles in both spatial and normalised flux coordinates.

Fig. 4.1 shows the effect of the mapping on the profile representation for a discharge in which the plasma is displaced vertically during a phase with stationary plasma parameters (I_p plateau). The unmapped profiles follow the 20cm shift of the magnetic axis, equivalent to 5 times the spatial resolution of a single observation volume. In mapped coordinates, the profile maxima and shape do not depend on vertical location of the magnetic axis, since the electron density and the ohmic heating power are maintained almost constant. The representation in normalised flux coordinates shows furthermore that the profiles are symmetric with respect to the magnetic axis within the uncertainties of the measurement.

Whilst the choice of normalised flux coordinates is a helpful and convenient representation, a number of factors can lead to the creation of poloidal asymmetries and hence errors in the mapped profiles. For example, transient asymmetries near the discharge centre have been observed on soft X-ray emissivity profiles in several ohmic H-modes which may be caused by asymmetries on T_e and n_e profiles. It is also known that plasma configurations limited on the central column are characterized by in/out asymmetries in T_e and n_e near the LCFS. The same applies to diverted discharges in which the poloidal field null, or X-point, is generally a region of cold and dense plasma from which radiation losses are high. Magnetic islands can also create noticeable asymmetries on the profiles depending on the island mode numbers.

In addition to the plasma induced asymmetries listed above, systematic errors can also occur arising from inaccuracies in the flux surface geometry and the coordinates of the magnetic axis (r_0, z_0) obtained from the equilibrium reconstruction. Such inaccuracies can reach 1-2 cm and sometimes lead to apparent asymmetries on the mapped profiles.

4.2 Explanation of the Profile Analysis

4.2.1 The Interpolation Scheme

A scheme suitable for the routine analysis of T_e, n_e and p_e profiles in normalized flux coordinates should be sufficiently flexible that interpolation through the data points in the presence of frequent variations should be possible without requiring frequent user intervention. Such variations arise, for example, during sawtooth oscillations, leading to perturbations on the T_e profile near the plasma centre, or during H-mode discharges where the edge n_e gradient is steep. The computed p_e profiles can be sensitive to either of these features.

Since the profiles are represented in normalised flux coordinates, the profile fits, $s(\rho)$, must be symmetric with respect to the magnetic axis ($\rho=0$). This implies that

$$\left.\frac{\partial s}{\partial \rho}\right|_{\rho=0} = \left.\frac{\partial^3}{\partial \rho^3}s\right|_{\rho=0} = 0 \tag{4.2}$$

We further impose a vanishing curvature at the LCFS,

$$\left.\frac{\partial^2}{\partial \rho^2}s\right|_{\rho=1} = 0 \tag{4.3}$$

This latter boundary condition does not result from the choice of the coordinate system, but considerably reduces artificial structures on the fitted profiles near the plasma edge, where data points may be missing or contain large uncertainties.

We have chosen an interpolation method based on cubic B-splines (degree k=3) as primary base functions (see also [13], [45]). Cubic B-splines possess continuous derivatives up to the 2nd order and are characterised by single data points, called knots. In what follows, J will denote the number of knots, λ, within the closed interval [0:1]. For the ensemble of knots, we use the following ordering:

$$\lambda_{-2}<\lambda_{-1}<\lambda_0<\lambda_1=0<....<\lambda_J=1<\lambda_{J+1}<\lambda_{J+2}<\lambda_{J+3} \tag{4.4}$$

A single cubic B-spline, $b_j(\rho_m)$ is defined on an equispaced 1-dimensional grid:

$$0=\rho_1<\rho_m<\rho_M=1 \qquad (m=1....M,\ M=41 \text{ on TCV}) \tag{4.5}$$

Each cubic B-spline is localized, positive and only non-zero for $\lambda_{j-2}<\rho_m<\lambda_{j+2}$ (j=0,1....J+1). The (J+2) splines, b_j can be normalized, $\sum b_j = 1$, constituting in this case a full set of base functions. Any linear combination of these B-splines maintains the initial continuity properties. The boundary conditions are then imposed by finding the subspace of base functions, u_l (l=1,....,J-1) (fig. 4.2), for which the constraints are satisfied (the nullspapce of the matrix **R**). Applying a singular value decomposition [17], the matrix of constraints, **R**

$$R = \begin{bmatrix} b_0'(0) & \dots & b_{J+1}'(0) \\ b_0'''(0) & \dots & b_{J+1}'''(0) \\ b_0''(1) & \dots & b_{J+1}''(1) \end{bmatrix} \tag{4.6}$$

is decomposed into three matrices,

$$R = DSF^T \tag{4.7}$$

where **S** is a diagonal matrix of the same dimension as **R**, with non-negative diagonal elements (the singular values of **R**) in decreasing order, and **U** and **F** are unitary matrices whose dimensions correspond respectively to the number of rows and columns of **R**. The column vectors of **F** which are not associated with the singular values just span the nullspace of **R** and can be integrated into a matrix **V**. We obtain then a new set of base functions using:

$$U = BV = \begin{bmatrix} b_0(\rho_1) & \dots & b_{J+1}(\rho_1) \\ \dots & \dots & \dots \\ b_0(\rho_M) & \dots & b_{J+1}(\rho_M) \end{bmatrix} \times \begin{bmatrix} v_{0,1} & \dots & v_{0,J-1} \\ \dots & \dots & \dots \\ v_{J+1,1} & \dots & v_{J+1,J-1} \end{bmatrix}, \tag{4.8}$$

which establishes that:

$$\sum_{l=1}^{J-1} c_l u_l'(0) = \sum_{l=1}^{J-1} c_l u_l'''(0) = \sum_{l=1}^{J-1} c_l u_l''(1) = 0\ . \tag{4.9}$$

Least squares minimization may now be applied as a first step in finding the spline $s(\rho_n) = \sum c_l u_l(\rho_n)$ which gives the best fit to the N data-points of a single profile.

We must therefore determine the spline, s(ρ) for which the expression

$$\chi^2 = \frac{1}{N-J+1} \sum_{n=1}^{N} \frac{(y_n - s(\rho_n))^2}{\sigma_n^2} \tag{4.10}$$

is minimized. The σ_n in eqn. 4.10 denote the estimated uncertainties in the measured data y_n. Substituting the expression for $s(\rho_n)$ into eqn. 4.10, we obtain:

$$\chi^2 = \frac{1}{N-J+1}\sum_{n=1}^{N}\left(\frac{y_n(\rho_n)}{\sigma_n} - \sum_{l=1}^{J-1}\frac{c_l u_l(\rho_n)}{\sigma_n}\right)^2 \tag{4.11}$$

for which an equivalent matrix equation may be written:

$$\chi^2 = \frac{1}{N-J+1}(\vec{y} - \boldsymbol{W}\vec{c})^T(\vec{y} - \boldsymbol{W}\vec{c}) \tag{4.12}$$

where $\vec{y}$ and $\vec{c}$ are column vectors with $(\vec{y}^T = y_1/\sigma_1, \ldots, y_N/\sigma_N)$, $\vec{c}^T = (c_1, \ldots, c_{J-1})$ and $\boldsymbol{W}$ is now an (N,J-1)-matrix including the measurement uncertainties:

$$\boldsymbol{W} = \begin{bmatrix} u_1(\rho_1)/\sigma_1 & \ldots & u_{J-1}(\rho_1)/\sigma_1 \\ \ldots & \backslash & \ldots \\ u_1(\rho_N)/\sigma_N & \ldots & u_{J-1}(\rho_N)/\sigma_N \end{bmatrix} \tag{4.13}$$

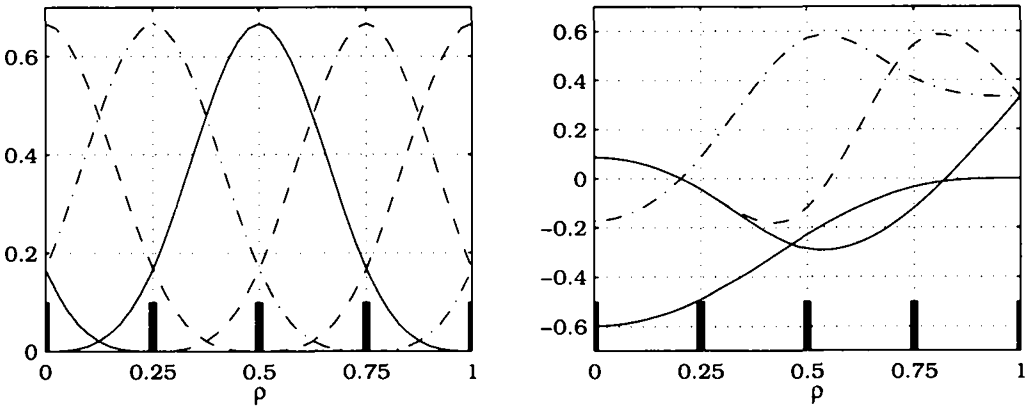

Figure 4.2: Representation of the full set of 7 Cubic B-splines (left) and the corresponding set of 4 base functions u_l (right) when J=5 equispaced knots are chosen on the interval [0;1].

We note that according to the theorem of Schoenberg-Whitney [13], only if at least one data point, $y_n(\rho_n)$ lies between each pair of neighbouring knots, will the matrix $\boldsymbol{W}$ have its full column rank (J-1):

$$\lambda_j < \rho_n < \lambda_{j+1} \qquad (j=1,\ldots,J-1) \tag{4.14}$$

The vector of spline coefficients, $\vec{c}$ can now be computed by solving, in a least squares sense, the overdetermined system of linear equations, $\vec{y} = W\vec{c}$. The ordinary least squares estimator for the spline coefficients in the vector $\vec{c}$ is then given by:

$$\vec{c} = (W^T W)^{-1} W^T \vec{y} \tag{4.15}$$

This solution for the minimum χ^2 in eqn. 4.12 is sensitive to the uncertainties on individual data points. Knowing the coefficients $\vec{c}$, the spline can be calculated on any grid within the interval [0;1].

4.2.2 *Location of the Knots*

A basic criterion for the evaluation of the fit quality is the χ^2-value. Assuming that the scheme described in the previous section leads to the best fit spline *s(ρ)*, the optimal number and location of the knots must still be determined. Using empirical knowledge regarding the approximate shape of a large number of T_e, n_e and p_e profiles, we opt for a fixed relation between the number of knots and their locations leading to the following algebraic descriptions:

1) T_e profiles: $$\lambda_{j(T_e)} = \left[0, \frac{1}{J-1}, \ldots, \frac{J-2}{J-1}, 1\right]$$

2) n_e, p_e profiles: $$\lambda_{j(n_e, p_e)} = \left[0, \frac{1}{J-3}, \ldots, \frac{J-4}{J-3}, \frac{2J-7}{2J-6}, \frac{6J-19}{6J-18}, 1\right] \tag{4.16}$$

To maintain sufficient accuracy in the profile fits, the number of knots, J must not be too small. If J is too large however, the profile fit is strongly affected by uncertainties in the data values and susceptible to spurious oscillations. We obtain the optimal number of knots by observing the evolution of the χ^2-parameter as a function of the number of degrees of freedom (N-J+1), where N is the number of data points, or equivalently the number of knots. In general, for a given collection of profiles, χ^2 will decrease continuously with increasing J finally reaching a relatively constant value. We therefore accept the smallest number of knots which attains this limit in χ^2. Fig. 4.3 shows the results of an analysis of a set of 120 profiles measured in 120 different L-mode limited discharges, using the detection system with 10 observation volumes in the upper part of the vacuum vessel. We find that 5 knots is optimal for T_e profiles, J=5, whilst n_e and p_e profiles require a larger number, J=6. Fig. 4.4 shows the variation of the profile fits for a single profile as a function of the number of knots.

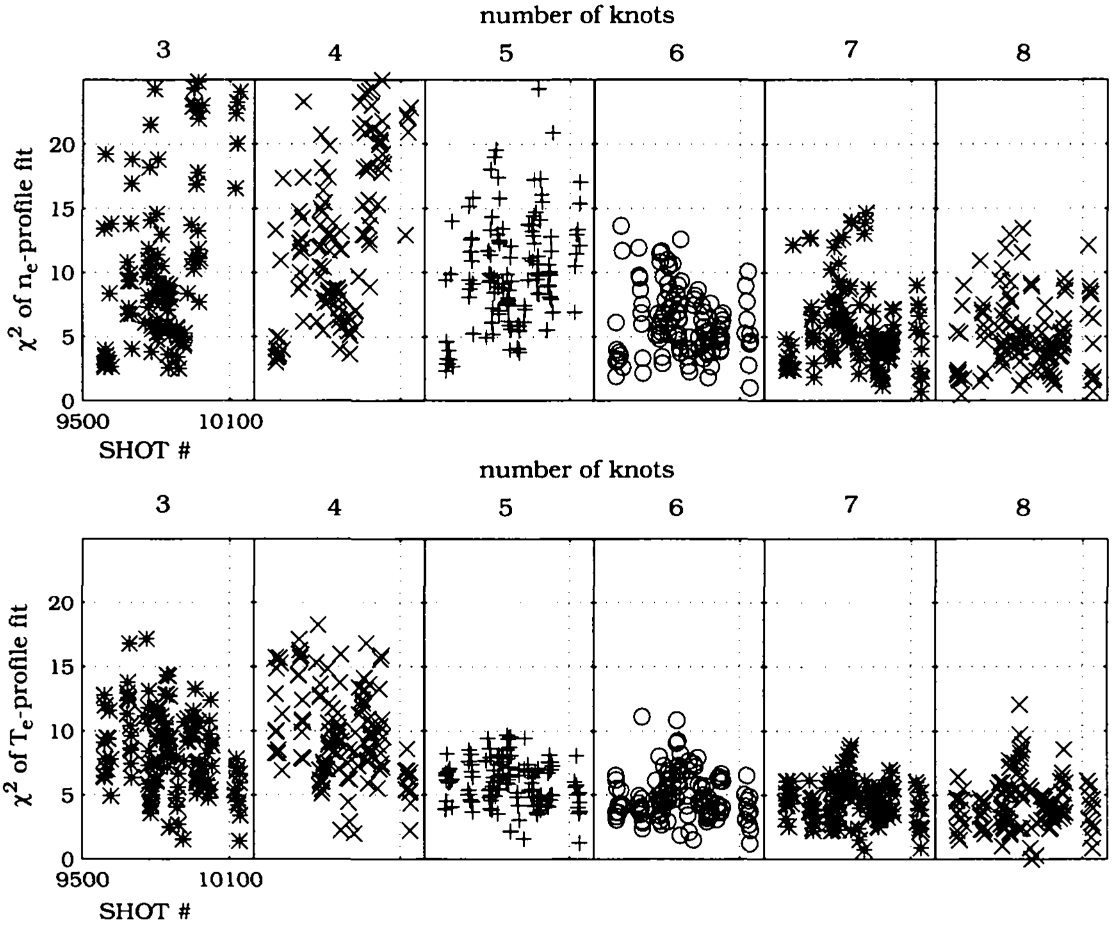

Figure 4.3: "Quality of fit" analysis for T_e and n_e profiles. Each plot window in the lower part of the figure contains the χ^2 data of 120 T_e profile fits for a fixed number of knots. The plot windows in the upper part contain the corresponding χ^2-data for the n_e profile fits.

It is clear, however, that the choice of a fixed set of knots can lead to difficulties in several situations. When only a few observation volumes cover the poloidal plasma-cross section, or if certain observation volumes cannot be used due to signal-to-noise considerations or hardware problems (saturation of amplifiers or digitizers) there may not be sufficient data points in the interval between two adjacent knots. The Schoenberg-Whitney theorem (eqn. 4.14) is then no longer respected and the inverse of the matrix product, $W^T W$ cannot be computed. In such cases, we do not consider the smaller knot of the pair $(\lambda_j,\lambda_{j+1})$, $\lambda_j<\lambda_{j+1}$, so that the number of degrees of freedom for the best fit spline $s(\rho)$ is reduced by 1.

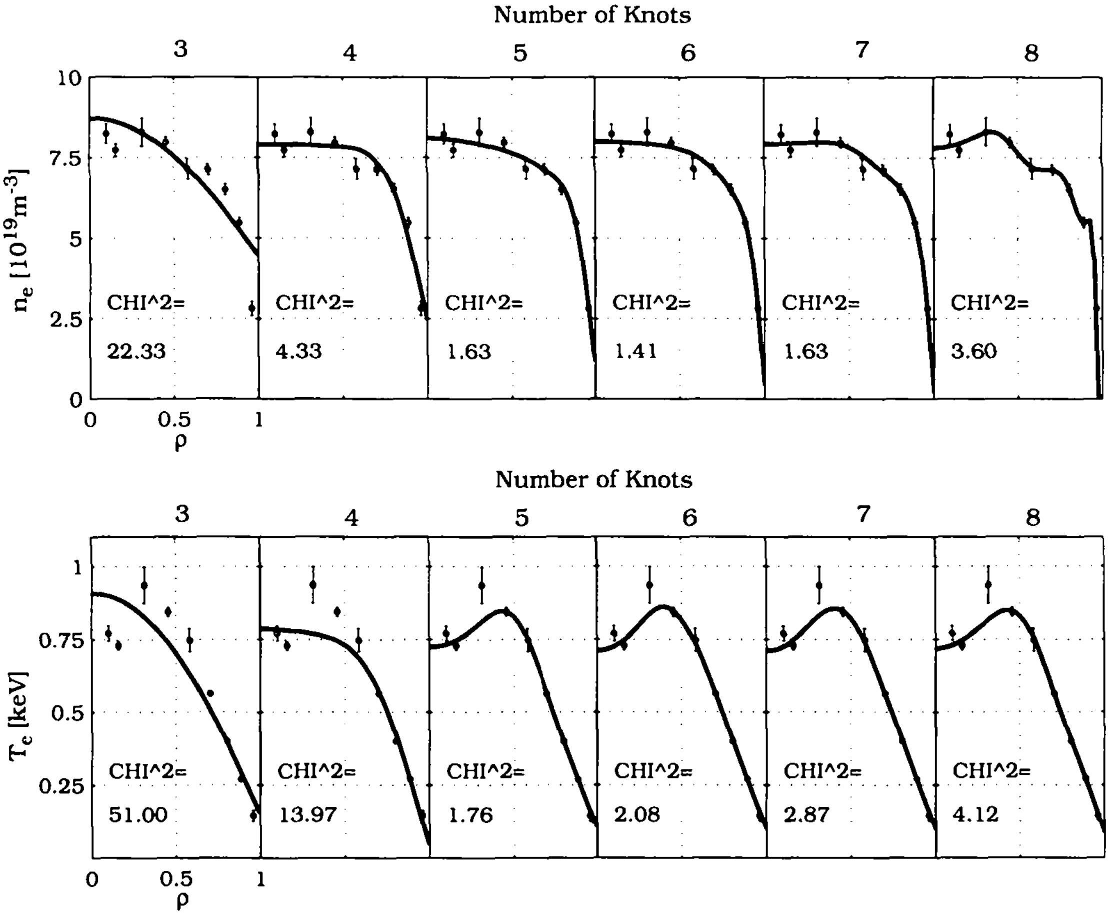

Figure 4.4: T_e and n_e profile fits for various numbers of knots (discharge #9969, t=0.75s).

4.2.3 Error Analysis of the Profile Fits

The errors associated with each profile fit can be subdivided into two categories: those with a global character (global errors) and those with a more local character (local errors). An appropriate combination of both types gives an error estimation for each sample of a profile fit.

1) The global error is simply determined by the χ^2-value for the profile fit.

If $\chi^2 \approx 1$, the average distance between the measured data, $y_n(\rho_n)$ and the best fit spline, $s(\rho_n)$ is close to the corresponding estimated uncertainties.

2) The local error represents the uncertainty of each single point in the best fit spline on the chosen grid (eqn. 4.5), $s(\rho_m)$ due to uncertainties in the measured data. The local error becomes large if one of the splines, $c_l u_l$, which locally determines the best fit spline, $s(\rho_m)$ has a large uncertainty. This means that the corresponding coefficient, c_l is not well determined. To estimate the uncertainties in the spline coefficients, we first calculate the covariance matrix:

$$C_{\vec{c}} = (W^T W)^{-1} W^T \Omega W (W^T W)^{-1} \tag{4.17}$$

where Ω represents the covariance matrix of the measured data. This contains only diagonal elements since each data sample represents an individual measurement and the corresponding uncertainties are therefore uncorrelated:

$$\Omega = \begin{bmatrix} \sigma_1^2 & 0 & 0 \\ 0 & \backslash & 0 \\ 0 & 0 & \sigma_N^2 \end{bmatrix}$$

The covariance matrix, C_S of the best fit spline can be computed using only the diagonal elements of the covariance matrix, $C_{\vec{c}}$:

$$C_S = Z diag(C_{\vec{c}}) Z^T \tag{4.18}$$

where

$$Z = \begin{bmatrix} u_1(\rho_1) & \dots & u_{J-1}(\rho_1) \\ \dots & \backslash & \dots \\ u_1(\rho_M) & \dots & u_{J-1}(\rho_M) \end{bmatrix} \tag{4.19}$$

The local error estimate, $\sigma_{s,m}$ of each sample of the spline is then just the square root of the corresponding diagonal element in $\mathbf{C_S}$.

Including both local and global errors, a reasonable error estimation for each sample of the interpolating spline is therefore given by the product:

$$\Delta_{s,m} = \sigma_{s,m}\sqrt{\chi^2} \qquad (4.20)$$

Fig. 4.5 shows the result of the spline error estimation for different T_e and n_e profiles in a single discharge (#9932). This representation gives a reasonable picture of the correlation between structures of the best fit spline and the corresponding profile. For example, the T_e profile fit at t=0.75s clearly shows a hollow shape, even though the profile has been measured during a sawtooth rise. In this particular case, the hollow shape is not significant within the profile error estimation and even a monotonic profile fit would be in agreement with the estimated uncertainties.

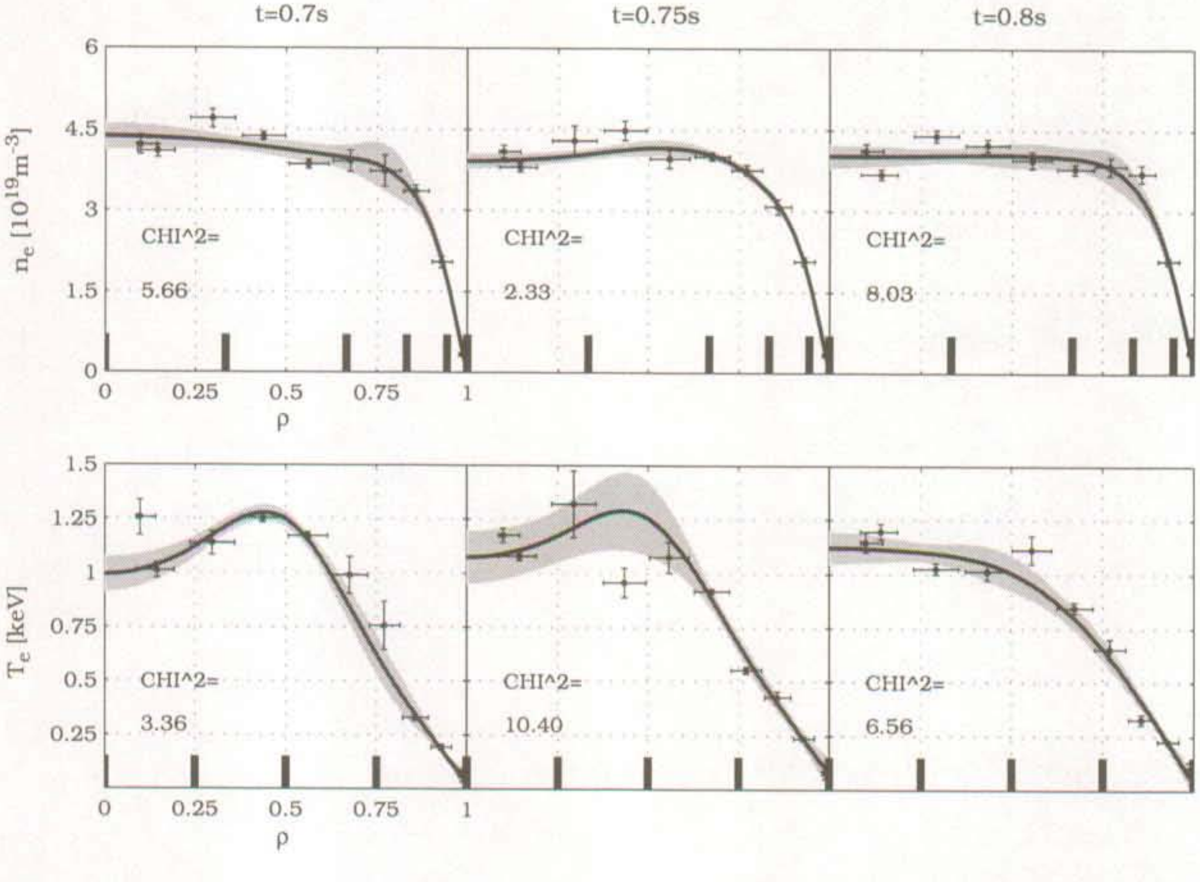

Figure 4.5: Representation of different T_e and n_e profile fits (discharge #9932, κ_a=1.73, δ_a=0.28, q_a=3.1, $<n_e>_L$=3.5·10^{19}m^{-3}). Data points ('o'-symbols) are shown with vertical and horizontal errorbars (spatial resolution of the observation volumes in normalised coordinates). The patched surfaces show the results of the spline error estimates. The knot location is indicated by the vertical bars on the bottom of each plot window.

4.2.4 Application of the Profile Analysis

The spline fitting described above has been incorporated into a MATLAB routine which computes a series of quantities using measured T_e and n_e profiles and the flux surface geometry from an equilibrium reconstruction (Table 4-1). Each of these quantities, together with the calculated uncertainty, is stored under MDS+ and is therefore generally accessible.

Table 4-1: Routinely Calculated T_e, n_e and p_e Profile Parameters

Parameter	Symbol	Expression
Electron temperature (density, pressure) on magnetic axis	$T_{e,0}$ ($n_{e,0}$, $p_{e,0}$)	
Volume averaged electron temperature (density, pressure)	$\langle T_e\rangle_V^{TH}$ ($\langle n_e\rangle_V^{TH}$, $\langle p_e\rangle_V^{TH}$)	$\frac{1}{V}\int_0^1 T_e(\rho)\frac{dV}{d\rho}d\rho$
Energy content of plasma electrons	W_e	$\frac{3}{2}\int_0^1 p_e(\rho)\frac{dV}{d\rho}d\rho$
Total number of plasma electrons	N_e	$\int_0^1 n_e(\rho)\frac{dV}{d\rho}d\rho$
Line integrated electron density at R=0.9m	$\bar{n}_e^{TH}$	$\int_{-z(LCFS)}^{z(LCFS)} n_e(R=0.9)dz$
Ratio of $\bar{n}_e^{FIR}$ to $\bar{n}_e^{TH}$ at R=0.9m	R_{TH}^{FIR}	$\frac{\bar{n}_e^{FIR}(R=0.9m)}{\bar{n}_e^{TH}}$

4.2.5 Limits and Possibilities for Improvement

The profile analysis method presented here does not always yield satisfactory fits, especially in discharges where data near the plasma edge are unavailable or strongly affected by systematic errors. In addition, for certain discharge types, the spatial resolution given by the size of the observation volumes may not be high enough for a correct representation of the profiles. In these cases and for a given set of base functions, the fitted profiles tend to show an artificially non-monotonic structure. Such distortions affect, of course, the calculation of quantities derived from these profiles (Table 4-1). Whilst the errors introduced in this way may still be acceptable in so far as integrated quantities ($\bar{n}_e^{TH}$, N_e, W_e) are concerned, they become unacceptable when analysis of spatial gradients is required. It is therefore of interest to investigate how such "artefacts" can be avoided.

One possible option consists in applying algorithms [13] which employ a fixed number of knots, but allow them to be placed at variable locations. This option has not yet been tested within the framework of the TCV Thomson profile analysis.

An alternative approach could be to seek minimization of a penalty function, Φ, in place of the standard χ^2-function. The former can be defined as:

$$\Phi = \frac{1}{2}\chi^2 + \alpha F \tag{4.21}$$

where F is an appropriately chosen functional and α a constant weighting parameter. For T_e profiles we have selected the functional

$$F_{Te} = \int_0^1 \frac{(\tilde{T}''_e)^2}{\tilde{T}_e} d\rho, \quad \tilde{T}'_e = \frac{d\tilde{T}_e}{d\rho} \quad \text{and} \quad \tilde{T}_e(\rho) = \frac{T_e(\rho)}{\langle T_e \rangle_V^{TH}} \tag{4.22}$$

Minimising F implies a minimization of the absolute value of $\tilde{T}''_e$, which would be the case of a 2nd order regularisation. However, the denominator, $\tilde{T}_e$ weights the minimization in the sense that for a fixed contribution of $(\tilde{T}''_e)^2/\tilde{T}_e$ to the integral, the absolute value of the curvature, $(\tilde{T}''_e)^2$ is allowed to be larger for data points where $\tilde{T}_e$ itself is large than for data points where $\tilde{T}_e$ is small. This means that the minimization of the curvature is strongest when the values of $\tilde{T}_e$ are smallest. For T_e-profiles in ohmically heated plasmas, this is a reasonable assumption. The central T_e is always larger than that in the outer regions of the plasma and shows features due to sawtooth oscillations, depending on the delay between the sawtooth crash and the instant, when the T_e-profile is recorded. On the other hand, significant curvature of the profile in the edge region where T_e is small would not be expected when the plasma is ohmically heated. By employing the proposed penalty functional, improvements can be achieved mainly for the profile analysis near the plasma edge (fig. 4.6). A value of the parameter α=0.1 reduces negative curvatures, but still admits hollow central profiles.

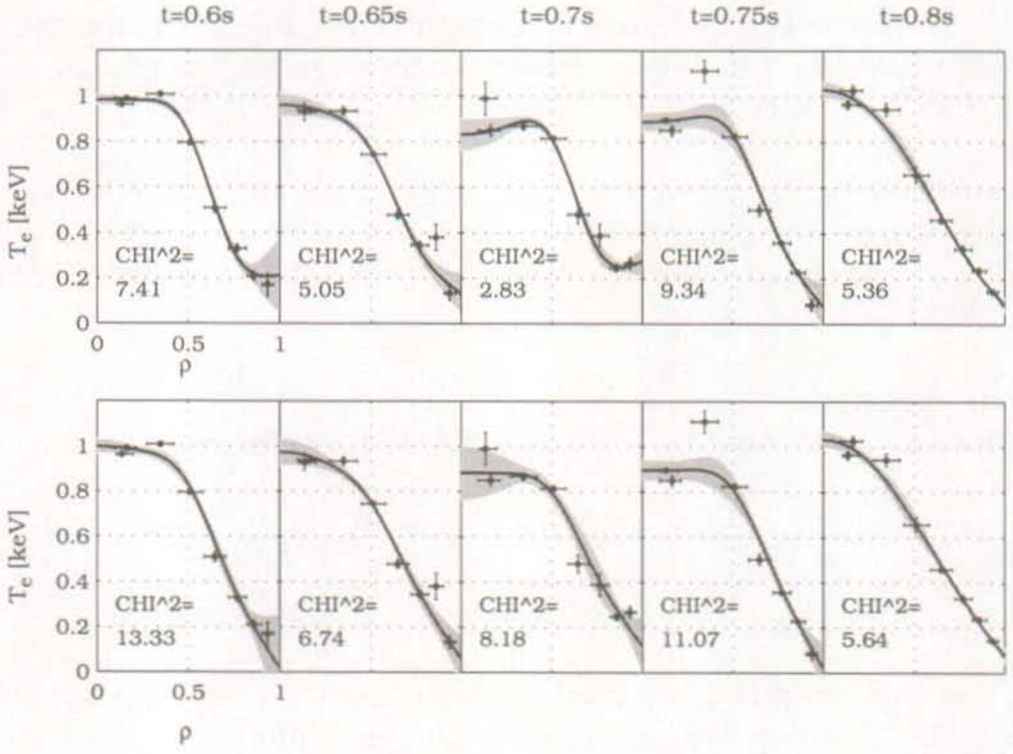

Figure 4.6: *T_e profile fits for different time slices of discharge #9594 (κ_a=1.54, δ_a=0.28, q_a=3.4, $\langle n_e \rangle_L$=3.4·$10^{19}m^{-3}$.). The plots in the upper row of the figure show the results obtained from the usual profile interpolation procedure. The plots in the lower row show the results using the penalty function described in the text. The larger uncertainties of the splines in the latter case result from the increase in the χ^2 values of the fits.*

For n_e and p_e profiles the following functionals have been tested:

$$F_{p_e} = \int_0^1 \frac{(\tilde{p}_e'')^2}{\tilde{p}_e} d\rho; \qquad F_{n_e} = \int_0^1 (\tilde{n}_e'')^2 \tilde{n}_e d\rho \tag{4.23}$$

These functionals cannot, however, sustain satisfactory profile interpolation in the case of inaccurate or missing edge measurements. Fig. 4.7 shows n_e profiles for the occasionally observed case of a discharge in which all the observation volumes are located inside the LCFS. The usual fitting procedure yields negative n_e values near the LCFS (case a)), whilst the use of a penalty functional with α=0.01 would result in a rather inaccurate fit (case b)). As a consequence, these penalty functionals have not been regularly applied to the analysis of Thomson data. Negative profile data are simply set to zero in order to maintain inaccuracies in derived quantities (N_e, W_e, R_{TH}^{FIR}) as low as possible.

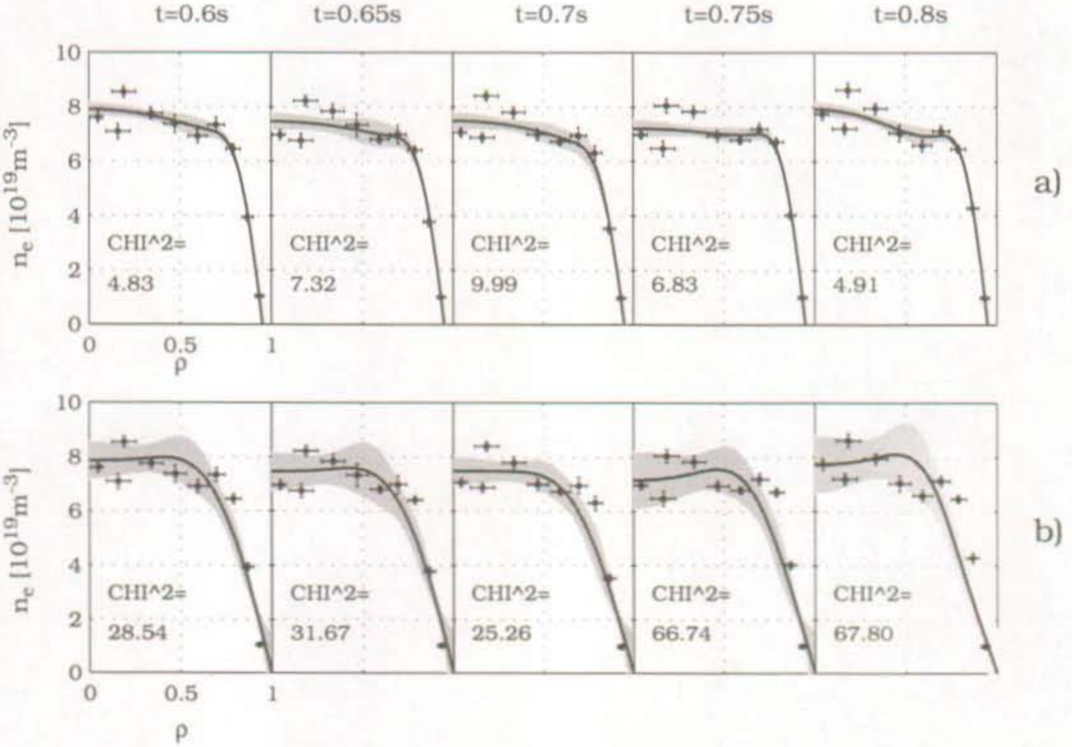

Figure 4.7: *n_e profile fits for different time slices of discharge #10023 (κ_a=1.79, δ_a=0.11, q_a=3.9, $\langle n_e \rangle_L$=6.4·10^{19}m^{-3}). The plots in the upper part of the figure show the results obtained from the usual profile interpolation procedure. The plots in the lower part show the results using the penalty function described in the text.*

5 T_e and n_e Profiles in Different Discharge Conditions on TCV

5.1 Sawtooth Signatures on T_e Profiles

The presence of a q=1 surface in a tokamak is usually accompanied by characteristic oscillations in the plasma soft X-ray emissivity. According to present understanding, this is the sign of a relaxation process tending to maintain the central q-value, q_0, close to 1 and is associated with the appearance of an m=1 internal kink mode becoming unstable if $q_0<1$. During each oscillation period, the central electron temperature rises steadily from some initial level prevailing in the absence of the oscillations. This increase is then suddenly interrupted by the onset of MHD-activity and the electron temperature "crashes" back to its initial value. This crash also provokes a change in the spatial T_e profile, with T_e decreasing inside the q=1 surface and increasing outside as a consequence of the outward propagating heat pulse. Since the soft X-ray emissivity is particularly sensitive to variations in T_e, the typical "sawtooth" like modulations observed on these diagnostic signals are the best indicator of this MHD-activity. Moreover, if as in the case of TCV, soft X-ray emissivity profiles are available, the q=1 surface can be roughly located by seeking the points at which the sawtooth oscillation changes sign.

For typical operating conditions on TCV, the sawtooth period is in the range 2.5→10ms and is therefore much faster than the actual TS system sampling rate. Nevertheless, it is possible to construct the temporal evolution of the profile change during a sawtooth cycle by sampling over a steady-state period with regular sawteeth. In this case, we rely on the fact that, in general, the sawtooth period and the time interval between laser pulses do not coincide. The TCV-discharges #7109 and #7751 shown in fig. 5.1 are two examples characterised by such an extended interval of almost stationary I_p and $\bar{n}_e^{FIR}$ and fairly regular MHD-activity (as can be seen on the trace T_e^{softX} - the electron temperature evaluated from soft X-ray emission).

Each grid point on the 3D representations of the T_e profile temporal evolution shown in fig. 5.2 represents an actual measurement. We could show that the fluctuations observed at different locations are correlated with sawtooth oscillations. This can be seen more clearly by computing the delay between the time of the profile measurement and that of the preceding sawtooth crash. Fig. 5.3 compiles the temperatures measured at different observation volumes plotted versus this delay for the discharges of fig. 5.1. In both cases, we observe a steady rise in T_e at locations close to the plasma centre, whilst T_e at the outer locations near the LCFS remains constant or decreases. Comparison of the observation volumes where the temporal derviative of T_e, $\Delta T_e/\Delta\tau_D$ changes sign with the points corresponding to the intersection of the laser chord and the sawtooth inversion radii determined from soft X-ray emissivity profiles yields very good agreement. For discharge #7109, the intersection with the q=1 surface is located at z=0.42m, for discharge #7751 at z=0.34m. The accuracy in both cases is ±2.5cm and is of the same order of magnitude as the spatial resolution of T_e profiles. The amplitude of central T_e variations ($\Delta T=\pm 15\%$) is also in reasonable agreement with T_e measurements from soft X-ray emission.

Regular analysis of sawtooth signatures using the present TS system requires fairly long (≥0.5s) steady-state periods in order for the sawtooth period to be encompassed by a sufficient number of laser pulses. Applying the time delay method described above to shorter periods would require an increased sampling frequency. This could be accomplished by using a cluster of synchronised Nd:YAG lasers or, alternatively, by synchronising individual laser pulses with the sawtooth crashes. Both options will be included in future upgrades of the existing TS system.

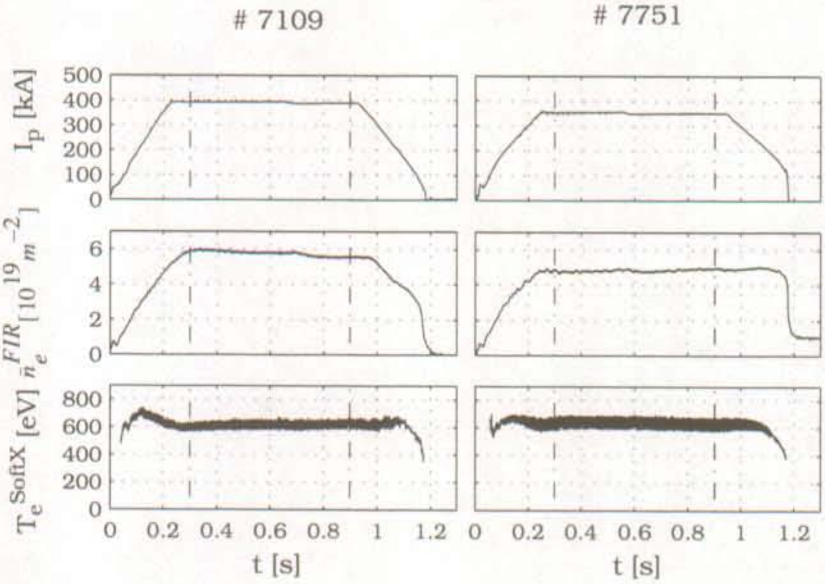

Figure 5.1: Temporal evolution of plasma parameters for TCV-discharges #7109 (left) and #7751 (right). The dashed lines show the stationary time interval chosen for this analysis.

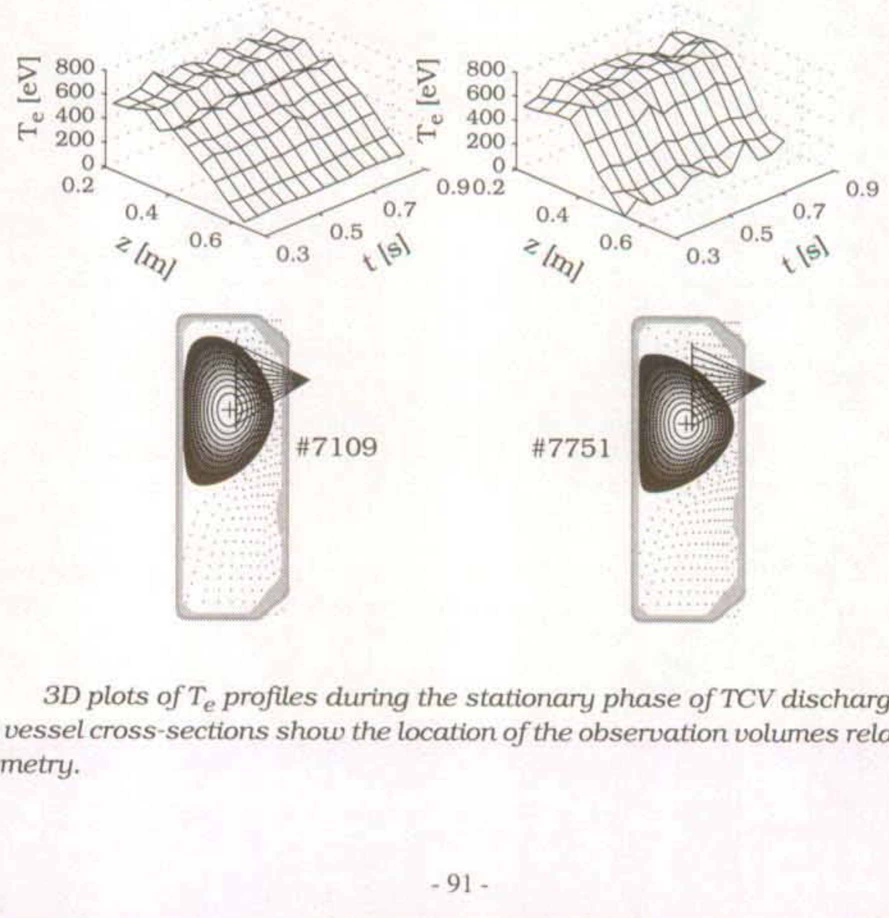

Figure 5.2: 3D plots of T_e profiles during the stationary phase of TCV discharges #7109 and #7751. The vessel cross-sections show the location of the observation volumes relative to the flux surface geometry.

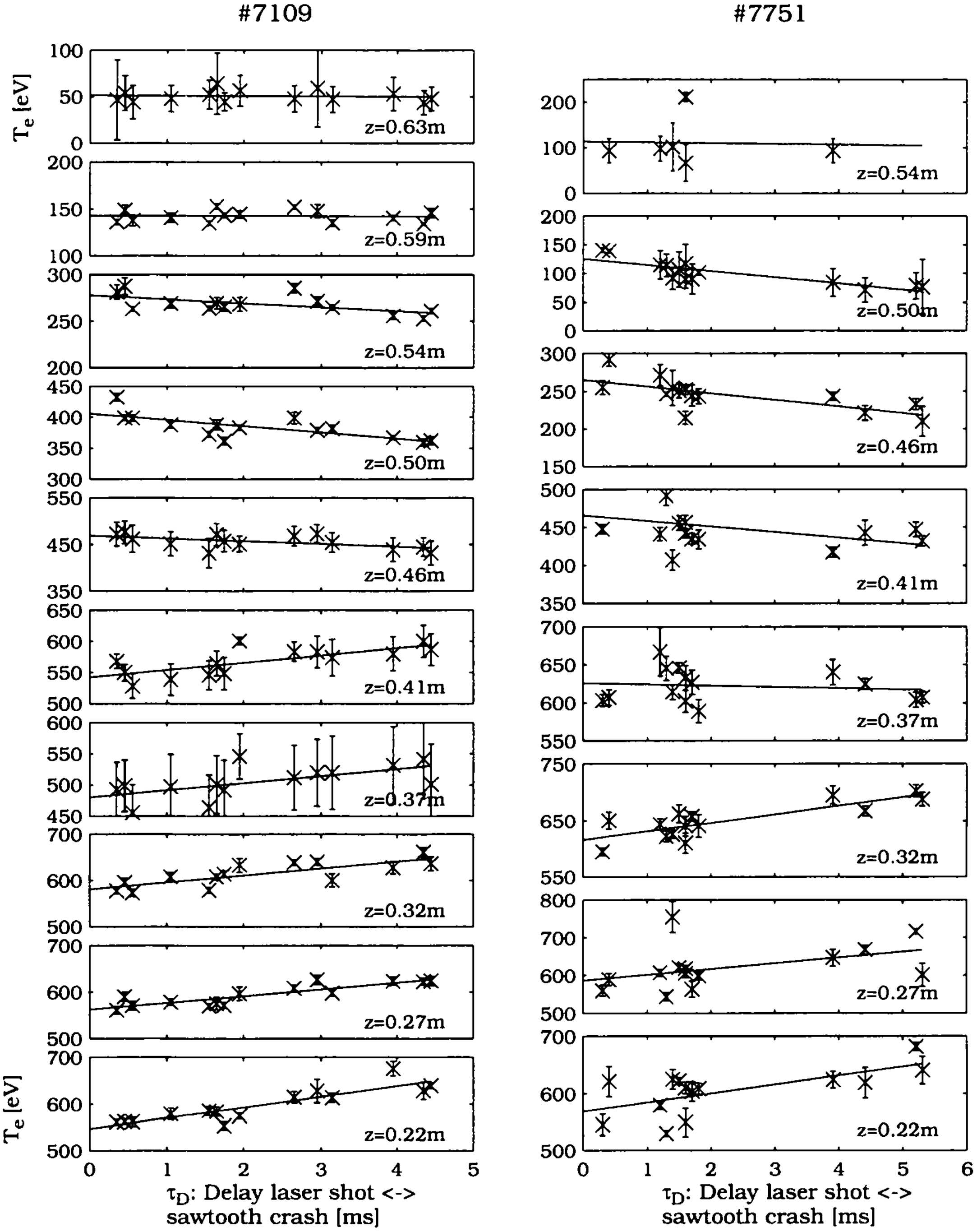

Figure 5.3: T_e measurements versus the delay between a laser pulse and the preceding sawtooth crash (τ_D). On the left, ten observation volumes for discharge #7109. On the right, eight observation volumes for discharge #7751.

5.2 Comparison of Density Measurements from Interferometry and Thomson Scattering

The current FIR-interferometer measures the line integrated electron density along 6 radially separated vertical chords (Section 3.1.2.2). One of these chords, at R=0.9m, corresponds to the radial position of the vertical TS system, albeit in a poloidal sector displaced toroidally by 180°. Owing to its high absolute accuracy (better than 5% at $\bar{n}_e \geq 10^{19}\mathrm{m}^{-3}$), the FIR line integrated density, $\bar{n}_e^{FIR}$, is used as a reference for comparison with the calculated line integrated density, $\bar{n}_e^{TH}$, obtained from TS data. To compute $\bar{n}_e^{TH}$ along any chord, the n_e profiles are first interpolated by a fit in normalised flux coordinates (Section 4.2). The fitted profile is then projected onto the vertical chords of the interferometer and integrated between the two points at which the given chord intersects the LCFS. The computed line integrated density obtained from TS data is therefore restricted to a measurement of the electrons in the confined plasma. In contrast, the FIR measurement also includes contributions from those electrons in the plasma scrape-off layer or diverted regions.

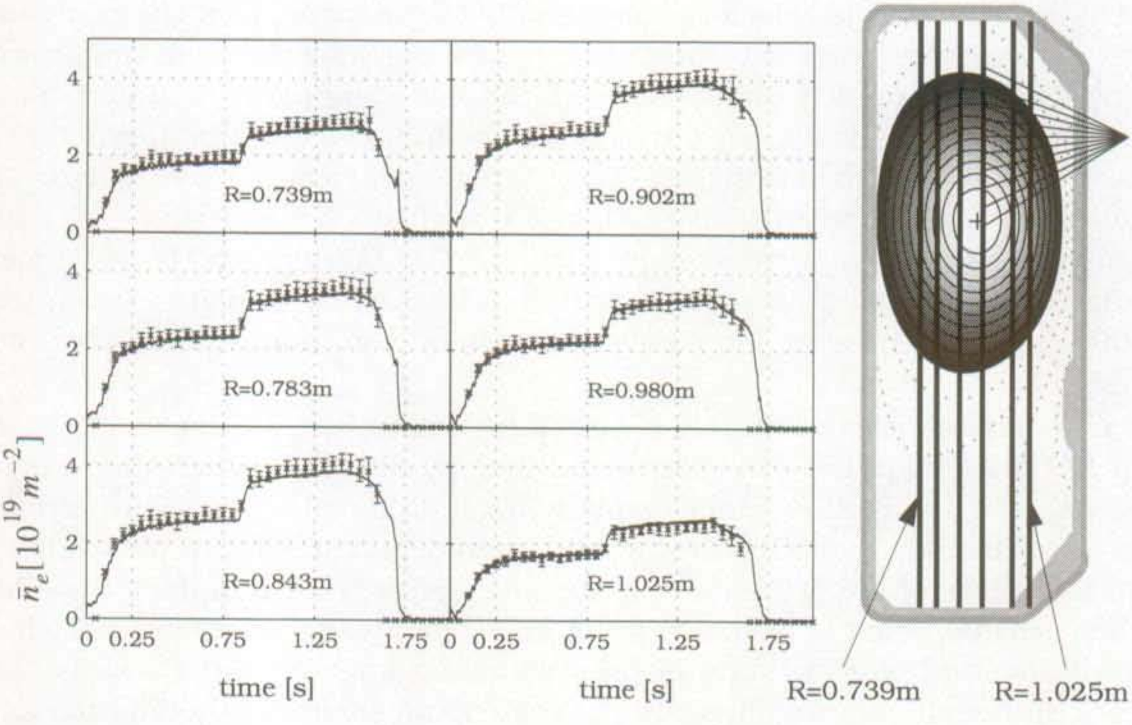

Figure 5.4: Comparison of the line integrated electron densities from FIR (solid lines) and TS (crosses) measurements for TCV discharge #9690 at the 6 vertical chords (shown on the right for flux surfaces at t=1.2s).

Fig. 5.4 shows the temporal evolution of $\bar{n}_e^{FIR}$ and $\bar{n}_e^{TH}$ for the 6 vertical chords in a limited discharge at moderate elongation (κ=1.55). The good agreement in all cases confirms the absolute values of the n_e profiles obtained from Thomson scattering and based on Raman calibration. Since, in this case, we find agreement for all radial positions, we conclude that the residual density outside the LCFS can be neglected for this configuration.

Occasional discrepancies between the TS and FIR n_e measurements in other discharges can be attributed to instrumental errors. Identified sources of error are; a) inconsistencies in the measurement of the laser pulse energy and b) dynamic misalignment of the detection optics due to magnetic field effects:

a) Since the absolute measurement of n_e is based on signals which must be normalized to the laser pulse energy monitor, errors in the energy measurement will translate into errors in n_e. There are indications that over long periods of time, the laser beam characteristics (direction, divergence) can change in such a way that the laser pulse energy and the scattering measurement are affected differently. In order to reduce these effects to a minimum, it is important that the laser has attained thermal equilibrium before a measurement is made.

b) The camera lenses of the detection optics must be inserted in between the poloidal field coils for measurements to be made. Fast transient currents are frequently driven through these coils, particularly when the plasma shape is changed or an X-point is formed. Since the lenses are mounted in metallic housings (Al-alloy), eddy currents can be induced and the interaction of these currents with the strong toroidal magnetic field leads to a torque on the optic supports. Under certain conditions these effects have caused a dynamic misalignment of the optical system during a TCV discharge. The recent exchange of the metallic housings for units fabricated in a high temperature (<200°C), plastic material should eliminate these field induced perturbations.

It is now general practice on TCV to compare n_e data from Thomson scattering with FIR line-integrated measurements, thereby deriving a correction factor, $R^{TH} = \bar{n}_e^{FIR}/\bar{n}_e^{TH}$, which is applied equally to all data points on a given profile. This factor is usually rather close to unity and departures from this value are good indicators of the presence of systematic errors. An example of the effect of the correction factors is shown in fig. 5.5 for a diverted discharge in which the full diverted configuration is present in the interval, t=0.35→1.3s. The curves in the left column illustrate the systematic errors on the TS measurements for this case. Renormalization by the correction factor, R^{TH} greatly reduces the differences (right column). A transient drop, stronger in $\bar{n}_e^{TH}$ than in $\bar{n}_e^{FIR}$ is also discernible at t=0.3s, coincident with the change from a limited to a diverted plasma configuration. Subsequently, $\bar{n}_e^{FIR}$ remains slightly higher than the corrected $\bar{n}_e^{TH}$ along the inner vertical chords (R=0.739m and R=0.783m) for the duration of the diverted phase. This effect is due to the intersection of these chords with the region of high density in the vicinity of the outer divertor strike zone. For the chords at R=0.739m and R=0.783m, the estimated line averaged densities contributed by the diverted plasma are $\langle n_e \rangle_L=8.0^{18}m^{-3}$ and $\langle n_e \rangle_L=6.0*10^{18}m^{-3}$ respectively. This corresponds to approximately 15-20% of $\langle n_e \rangle_L$ along the central chord.

For the remainder of this thesis, unless otherwise stated, all reported TS measurements (n_e, p_e profiles and derived parameters such as plasma energy) have been subject to the correction factor R^{TH}.

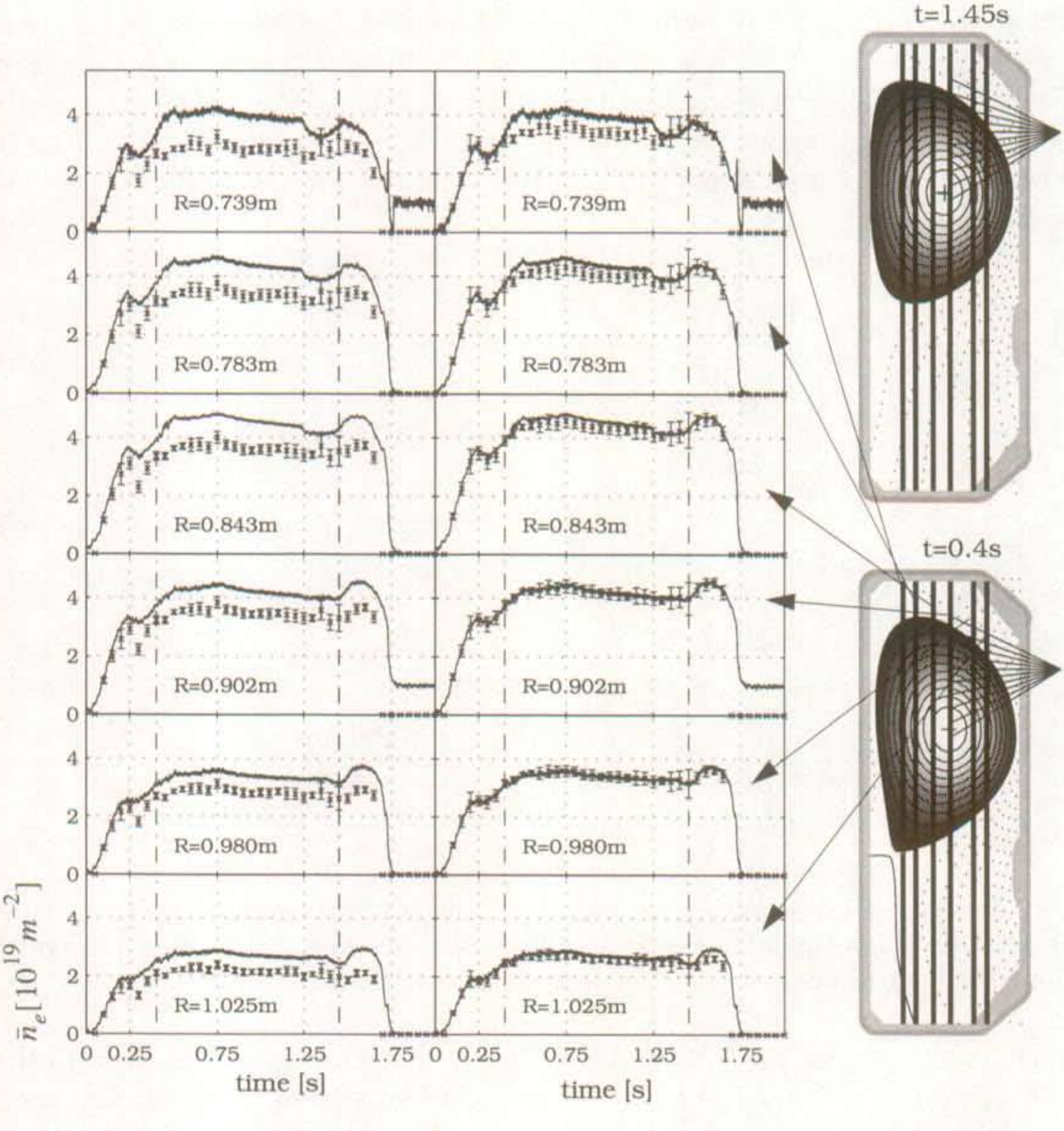

Figure 5.5: Comparison of the line integrated electron densities from FIR (solid lines) and TS (crosses) measurements for discharge #10095. On the left, the TS data are plotted before normalization by the correction factor, R^{TH} (see text). The curves on the right are obtained after correction. The flux surface plots at far right show the magnetic equilibria just after the formation of the divertor (bottom) and at the end of the discharge in the limited phase.

5.3 T_e and n_e Profiles in ELM-free, Ohmic H-modes

First seen on ASDEX [65], a mode of improved energy confinement, the H-mode, has since been observed in many tokamaks. A transition from the ordinary phase of low confinement, the L-mode, into H-mode can be characterized by a rapid drop of hydrogenic line emission. Whilst the spatial and temporal resolutions of the current TS system are too low to observe the detailed evolution of the transition, measurements before and after the transition show an increase in both T_e and n_e across the entire profile, together with a steepening of the gradients near the edge, indicative of the formation of a transport barrier in this region. Following an L-H transition in TCV, edge T_e values of about 200eV have been measured, compared with 50→100eV in L-mode (fig. 5.6). The edge electron density and global energy confinement usually rise by about a factor of 2.

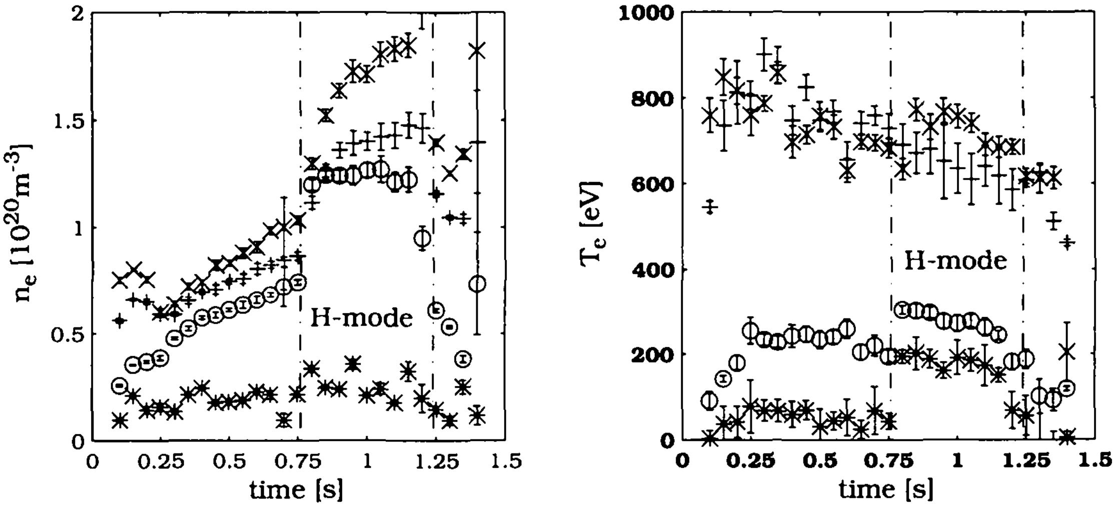

Figure 5.6: Temporal evolution of n_e and T_e profiles in ELM-free, ohmic H-mode (discharge #7435, SNL configuration): '' symbols refer to the plasma edge, 'o' to 90% of the normalized plasma radius, '+' to plasma mid-radius, 'x' to the plasma centre.*

In both ELM-free and ELMy H-mode phases, little change is observed in the T_e profiles. In contrast, in ELM-free H-mode phases, strong peaking of n_e profiles has been frequently observed on TCV (Pietrzyk, [44]), indicating an increase in the inward particle pinch. The two examples in fig. 5.7 illustrate how the n_e profile evolution can behave differently in otherwise ostensibly similar ELM-free H-mode discharges.

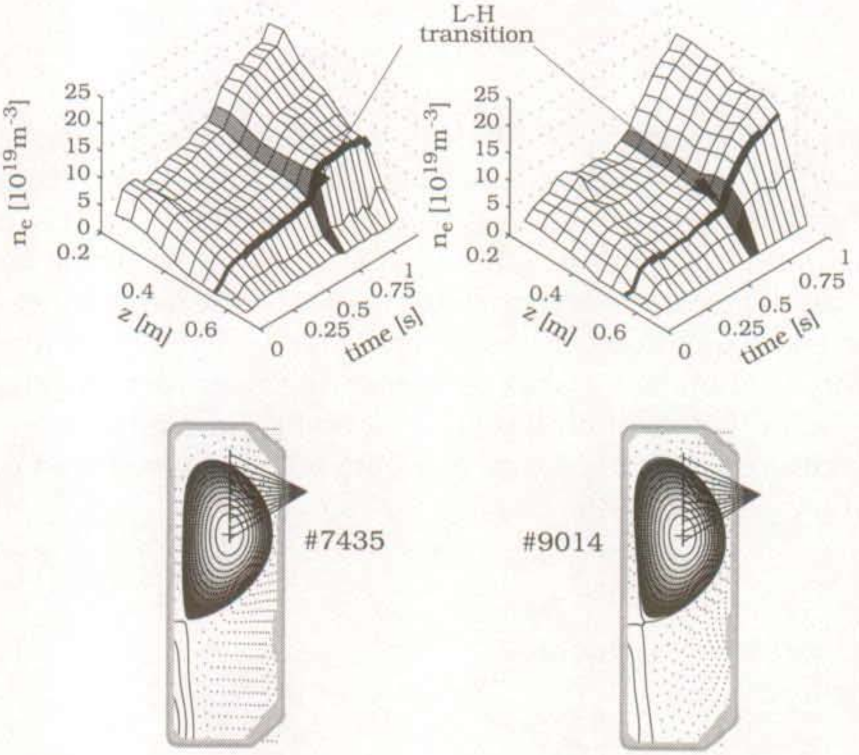

Figure 5.7: Temporal evolution of n_e profiles in two ELM-free, H-mode SNL discharges. Discharge #7435 shows a strong peaking of the n_e profiles in the plasma centre, whilst the n_e profiles of discharge #9014 remain fairly flat.

5.4 Performance of the Vertical System Equipped with 25 Polychromators

A rapid inspection of the many discharge configurations possible on TCV (Section 3.1, fig. 3.2) amply demonstrates that the TS system equipped with 10 observation volumes (compare also the particular configuration of fig. 3.4) cannot, in many cases, cover the poloidal plasma cross-section. Although redistribution of the observation volumes can (and has in the past) offer a partial solution, such modifications require complete readjustment of the detection system and must therefore be followed by an absolute Raman scattering calibration (Section 3.4.2.2). To render the TS diagnostic compatible with almost all possible TCV equilibria, the number of observation volumes has recently been increased to 25 and measurements can now be made in the range z=-0.50→0.64m.

5.4.1 T_e and n_e Profiles in Highly Elongated Plasmas

The creation of highly elongated plasmas is hampered by axisymmetric vertical instabilities whose growth rates rises non-linearly with increasing elongation [21]. These growth rates are too fast to be stabilised by the TCV poloidal field coil system such that in-vessel stabilisation coils are required. Installation of such a fast coil system was completed in 1996. At the same time, delivery was taken of the companion power supply and highly elongated plasmas are now routinely produced on TCV. Work is presently under way to extend performance up to the TCV elongation design limit (κ=3). For comparison, the highest elongation achieved to date on any machine is κ=2.5, produced on the DIII-D tokamak [30].

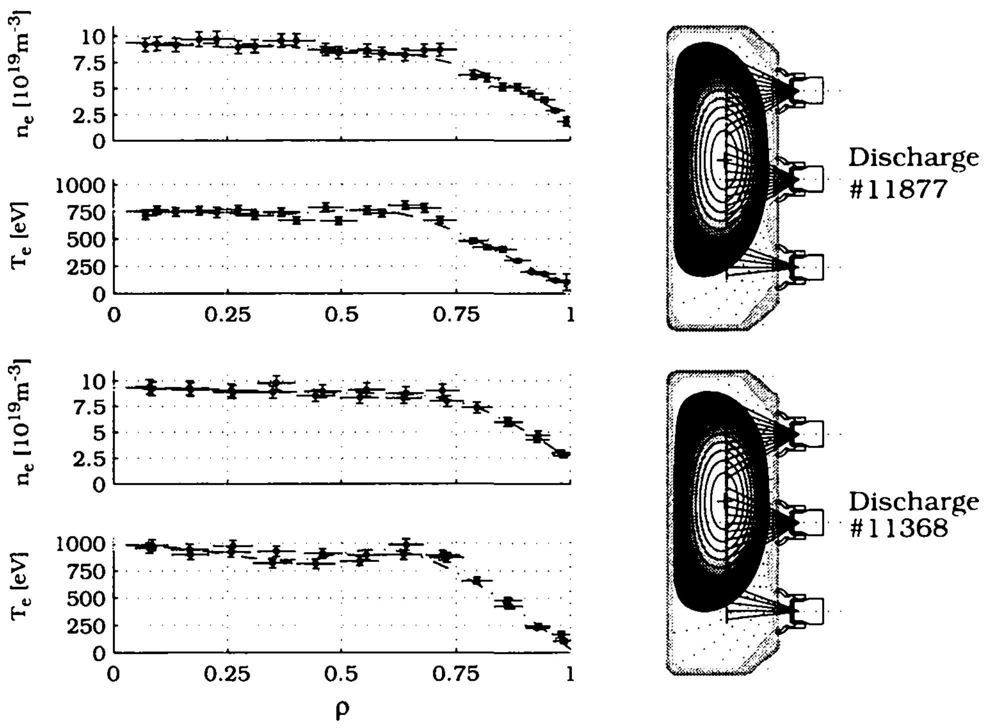

Figure 5.8: T_e and n_e profiles in two highly elongated TCV discharges, top: discharge #11877 at t=0.7s (q_a=2.9), bottom: discharge #11368 at t=0.6s (q_a=2.5).

Amongst the numerous TCV discharges already produced with κ>2, two examples serve both to demonstrate the capability of the new TS arrangement and to highlight major achievements on TCV with regard to elongation (discharge #11877, κ_{max}=2.45) and plasma current (discharge #11368, $I_{p,max}$=1.025MA). In each case, the 25 observation volumes encompass the full vertical extent of the poloidal plasma cross-section. For both discharges, the high plasma current yields an edge safety factor close to the stability limit, q_a=2. As shown on fig. 5.8, in such low q_a cases, the measured T_e and n_e profiles are found to be flat inside the central plasma regions. Plotting the measurements in the usual normalized flux coordinates also clearly demonstrate that the profiles are symmetric within measurement errors.

Using the scaling expressions (for reasonably low κ) to be obtained in the following chapter (eqn. 6.5, eqn. 6.6) relating profile peaking factors, $\hat{T}_e$ and $\hat{n}_e$ with q_a, κ_a and δ_a, extrapolations can be made to these new, higher values of elongation. Fig. 5.9 shows that $\hat{n}_e$ and $\hat{T}_e$ can be reasonably estimated within the accuracy of the scaling expressions, although the current plateau is only rather short for these discharges. Since only a few discharges have presently been analysed, no attempt has yet been made to adapt the scaling expressions for highly elongated plasmas.

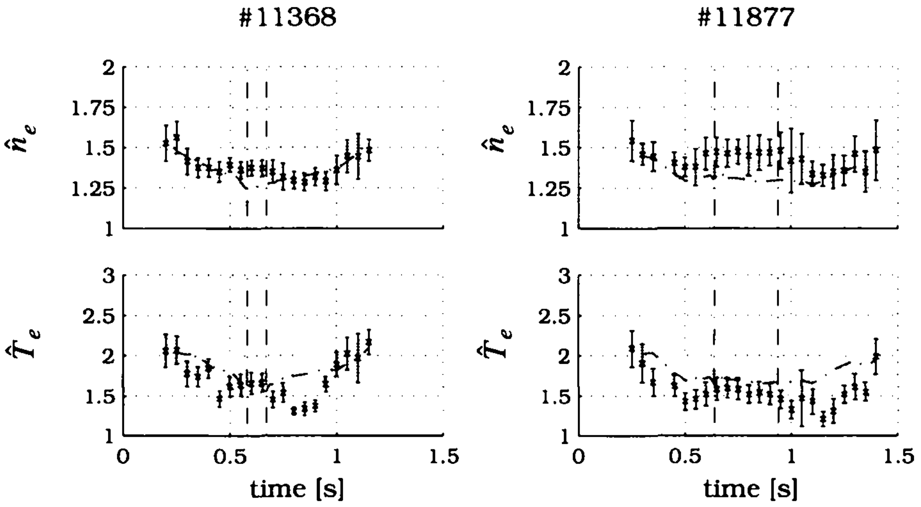

Figure 5.9: Peaking factors for T_e and n_e profiles. The patched surfaces illustrate the spread of the peaking factors in the established scaling functions. The dash-dotted lines indicate the interval of stationary plasma current.

5.4.2 T_e and n_e Profiles in Plasmas with "Exotic" Shapes

Following the installation of the modified TS detection system, an experimental campaign began with the aim of studying the energy confinement properties of exotically shaped plasmas. This campaign is devoted both to enlarge the present TCV shape confinement database (Section 6.1) and to support the concept of the '*Shape Enhancement Factor*' defined by eqn. 7.13. These so-called "exotic" shapes can be distinguished by a new parameter, λ, describing poloidal plasma cross-sections changing from rhomboidal (λ=-.5 and δ=0) to quadrangular (λ=+1 and δ=0).

Amongst the discharges of this campaign (characterized by moderate elongation, $\kappa \approx 1.55$ and zero triangularity), two have been selected representing extreme cases in terms of λ and for which a reasonably long steady-state phase was achieved (≈0.8→1s, fig. 5.10):

a) Discharge #11955: λ=-0.15, q_a=3.3→3.6
b) Discharge #11957: λ=0.5, q_a=3.05→3.2

Within the accuracy of the measurement, both T_e and n_e profiles are symmetric with respect to the magnetic axis. In both cases, sawtooth oscillations influence the T_e profile throughout the entire discharge duration.

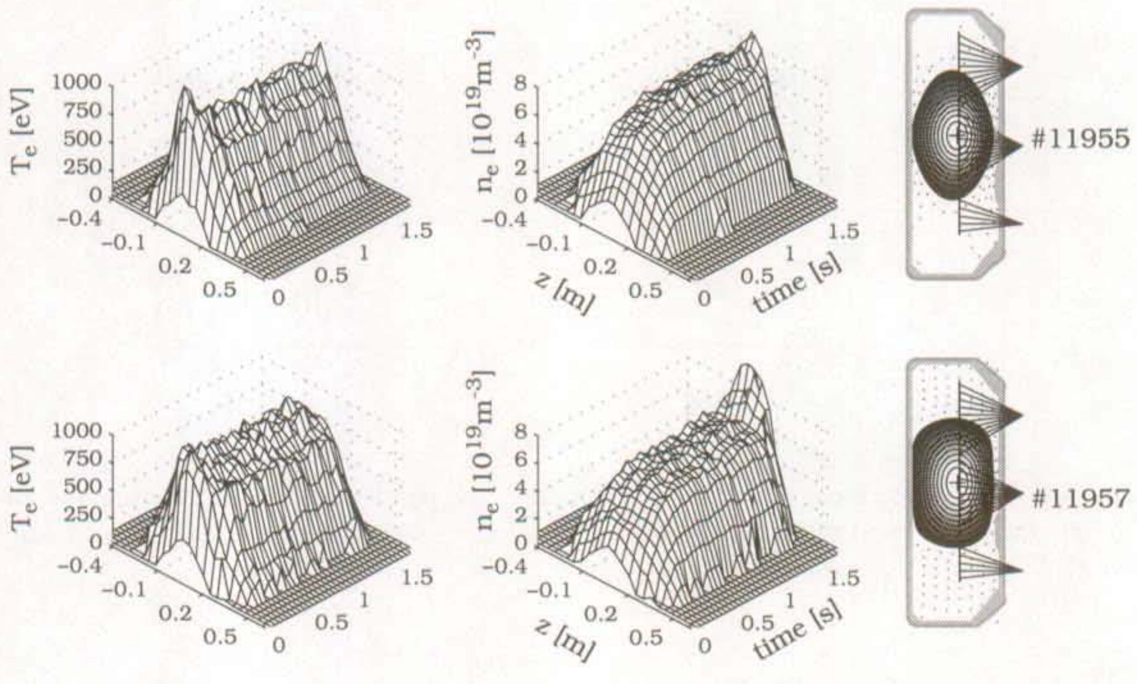

Figure 5.10: T_e and n_e profiles TCV discharges with exotic shapes

The T_e and n_e profile shapes can be reasonably well described by the peaking factor scaling expressions (Section 6.2.3). The examples selected do not show a clear influence of the parameter λ on the profile peaking (fig. 5.11), although in the case of λ=-0.15, the measured temperature peaking factor appears to be slightly higher than predicted.

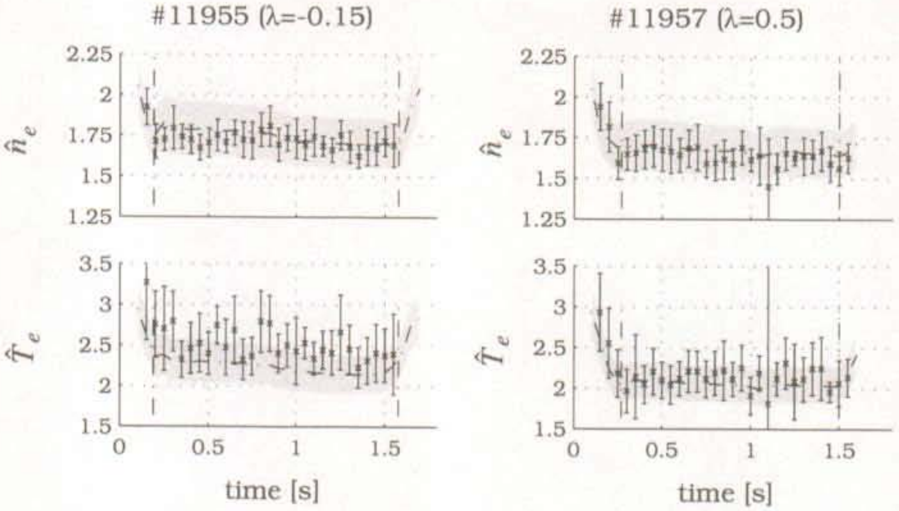

Figure 5.11: Peaking factors for T_e and n_e profiles in two plasmas with 'exotic' shapes. The patched surfaces illustrate the spread of the peaking factors in the established scaling functions. The dash-dotted lines indicate the time interval of stationary plasma current

For the electron energy confinement time, τ_{Ee} (see definition in Section 7.1) values between τ_{Ee}=17.4ms (discharge #11955) and τ_{Ee}=20.2ms (discharge #11957) are obtained. Further analysis is now required to determine whether or not these differences can be explained by the combination of the two effects proposed in Chapter 7, geometric effects described by the *'Shape Enhancement Factor'* and heat flux degradation.

6 Influence of Plasma Shaping on T_e and n_e Profiles in Ohmically Heated Plasmas

The unique flexibility of TCV allows a large number of plasma shapes with varying elongation and triangularity to be created (Section 3.1). This permits exploration of the influence of shape on plasma parameters such as the energy confinement time (Chapter 7) or the profiles of T_e and n_e. In this chapter we employ statistical analysis to isolate those parameters having the most significant effect on T_e and n_e profile shapes and to describe their variation by means of simple scaling expressions. The expression derived for the T_e profile shape dependence will be compared to the well-known principle of profile consistency, allowing the validity of this principle to be examined for the case of highly elongated plasma shapes.

6.1 Conditions of the Experimental Study

An extended experimental campaign has been dedicated to the study of shape variation effects in ohmic L-mode discharges. To ensure sufficient coverage by the TS observation volumes, the discharges were located in the upper half of the vacuum vessel and limited on the graphite tiles protecting the central column. The discharges are characterized by shape variations from almost circular to highly elongated, κ_a=1.06→1.86 and from highly D-shaped configurations with strong positive triangularity to inverse D-shaped plasmas with negative triangularity, δ_a=-0.41→0.72. In what follows, δ_a, κ_a, and q_a refer to parameters measured at the LCFS.

For such a wide range of shapes (fig. 6.1), the same plasma current cannot be employed for all cases. In part, this is due to the inevitable variations of q_a with plasma shape, but also because the smallest configurations cannot support the largest currents (q_a falls below the edge safety limit for ballooning modes, q_a<=2), whilst the largest equilibria cannot be produced at the lowest currents (operation at high q_a encounters vertical stability and density limits). In order to encompass the required variation in q_a, q_a=2.3→6, the plasma current had been scanned in the range, I_p=105→565kA.

To investigate the dependence of confinement on density, the line averaged electron density has also been varied in the range, $\langle n_e \rangle_L = 2.9 \cdot 10^{19} \rightarrow 8.5 \cdot 10^{19} m^{-3}$, with two separate density plateaux achieved in each discharge. In total, 230 different parameter combinations in the (κ_a, δ_a, q_a, $\langle n_e \rangle_L$)-space have been achieved in 124 discharges. Each discharge includes an I_p plateau of approximately 0.8s duration and a short n_e ramp between t=0.9s and t=1.0s linking the two regions of different density. Steady-state conditions over time intervals of several energy confinement times (up to 35ms in ohmic L-mode discharges on TCV) have been attained within the two separate time periods: t_1=0.6s→0.8s, t_2=1.1s→1.3s, allowing 5 TS profiles to be obtained in each interval. Maintaining stationary discharge conditions is a suitable way to eliminate time dependent terms in energy balance equations and, in particular, allows the energy confinement time to be expressed in a rather simple way. When analysing the data from these discharges, plasma parameters and profiles have been averaged within each of the two time intervals.

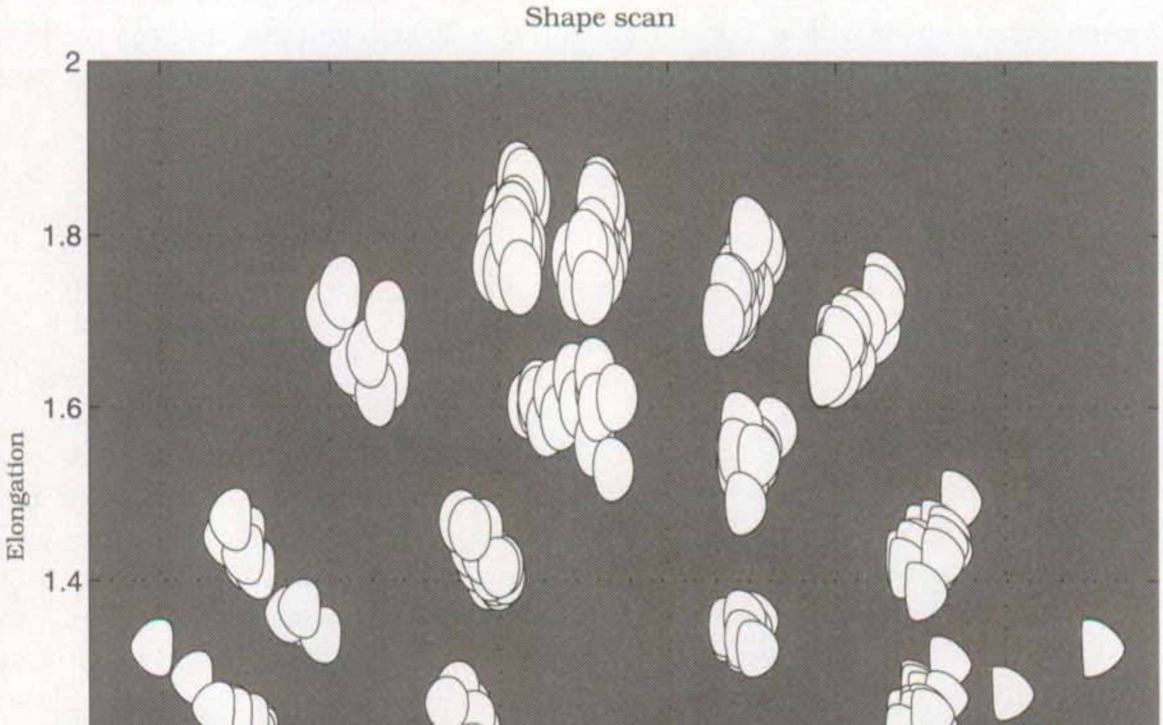

Figure 6.1: Shape scan of all discharges created during the confinement study showing the 16 domains in the (κ,δ)-parameter space. Slight variations in the shape within each domain reflect the scans in q_a and $\langle n_e \rangle_L$.

6.2 Variation of Profile Shapes with Plasma Parameters

6.2.1 Interpolation of T_e and n_e Profiles

Since the profile analysis is used both to investigate the energy confinement dependence on plasma shape and to compute T_e gradients just inside the LCFS for use in analysing heat flux variations, the profiles must be smooth and free from artificial structures, particularly in the edge region. As a convenient way to compensate for the relatively coarse spatial resolution and occasional inconsistencies in the experimental data, we impose constraints on the profile fits and their gradients. In the absence of any localized energy (off-axis heating) or particle source (pellets), it is reasonable to require profile fits which have negative gradients near the plasma edge, far from the domain of sawtooth activity and which are positive everywhere. Since the profile fits are performed in normalized flux coordinates (ρ), this constraint on the gradients also applies to the derivatives, $d/d\rho$ in this coordinate system. Two further boundary conditions on the profile fits - symmetry with respect to the magnetic axis and vanishing curvature on the LCFS - are already included in the set of base functions used for the interpolation. We note that other than the requirement for positive values at the LCFS, no further constraints are imposed on the absolute fitted values of T_e and n_e.

An initial fit is performed without constraints (Section 4.2) in order to find the base function coefficients. These coefficients serve as the starting set for a non-linear χ^2-optimization routine. Since we expect the final solution to be close to the initial fit without constraints, the routine is used iteratively to compute new base function coefficients that minimize χ^2 for the profile fit according to the specified constraints. The effect of sawtooth oscillations on the profiles is reduced by averaging the 5 TS profiles measured during each 200ms interval. The T_e and n_e profile fits obtained in this way are thus considered to be representative of the stationary phase. To perform the averaging, each experimental profile is projected onto ρ-coordinates. The (maximum of 5) experimental samples are then combined and interpolated by a single profile fit (fig. 6.2). In contrast to a simple average, this procedure has the advantage of automatically accounting for possible changes in the flux surface geometry with respect to the observation volumes, even during each stationary phase.

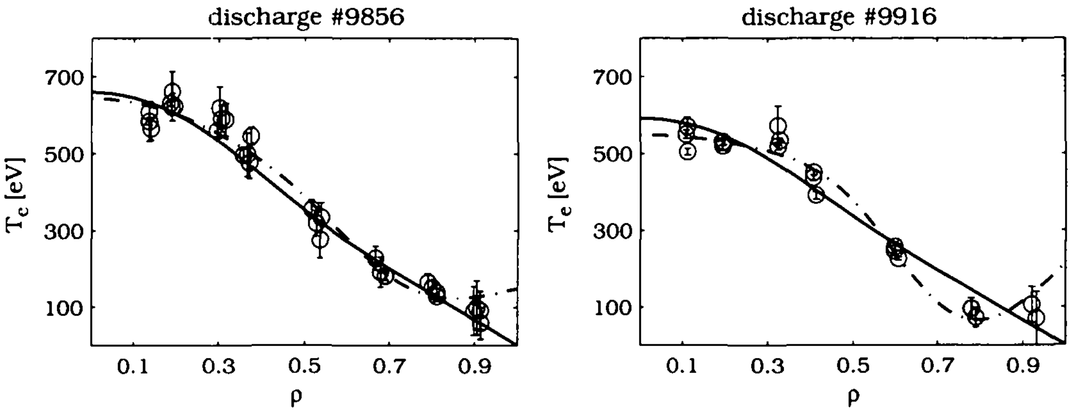

Figure 6.2: Effect of constraints on T_e profile fits in 2 different discharges. Solid lines show the profile fits with additional constraints, dash-dotted lines without constraints.

6.2.2 Characterisation of Profile Shapes - The Peaking Factor

Using the T_e and n_e profile fits described in the preceding section, an easily accessible shape parameter known as the peaking factor can be computed. In the case of the T_e profile fit, this has the form:

$$\hat{T}_e = \frac{T_e(\rho = 0)V}{\int_0^1 T_e(\rho')\frac{dV}{d\rho'}d\rho'} \tag{6.1}$$

where $T_e(\rho=0)$ is the (extrapolated) electron temperature on the magnetic axis and V the plasma volume.

To describe the dependence of $\hat{T}_e$, $\hat{n}_e$ on plasma parameters, we choose from a list of variables comprising the edge values of the 4 main parameters varied within the confinement study (q_a, κ_a, δ_a, $<n_e>_L$), the plasma current, the ohmic heating power, P_{oh}, the loop voltage, V_L and the effective ion charge, Z_{eff} (Table 6-1). Clearly, these 8 variables are not mutually exclusive. There is an obvious link between P_{oh}, V_L and I_p and q_a increases with decreasing I_p when other plasma parameters are fixed. A principal component analysis ([8], [32]) has been performed which statistically confirms these trends and justifies the exclusion of P_{oh}, V_L and I_p from the list. By accounting for the correlation between the peaking factors, a further restriction in the number of independent parameters may be obtained. Table 6-2 shows the calculated matrix of correlation coefficients and clearly illustrates that $\hat{T}_e$ and $\hat{n}_e$ are strongly correlated with q_a and anti-correlated with κ_a. To limit the number of variables to those having the most significant influence on profile peaking, only correlations with κ_a and q_a are retained in the analysis to follow.

Table 6-1: Variation of plasma parameters within the shape-confinement database

	q_a	δ_a	κ_a	$<n_e>_L$ [10^{19} m^{-3}]	Z_{eff}	I_p [kA]	V_L [V]	P_{oh} [kW]
Min.	2.3	-0.41	1.06	2.9	1.3	105	1.1	178
Max.	6.0	0.72	1.86	8.5	5.1	565	2.1	1020
Mean	3.8	0.19	1.50	5.3	2.3	322	1.5	485

Table 6-2: Correlation coefficients between the shape parameters $<n_e>_L$, q_a, κ_a, δ_a, Z_{eff} and the peaking factors $\hat{T}_e$ and $\hat{n}_e$

	$\hat{T}_e$	$\hat{n}_e$	$<n_e>_L$	q_a	δ_a	κ_a	Z_{cff}
$\hat{T}_e$	1	/	-0.14	0.89	-0.09	-0.54	-0.11
$\hat{n}_e$	/	1	0.01	0.81	-0.26	-0.34	-0.07
$<n_e>_L$	-0.14	0.01	1	-0.07	0.17	0.08	-0.61
q_a	0.89	0.81	-0.07	1	0.11	-0.40	-0.23
δ_a	-0.09	-0.26	0.17	0.11	1	-0.15	-0.40
κ_a	-0.54	-0.34	0.08	-0.40	-0.15	1	0.18
Z_{eff}	-0.11	-0.07	-0.61	-0.23	-0.40	0.18	1

The strong dependence of the peaking factor, $\hat{T}_e$ on q_a confirms earlier results in Ohmic discharges obtained on ASDEX [8] and on JET [54]. The strong correlation between $\hat{n}_e$ and q_a and the weak dependence of $\hat{n}_e$ on $<n_e>_L$ have not, however, been observed on JET. The JET data rather show a strong n_e profile shape dependence on the Murakami parameter, $M = \langle n_e \rangle_L / B_{tor}$, varied in the range $0.44 \cdot 10^{19} m^{-3} T^{-1} \rightarrow 1.28 \cdot 10^{19} m^{-3} T^{-1}$. At the lowest M, the JET n_e profiles are strongly peaked in the plasma centre, but are flat at the highest M. This evolution is observed when B_ϕ decreases at constant $<n_e>_L$ and also when $<n_e>_L$ increases at fixed B_ϕ. In the TCV shape confinement database, M is varied in the range $2.03 \cdot 10^{19} m^{-3} T^{-1} \rightarrow 6.06 \cdot 10^{19} m^{-3} T^{-1}$. In contrast to the observations on JET, the TCV n_e profiles reveal a weak increase in the peaking factor with increasing M at constant B_ϕ=1.43T. With regard to the different ranges of M, more quantitative comparisons concerning the evolution of the $\hat{n}_e$ parameter on both machines would require the extension of the TCV database to lower values of M and, in particular, of $<n_e>_L$, since the maximum value of B_ϕ possible on TCV is 1.5T.

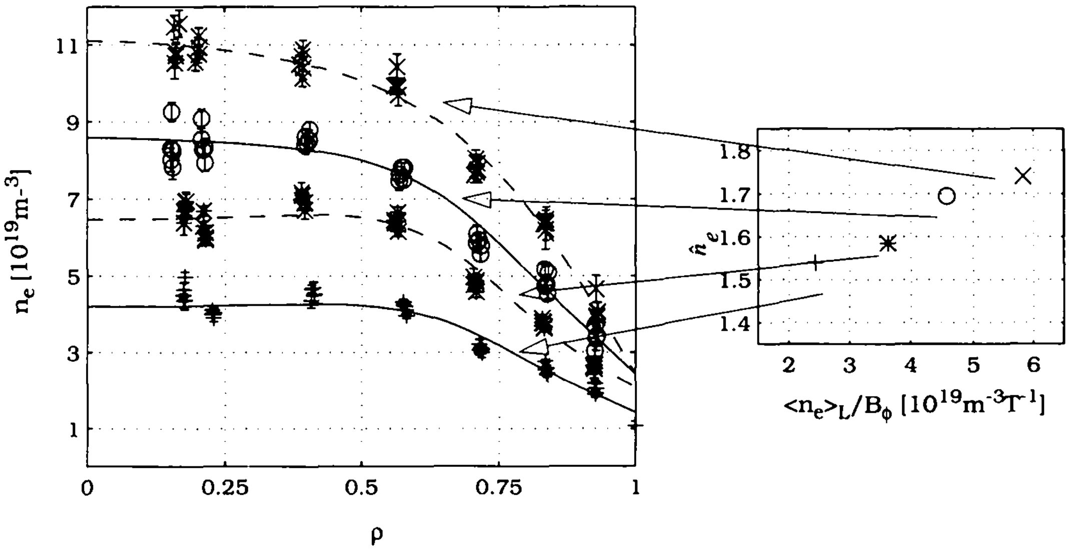

Figure 6.3: Influence of $<n_e>_L$ on the peaking of n_e profiles. On the right: peaking factor as a function of the Murakami-parameter. On the left, n_e profiles in ρ-coordinates for 4 values of the peaking parameter. The profiles have been obtained in a narrow range of κ_a, δ_a and q_a: $1.41 \le \kappa_a \le 1.45$, $0.49 \le \delta_a \le 0.55$, $4.37 \le q_a \le 4.8$.

6.2.3 Scaling Laws for the Peaking Factors

The correlation analysis described above indicated that both peaking factors, $\hat{T}_e$ and $\hat{n}_e$ are mostly influenced by q_a and κ_a. In a qualitative sense, this result can be substantiated simply by inspecting the profile fits themselves. More quantitative statements can be derived using log-linear regression analysis to produce scaling law expressions.

To demonstrate the profile variation with q_a and κ_a, fig. 6.4 and 6.5 show the response of $n_e(\rho)$ and $T_e(\rho)$ to significant changes in the two parameters. To exclude residual effects due to changes in other parameters, the profiles are chosen such that relative variations in these parameters are weak with respect to the change in the variable of interest.

The positive correlation between $\hat{T}_e$, $\hat{n}_e$ and q_a results in increased peaking as q_a increases. In the case of $\hat{T}_e$, this phenomenon is known as "profile consistency" for discharges characterized by sawteeth ([2],[12]) and has already been observed on other tokamaks in the ohmic regime ([8],[26],[66]). We note that the evolution of the peaking factor is more pronounced for the T_e profile fits than for the n_e profile fits. At low q_a, the T_e profile fits may even be hollow in the plasma centre (fig. 6.4). As q_a increases, sawtooth effects on the T_e profiles may be suppressed to a greater degree, since the sawtooth inversion radius is shown to be inversely proportional to q_a (Section 6.2.4, fig. 6.8).

The relation between $\hat{T}_e$, $\hat{n}_e$ and κ_a behaves inversely (fig. 6.5) to the q_a dependence and has to our knowledge not yet been analysed on other tokamaks (since most devices are limited to circular discharges or discharges at fixed elongation). We note that the electron energy confinement time increases with κ_a and slightly with q_a (Chapter 7). At the same time, the peaking factors increase with q_a and decrease with κ. These opposite trends make it difficult to establish a direct link between the profile peaking and the electron confinement.To analyse the peaking effects more quantitatively in terms of scaling law expressions, we choose a logarithmic-linear regression model [8]. This model is of the simple form:

$$\vec{y} = X\vec{\beta} + \vec{\varepsilon} \tag{6.2}$$

where the column vector $\vec{y}$ denotes the logarithm of all measurements of the dependent variable ($\hat{T}_e$ or $\hat{n}_e$), each column of the matrix $\mathbf{X}$ denotes the logarithmic value of the corresponding independent variable (q_a or κ_a), $\vec{\beta}$ is a vector of regression parameters and $\vec{\varepsilon}$ the vector of assumed random disturbances. For a comprehensive description of how $\vec{\beta}$ and the standard deviations of the different vector components, $\vec{\sigma}_{\vec{\beta}}$, are computed, the reader is referred to standard texts describing multivariate analysis [32].

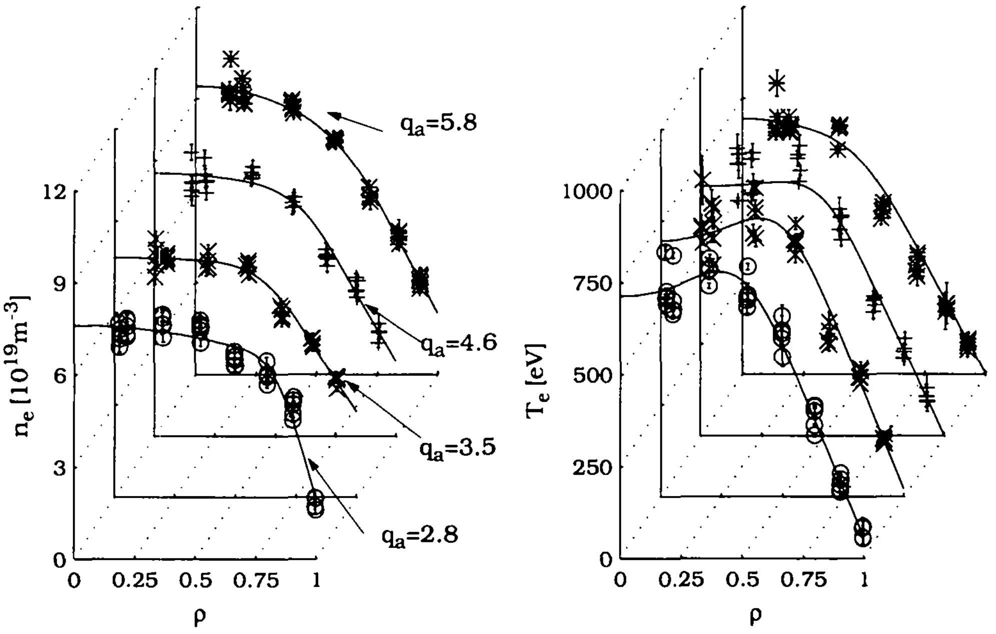

Figure 6.4: *Evolution of n_e and T_e profiles as a function of the edge safety factor q_a for $2.8 \le q_a \le 5.8$. The variations in other parameters are small with respect to the variations in q_a: $1.42 \le \kappa_a \le 1.50$, $0.52 \le \delta_a \le 0.55$, $6.2 \cdot 10^{19} m^{-3} \le \langle n_e \rangle_L \le 6.6 \cdot 10^{19} m^{-3}$, $1.5 \le Z_{eff} \le 2.1$.*

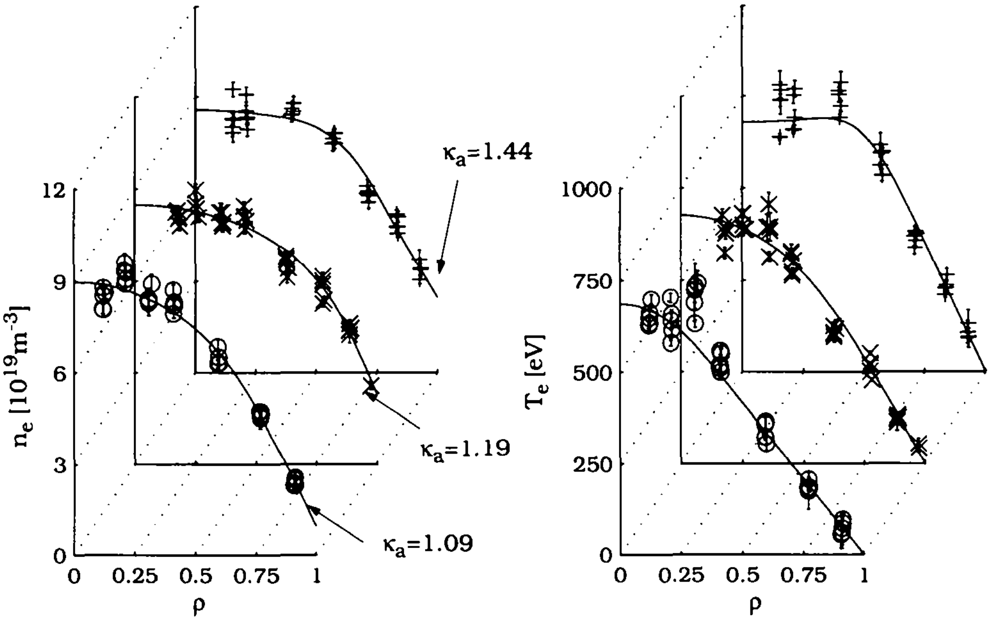

Figure 6.5: *Evolution of n_e and T_e profiles as a function of the elongation κ for $1.1 \le \kappa_a \le 1.45$. The variations in other parameters are small with respect to the variations in κ_a: $4.1 \le q_a \le 4.8$, $0.4 \le \delta_a \le 0.45$, $6.2 \cdot 10^{19} m^{-3} \le \langle n_e \rangle_L \le 6.5 \cdot 10^{19} m^{-3}$, $1.4 \le Z_{eff} \le 1.9$.*

The root mean square error (RMSE) of the fit is defined as:

$$RMSE = \sqrt{\frac{(\vec{y}-\hat{y})^T(\vec{y}-\hat{y})}{N-p}} \tag{6.3}$$

where $\hat{y}$ denotes the vector of the data to be fitted, N the number of available data points and p the number of degrees of freedom (N=201, p=2 for the case described here). Since $\vec{y}$ contains the logarithm of the dependent variable, the RMSE-value defines the relative error in the physical quantity. A second important parameter for the goodness of fit is the correlation coefficient R, which is a measure of the ratio of the standard deviation of the fit with respect to that of the data:

$$R = \left(\frac{\sum_{i=1}^{N} (\hat{y}_i - \bar{y})^2}{\sum_{i=1}^{N} (y_i - \bar{y})^2} \right)^{1/2} \tag{6.4}$$

Applying this two parameter regression model to the profile fits leads to the following result for the peaking parameters:

$$\hat{T}_e = (1.0 \pm 0.09) q_a^{0.76 \pm 0.011} \kappa_a^{-0.32 \pm 0.035} \qquad R_{\hat{T}_e} = 0.96$$

$$\hat{n}_e = (1.0 \pm 0.11) q_a^{0.47 \pm 0.014} \kappa_a^{-0.18 \pm 0.043} \qquad R_{\hat{n}_e} = 0.75 \tag{6.5}$$

We note that the scaling expression for $\hat{T}_e$ is in reasonable agreement with experimental data ($R_{\hat{T}_e} = 0.96$), although $\hat{T}_e$ is most often available only via an extrapolation of the profile fits to the magnetic axis. This result also emphasizes the role of the elongation in the evolution of the T_e profile peaking. Neglecting the κ-dependence in the regression analysis would immediately yield a significant decrease in the fit quality ($R_{\hat{T}_e} = 0.78$).

The scaling for $\hat{n}_e$ produces a poorer fit ($R_{\hat{n}_e} = 0.75$) which can only be improved by including additional variables in the log-linear regression. According to Table 6-2, a good first candidate is the triangularity, which may be integrated into the model using an appropriate transformation, $\delta' = (1-\delta)$ to avoid the logarithm of a negative variable. The 3-parameter fit increases the regression coefficient to $R_{\hat{n}_e} = 0.89$ and yields the following expression:

$$\hat{n}_e = (1.0 \pm 0.07) q_a^{0.53 \pm 0.011} \kappa_a^{-0.21 \pm 0.030} (1 - \delta)^{0.25 \pm 0.019}$$

(6.6)

Whether or not 2 or 3 parameters are used in the linear regression for the peaking factor dependence on κ_a and q_a, a dependence is clearly observed for both $\hat{T}_e$ and $\hat{n}_e$ (fig. 6.6). Generalization of these scaling expressions for $\hat{T}_e$ and $\hat{n}_e$ from circular to non-circular plasmas requires consideration of at least one shaping parameter. This would preferentially be the elongation due to the stronger correlation with the peaking factors compared to the triangularity.

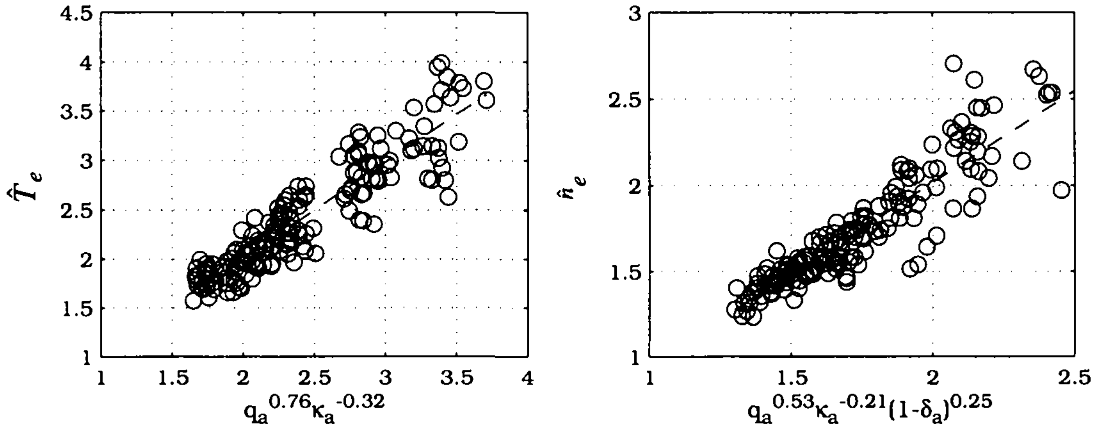

Figure 6.6 : Data and regression analysis fit for the T_e and n_e profile peaking factors.

6.2.4 Profile Consistency

According to Tang [62] and Arunasalam [2], the principle of profile consistency for ohmic limiter discharges can be defined by the statement that for a fixed q_a in quasi-steady state, unique resistive equilibrium profile shapes exist for the current density, j and q. Kadomtsev [26] describes the consistency as the consequence of an entropy principle which causes the plasma to relax towards states, where the total entropy (the minimum free energy) of the plasma does not change. Arunasalam [2] has analyzed a number of different transport models, none of which fully explains all the observed features (6.5) of consistency. We note that shape of T_e profiles is independent of the shape of additional heating power deposition profiles. Concerning ohmic heating power deposition profiles, fig. 6.7 shows a definite dependence of $\hat{T}_e$ on the ohmic power density peaking factor, $\hat{p}_{oh}$. The natural profile shapes are monotonic, and for discharges with sawteeth ($q(0)\approx 1$) and with q_a dependent T_e profile shapes the following relations can be obtained:

1) $\rho_{inv} \sim 1/q_a$

2) $\hat{T}_e = f(q_a)$

3) $T_{e,0}^{3/2} \sim B_\varphi Z_{eff}/V_L$

(6.7)

where ρ_{inv} is the sawtooth inversion radius. Relation 2) has already been discussed in Section 6.2.3. Relation 3) is an expression for the ratio between the quantity $T_e^{3/2}$ in the plasma centre and its average over the plasma-cross section for the case when the plasma is close to steady-state equilibrium and assuming Spitzer resistivity with a constant Z_{eff} profile. The j and T_e profiles can furthermore be linked by Ohm's law and constrained by:

4) $q^{*2/3} \le \hat{T}_e \le q^*$, (for $q(0)=1$)

(6.8)

where q^* represents the cylindrical equivalent safety factor, defined as:

$$q^* = \frac{1+\kappa_0^2(1+2\delta_0^2-1.2\delta_0^3)}{\kappa_0}\left(\frac{AB_0}{\mu_0 I_p R}\right) \qquad (6.9)$$

with A the poloidal plasma cross-section and κ_0 and δ_0 respectively the elongation and triangularity on the magnetic axis. Assuming that the discharges of the TCV confinement database are in steady-state conditions, most of the equilibria are highly non-circular. For comparison, most of the results published in [8] and [66]and have been obtained in circular discharges. Moreover, the T_e profiles are not always monotonic, especially at low to moderate q_a where hollow profile structures are observed in the central regions. We have nevertheless tested the basic predictions of the principle of profile consistency, mainly in order to investigate the possible consequences of varying the plasma elongation.

The validity of relation 2) has already been confirmed in Section 6.2.3 by the scaling expression for $\hat{T}_e$. In addition, fig. 6.8 shows that the predicted proportionality of relations 1) and 3) is roughly satisfied, although the scatter in the data points is large. In the case of ρ_{inv} versus $1/q_a$, this may be a consequence of the method that has been applied to determine ρ_{inv}. The latter is not directly obtained from analysis of the soft X-ray emissivity profiles, but is rather defined as the normalized coordinate of the flux surface tangential to the viewing chords of the soft X-ray cameras where the sawtooth signals change sign.The variations between the linear fit and the data in relation 3) are due partly to extrapolation errors in the determination of $\hat{T}_{e,0}^{3/2}$ and partly to the evaluation of Z_{eff} obtained from the central soft X-ray emissivity and impurity concentration measurements of the USX-spectrometer.

Concentrating now on relation 4), fig. 6.9 shows that this relation is satisfied by a large number of the discharges. This implies, that the basic assumption of a resistive equilibrium, for which $T_{e,0}^{3/2}/\langle T_e^{3/2}\rangle = j(0)/\langle j\rangle$, can also be maintained in strongly shaped plasmas.

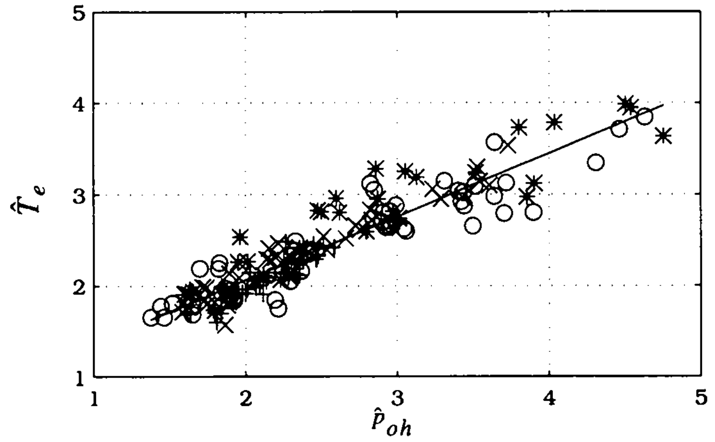

Figure 6.7: Temperature peaking factor $\hat{T}_e$ as a function of the ohmic power density peaking factor, $\hat{p}_{oh}$.

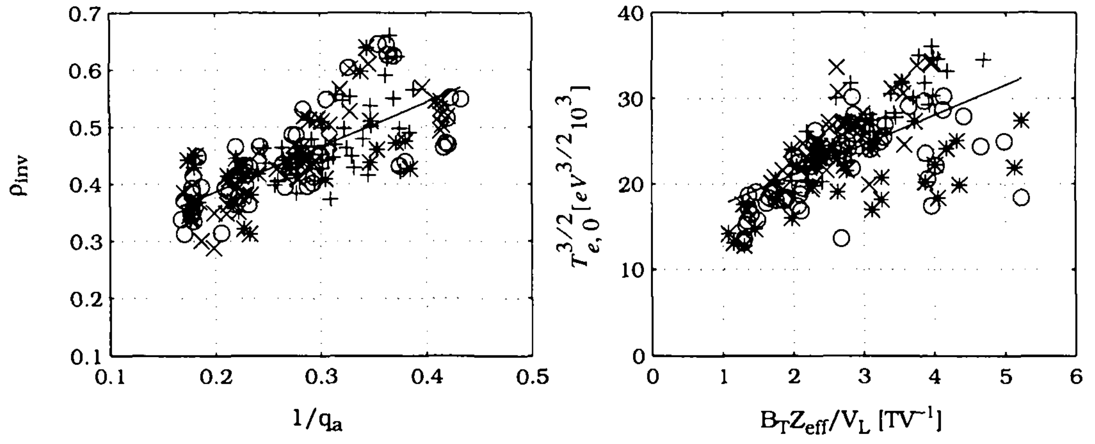

Figure 6.8: Adherence of TCV shape confinement database to the "profile consistency" relations 1) and 3) (eqn. 6.7). The different symbols correspond to the following elongation classes: '': $1.1 \leq \kappa \leq 1.3$, 'o': $1.3 \leq \kappa \leq 1.5$, 'x': $1.5 \leq \kappa \leq 1.7$, '+': $1.7 \leq \kappa \leq 1.9$*

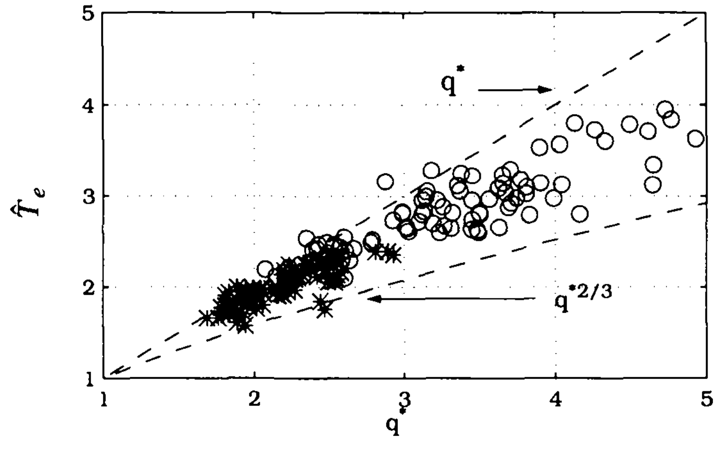

Figure 6.9: Peaking factor $\hat{T}_e$ versus the equivalent edge safety factor q^*. The 'o'-symbols represent strictly monotonic profiles, the ''-symbols, profiles with slightly hollow character in the centre.*

6.3 Summary

We have shown, that T_e and n_e profile shapes contain a distinct dependence on plasma parameters. Aside from the well known q_a dependence of the T_e profile peaking parameter, a clear dependence on κ_a is observed, leading to a flattening of the profile with increasing κ_a in contrast to the peaking implied by the increasing q_a. Simultaneously, the n_e peaking depends also strongly on q_a and κ_a, but only weakly on δ and appears to have no dependence on $<n_e>_L$.

Our results also demonstrate that the basic principle of profile consistency is well adhered to for strongly shaped plasmas, even though the effect has, to date, mainly been observed in and analyzed on circular discharges.

We note, that the parameter q_a has been used as an independent variable for the description of shape dependence in peaking factors or sawtooth inversion radii in order to remain in accordance with the cited references. However, in strongly shaped plasmas q_a may not be the most suitable choice, since q_a itself varies with shape whilst, e. g., I_p and A are kept constant. In order to clearly separate the dependence of any dependent variable on shape from the intrinsic dependence of q_a on shape, a more convenient choice may be the cross section averaged current density, $\langle j \rangle = I_p/A$ [73]. The scatter between the measured ρ_{inv} and the linear model would be considerably reduced (fig. 6.10).

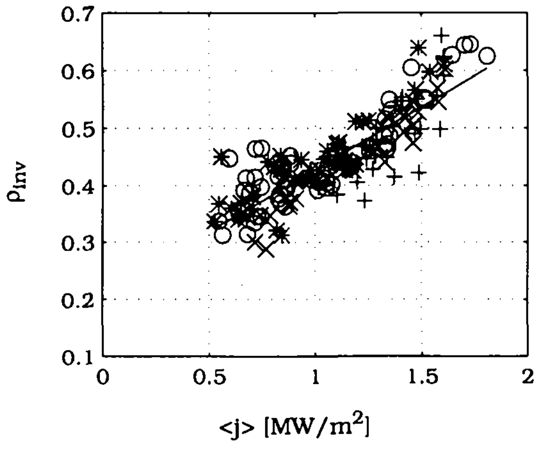

Figure 6.10: Dependence of sawtooth inversion radius on the poloidal cross section averaged current density (for the different elongation classes see fig. 6.8).

7 Influence of Plasma Shape on Confinement and Transport

7.1 Introduction

Together with plasma density and temperature, the energy confinement time must be maximized in a future fusion reactor, such that fusion power output exceeds the total power loss [74]. Empirical scaling laws (ITER89P, Rebut-Lallia-Watkins) have been derived using multi-machine databases in an attempt to describe the energy confinement time as a function of machine parameters. These databases already include the plasma elongation, but do not yet account for the triangularity.

Due to the unavailability of reliable ion temperature and density profile measurements in TCV, the total plasma energy, W_t could have been derived from magnetic equilibrium reconstructions via β_{pol}. Since these parameters are subject to major uncertainties (Chapter 8), the confinement behaviour of all TCV discharges will be characterized in the following by the electron energy confinement time, $\tau_{Ee} = W_e/P_{oh}$ in the case of steady-state discharge conditions, where P_{oh} denotes the total ohmic input power and W_e the energy stored in the plasma electrons. Assuming as usual, that n_e and T_e are constant on magnetic flux surfaces, W_e is obtained by volume integration of the TS electron pressure profiles (Table 4-1).

7.2 The Electron Energy Confinement Time and its Dependence on Shape Parameters

For fixed shape, the TCV shape confinement database (Section 6.1) shows that τ_{Ee} increases slightly with q_a and depends almost linearly on $\langle n_e\rangle_L$ (fig. 7.1). The $\langle n_e\rangle_L$-values used for the confinement study are limited to the domain in which τ_{Ee} does not yet show saturation with $\langle n_e\rangle_L$. This regime is often denoted by 'LOC' for linear ohmic confinement regime and follows a Neo-Alcator scaling law [41]: $\tau_{Ee} \sim q^* \langle n_e \rangle_L R_0^{-} a$, where q^* denotes the equivalent safety factor for a cylindrical plasma (eqn. 6.9).

In addition to the density dependence, τ_{Ee} is strongly influenced by the plasma triangularity. For q_a and $<n_e>_L$ approximately constant, τ_{Ee} increases slightly with elongation and decays strongly with triangularity for positive δ. Figs. 7.2 and 7.3 illustrate these trends in more detail. Typical values of τ_{Ee} range from 30ms at δ=0 and highest elongation to 10ms for highly positive δ ($\delta \approx 0.5$). The degradation in τ_{Ee} with δ is typically around a factor of 2, but can be a factor of 3 for the highest values of $<n_e>_L$. Several effects could lead to such a degradation, notably changes in MHD-activity or a strong increase in the radiated power with respect to the ohmic input power, P_{rad}/P_{oh}.

The observed MHD activity depends strongly on triangularity. Measured sawtooth amplitudes increase with positive δ, but almost vanish at negative δ. At highest triangularity, the temporal average of the thermal energy contained within the plasma core (inside the q=1 surface) and suddenly released in the direction of the plasma edge, amounts at most to 25% of the total power conducted to the edge [73]. The gradual disappearance of sawteeth at negative δ is accompanied by the onset of MHD-mode activity. The saturation of τ_{Ee} for negative δ, as seen on fig. 7.2, is very likely due to these MHD-modes, but the effect is not very pronounced in comparison with the decrease at positive δ.

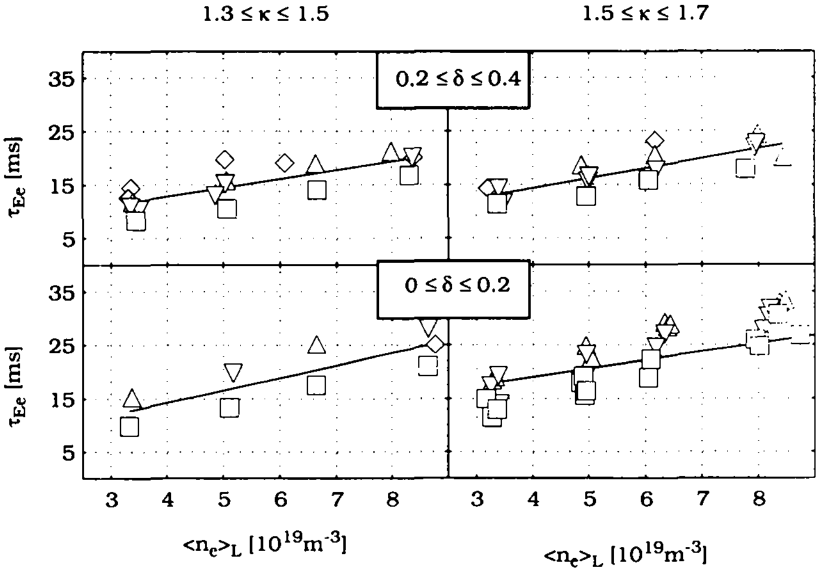

Figure 7.1: Increase of τ_{Ee} in TCV with $<n_e>_L$ in accordance with the Neo-Alcator scaling law. The symbols represent different classes of the edge safety factor, 'squares': $2.5 \le q_a \le 3.0$, 'up triangles': $3.0 \le q_a \le 3.5$, 'down triangles': $3.5 \le q_a \le 4$, 'diamonds': $4.0 \le q_a \le 4.5$.

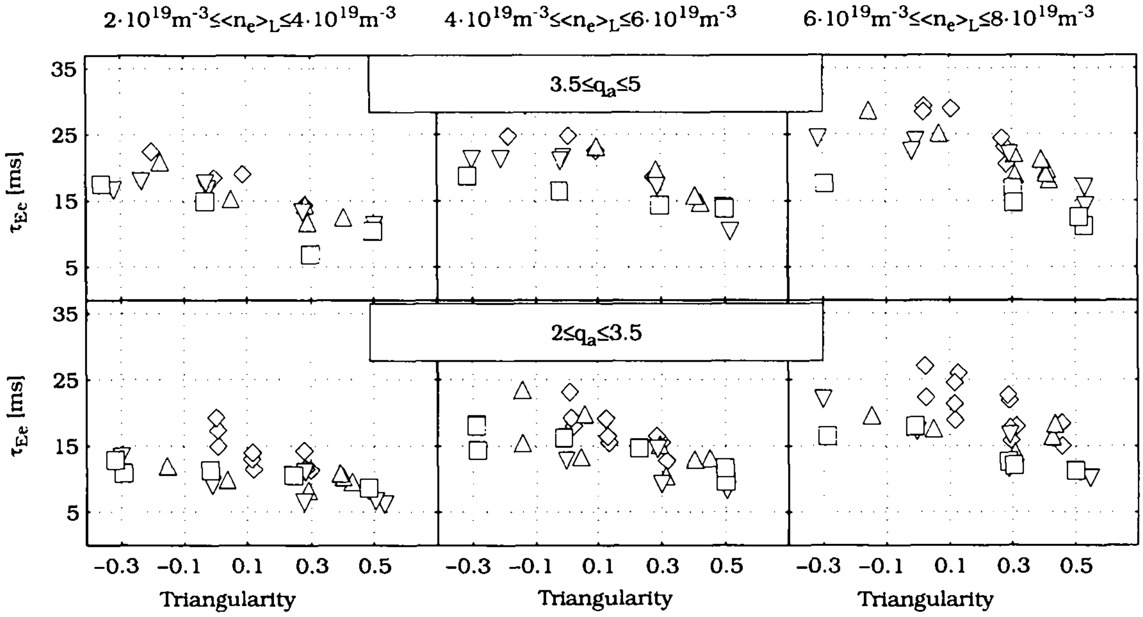

Figure 7.2: Evolution of τ_{Ee} with triangularity. The symbols represent different classes of the elongation κ, 'squares': $1.1 \le \kappa \le 1.3$, 'up triangles': $1.3 \le \kappa \le 1.5$, 'down triangles': $1.5 \le \kappa \le 1.7$, 'diamonds': $1.7 \le \kappa \le 1.9$.

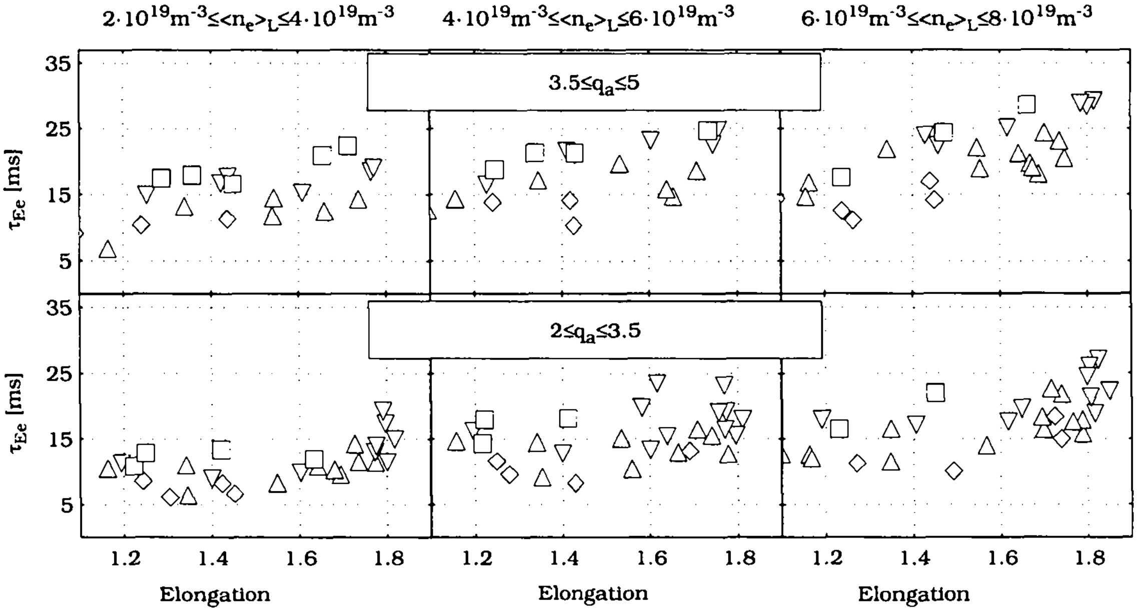

Figure 7.3: Evolution of τ_{Ee} in TCV with elongation κ. The symbols represent different classes of the triangularity, δ: 'squares': $-0.45 \le \delta \le -0.15$, 'up triangles': $-0.15 \le \delta \le 0.15$, 'down triangles': $0.15 \le \delta \le 0.45$, 'diamonds': $0.45 \le \delta \le 0.75$.

At negative δ and low κ, only 6 out of the 10 TS observation volumes are located within the confined plasma, so that only a limited number of data points are available to determine the shape of p_e profiles and their spline interpolations. Determination of the electron energy is therefore less accurate in these cases. The change in radiated power, P_{rad} follows the change in P_{oh}. The ratio P_{rad}/P_{oh} amounts to around 30%, decreasing with increasing δ and decreasing energy confinement [73]. MHD activity and radiative losses can therefore be excluded in seeking an explanation for the deterioration in electron energy confinement.

In searching for alternative origins of the observed decrease in confinement, we must also account for the effect of shape itself. Changing the plasma shape modifies the flux surface configuration and, in particular, the separation between adjacent surfaces. Since gradients in plasma parameters such as temperature and density change in the direction perpendicular to magnetic flux surfaces, modifications to the separation of these surfaces must lead to changes in these gradients. Thus, if the energy stored within a given surface is conserved, changes in the perpendicular temperature gradients will affect the conducted energy fluxes: $\vec{q} = \vec{q}_e + \vec{q}_i = -e(n_e\chi_e\vec{\nabla}T_e + n_i\chi_i\vec{\nabla}T_i)$, where $\chi_{e,i}$ denote the electron and ion heat diffusivities. For constant plasma energy content, a confinement deterioration must be caused by an increased outward heat flux, since MHD and radiated power effects have been excluded. Such an increase can be due to changes in the temperature gradients, or in the heat transport coefficients, or both.

In order to isolate the role of shape effects, a coordinate system is required in which profile representations are independent of the plasma current distribution. The coordinate system employed thus far in fitting the TS data will not suffice since the normalized flux coordinate, $\rho = \sqrt{1 - \Psi/\Psi_{AX}}$, depends on the poloidal flux function, Ψ. To circumvent this problem, Moret et al. [37] map onto a radial coordinate r^*, where r^* is equivalent to a distance on the outer equatorial plane, measured from the magnetic axis to the LCFS and normalized such that r^*=a on the LCFS. The thermal energy flux can then be written as:

$$\vec{q} = \vec{q}_e + \vec{q}_i = -e\left(n_e\chi_e\frac{dT_e}{dr^*} + n_i\chi_i\frac{dT_i}{dr^*}\right) \cdot \frac{d}{d\rho}r^*\vec{\nabla}\rho , \tag{7.1}$$

where the product $GGF = \frac{d}{d\rho} r^* \vec{\nabla}\rho$

(7.2)

defines the *Gradient Geometrical Factor*. Moret et al. [35] employ an equivalent definition in terms of the poloidal flux function:

$$\frac{d}{d\Psi} r^* \vec{\nabla}\Psi = \frac{d}{d\rho} r^* \frac{d\rho}{d\Psi} \frac{d\Psi}{d\rho} \vec{\nabla}\rho = \frac{d}{d\rho} r^* \vec{\nabla}\rho \, .$$

(7.3)

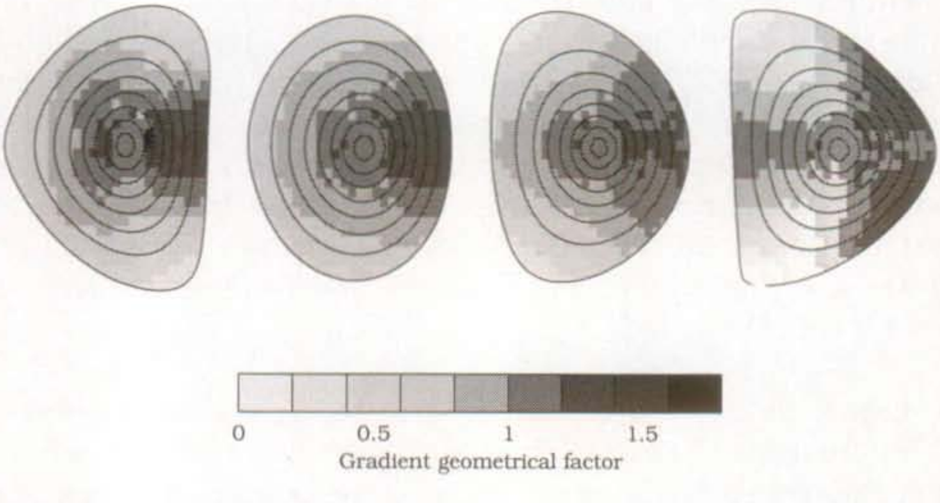

Figure 7.4: Graphical representation of the gradient geometrical factor.

Since all T_e and n_e profile fits are performed in ρ-coordinates, the GGF expressed in normalized flux coordinates will be used for convenience throughout this section. Fig. 7.4 illustrates graphically how the spatial distribution of the GGF evolves with shape parameters. Four equilibria have been selected, each with moderate elongation of $\kappa \approx 1.3$, but varying in triangularity from $\delta = -0.41$ to $\delta = 0.71$. The equilibrium flux surfaces at highest δ are clearly compressed towards the outer edge (with respect to the magnetic axis) due to the combined influence of the shape and the Shafranov shift. An enlarged domain with increased gradients almost symmetrically disposed with respect to the outer equatorial plane is therefore created near the plasma edge.

With decreasing δ, the region of increased gradients diminishes as the outer flux surfaces become increasingly separated. In this case, a large plasma volume benefits from locally reduced gradients, leading finally to a decrease in the heat conduction. These large variations of favourable/unfavourable gradient regions may partly or wholly explain the observed energy confinement decrease with increasing δ. As mentioned earlier, the changes in τ_{Ee} may also be due to changes in the transport coefficients themselves. We treat these two effects separately and analyse first the evolution of transport quantities with shape parameters.

Before considering in detail the link between transport coefficients and the ohmic power flux, we note that knowledge of real spatial gradients is necessary for the analysis of this effect. Although a representation in ρ or r^* coordinates gives a shape independent description, the corresponding derivatives ($d/d\rho$, d/dr^*) do not correspond to real spatial gradients and must therefore be complemented by appropriate geometrical factors (see eqn. 7.1). Fig. 7.5 presents two examples of T_e profiles and their derivatives in the different coordinate systems. The fitted profiles in ρ coordinates suggest almost constant derivatives of nearly equal value, $dT_e/d\rho \approx -1600\text{eV}$, close to the plasma edge. The underlying profile fits interpolate the profiles reasonably well - the slightly hollow profile of discharge #9616 is due to the sensitivity of the interpolation routine to individual error bars on the data points. In contrast, the derivatives in r^* coordinates show a slight decrease in the edge region. For completeness, we show also the profiles and their derivatives (d/dz) in the original spatial coordinate system. Comparing these derivatives with the derivatives in r^* coordinates gives an impression of how the derivatives evolve along the perpendicular coordinate axis.

It is important to note that flux surface averaged T_e gradients are required for the heat flux analysis. A derivation of the T_e profile fits in normalized coordinates must therefore be multiplied by the corresponding flux surface average of the spatial gradient in the coordinate ρ: $\langle \vec{\nabla} T_e \rangle = dT_e/d\rho \cdot \langle \vec{\nabla} \rho \rangle$ (fig. 7.6). The quantity $\langle \vec{\nabla} \rho \rangle$ on a given magnetic surface (41 surfaces, equidistant in the flux surface parameter, ρ from the magnetic axis to the LCFS) is obtained from the equilibrium reconstruction.

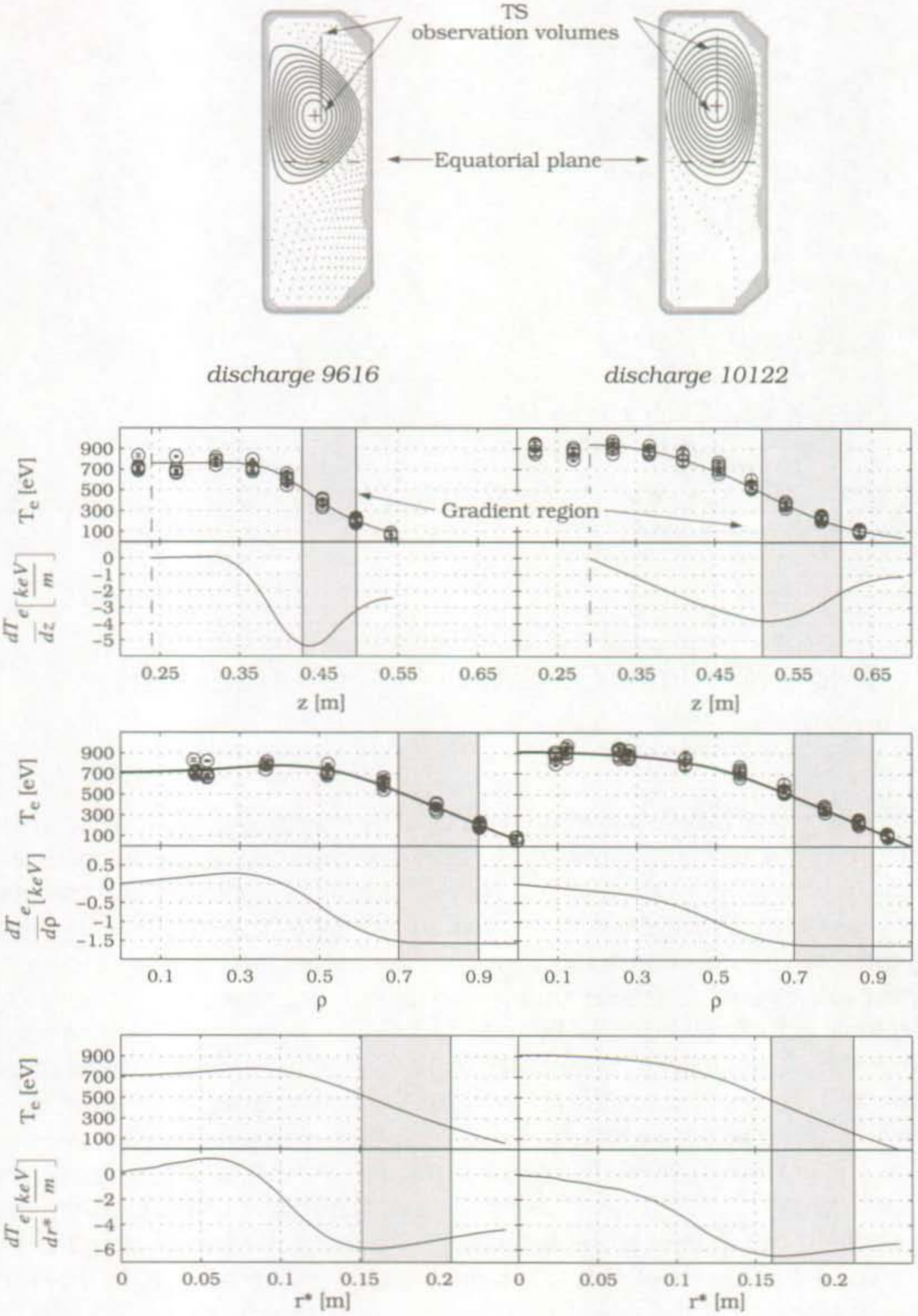

Figure 7.5: T_e profile fits and their derivatives for discharges #9616 and #10122 in a) spatial coordinates along a vertical chord R=0.9m [z], b) normalized flux coordinates [ρ] and c) normalized coordinates in the equatorial plane [r]. The patched area in all plots corresponds to the edge region $0.7 \leq \rho \leq 0.9$, where the T_e gradients are calculated on the basis of the derivative $dT_e/d\rho$.*

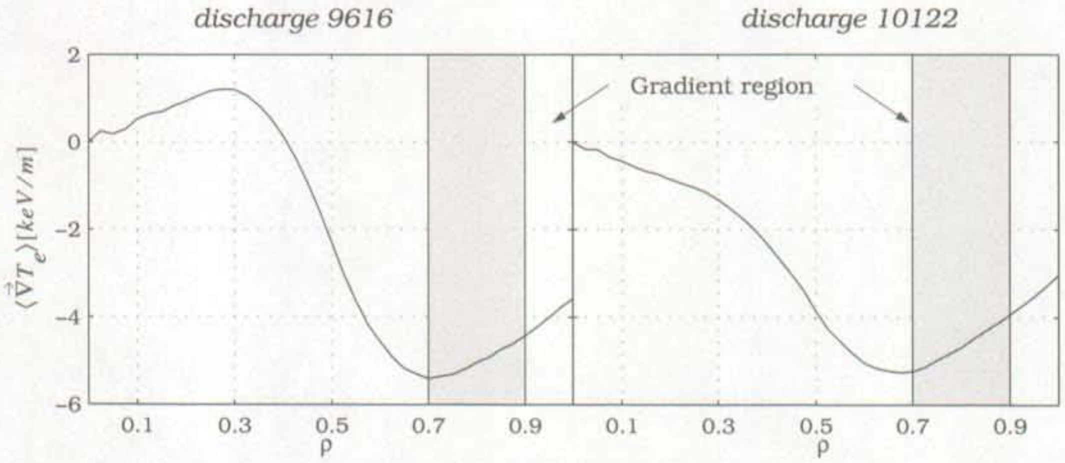

Figure 7.6 : Flux surface averaged T_e gradients $\langle \vec{\nabla} T_e \rangle$ for the same discharges as in fig. 7.5. We note the contribution of $\langle \vec{\nabla} \rho \rangle$ to $\langle \vec{\nabla} T_e \rangle$.

7.3 Degradation of Confinement with Heat Flux

The heat flux analysis is based on a flux surface averaged balance of the radial power fluxes for electrons and ions. Since this analysis is performed only for stationary plasma conditions, the energy content of electrons and ions is constant. The input ohmic heat flux must compensate the total losses resulting from convective and conductive energy losses of electrons and ions, electron radiative losses and charge exchange-losses of ions. Since the outermost plasma regions (ρ>0.9) will not be included in the analysis, the electron radiative loss terms can be neglected. Bolometric measurements during these discharges show that the plasma radiation is concentrated in a layer situated at ρ>0.9. Bremsstrahlung or recombination radiation from the plasma core amounts to generally less than 10% of the ohmic input power and, like CX-losses, can be neglected. On TCV, CX-losses have been estimated from NPA data and shown to be small in the case of H-modes [63]. Further results from a detailed ion energy balance in a series of ohmic L-mode discharges on ASDEX [60] performed under conditions comparable to those described here indicate CX-losses to be localized near the LCFS and to amount to less than 10% of the input power. This leads to the following equation describing the thermal flux balance (see also eqn. 7.1):

$$\langle\vec{q}_{oh}(\rho)\rangle = \langle\vec{q}_e\rangle + \langle\vec{q}_i\rangle = -e\left(n_e\chi_e\frac{dT_e}{d\rho} + n_i\chi_i\frac{dT_i}{d\rho}\right)\langle\vec{\nabla}\rho\rangle \tag{7.4}$$

in which the brackets <...> denote flux surface averaged quantities. We note that in this approximation, poloidal variations of the thermal diffusivities are effectively averaged for a given flux surface. The ohmic power flux density into a given flux tube, $\langle\vec{q}_{oh}(\rho)\rangle$, is obtained by volume integration of the ohmic power density within a given flux surface divided by the corresponding surface area S(ρ):

$$\langle\vec{q}_{oh}(\rho)\rangle = \int_0^{\rho}\left(j(\rho')\frac{V_L}{2\pi R}\right)\frac{d}{d\rho'}V d\rho'/S(\rho) \tag{7.5}$$

where *j* designates the current density profile computed from the equilibrium reconstruction and averaged over the poloidal cross-section of a flux surface. In eqn. 7.5, V_L denotes the surface loop voltage, $V_L = d\Phi_{LCFS}/dt$, where Φ_{LCFS} represents the total magnetic flux through the LCFS. Inductive corrections to V_L are unnecessary in steady-state conditions when the plasma current and internal inductance are time-independent.

Restricting our analysis to the case in which the heat transport is dominated by thermal conduction, allows the region inside the sawtooth inversion radius (where T_e profiles are supposed to be flat in steady-state conditions) to be neglected. The sawtooth inversion radii, obtained from line integrated soft X-ray measurements, are centred around ρ=0.4 and do not exceed ρ=0.67 for all of the discharges comprising the TCV shape-confinement database. The inner boundary of the heat flux analysis is therefore fixed at ρ=0.7, limiting the analysis domain to 0.7≤ρ≤0.9. This has the additional advantage of greatly reducing sawtooth perturbations on the TS profiles.

An additional small error in the calculation of $\langle\vec{q}_{oh}(\rho)\rangle$ may be introduced by the uncertainty on the computed *j(ρ)*. The surface integral of *j(ρ)* is, however, normalized to the measured I_p so that the consequent error in $\langle\vec{q}_{oh}(\rho)\rangle$ within the chosen domain is negligible in comparison with the overall errors inherent in the analysis.

Eqn. 7.4 as basis for the heat flux analysis requires density and temperature measurements of both the plasma electrons and the ions. Since T_i and n_i profiles are not yet available on TCV, the electron and ion loss channels cannot be distinguished. To overcome the lack of information on the ion channel, we define an effective heat diffusivity, χ_{eff}, assuming that the n_e and n_i profiles have the same shape, $n_i = c_i n_e$:

$$\chi_{eff} = \left(\chi_e + c_i \chi_i \frac{\langle \vec{\nabla} T_i \rangle}{\langle \vec{\nabla} T_e \rangle}\right) \tag{7.6}$$

With this definition, the power balance (eqn. 7.4) can be rewritten as:

$$\langle \vec{q}_{oh} \rangle = \langle \vec{q} \rangle = -e n_e \chi_{eff} \langle \vec{\nabla} T_e \rangle . \tag{7.7}$$

Fig. 7.7 shows the relation between $[\langle \vec{q} \rangle]$ and $[\langle \vec{\nabla} T_e \rangle]$ in the gradient region, $0.7 \le \rho \le 0.9$, for all values of κ and δ in the confinement database $3 \cdot 10^{19} \mathrm{m}^{-3} <= [n_e] <= 4.5 \cdot 10^{19}$. Here, $[\langle \vec{q} \rangle]$ and $[\langle \vec{\nabla} T_e \rangle]$ represent poloidal averages on a given flux surface, followed by an average over the gradient region. These averaged quantities are then used to extract a single value of χ_{eff}.

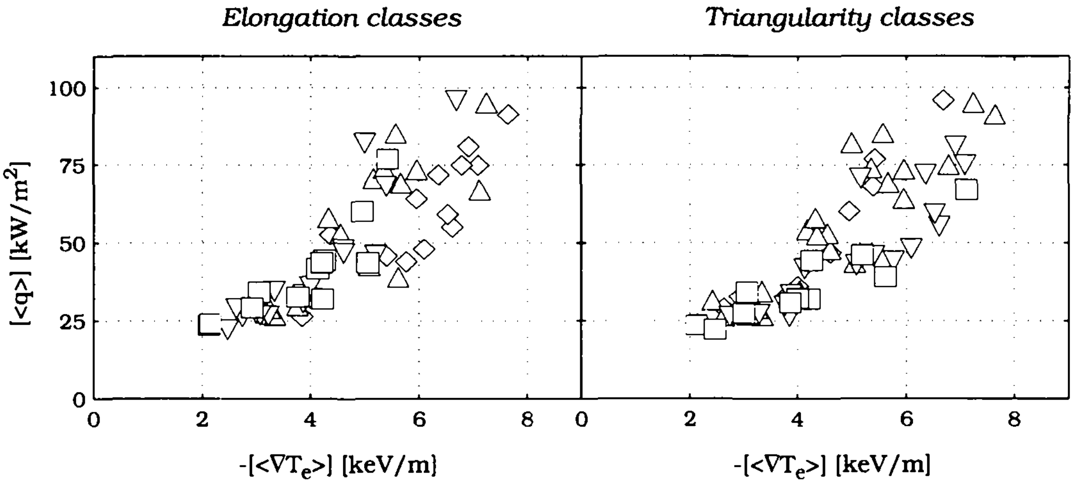

Figure 7.7: Heat flux versus the temperature gradient for all edge safety factors and the density range $3 \cdot 10^{19} m^{-3} <= [n_e] <= 4.5 \cdot 10^{19} m^{-3}$, where $[n_e]$ represents the average electron density in the gradient region. On the left, symbols represent different elongation classes, 'squares': $1.1 \le \kappa \le 1.3$, 'up triangles': $1.3 \le \kappa \le 1.5$, 'down triangles': $1.5 \le \kappa \le 1.7$, 'diamonds': $1.7 \le \kappa \le 1.9$. Symbols on the right represent equally distributed classes of triangularity for $-0.45 <= \delta <= 0.75$.

In the case of both varying δ and κ, fig. 7.7 suggests a non-linear relationship between the temperature gradient and the heat flux. No clear dependence on δ or κ is observed. The implication of fig. 7.7 is a dependence of χ_{eff} on $[\langle \vec{q}_{oh} \rangle]$, as shown in fig. 7.8. Within the measurement accuracy, the following linear dependence of χ_{eff} on $[\langle\vec{q}_{oh}\rangle]$ fits the data:

$$\chi_{eff} = \chi_0 + k_1[\langle\vec{q}_{oh}\rangle] \tag{7.8}$$

with $\chi_0=1.1\mathrm{m}^2/\mathrm{s}$ and $k_1=1.0\cdot10^{-2}\mathrm{m}^4/\mathrm{kJ}$. Eqn. 7.8 defines what we will later call the heat flux degradation of the electron energy confinement. Within the range of observed $[\langle\vec{q}_{oh}\rangle]$ values, χ_{eff} varies from 1.3 to $2.2\mathrm{m}^2/\mathrm{s}$.

In the light of the clear dependence of χ_{eff} on $[\langle\vec{q}_{oh}\rangle]$, we must now reconsider the initial assumption of a poloidally invariant χ_{eff}. To do so, we allow χ_{eff} to be a function of the local ohmic heat flux, $\vec{q}_{oh}$. Still wishing to express the power balance in terms of flux averaged quantities, we must replace eqn. 7.8 with:

$$\chi_{eff} = \chi_0 + k_1\left[\langle q_{oh}\rangle\frac{\langle(\vec{\nabla}\rho)^2\rangle}{\langle\vec{\nabla}\rho\rangle^2}\right] \tag{7.9}$$

where a geometry factor $\langle(\vec{\nabla}\rho)^2\rangle/\langle\vec{\nabla}\rho\rangle^2$ has been introduced. Moret [37] demonstrates that this factor varies only between 1.01 and 1.07 for all the configurations in the shape-confinement database. Within the accuracy of the measurements, a local dependence of χ_{eff} on $\vec{q}_{oh}$ cannot, therefore, be distinguished from a dependence on $\langle\vec{q}_{oh}\rangle$ and we retain the assumption of a poloidally invariant χ_{eff}.

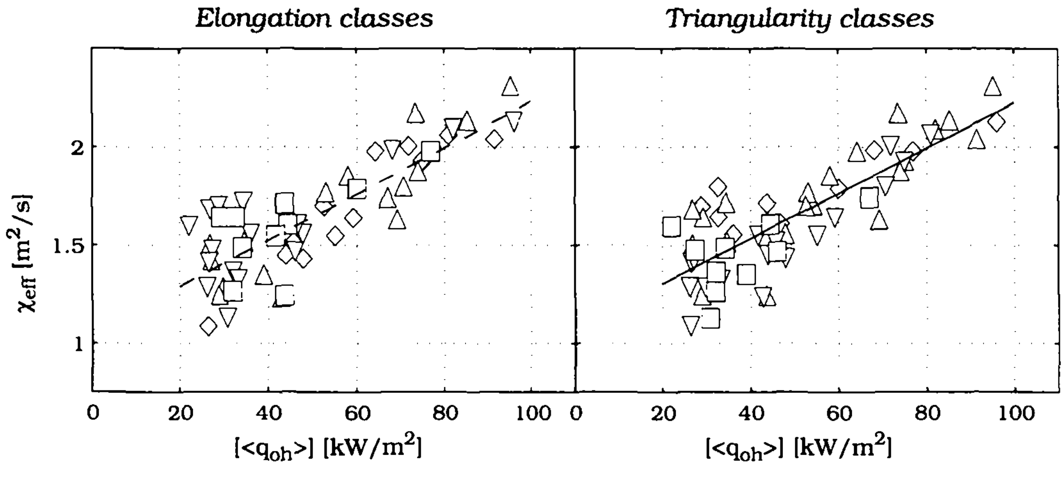

Figure 7.8: Effective heat diffusivity versus ohmic heat flux for the same data set as in fig. 7.7. The identification of the different classes of elongation and triangularity is also as in fig. 7.7.

It is clear that the power deposition profiles and temperature gradients will influence the electron energy confinement time, even if this quantity is obtained from volume integrated data. To account for the dependence of χ_{eff} on heat flux, we normalize the χ_{eff} of individual configurations, $\chi_{eff,n}$ to the arithmetic mean of $\chi_{eff,n}$ for all N configurations of the shape-confinement database:

$$c_{\chi,n} = N\chi_{eff,n} / \sum_{n=1}^{N} \chi_{eff,n} \qquad (7.10)$$

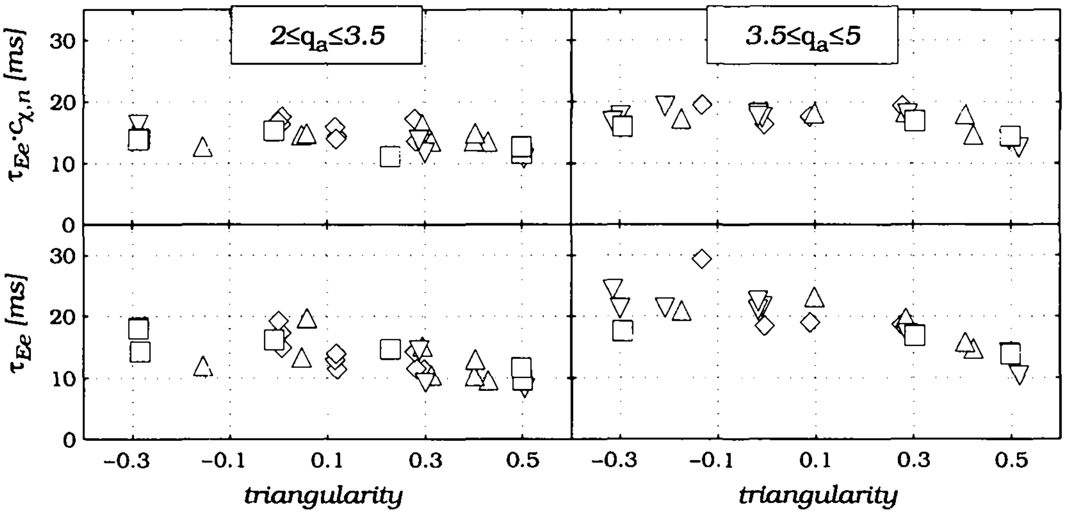

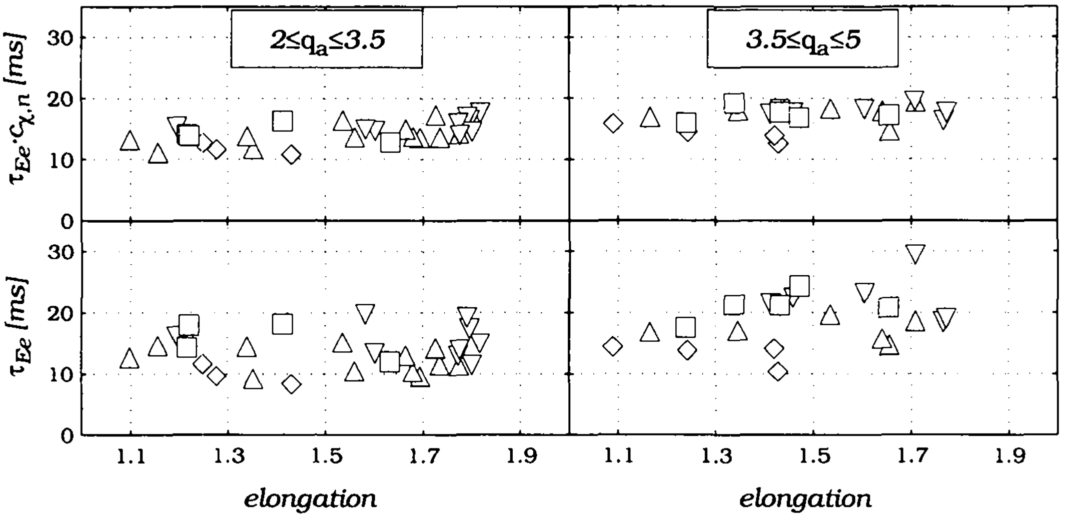

Figure 7.9 Effect of the heat diffusivity correction factor $c_{\chi,n}$ on τ_{Ee} as a function of triangularity and elongation for $3\cdot10^{19}m^{-3} \le [n_e] \le 4.5\cdot10^{19}m^{-3}$. The distribution and the symbols of the different elongation classes are as in fig. 7.7.

Using the factor $c_{\chi,n}$, the individual measurements of τ_{Ee} can be compensated for differences in the heat diffusivities caused by the ohmic heat flux. In fig. 7.9, τ_{Ee} with and without this compensation is plotted as a function of triangularity and elongation for two classes of the edge safety factor q_a. When τ_{Ee} is adjusted by the factor $c_{\chi,n}$ (upper curves) the dependence on δ and κ almost vanishes, except for a persistent decrease for $\delta>0.3$ at the higher q_a values and a slight increase with increasing κ.

7.4 The "Shape Enhancement Factor"

In the previous section, we observed that the dependence of τ_{Ee} on κ and δ could be partly explained by a heat flux dependent thermal diffusivity. The residual dependence of τ_{Ee} on κ and δ after normalisation by the factor $c_{\chi,n}$ indicates that geometrical effects arising from shape changes may also indirectly influence the transport via shape induced changes in spatial gradients. In order to express this local phenomena in a global sense for a given configuration, Moret et al. [36] have introduced the concept of the Shape Enhancement Factor (SEF), which determines the degree to which the shaping modifies the energy confinement time of a circular reference plasma.

We start with the definition of τ_{Ee} for an arbitrarily shaped plasma:

$$\tau_{Ee} = \frac{W_e}{\langle q_{oh}\rangle_a S} = \frac{3}{2\langle q_{oh}\rangle_a S}\int_0^a T_e(r^*)n_e(r^*)\frac{dV}{dr^*}dr^* \tag{7.11}$$

where $\langle q_{oh}\rangle_a$ denotes the heat flux through the LCFS and S the surface area of the LCFS. Rearranging and integrating the heat flux equation (eqn. 7.7) with the assumption that $\langle q_{oh}\rangle$, n_e and χ_{eff} are functions only of the radial coordinate r*, we can replace $T_e(r^*)$ in eqn. 7.11 by the expression:

$$T_e(r^*) = \int_{r^*}^{a}\frac{\langle q_{oh}\rangle}{n_e\chi_{eff}}\frac{d\rho}{dr^{*\prime}}\langle\vec{\nabla}\rho\rangle^{-1}dr^{*\prime} \tag{7.12}$$

The inverse of the GGF (eqn. 7.2) has thus been introduced into the equation for τ_{Ee}. The latter may now be compared with τ_{Ee}^{cir} for a cylindrical plasma with concentric flux surfaces. The cylindrical plasma has the same heat diffusivity, power deposition profile $\langle q_{oh} \rangle$ and horizontal diameter, but has a different outer plasma surface, S_{cir}. Following Moret et al. [37], the SEF therefore has the form:

$$H_s = \frac{S_{cir}\int_0^a n_e\left(\int_{r^*}^a \frac{\langle q_{oh}\rangle}{n_e\chi_{eff}}\frac{d\rho}{dr^{*\prime}}\langle\vec{\nabla}\rho\rangle^{-1}dr^{*\prime}\right)dV}{S\int_0^a n_e\left(\int_{r^*}^a \frac{\langle q_{oh}\rangle}{n_e\chi_{eff}}dr^{*\prime}\right)dV_{cir}} \tag{7.13}$$

where the GGF in the denominator no longer appears, being equal to 1 for the cylindrical reference plasma. The SEF may be regarded as a weighting of the profile function $\langle q_{oh}\rangle / n_e\chi_{eff}$ by the GGF. Values of $H_s>1$ indicate an improvement of the energy confinement time for a shaped plasma in comparison with the circular reference case. Fig. 7.10 shows the SEF for all discharges in the shape confinement database. The SEF exhibits a dependence on triangularity and elongation similar to that of τ_{Ee} (fig. 7.2). From a geometrical point of view, the most favourable shape has negative triangularity and the highest possible elongation.

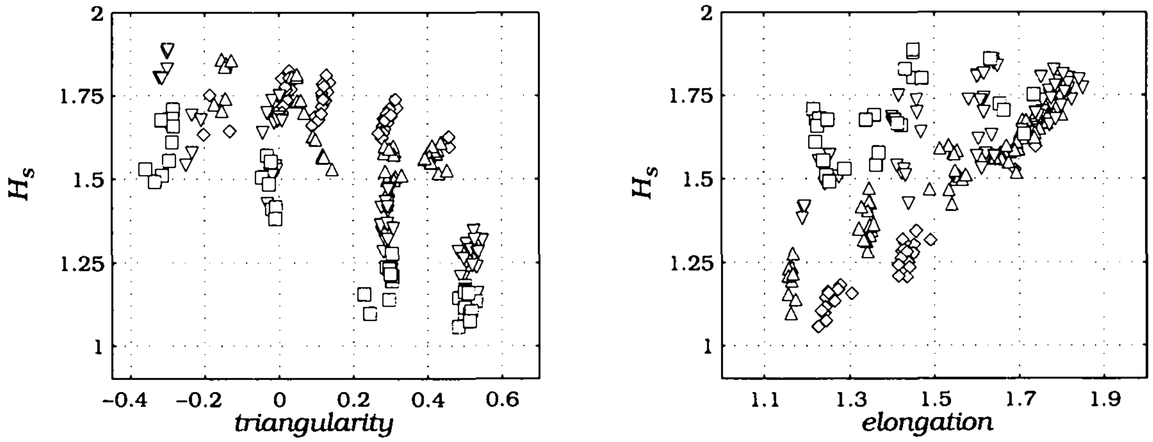

Figure 7.10: SEF for all discharges of the TCV shape confinement database. The distribution and the symbols of the different elongation and triangularity classes are the same as in fig. 7.7.

The SEF can now be combined with the correction factor, $c_{\chi,n}$ describing the heat flux dependence of χ_{eff} to give a single factor, $c_{\chi,n}/H_s$ which may be used to correct electron energy confinement times measured in discharges of varying shape, $\tau_{Ee}^{cor} = \tau_{Ee} c_{\chi,n}/H_s$. As fig. 7.11 clearly illustrates, the application of this correction factor almost completely eliminates any dependence of τ_{Ee} on triangularity and elongation.

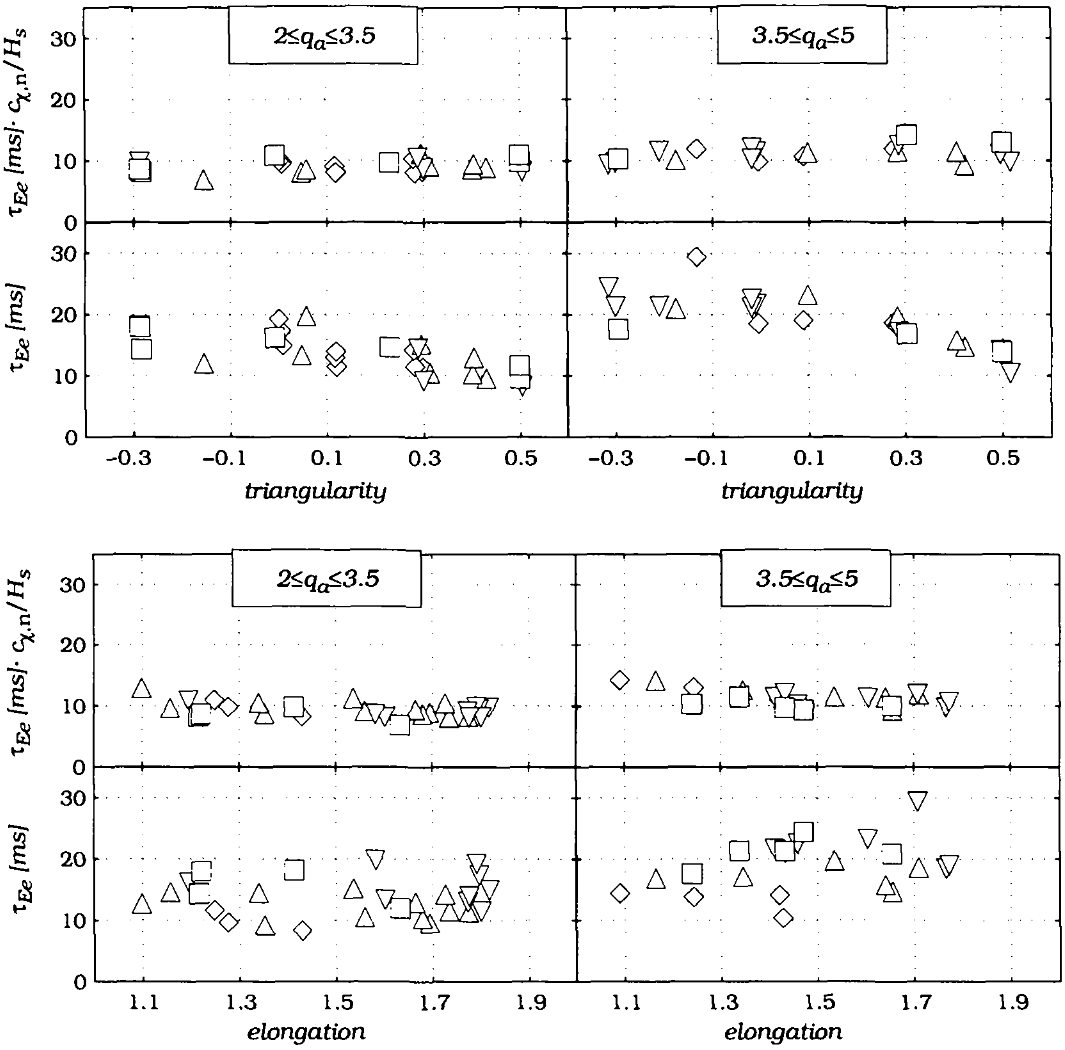

Figure 7.11: Effect of the correction factor for the heat diffusivity, $c_{\chi,n}$, and the shape enhancement factor, H_S on the decrease in confinement with triangularity. The classes for n_e, q_a, and the distribution of the symbols are as in fig. 7.7.

7.5 *The Possible Role of the Ions in the Heat Transport*

As we have already noted, the analysis of confinement dependence on shape described here is performed on the basis of coupled ion and electron temperature and density profiles linked by an expression for the effective heat diffusivity (eqn. 7.6). It is therefore instructive to consider the possible consequences of a changes in the ion edge parameters during the shape scan.

The heat flux degradation and the consequent reduction in energy confinement time are accompanied by lower temperatures and higher loop voltages for fixed n_e. The reduction in τ_{Ee} is furthermore concomitant with an increase in Z_{eff} [71], which also leads to an increase in V_L. According to neoclassical modelling of the ion heat diffusivity, χ_i [10], the inclusion of impurity particle effects results in a χ_i which is more than a factor of Z_{eff} larger than the ion heat diffusivity of a pure deuterium plasma. In the TCV shape-confinement study, a linear dependence of both Z_{eff} and χ_{eff} on $[\langle\vec{q}_{oh}\rangle]$ is observed (fig. 7.12), the effect being stronger for Z_{eff}. The latter changes by more than a factor of 2 compared with about 50% for χ_{eff}. Since we only measure energy confinement properties, temperature and density profiles of the electrons, possible changes of ion transport properties can only be noticed due to changes in the electron-ion energy exchange term which compensates the diffusive losses for the ions. Assuming an increase of χ_i proportional to Z_{eff} in agreement with the neoclassical description of χ_i [10], we can estimate changes in other quantities defining χ_{eff}, namely χ_e, and $\langle\nabla T_i\rangle/\langle\nabla T_e\rangle$ in the gradient region. If we assume χ_e=χ_i for any value of χ_i, $\langle\nabla T_i\rangle/\langle\nabla T_e\rangle$ would need to decrease by approximately 30% to explain the increase in χ_{eff} by 50%, when χ_i changes by more than factor of 2. If we assume, however, $\nabla T_i = \nabla T_e$ for all discharges and χ_i=1m^2/s at the lowest values of Z_{eff} (appendix C)), χ_e would reach between 0.4m^2/s (Z_{eff}=2 and χ_i=1m^2/s) and 0.7m^2/s (Z_{eff}=4.2 and χ_i=2.2m^2/s). The ratio χ_e/χ_i would decrease from 0.4 to 0.3, indicating that the ion loss channel (due to the electron-ion heat exchange) would become more important at higher Z_{eff}. Whilst the available measurements are still insufficient to confirm or to refute the validity of either speculation, it appears to be very likely, that the ions play an important role in the observed heat flux degradation.

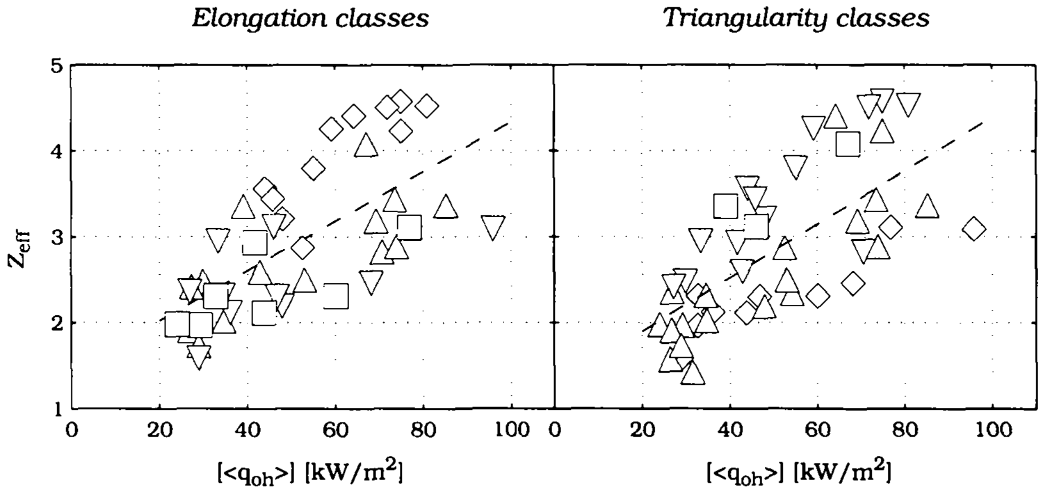

Figure 7.12: Effective ion charge Z_{eff} versus heat flux for the same data set as in fig. 7.7. For the distribution and symbols of the different classes of elongation and triangularity see also fig. 7.7.

7.6 Conclusions

A thorough analysis of T_e gradients in a selected zone near the plasma edge during shaping experiments on TCV has identified a non-linear relationship between the heat flux and the poloidally averaged T_e gradient, $\langle \vec{\nabla} T_e \rangle$. Such behaviour is indicative of a degradation in energy confinement. This non-linear dependence can be expressed as an approximately linear increase of the effective heat diffusivity with the ohmic heat flux crossing a particular magnetic surface. Since the effective ion charge increases as confinement degrades, the degradation could also be attributed to a change in transport properties of the bulk plasma ions, but there is presently insufficient experimental data to confirm or refute this hypothesis.

The transport is also influenced by the plasma shaping which modifies the flux surface separation and hence the local T_e gradient. These effects can be described by a purely geometrical factor which can be used to renormalize the observed energy confinement to that expected for a purely circular plasma with the same ohmic input flux. The combination of corrections for the heat flux dependence of the thermal diffusivity and the geometrical variation can explain the observed confinement dependence on δ and κ, without the need to invoke shape dependent transport coefficients.

8 *Influence of Constraints from Measured Pressure Profiles on the Equilibrium Reconstruction*

8.1 *The Equilibrium Reconstruction Code LIUQE*

8.1.1 *The Standard Version ("Magnetic" LIUQE)*

The reconstruction of magnetic equilibria on TCV from magnetic measurements of fluxes, fields and currents outside the plasma is essential for evaluation of the magnetic flux surface geometry and the computation of the plasma current distribution, j, the safety factor profile, q and kinetic plasma parameters, W_t, β_{tor}, β_{pol} (see appendix D). The equilibrium is reconstructed by solving the basic ideal MHD-equilibrium equation ($\vec{\nabla} p = \vec{j} \times \vec{B}$) for an axisymmetric plasma in toroidal geometry:

$$R\frac{\partial}{\partial R}\frac{1}{R}\frac{\partial \Psi}{\partial R} + \frac{\partial^2 \Psi}{\partial z^2} = -\mu_0 R j_\varphi \tag{8.1}$$

where j_φ denotes the toroidal current density and Ψ is constant on a magnetic flux surface, $\Psi = -RA_\varphi$. The toroidal component of the magnetic field vector potential, A_φ is proportional to the poloidal flux within this surface. After some algebraic transformations, eqn. 8.1 yields the so-called Grad-Shafranov equation [58]:

$$\Delta^* \Psi = -\mu_0 R^2 p_t' - TT' \tag{8.2}$$

The prime denotes differentiation with respect to Ψ, p_t is the total plasma pressure and the toroidal current density has been expressed by:

$$j_\varphi = Rp_t' + \frac{TT'}{\mu_0 R}$$

(8.3)

where the current function, $T = RB_\varphi$, reflects the effect of the plasma current on the vacuum toroidal magnetic field, $B_{\phi,O}$ ($B_{\phi,O} \approx B_0 R/R_O$). Since $\beta_{pol} < 1$ in ohmically heated discharges on TCV, the ratio $B_\phi / B_{\phi,0} > 1$ (B_ϕ the central toroidal field in the presence of plasma) and the plasma is therefore paramagnetic. The two expressions, p_t' and TT', are equilibrium dependent source functions which are constant on a magnetic flux surface and depend only on Ψ. They may be represented by linear combinations of base functions, U_n in terms of the normalized poloidal flux, Φ:

$$p_t' = \sum_{n=1}^{N_p} a_n U_n(\Phi)$$

$$TT' = \sum_{n=1}^{N_T} b_n U_n(\Phi)$$

(8.4)

where Φ is defined as $\Phi = (\Psi - \Psi_{Lim})/(\Psi_{ax} - \Psi_{Lim})$ with Ψ_{Lim} and Ψ_{ax} respectively the values of the poloidal flux function at the LCFS and on the magnetic axis.

To solve the intrinsically non-linear reconstruction problem, the LIUQE code has been developed and is used routinely on TCV [19]. In LIUQE, a non-linear least squares fitting algorithm computes values of the free parameters, a_n and b_n of the two source functions which minimize the error function:

$$\chi^2 = \sum_k \sum_{i(k)} \left(\frac{M_{k,\,i(k)} - C_{k,\,i(k)}}{\sigma_{k,\,i(k)}} \right)^2$$

(8.5)

The summation indices k and $i(k)$ extend over the type and the corresponding number of measured, M_k and calculated data, C_k. The corresponding weights are denoted by the uncertainties, σ_k attributed to the data. In its basic version, LIUQE incorporates measurements and error estimates of relative poloidal fluxes (flux difference between two neighbouring poloidal flux loops, k=*rfl*, poloidal field probes, k=*bpol*, vessel, k=*iv*, and coil currents, k=*ic*. Following a successful reconstruction, LIUQE deduces the spatial flux surface geometry, shape parameters κ, δ and important parameters such as q_a, I_p, l_i, etc.

In general, LIUQE also computes kinetic plasma parameters such as β_{pol}, β_{tor}, the total plasma energy, W_t or parameters within the plasma column, for example, the location of the q=1 surface or the safety factor on the magnetic axis, q_0. The calculation of any of these parameters involves one or both of the two unknown source functions, p_t' or TT'. Hofmann and Tonetti [19] have shown that, if analytic input profiles are used, an appropriate choice of the combination of base functions ($N_p=1$, $N_T=2$) allows β_{pol} and q_0 to be determined with a statistical uncertainty of less than 5% in the case of random measurement errors of +/- 2%. A number of terms, $(N_p+ N_T)>3$ in the eqns. 8.4 would lead primarily to large uncertainties in q_0. However, even for a restricted number of degrees of freedom, systematic uncertainties in W_t and q_0 can be substantial.

The first column of fig. 8.1 demonstrates these uncertainties for TCV discharge #7332 during the period of constant plasma current ($I_p \approx 410$kA). At t=0.42s, this SNL-discharge made a transition from L-mode to an ELM-free, H-mode phase. Just after the transition, the computed q_0 becomes greater than 1, even though sawtooth oscillations are clearly present on the normalized trace of the temperature, T_e^{softX} (centrally weighted electron temperature derived from line integrated soft X-ray emissivity measurements). Apparently a change in the current density profile accompanies the change in the plasma confinement mode, but a q=1 surface should always be present if sawtooth activity is observed.

The second column of fig. 8.1 demonstrates the uncertainties in the calculated W_t for shot #7412. The ratio, W_t/W_e, between the total plasma energy content and the total electron energy content implies that $W_t \approx W_e$ during the L-mode phase. This could, in part, be explained by an error in W_e of the order of 10%. At a line averaged electron density of $\langle n_e \rangle_L \approx 7 \cdot 10^{19}$ m^{-3} and for $Z_{eff}<2$, however, a more important ion energy fraction would be expected.

Fig. 8.2 shows the TS profiles of electron pressure during the phase when $W_t \cong W_e$ in discharge #7412. Also illustrated are the total pressure profiles assumed by LIUQE. Clearly, *"magnetic"* LIUQE assumes p_t profiles which are not in agreement with experimental data obtained from Thomson scattering. For the case shown here, the assumed p_t profiles appear much more peaked than would be expected from the electron pressure component. Since the difference must be attributed to the ions, the implication of p_t profiles with twice the amplitude of the experimental p_e profiles ($p_t \approx 2p_e$ near ρ=0) would seem unrealistic.

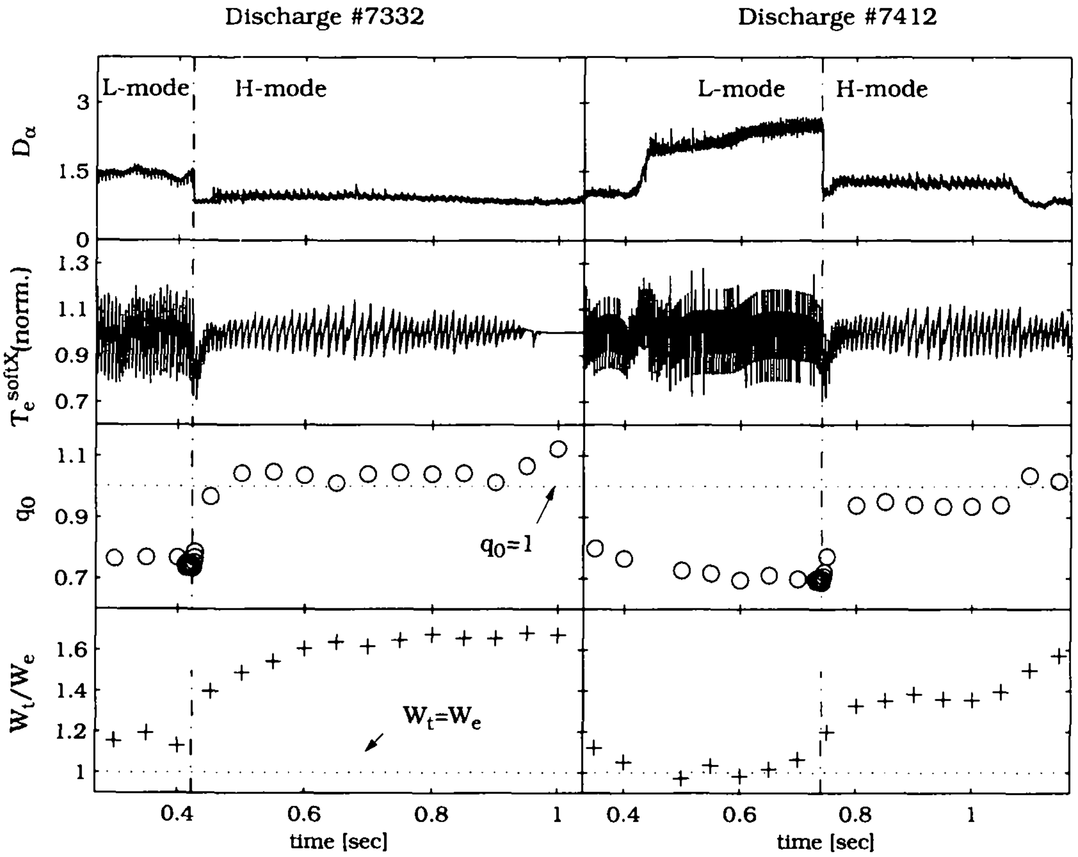

Figure 8.1: Temporal evolution during the I_p plateau of D_α, normalized T_e^{softX},q_0 and W_t/W_e for two ELM-free, H-mode discharges

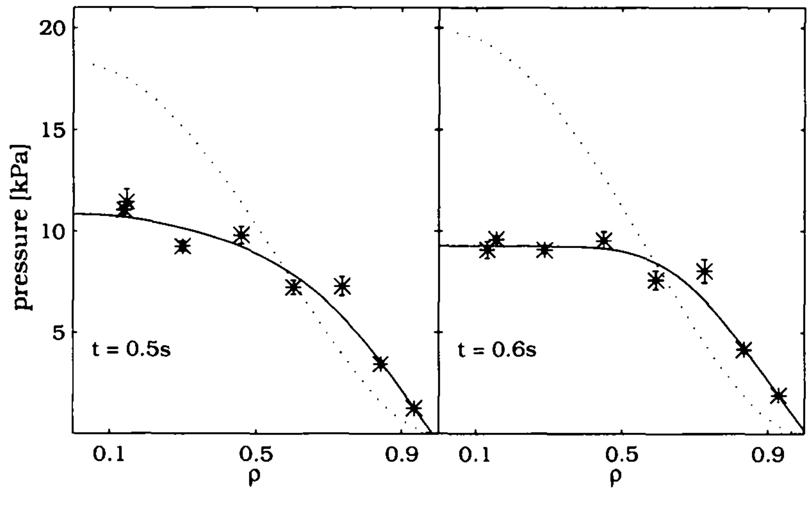

Figure 8.2: TCV discharge #7412: p_t profile assumptions (dotted lines) from "magnetic" LIUQE together with p_e profiles ('' symbols) and their fits (solid lines) from Thomson scattering at the time slices for which W_t<W_e.*

It has been shown [16] that the inconsistencies of a reconstruction based on magnetic measurements can be overcome if p_t profiles are imposed, where TS measurements can be used to provide the data for the p_e profiles. Unfortunately, equivalent measurements for the ion component are more difficult to obtain and adequate diagnostic equipment is not yet available on TCV. Ion pressure profiles have therefore been computed using the p_e profiles together with a simple equilibrium model. The varying assumptions adopted in these models will be described in detail below. In some cases, such assumptions can remove ambiguities in the equilibrium reconstruction.

In addition to experimental pressure profiles, other data can be provided as input to the reconstruction. For example, polarimetric measurements of B_θ via the Faraday rotation effect [50] can provide the q-profile. Further ways to constrain LIUQE may be based on diamagnetic loop measurements yielding β_{pol} and hence $\int pdV$, or on tomographic reconstructions of the soft X-ray emissivity profiles which permit the spatial location of the sawtooth inversion radius and hence the q=1 surface to be identified [1].

8.1.2 The Version with Additional Constraints, in particular Pressure Profiles ("Kinetic" LIUQE)

Imposing additional constraints on the equilibrium reconstruction allows a larger number of base functions to be included in the source functions p_t' and TT' in the Grad-Shafranov equation. Using a statistical error analysis of 270 reconstructions of a D-shaped equilibrium, Hofmann and Tonetti have shown [19] that constraints from Faraday rotation measurements would permit an increase in the number of free source function parameters (eqn. 8.4) from 3 to 4. Since, in this study, the smallest statistical fluctuations on the observed plasma parameters (β_{pol}, l_i, μ, q_0) were achieved for equal numbers of free parameters for p_t' and TT (N_p=N_T=2), the same distribution of degrees of freedom will be employed here for the reconstruction with constraints from the kinetic pressure profiles.

A set of interpolating base functions must still be established. The *"kinetic"* version of LIUQE provides for a choice of 3 different types to represent the source functions $p_t'$and TT' (fig. 8.3). The current version of LIUQE does not yet permit the base functions to be modified for different times in the discharge being analysed. The base functions are represented in a normalized coordinate system, where the LCFS corresponds to Φ=0 (Table 8-1). The transformation $\Phi = 1 - \rho^2$ maps this coordinate system onto the familiar normalized flux coordinates, ρ.

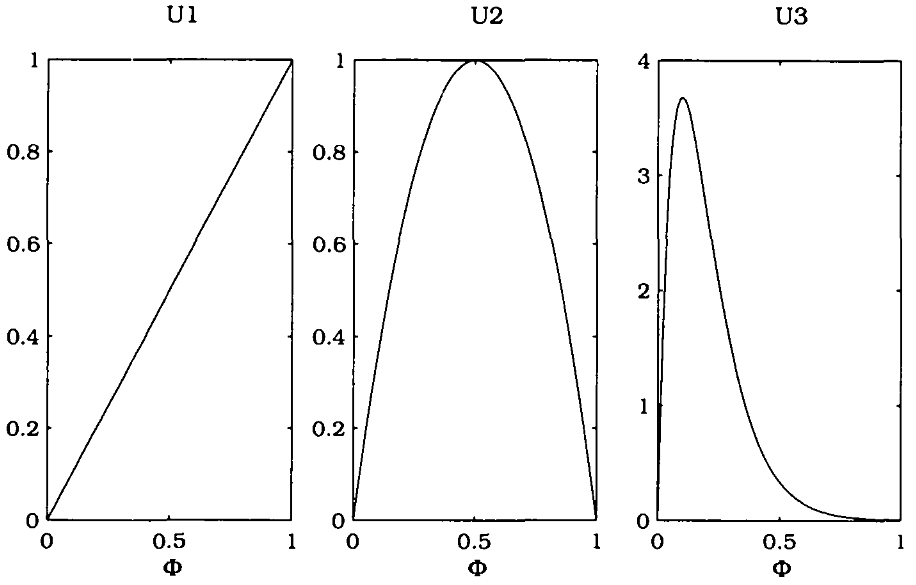

Figure 8.3: The set of possible base functions for the equilibrium reconstruction. The location of the magnetic axis corresponds to Φ=1, the location of the LCFS to Φ=0.

Table 8-1: Base functions

U1	Φ
U2	$1-(2\Phi-1)^2$
U3	$\alpha^2\Phi e^{-\alpha\Phi}$; $\alpha=10$

Depending upon the shape of the p_t profiles, two linear combinations of base functions can be chosen to represent the derivative of the p_t fit:

$$p_t'(\Phi) = a_1U_1 + a_2U_2 \quad \text{(Option 1)}$$

$$p_t'(\Phi) = a_1U_1 + a_3U_3 \quad \text{(Option 2)}$$

(8.6)

Once the equilibrium is established, the p_t fit is obtained by integration and by imposing a vanishing pressure on the LCFS. Option 1) leads to more accurate fits (characterized by the corresponding χ^2_{pr} values) in the case of relatively flat edge pressure gradients, whilst option 2) is better suited to the description of steep gradients. Fig. 8.4 shows typical examples of p_t profile fits in L- and H-mode together with the corresponding χ^2_{pr} values. In this case, the p_t profile is assumed to be proportional to the measured p_e profile, $p_t=1.4p_e$ (Section 8.2.3.1). When using option 2) in favour of option 1), the χ^2_{pr} value increases for the L-mode profile fit and decreases for the H-mode profile fit. Since we are unable to impose a constraint on the source function TT', the set of base functions employed in the "*magnetic*" LIUQE reconstructions will also be used in the "*kinetic*" LIUQE calculations reported below:

$$TT'(\Phi) = b_1 U_1 + b_2 U_2 \qquad (8.7)$$

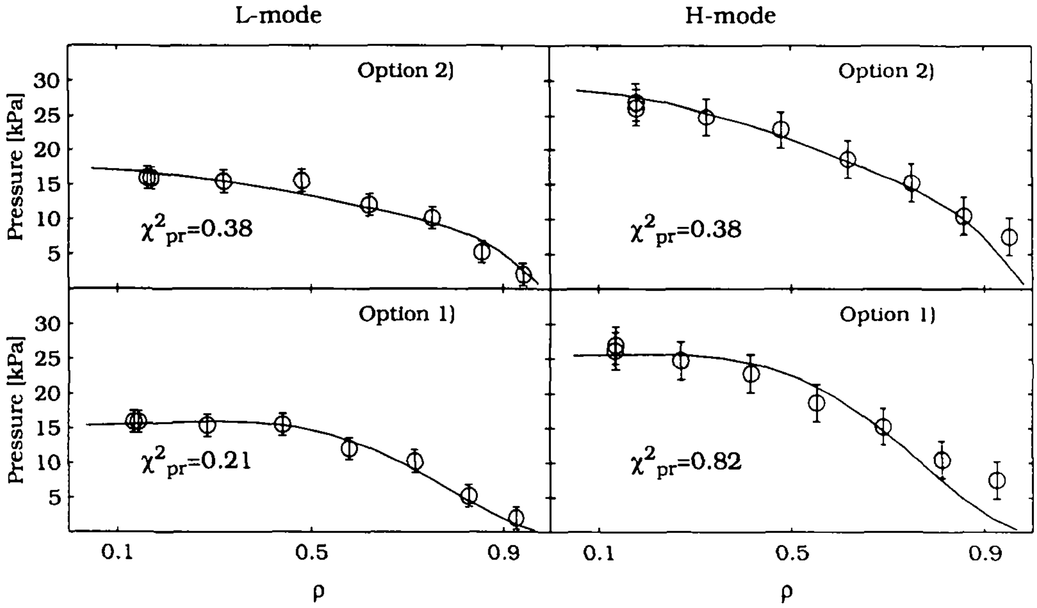

Figure 8.4: The curves on the left the measured L-mode p_t profile ('o'-symbols) along with the reconstructed profile for two different sets of base functions (solid lines). On the right, similar analysis has been applied to profiles measured after the H-mode transition when the edge pressure rises (discharge #7412).

8.1.3 Using LIUQE with Additional Constraints

As already indicated in Section 8.1.1, LIUQE computes iteratively until Ψ has converged. If the value of χ^2 for the measured and calculated data falls below a preset limit, $\chi^2 \leq 4$, the solution is accepted. Typical values of χ^2 for a "*magnetic*" LIUQE range between 0.1 and 0.5. The contribution of each single group of magnetic measurements to the total χ^2 varies from $\chi^2_{bpol} \approx 0.1$-0.5 in the case of the full set of poloidal field coils and $\chi^2_{iv} \approx 0.02$-0.07 for the measured vessel currents.

For the *"kinetic"* LIUQE reconstructions, we do not wish the additional constraints on the p_t profiles to compromise the convergence behaviour of the purely *"magnetic"* reconstruction. The additional pressure constraint should therefore have a weight comparable to the weights of the magnetic measurements, such that the resulting χ^2_{pr} value on the p_t fits is of the same order as χ^2_{bpol}. This means that the estimated error bars, σ_{p_t} on the input p_t profiles should represent a reasonable compromise between the different criteria. Those should be large enough to allow p_t profile fits within the fixed convergence limits of the reconstruction, but sufficiently small that the profile features are well reproduced. We therefore choose error bars on the data points of each p_t profile to be greater or at least equal to 10% of the absolute profile maximum:

$$\sigma_{p_t}(r, z, t) \geq 0.1 max(p_t(r, z, t)) \tag{8.8}$$

Under these conditions, the basic magnetic parameters (κ,δ) computed from a magnetic or a kinetic reconstruction should not differ greatly, provided that the χ^2 values remain comparable.

Before we finally use the TS p_e profiles for evaluation of the p_t profiles, we must consider the systematic errors on the former that arise from systematic errors on the n_e profiles. These errors are minimized by comparing the computed line-integrated densities from TS n_e profiles, $\bar{n}_e^{TH}$ with those measured directly, $\bar{n}_e^{FIR}$ using the FIR interferometer (Section 5.2). Since the computation of $\bar{n}_e^{TH}$ requires the TS n_e profiles to be projected onto normalized flux coordinates, a *"magnetic" LIUQE* necessarily preceeds any *"kinetic" LIUQE* calculation.

8.2 Evaluation of Total Plasma Pressure Profiles

8.2.1 Motivation

A calculation of the p_t profile requires knowledge of the partial pressure profiles of each charged species in the plasma. For sufficiently low impurity concentrations however, only electrons and fuel ions contribute. On TCV, Thomson scattering provides n_e, T_e and therefore p_e profile measurements, but no measurement of the ion pressure profile is currently available. The plasma ion density profile, n_i can only be estimated on the basis of Z_{eff} measurements in combination with measurements of the main plasma impurity ion (B, C, N, O) concentrations, assuming the n_i profiles to be proportional to the n_e profiles. With respect to the ion temperature, we can at best obtain local measurements from two diagnostics: a neutral particle analyser (NPA) and visible CX-spectroscopy (Section 3.1.2).

The NPA nominally provides a central ion temperature, $T_i^{NPA}=T_i(\rho=0)$, whilst CX-spectroscopy measures a temperature, T_i^{CX} which is located near the plasma edge ($\rho \approx 0.75$). In both cases, precise localisation of the measured T_i values is not possible. Worse still, the zone to which the T_i value can be attributed varies with plasma conditions, in particular with the electron density. As shown in fig. 8.5, these uncertainties lead to further unexpected trends when the ratios $T_i^{NPA}/T_e(\rho=0)$ and $T_i^{CX}/T_e(\rho=0.75)$ are plotted as a function of n_e. The plotted data are taken from the TCV shape confinement database and the T_e and n_e data are obtained from profile fits to the TS data.

Beginning from a density, $<n_e>_L=4 \cdot 10^{19} m^{-3}$, in an ohmic plasma one would expect T_i to approach T_e as n_e increases, since the electron-ion energy equilibration time, τ_{ei}^{eq} becomes shorter and the energy exchange more efficient. One explanation for the contradictory behaviour apparent in fig. 8.5 would be a density dependent spatial location of the plasma volume elements from which the deuterium neutrals or the visible photons escape. Since at present this n_e dependence has not yet been determined or calculated from a model, the T_i data on TCV are difficult to interpret.

Two different models have thus been adopted from which the ion contribution to the p_t profiles can be deduced from the measured p_e profiles. The simplest model assumes p_t to be proportional to p_e, $p_t=M \cdot p_e$ (Section 8.2.3.1), whilst a more elaborate and more realistic version derives the ion contribution, p_i from a transport model, $p_t=p_i+p_e$ (Section 8.2.3.2).

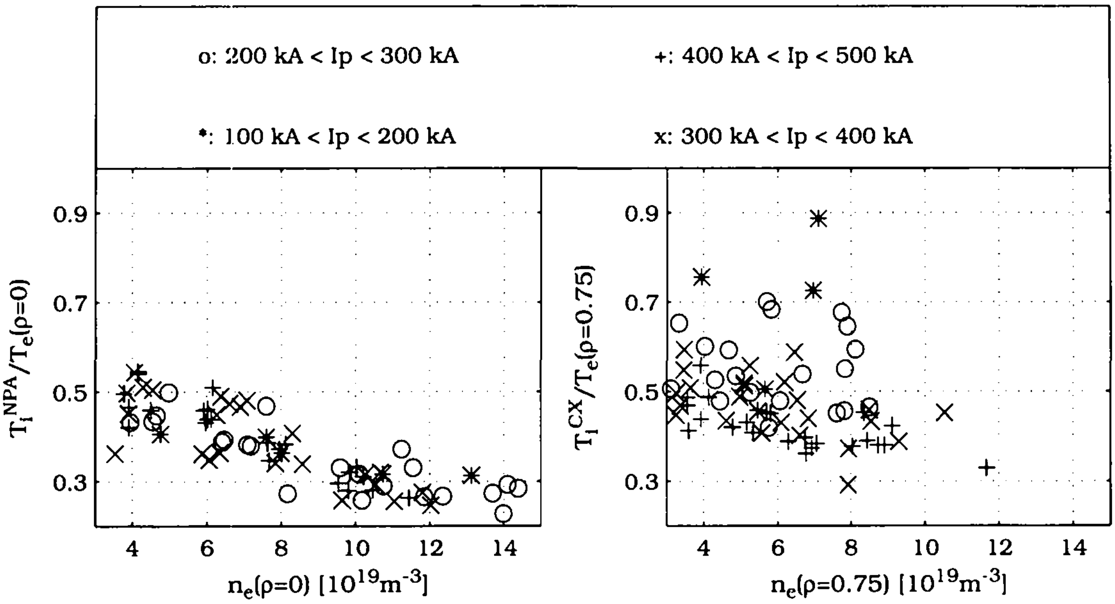

Figure 8.5: T_i/T_e ratios from NPA (left) and visible CX-spectroscopy measurements (right) as a function of n_e.

8.2.2 Selection of a Data Base

A database (called DIOP) of 17 representative TCV discharges has been chosen for the analysis. Two are ELM-free, H-mode discharges in a SNL-configuration (#7332, #7412), 8 are limited on the central column (#7706 - #7766) and further 7 are selected from a campaign of L-mode discharges in the so-called TCV 'Standard' SNL L-mode configuration (#8430 - #8450). The confined plasma in each case is located in the upper part of the vacuum vessel ($z \approx 0.25$ m) so that the Thomson scattering observation volumes (from z=0.23 m to z=0.64 m) cover at least one half of the poloidal plasma cross-section.

Table 8-2 lists the essential discharge parameters for these shots. The volume average of T_e, $\langle T_e \rangle_V$, is calculated from the profile fits of the TS T_e data, $\langle n_e \rangle_L$ is obtained from FIR interferometer data and all other parameters from the *"magnetic"* LIUQE reconstruction. All data are averages over 10-13 samples within a time period of the order of 0.5 sec, although the latter varies depending on the interval in each individual discharge for which steady-state conditions were maintained. Within the stationary phase the main plasma parameters generally stay within ±10% of their average values, except during H-mode shots with an ELM-free phase in which $\langle n_e \rangle_L$ rises quickly from

$<n_e>_L \approx 6\cdot 10^{19}\ m^{-3}$ in L-mode up to $<n_e>_L \approx 1.2\cdot 10^{20}\ m^{-3}$ at the end of the H-mode phase. For the standard discharges, $<n_e>_L$ varies by about 20% around the average value given in the Table 8-2. This is due to a gas cut at t=0.75 s which leads to a slow density decay (used to calculate global recycling times).

Table 8-2: Data base for the modelling of ion pressure profiles (DIOP)

SHOT	I_p [kA]	P_{oh} [kW]	$<T_e>_V$ [eV]	$<n_e>$ V $[10^{19}m^{\wedge-3}]$	Z_{eff}	κ_{95}	δ_{95}	q_{95}	R_{ax} [m]	z_{ax} [m]
7332	419	678	384	11.7	1.8-2.7	1.59	0.42	2.25	0.89	0.25
7412	424	714	446	9.3	1.8-2.5	1.58	0.41	2.31	0.88	0.25
7706	256	331	306	6.9	2.0	1.46	0.08	3.35	0.89	0.23
7708	294	406	361	5.7	2.2	1.47	0.07	2.83	0.88	0.23
7754	418	641	410	7.4	2.4	1.65	0.25	2.61	0.88	0.23
7755	458	764	437	7.4	2.6	1.65	0.25	2.44	0.88	0.23
7763	457	755	450	6.8	2.7	1.67	0.25	2.46	0.88	0.23
7765	529	865	492	6.7	2.7	1.68	0.27	2.62	0.88	0.23
7766	458	678	452	6.6	2.5	1.87	0.26	2.88	0.88	0.23
8430	376	579	345	5.3	1.4	1.82	0.38	2.61	0.89	0.25
8437	376	565	363	5.1	1.4	1.60	0.38	2.60	0.89	0.25
8441	376	540	393	4.7	1.4	1.60	0.38	2.59	0.89	0.25
8442	377	550	380	4.9	1.4	1.60	0.38	2.59	0.89	0.25
8444	376	562	354	5.3	1.4	1.61	0.38	2.61	0.89	0.25
8449	377	525	403	4.5	1.5	1.60	0.38	2.59	0.89	0.25
8450	377	536	384	4.8	1.4	1.60	0.38	2.58	0.89	0.25

8.2.3 Models for Total Plasma Pressure Profiles

8.2.3.1 Ion Pressure Proportional to the Electron Pressure

In this case we assume that the p_i profile is simply proportional to the p_e profile and thus to the p_t profile. This proportionality further implies that the p_e and p_t profile shapes are identical in each coordinate system:

$$p_t(([r,z],[\Psi],[\rho]),t) = Mp_e(([r,z],[\Psi],[\rho]),t) \tag{8.9}$$

where the proportionality factor M can be a function of global plasma parameters. A fixed value, M=1.4 has been obtained with the following assumptions: $T_i \approx 0.5 \cdot T_e$ for $<n_e>_L = 5 \cdot 10^{19} m^{-3}$ [9], $Z_{eff} \approx 1.8$ ($n_C/n_e \approx 2\%$, $n_B/n_e \approx 1\%$) and $n_i/n_e \approx 0.85$ [71]. According to more recent reports concerning the ion energy transport in ohmic discharges [60], the ratio $T_i/T_e \approx 0.5$ given by de Chambrier, would appear to be underestimated. The estimate of W_t based on this model for the p_t profiles should be considered as a lower limit on the total plasma energy.

8.2.3.2 Deriving the Ion Pressure Profile from a Transport Model

In this second, more complicated model, proportionality between the p_t and p_e profiles is no longer assumed. Profiles of n_i and T_i are instead estimated from measured T_e and n_e profiles, uniform impurity concentrations and Z_{eff}. To keep the model as simple as possible, we restrict the analysis to stationary plasma conditions in which I_p and $<n_e>_L$ do not change by more than 10%. This limitation excludes the ELM-free H-mode shots from the analysis. To overcome the problem of sawtooth oscillations which modify the internal distribution of the plasma energy and produce strong signatures on the T_e profiles (Section 5.1), we make use of the random phase between sawteeth (period≈3-6ms) and the Thomson scattering sampling rate (Δt_{TS}=50ms).

Up to 12 T_e and n_e profiles can be associated with each discharge. Reducing the effect of sawtooth oscillations on the profiles by a suitable profile average, the shape and the amplitude of T_e and n_e profiles is therefore considered to be frozen during the stationary phase. To obtain the profile fits we apply the same method as in Section 6.2.1. Typical T_e and n_e profile fits are shown in fig. 8.6 for the limited discharge #7708. The central electron temperature of the T_e profile fit is in good agreement with T_e^{softX} which shows sawtooth oscillations with $\delta T_e \approx \pm 5\%$ around T_e^{softX}=760eV.

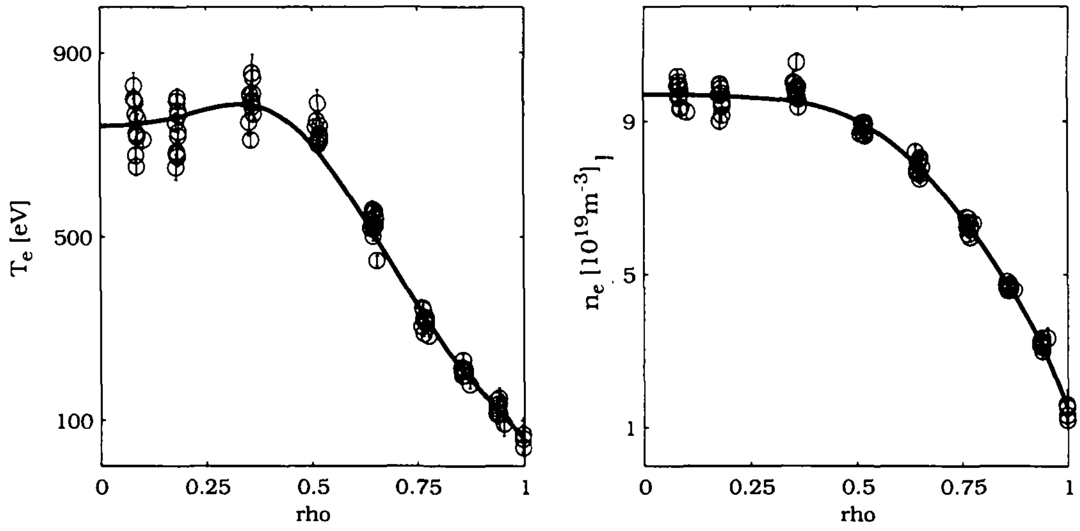

Figure 8.6: *Illustration of averaged T_e and n_e profiles on for discharge #7708.*

The assumption of single T_e and n_e profiles during the entire stationary phase results in single T_i and n_i profiles obtained by transport modelling as described below. The resulting averaged p_i profile is then summed with the individual p_e profiles of each time-slice:

$$p_t(([r,z],[\Psi],[\rho]),t) = p_i(([r,z],[\Psi],[\rho])) + p_e(([r,z],[\Psi],[\rho]),t) \tag{8.10}$$

8.2.3.2.1 Evaluation of the T_i Profile from the Ion Heat Diffusion Equation

The ion energy transport is modelled with a simple equation for the ion energy density, w_i:

$$\frac{\partial w_i}{\partial t} = -\vec{\nabla}\vec{q}_{diff} + p_{ei} \tag{8.11}$$

where $\vec{q}_{diff}$ denotes the diffusive ion heat flux and p_{ei} the rate of collisional energy transfer from the electrons to the ions. Expressions for p_{ei} and $\vec{q}_{diff}$ will be given later. Within the framework of this model, the collisional transfer represents the only energy source for the ions. As discussed below, convective energy losses, losses due to charge-exchange recombinations or energy gain due to direct ohmic heating of the ions are neglected.

According to results obtained in ohmic L-mode discharges on ASDEX [60], convective energy and charge-exchange recombination losses for $\langle n_e \rangle_L \approx 5 \cdot 10^{19} m^{-3}$ and $P_{oh} \approx 400$ kW are limited to about 10% of the total ohmic input power and are located near the plasma edge. Since the convective energy losses near the edge decrease with higher $\langle n_e \rangle_L$ and increase with higher T_e, the effects of $\langle n_e \rangle_L$ and P_{oh} are in opposite directions. However, since the differences in P_{oh} and $\langle n_e \rangle_L$ with respect to the reference values above are within a factor of about 2 for the TCV discharges in the DIOP database (Section 8.2.2), we do not expect a significant increase in convective losses with respect to the estimated value of 10%. Charge-exchange losses are sensitive to T_e and n_e at the edge and also to the neutral density, which rises sharply near the edge. Since neutral density profiles are not yet available on TCV, a difference between the CX loss estimation given in the reference [60] and expected CX losses on TCV can hardly be evaluated and CX losses are neglected.

Direct ohmic heating of the ions is limited to the density gradient region ($\rho \geq 0.8$) due to the bootstrap character of the driven ion component [67] and can reach 10-15% of the total ohmic heating power. Such heating may partially compensate the ion energy losses near the edge. However, since there is no experimental evidence for such effects on TCV and since the final model uses simple approximations (χ_i^C=const. across the whole plasma volume), we neglect this effects in what follows.

Assuming stationary conditions, $\frac{\partial w_i}{\partial t} = 0$, eqn. 8.11 reduces to:

$$\vec{\nabla} \vec{q}_{diff} = p_{ei} \tag{8.12}$$

The RHS of eqn. 8.12 describes the energy transfer from the electrons to the ions per unit volume and per unit time:

$$p_{ei} = \frac{3}{2} \frac{e n_e (T_e - T_i)}{\tau_{ei}^{eq}} \tag{8.13}$$

$$\tau_{ei}^{eq} = \frac{(2\pi)^{1/2} A 3\pi\varepsilon_0^2 m_p T_e^{3/2}}{Z^2 n_i m_e^{1/2} e^4 \ln\Lambda} \tag{8.14}$$

where $T_{e,i}$ are in eV, τ_{ei}^{eq} is the electron-ion energy equilibration time [34] and lnΛ denotes the Coulomb logarithm for electron-ion collisions:

$$\ln\Lambda = 24 - \ln\left(\frac{(n_e 10^{-6})^{1/2}}{T_e}\right), \; n_e \text{ in } [\mathrm{m}^{-3}] \tag{8.15}$$

where, since are concerned only deuterium majority ions, A=2 and Z=1.

The diffusive heat losses are proportional to $\vec{\nabla}T_i$, $\vec{q}_{diff} = -en_i\chi_i\vec{\nabla}T_i$. Since n_i, n_e, T_i, T_e and the ion heat diffusivity, χ_i are considered to be constant on flux surfaces, a flux-surface-averaged form of eqn. 8.12 can be written [63] using the expressions for $\vec{\nabla}\vec{q}_{diff}$ and p_{ei}:

$$\frac{1}{V'(a^*)}\frac{\partial}{\partial a^*}\left(S(a^*)\chi_i n_i \frac{\partial T_i}{\partial a^*}\right) = \frac{3}{2} n_e \frac{T_i - T_e}{\tau_{ei}^{eq}}, \tag{8.16}$$

where:

$a^* = a\rho$ = radial coordinate labelling a flux surface

$V(a^*) = 2\pi^2 R_0 a^{*2}\kappa$ = plasma volume within a flux surface

$$V'(a^*) = \frac{\partial V}{\partial a^*}$$

$$S(a^*) = V'(a^*)\langle\vec{\nabla}\vec{\nabla}a^*\rangle = (2\pi^2)R_0 a^*\kappa\left[\frac{1+\kappa^2(1+2\delta^2)}{2\kappa^2}\right]$$

= outer area of a flux surface

The expressions for $V(a^*)$ and $S(a^*)$ presuppose a concentric, elliptic geometry for the flux surfaces. The effect of the Shafranov shift, which displaces the geometrical centre of inner surfaces with respect to the outer surfaces, is therefore not taken into account, but a correction for the triangularity is included in the expression for $S(a^*)$.

8.2.3.2.2 Solving the Differential Equation; The Numerical Scheme (Crank-Nicholson)

Eqn. 8.16 is a 1-dimensional, parabolic, 2nd-order differential equation for T_i in the surface label coordinate a^*. In order to allow discretisation with an implicit Crank-Nicholson scheme [55] valid for $0 < a^* < a$, the following transformations are applied:

$$P(a^*) = -\frac{3}{2}\frac{V'(a^*)n_e}{\tau_{ei}^{eq}}$$

$$Q(a^*) = \frac{3}{2}\frac{V'(a^*)n_eT_e}{\tau_{ei}^{eq}}$$

$$D(a^*) = S(a^*)\chi_i n_i, \tag{8.17}$$

which results in:

$$\frac{\partial}{\partial a^*}\left(D(a^*)\frac{\partial T_i}{\partial a^*}\right) + P(a^*)T_i + Q(a^*) = 0 \tag{8.18}$$

According to the Crank-Nicholson method, an implicit finite difference approximation of eqn. 8.18 is given by:

$$\frac{1}{\Delta a^{*2}}\left[D_{j+\frac{1}{2}}(T_{i,j+1} - T_{i,j}) - D_{j-\frac{1}{2}}(T_{i,j} - T_{i,j-1})\right] + P_jT_{i,j} + Q_j = 0\text{, j=2,..., N-1} \tag{8.19}$$

Eqn. 8.19 represents a time-independent system of (N-2) equations for the N unknown ion temperatures, $T_{i,j}$. We thus require two boundary conditions for $T_{i,1}$ and $T_{i,N}$. Since the T_i profiles are represented in radial coordinates, one boundary condition is to set the T_i gradient to zero on the magnetic axis. The second makes use of the assumption that near the plasma edge the higher collisionality brings T_i close to T_e (fig. 8.7, Section 8.2.3.2.3):

$$1) \quad T_{i,2} - T_{i,1} = 0$$

$$2) \quad T_{i,N} = T_e(a^* = a)$$

$$(8.20)$$

We thus obtain a tri-diagonal system of N linear equations for the ion temperatures $T_{i,j}$:

$$Y\vec{T}_i = -(\Delta a^*)^2\vec{Q} \quad \text{with}$$

$$Y_{11} = -Y_{12},\ Q_1 = 0 \text{ and}$$

$$Y_{NN} = 1,\ Q_N = -\frac{T_{i,N}}{\Delta a^{*2}}.$$

$$(8.21)$$

Multiplying eqn. 8.21 by the inverse of **Y** yields the desired solution for $\vec{T}_i$.

The functions T, P, and Q are defined on an equidistant grid, $\Delta a^* = a/(N-1)$, with the grid points for the 3 functions placed such that $P_1 = P(0)$ and $P_N = P(a)$. This grid definition does not violate the restriction $0 < a^* < a$ for eqn. 8.18, since P_1 and P_N do not appear in the diagonal elements of **Y**. The function D is computed on an auxiliary grid shifted by $\Delta a^*/2$: $D_{3/2} = D(\Delta a^*/2)$ and $D_{N-1/2} = D(a - \Delta a^*/2)$. Using N=41 grid points, the unknown $T_{i,j}$ are determined with the same resolution as the fitted TS T_e and n_e profiles ($\Delta a^* = \Delta\rho \cdot a = 1/41 \cdot a$, Section 4.2.1).

8.2.3.2.3 Estimation of the Ion Heat Diffusivity

Before attempting to solve the heat diffusion equation 8.16, we require an expression for the ion heat diffusivity, χ_i and must therefore decide on a model for the ion thermal transport. Using the neoclassical approach, we can write $\chi_i \sim \rho_{i\Theta}^2/\tau_{ii}$, where $\rho_{i\Theta}$ is the poloidal Larmor radius (equivalent to the step width of a random walk) and τ_{ii} the ion-ion collision time for momentum transfer (time between 2 steps). Since both $\rho_{i\Theta}$ and τ_{ii} are functions of T_i, the solution of eqn. 8.16 becomes non-linear. In this study we therefore assume a χ_i which is constant across the plasma radius, choosing a fixed value, χ_i^C according to the neoclassical model proposed by Chang and Hinton [10]. The model includes the effect of impurity particles for finite aspect ratio and is in reasonable agreement with experimental observations on ASDEX [60]. For the calculation of χ_i^C, we have chosen a reasonable set of parameters for a L-mode plasma in the banana-plateau transition regime at plasma mid-radius (see appendix B). This estimation yields:

$$\chi_i^C \approx 1.1 m^2/s \tag{8.22}$$

To verify that this approximation leads to reasonable and consistent T_i profiles, we check that on 40 equidistant flux surfaces (Δa^*=const.) between the magnetic axis and the LCFS, both of the following constraints are satisfied:

$$\begin{aligned} &1) \quad q_{oh} - q_{ei} \geq 0 \\ &2) \quad q_{ei} \geq 0 \end{aligned} \tag{8.23}$$

Constraint 1) fixes the upper limit on the collisional energy transfer from the electrons to the ions to be equal to or less than the ohmic power influx. It represents the simplest case in which the only losses from the electrons are due to equipartition. Constraint 2) fixes an upper limit on the diffusive electron heat flux. One possible representation of this model case would be a plasma with T_i=T_e everywhere across the plasma radius.

As already indicated at the beginning of this section, a neoclassical model of the ion heat diffusivity makes eqn. 8.16 non-linear and does not permit a direct solution via eqn. 8.21. In order to calculate a more accurate χ_i profile, this equation can, however, be applied iteratively. Assuming first a constant χ_i, eqn. 8.21 is used to compute a zero-order T_i profile. This is then used to calculate a zero-order χ_i profile. The iteration continues until the T_i profiles of 2 subsequent loops satisfy a given convergence criterion. The scheme is stable against variations of the initial χ parameter value and usually requires less than 20 cycles to establish T_i profiles converged to within $\sum_j \left\| T_{i,j}^{n+1}((j-1)\Delta a^*) - T_{i,j}^{n}((j-1)\Delta a^*) \right\| \leq 10^{-9} eV$.

Fig. 8.7 shows the resulting T_i profiles for a limited (#7706) and diverted SN-Ldischarge (#8430) for the case of fixed and iterated neoclassical thermal diffusivities. Only for discharge #7706 is there a noticeable difference between the T_i profiles, with a calculated central T_i of 680 eV for the transport model and 610 eV for the neoclassical model (cf. T_e=770eV). The neoclassical model also predicts that $q_{oh} \approx q_{ei}$ ($q_{oh} \approx 1.9$ kW/m^2) across the innermost flux surface for this discharge. Even considering additional ion loss mechanisms, diffusive losses dominate in the plasma centre and can only be compensated by the gain due to collisional energy transfer. Despite the uncertainties in the estimation of q_{ei}, the proximity of q_{ei} to q_{oh} indicates that our neoclassical model gives a lower boundary on the expected T_i profile.

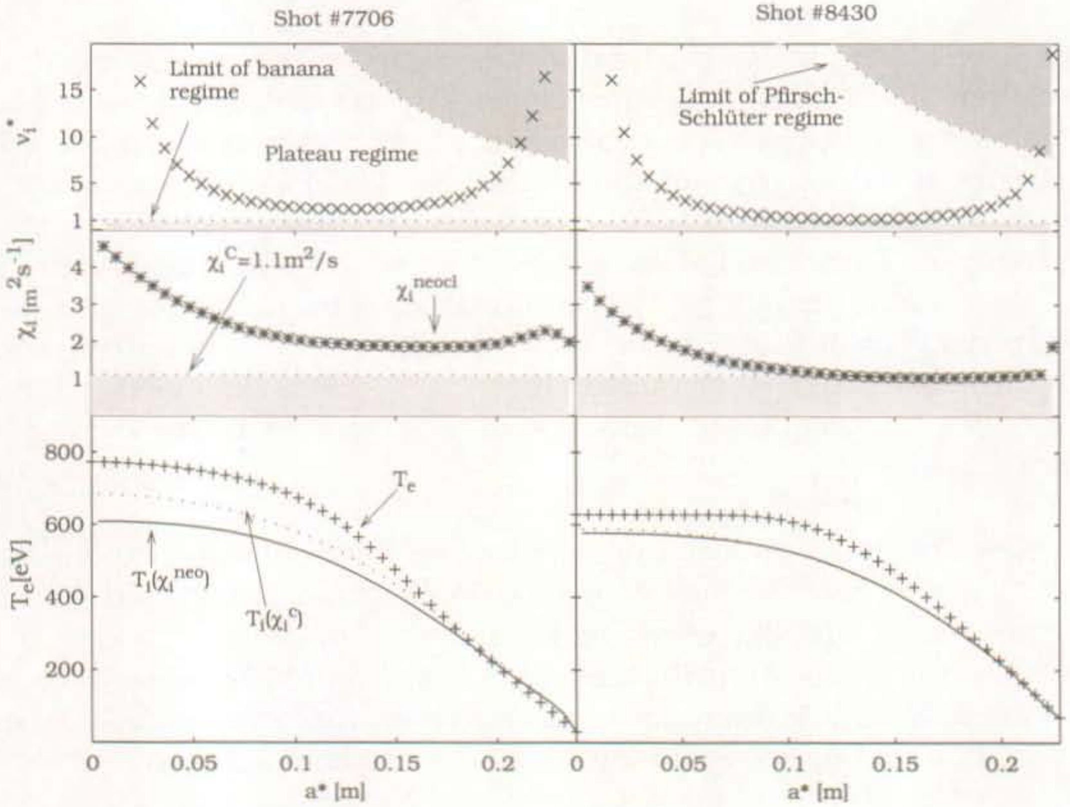

Figure 8.7: T_i profiles corresponding to a neoclassical calculation of χ_i, including a dependence on a^* (solid lines), and using a constant χ_i (dotted lines) for two discharges of the DIOP database (for plasma parameters see Table 8-2). The T_e profiles are represented by '+'-symbols. Also shown are the corresponding values for χ_i (''-symbols) and ν_i^* ('x'-symbols) according to the neoclassical model*

For discharge #8430, there do not appear differences in the T_i profiles computed from the two different models. We also note that the $\chi_i^{neo} \cong \chi_i^C$ across a large fraction of the plasma radius. The neoclassical calculation further indicates that the ions in both discharges are in the plateau regime across most of the plasma, with the effective collisionality, ν^* approaching even the banana regime value near the plasma mid-radius for discharge #8430.

The calculated T_i profiles in fig. 8.7 give a good impression of the differences amongst the discharges comprising the DIOP database. The neoclassical T_i profiles for limited discharges are typically 10% below those from the transport model and 20% below the averaged T_e profiles. Since the bulk ion density in these types of discharges is around 70% of the electron density (in accordance with the estimation described in section 8.2.3.2.4), the ion contribution to p_t is typically 40%. A discrepancy of 10% in the T_i values for the 2 different models therefore leads to a discrepancy of 5% in the p_t profiles and will not significantly influence the results of the "*kinetic*" LIUQE reconstructions to be described later. A similar conclusion is even more appropriate for the SNL-discharges, since the T_i profiles from both models are almost identical.

Comparison of the power transfer from the electrons to the ions with the total ohmic input power shows the importance of the ion energy transport and the associated energy losses. The total ohmic power varies between 300kW and 860 kW for the discharges of the DIOP database. Fig. 8.8 shows the ratio P_{ei}/P_{oh} as a function of $<n_e>_L$ for 3 values of the radial coordinate: a*=0.5a, a*=0.75a, a*=a. For this set of discharges at least, there is no clear dependence of P_{ei}/P_{oh} on a*, although p_{ei} increases with n_e (eqn. 8.13). For a*=0.5a, the ratio is generally > 40% increasing at larger radii (a*=0.75a) and decreasing towards the plasma edge. At medium to high $<n_e>_L$, this is explained by the model T_i profiles being equal or even exceeding T_e profiles in the outer plasma regions.

With regard to the T_i profiles from the transport model (with fixed χ_i^C), constraint (1) of eqn. 8.23 is roughly satisfied. For T_i values everywhere 10% lower than our predicted profile, we would require $\chi_i^C \cong 2m^2/s$ (cf. $\chi_i^C \cong 1.1m^2/s$ used to generate the profiles). In this case, ion losses would be close to or would even exceed the ohmic input power at a given radius. Since the electrons are also subject to energy losses (Bremsstrahlung and line radiation near the edge can account for 20-25% of the ohmic power in limited discharges [36]), a value of $\chi_i^C \cong 2m^2/s$ would not appear to be compatible with ion-electron energy transfer. This gives us confidence that the T_i profiles generated from the transport model are reasonable approximations.

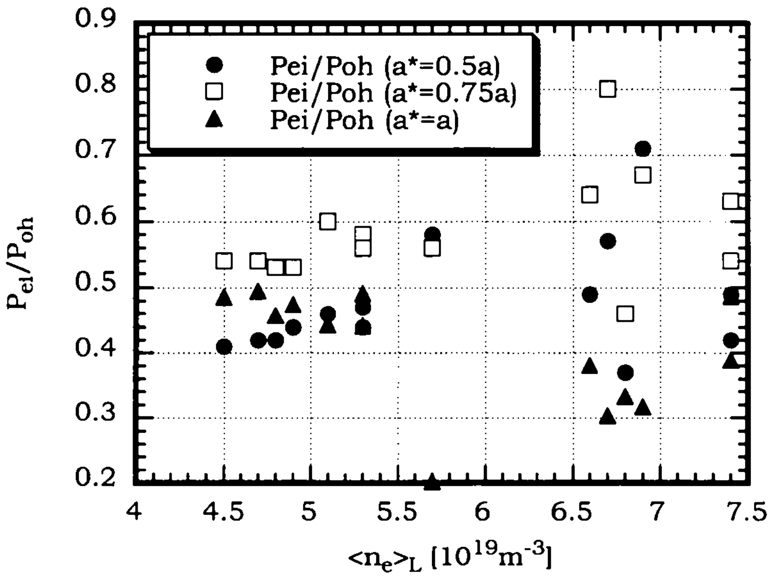

Figure 8.8: *P_{ei}/P_{oh} at 3 different plasma radii calculated with the averaged T_i, T_e, n_i and n_e profiles using the simplified ion heat diffusion equation.*

8.2.3.2.4 Determination of the Ion Concentrations

Our transport model assumes that $n_i \sim n_e$ everywhere. The same simplification is applied to the impurity ion concentrations, $c_z = n_Z/n_e$, where the ions are assumed to be fully ionized. This implies a spatially constant Z_{eff}. When the impurity concentrations are known, c_i and Z_{eff} may be obtained from:

$$c_i = 1 - \sum_{Z \neq 1} c_Z Z$$

$$Z_{eff} = 1 + \sum_{Z \neq 1} c_Z Z(Z-1) \tag{8.24}$$

Relative impurity concentrations of B, C, N and O from USX-spectroscopic measurements are available for all of the DIOP-database discharges (Table 8-2). Since the USX data are subject to uncertainties of about a factor of 2 [71], independent measurements of Z_{eff} are required to obtain a reasonable estimate of Z_{eff} and c_i. Assuming an equal uncertainty for all measured concentrations, values of Z_{eff} calculated from X-ray tomography and IR-Bremsstrahlung measurements are used to adjust the individual ion concentrations:

$$c_i = 1 - \frac{Z_{eff}^{XTOMO,\,IR} - 1}{Z_{eff}^{USX} - 1} \sum_{Z \neq 1} c_Z^{USX} Z \tag{8.25}$$

8.3 Results from Equilibrium Reconstructions with Kinetic Constraints

We show in this section that the kinetic equilibrium reconstruction is sensitive to constraints imposed by the pressure profile and that, to within reasonable accuracy of 20%, parameters such as W_t are consistent with these constraints. The availability of different sets of base functions for the profile fits, allows the interpolation to be adapted to minor specific features on the p_t profiles. In section 8.1.2 (eqn. 8.6), two options for the possible choice of base functions were identified. They lead to different p_t profile fit characteristics near the plasma edge.

Option (1) leads to a better description of pressure profiles in L-mode discharges

Option (2) is more suitable for the fitting of H-mode profiles.

It is also important to quantify the influence of the choice of model used to generate the total pressure profiles (Section 8.2.3) on the constrained LIUQE output.

8.3.1 Influence of the Selection of Base Functions

8.3.1.1 Role of the Pressure Profiles

Fig. 8.9 clearly shows the large discrepancy (note the difference in the χ_{pr}^2 values) between the p_t data and p_t profiles used by the magnetic reconstruction (see also fig. 8.4). Unrealistic approximations lead to the contradictions between W_t and W_e mentioned in section 8.1.1. The edge pressure is usually underestimated, $p_t(\rho=1)<p_e$, whilst the central value tends to be overestimated, $p_t(\rho=0)>2\cdot p_e$. Steep edge gradients in p_t cannot be accurately described by either of the two "kinetic" LIUQE options, although the base functions of option (2) produce a globally better fit to the p_t profiles. Both options use the model where p_t is proportional to p_e, $p_t=1.4\cdot p_e$, and combinations of base functions forcing $p_t=0$ on the LCFS. This constraint is clearly too restrictive for H-mode pressure profiles, but the L-mode profiles are reasonably well fitted.

To obtain a more general conclusion with regard to the fit quality, the values of χ_{pr}^2 for all the pressure profiles in the DIOP database have been averaged (Table 8-3). From this point of view, we conclude that the p_t fits generated according to option (1) are better suited for L-mode plasmas whilst option (2) should be applied for H-mode profiles.

Table 8-3: χ_{pr}^2 values of p_t fits

Type of discharge	Option (1)	Option (2)
ELM-free H-mode	0.91	0.63
Limiter L-mode	0.58	0.81
SNL L-mode	0.77	1.26

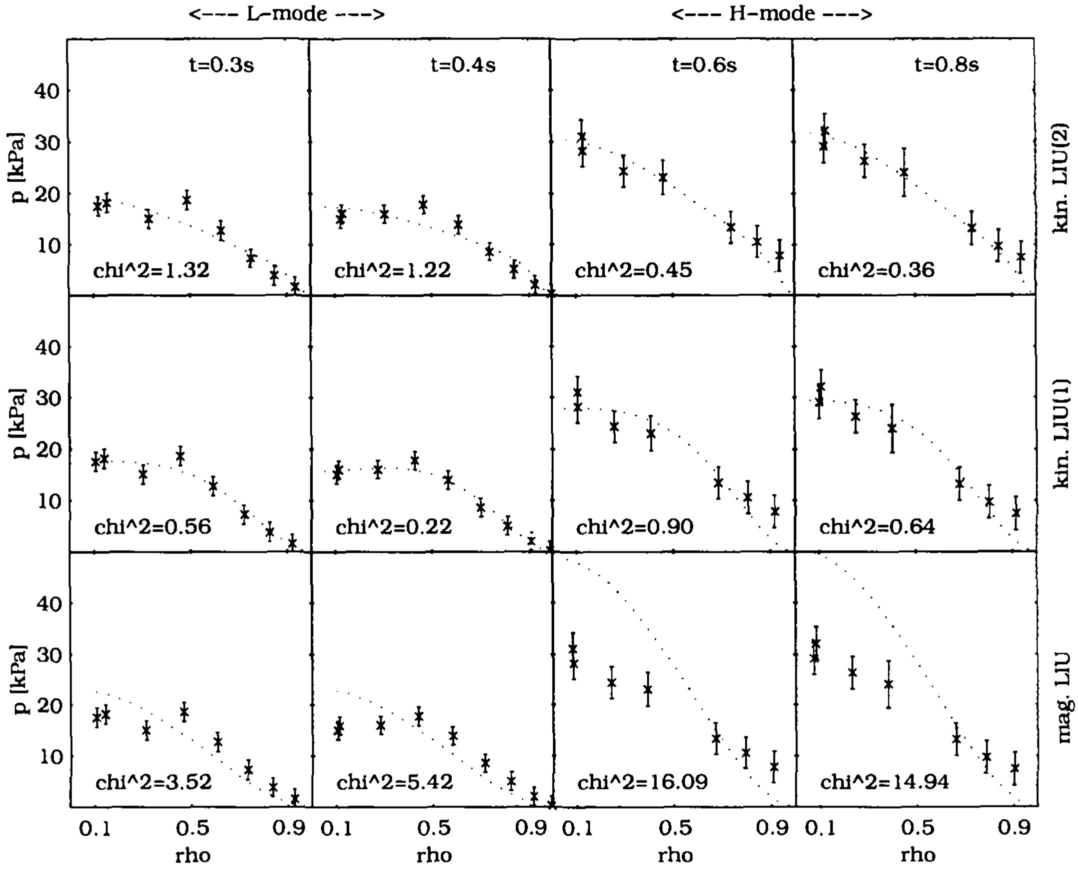

Figure 8.9: TCV discharge #7332: p_t profile assumptions from the "magnetic" LIUQE reconstruction together with the p_t fits from the two options of the "kinetic" LIUQE reconstruction.'x' symbols represent the modelled p_t profiles ($p_t = 1.4 \cdot p_e$), dotted lines the p_t profile fits from LIUQE reconstructions. The 2 columns on the left represent time slices in the L-mode phase of the discharge, the 2 columns on the right the H-mode phase.

8.3.1.2 Effect on W_t

The disagreement between *"magnetic"* LIUQE and experimental data becomes particularly evident when the derived quantity W_t for the total energy is lower than the W_e values obtained from Thomson scattering and applying only to the electron component. If a constrained p_t profile is to be compatible with the magnetic measurements, a *"kinetic"* LIUQE should converge to a given W_t according to $W_t = 3/2 \cdot \int p_t dV \approx M \cdot 3/2 \cdot \int p_e dV$. The reproducibility of the proportionality factor, M=1.4 is therefore an indication of the self-consistency of the solution. Fig. 8.10 shows that self-consistency is obtained to within 20% for both *"kinetic"* LIUQE options. Apart from intrinsic inaccuracies due to the model assumptions, systematic deviations of the ratio W_t/W_e from the proportionality factor can be explained by the inaccurate interpolation of p_t profiles in H-mode near the plasma edge (compare also fig. 8.2). The fluctuations in the ratio are also partly due to the fact that the p_t profiles are interpolated and integrated by LIUQE and the p_e profiles by separate analysis routines, each of which use different sets of base functions. Since the absolute value of the calculated kinetic W_t depends on M, a *"kinetic"* LIUQE reconstruction cannot remove the absolute uncertainties on W_t. Using *"kinetic"* LIUQE reconstructions would certainly, however, reduce the scatter in quantities as β_{pol} and β_{tor}.

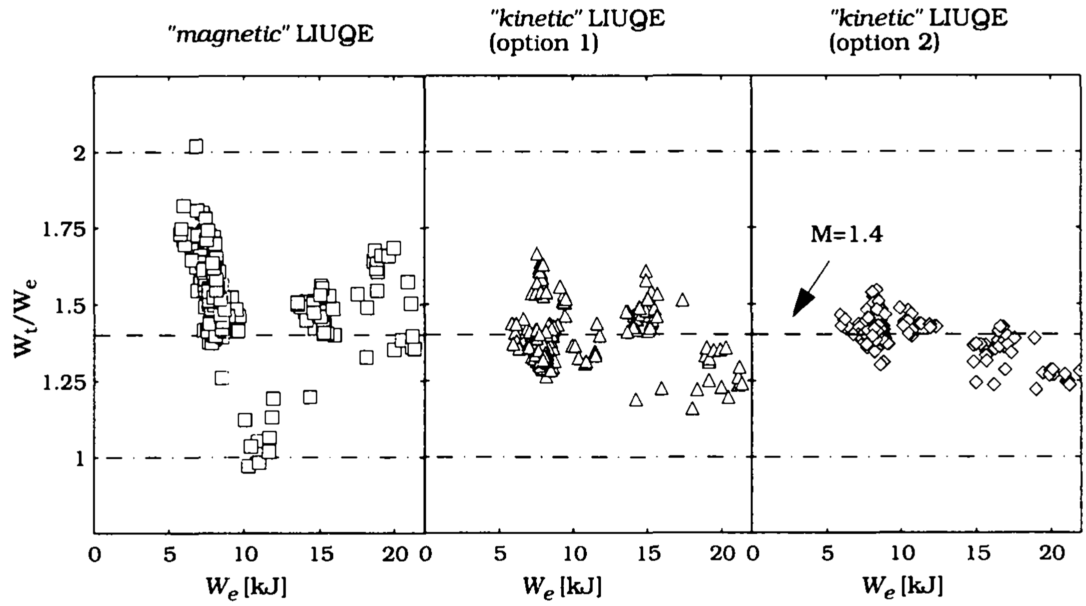

Figure 8.10: Ratio W_t/W_e for all discharges of the DIOP database

8.3.1.3 Effect on q_0

For each shot in the database, sawtooth oscillations are observed in the X-ray flux. In this case we expect $q_0 \leq 1$ [25]. In most L-mode cases, the equilibrium reconstruction produces a central q-value which is in agreement with this expectation. For discharges which are characterized by a long (≥0.5 s) ELM-free H-mode phase (e.g. discharges #7332 and #7412), the L-H transitions are accompanied by a reduction in the sawtooth frequency and an increase in q_0 within 100ms, although both parameters are not necessarily coupled. This rise time is shorter than typical current diffusion times on TCV (≈500ms for T_e=500eV and Z_{eff}=2) and is due to an apparent change in the reconstructed current density profile after the L-H transition. This apparent change on the q_0 traces from *"magnetic"* LIUQE is over-pronounced (fig. 8.11), since, in discharge #7332 for example, *"magnetic"* LIUQE gives $q_0 > 1$ during a large fraction of the H-mode phase and this in spite of clear sawtooth oscillations. The computed q_0 of discharge #7412 shows an additional rise towards the end of the discharge, coincident with the movement of the outer divertor strike zone from the bottom of the vessel to the inner wall.

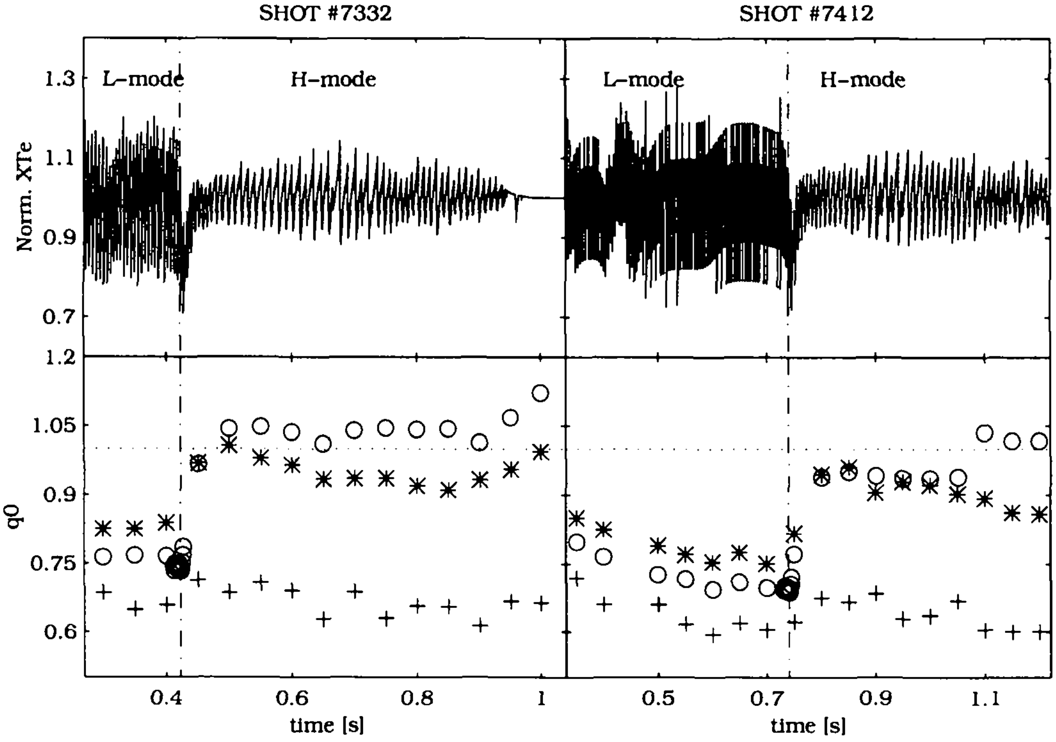

Figure 8.11: q_0 traces for three types of reconstruction. 'o' symbols represent the magnetic LIUQE, '' symbols kinetic LIUQE (option (1)), '+' symbols kinetic LIUQE (option (2)) (discharges #7332 and #7412).*

The corresponding traces from the *"kinetic"* LIUQE, option (1) show a reduction in the q_0 increase following the L-H transition, with $q_0<1$ during the H-mode phase. The computed values using option (2) fluctuate around a low value of $q_0 \approx 0.7$ and do not show any significant change at the transition. Since the input p_t profiles are identical, the discrepancies between the two kinetic q_0 traces point to the fact that the change from a magnetic to a kinetic reconstruction has a less significant effect on the calculated j_φ profile (fig. 8.12, discharge #7332) than modifications of the base functions which interpolate the p_t profiles. A more general analysis of the uncertainties in the magnetic and kinetic measurements is required if we are to determine whether or not the apparent change in j_0 is real or an artefact (section 8.3.1.4), since it cannot be clearly confirmed by changes in the temporal evolution of measured $T_e^{3/2}$ profiles.

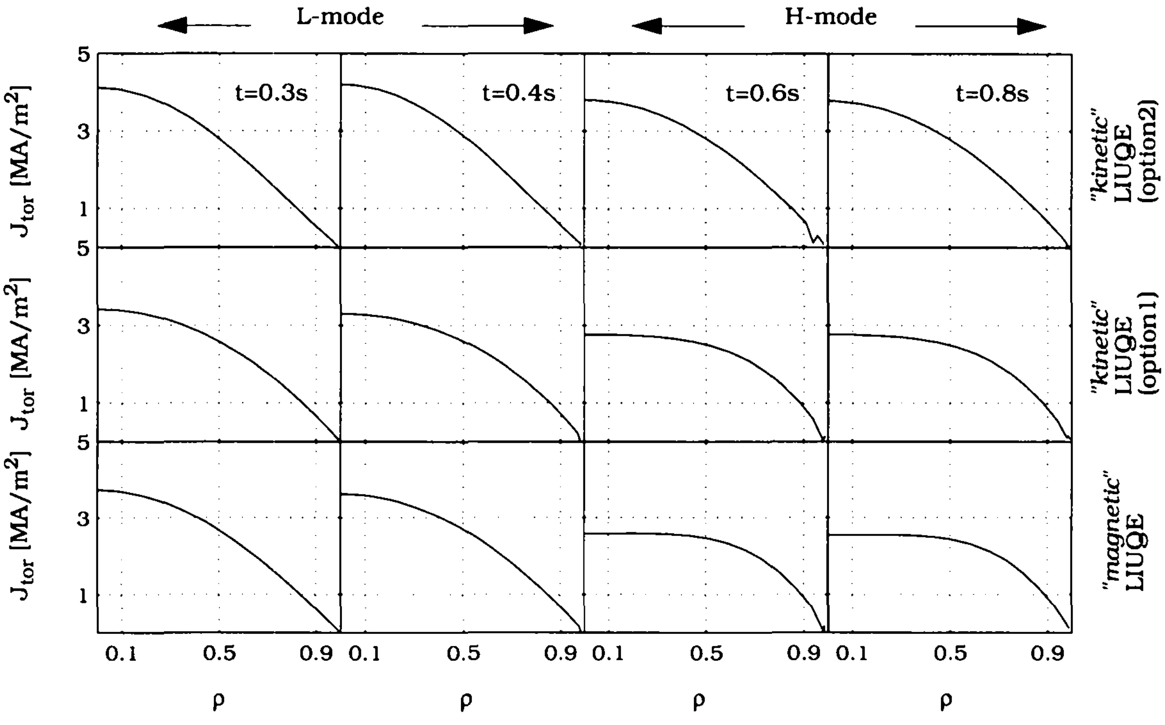

Figure 8.12: Current density profiles from the LIUQE reconstructions. The two columns on the left represent time slices in the L-mode phase of the discharge, the two on the right, the H-mode phase (discharge #7332). See also fig. 8.9 showing the corresponding p_t profiles for the same time slices.

8.3.1.4 *Effect on Flux Surface Geometry*

The differences in q_0 and the current density profile obtained from the two *"kinetic"* LIUQE options raises the question of whether or not the change is restricted to the two example discharges chosen, or whether it can be generalized to all discharges. Changes in the j_φ profile and hence the flux surface geometry lead to changes in the internal inductance, l_i, an indicator of the j_φ profile peaking. When the *"magnetic"* LIUQE reconstruction is used as a reference for l_i, the ratios with the corresponding kinetic reconstruction parameters (l_i^{kin1}/l_i^{mag}, l_i^{kin2}/l_i^{mag}) should thus reflect these changes.

The left hand column of fig. 8.13 clearly shows that option (1) does not significantly change l_i, with the ratio l_i^{kin1}/l_i^{mag} fluctuating by about 10% around unity. In contrast, the ratio l_i^{kin2}/l_i^{mag} is without exception larger than 1. This implies that in general, the j_φ profile from a *"kinetic"* LIUQE reconstruction using option (2) is more strongly peaked than the j_φ profile of a *"magnetic"* LIUQE reconstruction. This systematic change in the evaluated flux surface geometry is also noticeable in the calculated plasma electron energy content (right hand column of fig. 8.13).

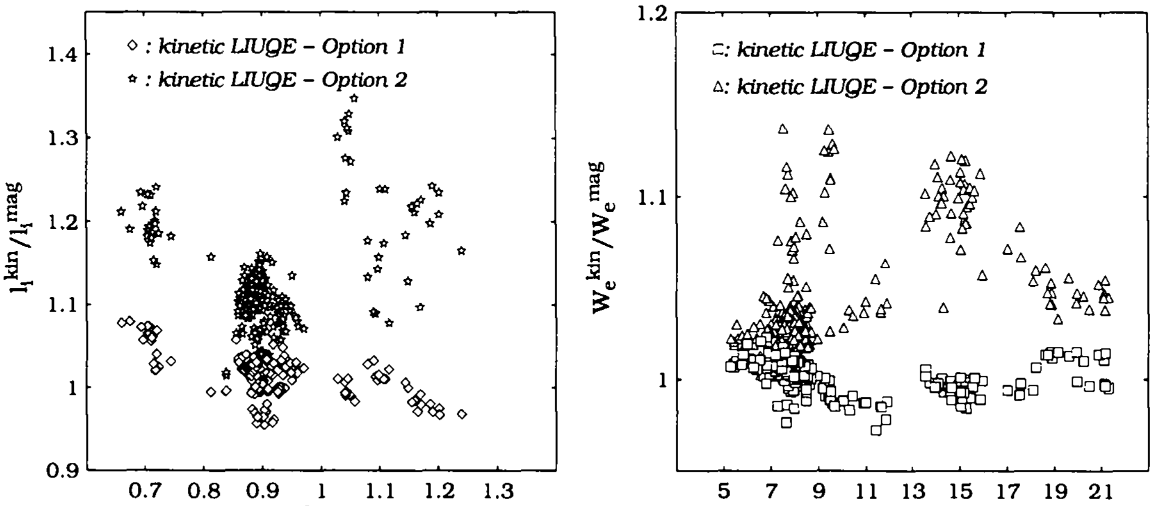

Figure 8.13: Internal inductance, l_i and W_e for two kinetic LIUQE reconstructions (options (1) and (2)), normalized to the corresponding parameters of the magnetic LIUQE reconstruction

The differences discussed above are of particular interest in the case of the two ELM-free, H-mode discharges. In section 8.3.1.1 we have shown that only in this kind of discharge does the 2nd set of base functions (option (2)) produce more accurate p_t fits. It was not clear at that point, however, whether or not this combination leads to a better equilibrium reconstruction.

Comparison of the data in Table 8-4 from the *"magnetic"* and *"kinetic"* LIUQE (option (1)) reconstructions shows that the latter does not significantly influence the quality of the reconstruction.

For the *"kinetic"* LIUQE reconstruction (option (2)) the gain in accuracy (smaller χ^2_{pr}) of the p_t profile fits is offset by the increased inaccuracy of the fitted poloidal field measurements, $\chi^2_{bpol,\,LIU(2)}$. Since $\chi^2_{LIU(2)}$ is more than 10% greater than χ^2_{MAG}, option (2) does not yield an overall improvement in the reconstruction. Although these conclusions are based only on a statistical average for two discharges, the same trends are observed for each time step of the discharge.

Table 8-4: χ^2-Evaluation of Equilibrium Reconstructions

	Discharge #7332			Discharge #7412		
	magnetic LIUQE	kinetic LIUQE (option 1)	kinetic LIUQE (option 2)	magnetic LIUQE	kinetic LIUQE (option 1)	kinetic LIUQE (option 2)
χ^2	0.25	0.31	0.45	0.52	0.55	0.67
χ^2_{pr}		0.81	0.44		0.82	0.34
χ^2_{bpol}	0.20	0.24	0.69	0.36	0.35	0.81
χ^2_{rfl}	0.72	0.72	0.85	1.44	1.44	1.56
χ^2_{ic}	0.07	0.06	0.08	0.21	0.21	0.21
χ^2_{iv}	<0.01	<0.01	<0.01	<0.01	<0.01	<0.01

Table 8-4: χ^2 analysis of ELM-free phases of H-mode discharges. χ^2_{pr} results from the p_t profiles, χ^2_{bpol} from the poloidal field, χ^2_{rfl} from the relative poloidal flux, χ^2_{ic} from poloidal coil current and χ^2_{iv} from vessel current measurements.

Fig. 8.14 shows how the different types of reconstruction influence the flux surface geometry. Using option (1), there are only insignificant changes in shape parameters and a slight increase in q_a compared with the *"magnetic"* LIUQE reconstructions. Using option (2), however, we observe variations in shape parameters (κ, δ, q) of the order of 5%. Changes of this magnitude in κ are already sufficient to affect the analysis of the growth rate of vertical instabilities [21]. An equilibrium solution which is optimized for p_t fits thus leads to a different flux surface geometry.

In order to decide which option of the *"kinetic"* LIUQE should be employed in the equilibrium reconstruction, we must consider the magnetic measurements in preference to the total pressure profiles, for which only the electron contribution is measured. Based on a χ^2 criterion alone, option (1) would appear more satisfactory. We recall, however, that option (2) represents an interesting alternative for the case of peaked pressure profiles. Since the reconstructed j_φ profiles and the resulting flux surface geometries lead in this case to a more inaccurate fit of the magnetic measurements, a modified set of base functions for the description of the TT' profiles (eqn. 8.3) might yield better results.

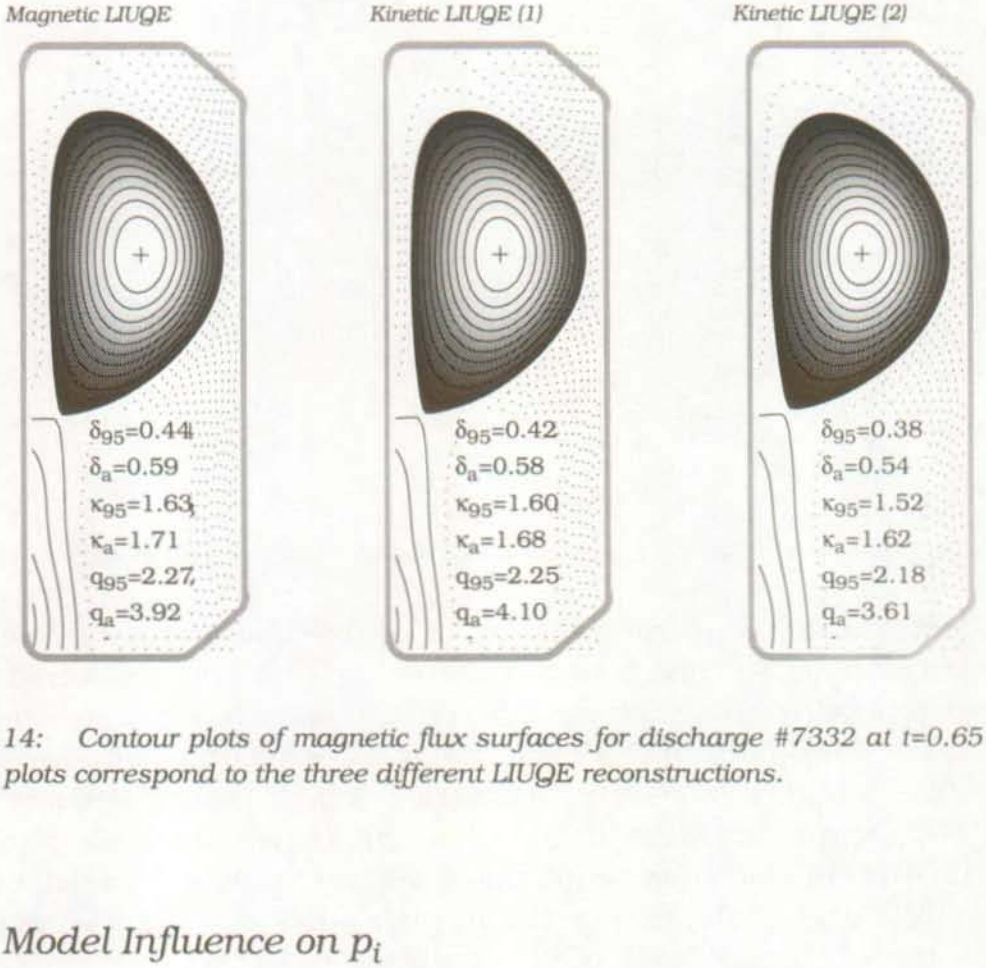

Figure 8.14: Contour plots of magnetic flux surfaces for discharge #7332 at t=0.65 s. The 3 different plots correspond to the three different LIUQE reconstructions.

8.3.2 Model Influence on p_i

A possible method by which the ion pressure profile may be obtained from the measured electron data and a simple transport model has been described in Chapter 8.2.3 (equations 8.9. and 8.10). The transport model imposes a certain number of conditions, of which the requirement for time independent I_p and $\langle n_e \rangle_L$ is satisfied only in the case of L-mode discharges in the DIOP database. Using these discharges we can examine the relative influence on the reconstruction of a change in the transport model compared with a modification of the base function set. To this end, a χ^2 evaluation similar to that presented in Table 8-4 has been performed for the whole set of L-mode discharges. In the case of "*kinetic*" LIUQE, option (2), no improvement in the χ^2 values of any magnetic or pressure profile was obtained, regardless of the transport model. We concentrate, therefore, on studying the effect of transport on the reconstruction resulting from "*kinetic*" LIUQE, option (1).

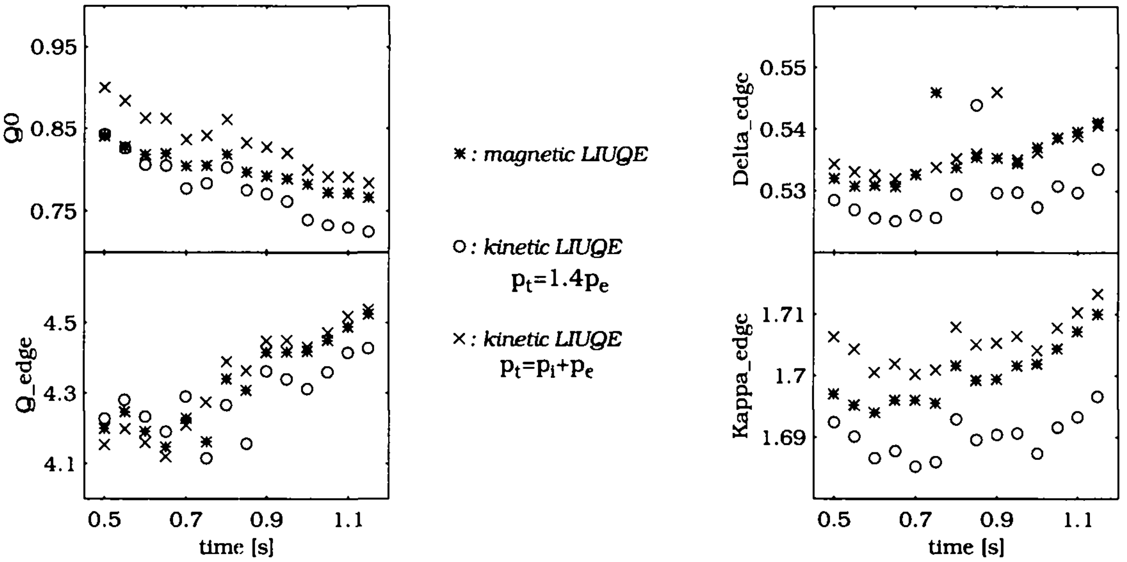

Figure 8.15: Discharge #8430: q_0, q_a, κ_a and δ_a traces for selected LIUQE reconstructions

Fig. 8.15 shows the temporal evolution of selected plasma parameters from discharge #8430 for the magnetic reconstruction and from the kinetic reconstructions corresponding to the two different transport models. For those plasma parameters depending on the magnetic measurements the influence of the model choice is hardly noticeable. In contrast, kinetic parameters such as the ratio W_t/W_e clearly depend on the model assumptions used in the reconstruction. In the case of discharge #8430 (fig. 8.16), the transport model leads to a significantly higher evaluation of the p_t profile than the simple model and therefore yields a higher value of W_t. As shown in fig. 8.17, this is generally true for all L-mode discharges in the database. The ratio W_t/W_e is situated in the approximate range of 1.6-1.9. We recall that the constant factor in the simple model is M=1.4.

The transport model implies an increased ion contribution of between 10% and 25%. Since, for underlying plasma ion concentrations, we have found values in the range from 65% to 90%, the increase is mainly due to higher ion temperatures. The T_i profiles require much higher T_i values than those estimated from the assumption $T_i \approx 0.5T_e$ used to obtain the model factor M=1.4. Typical examples of T_i profiles for two types of L-mode discharges have already been presented in fig. 8.7. The T_i profiles obtained from the transport model are in general about 10% below the T_e profiles in the plasma centre and coincide near the plasma edge. This observation is in fairly good agreement with recent results published by Simmet for ASDEX [60], suggesting again that the T_i profiles obtained from the transport model are reasonable.

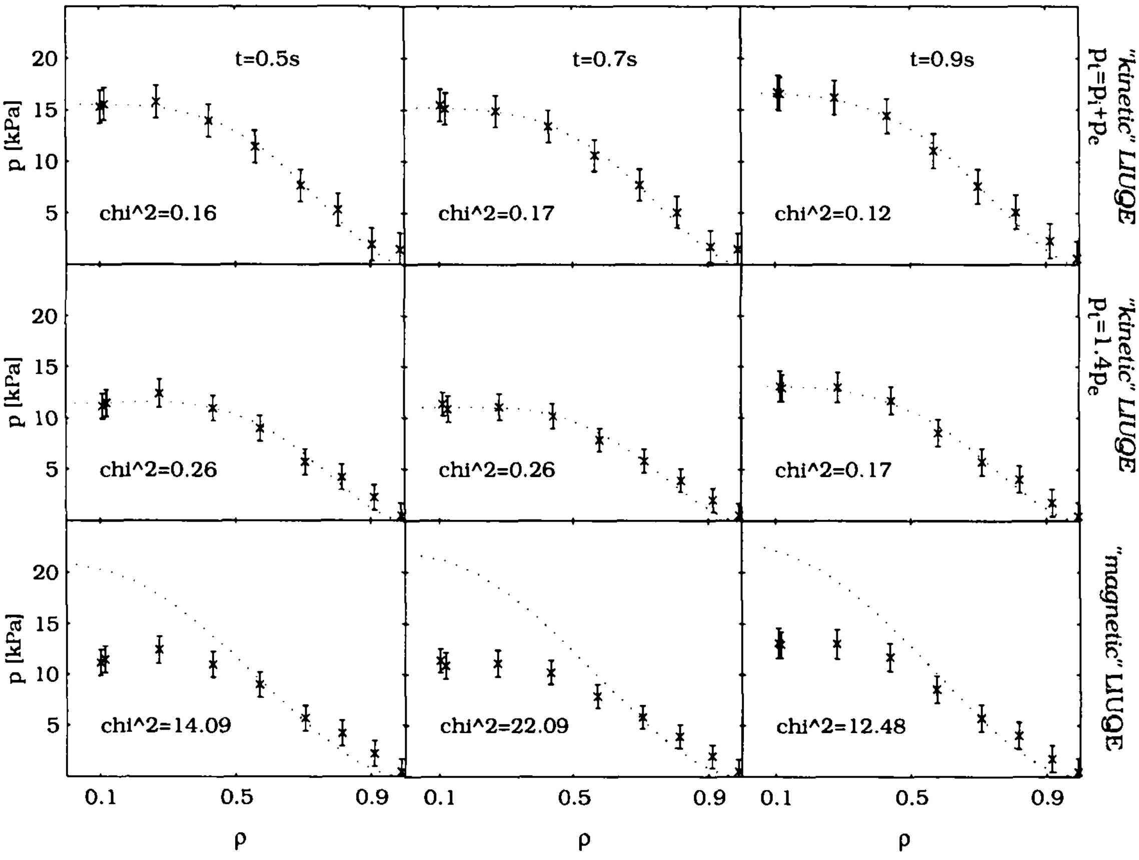

Figure 8.16: p_t profile assumptions from the "magnetic" LIUQE reconstruction compared with the p_t fits from the two transport models applied to the "kinetic" LIUQE reconstruction. 'x' symbols represent the modeled p_t profiles, dotted lines the p_t profile fits from the LIUQE reconstructions. Each column represents a different time slice in the L-mode phase of discharge #8430.

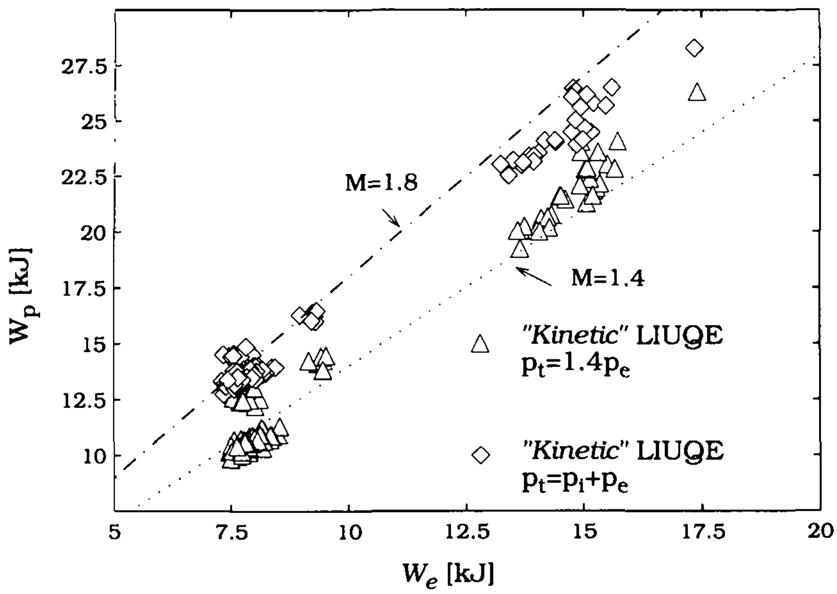

Figure 8.17: Ratio between W_t and W_e for all L-mode discharges in the DIOP database. Only data obtained from the transport model (p_t=p_i+p_e) and the simple model (M=1.4·p_e) are shown.

8.4 Conclusions

Our studies using three different versions of the TCV equilibrium reconstruction code, LIUQE have shown that kinetic constraints are reasonably compatible with the magnetic measurements. A solution for the equilibrium can be obtained by providing an appropriate weight to the total pressure profile constraint with respect to magnetic measurements, without the need to modify the usual constraint on the accuracy of the equilibrium solution ($\chi^2 \leq 4$). "*Kinetic*" LIUQE reconstructions using p_t profiles that are simply scaled from measured p_e profiles using a constant factor, M=1.4 remove fundamental inconsistencies in the calculated plasma parameters q_0 or W_t. Depending on the edge profile gradients, for the commonly used polynomial base functions describing the p_t profiles, a clear difference in the quality of the p_t fits is observed. The conventional set of base functions is well suited to L-mode profiles, but cannot describe the steep edge gradients in p_t profiles during H-mode. The "*kinetic*" LIUQE reconstruction is self-consistent in the sense that the output value of the ratio W_t/W_e after a reconstruction lies within 20% of the input for M=1.4.

Using the same input constraint, a different set of base functions for the p_t fits has been integrated into the *"kinetic"* LIUQE code, with one polynomial base function being replaced by an exponential function with a strong peak near the plasma edge. The quality of p_t profile fits in H-mode indeed increases, but at the cost of a simultaneous degradation in the L-mode fit quality. The qualitative improvement of the H-mode p_t profile fits is, however, generally accompanied by a low q_0 and a significant increase in the χ^2 (using all the measured data) of about 20-30%, due to the strong increase in χ^2_{bpol} for the poloidal magnetic field measurements. This combination of base functions leads to noticeable changes in calculated j_φ profiles. This discrepancy indicates a problem in the modelling of the ion contribution - the "real" p_t profile may be different from that we are trying to impose. The clear influence of the choice of base functions on the equilibrium solution should stimulate the search for a more suitable set when more accurate T_i measurements or T_i profiles become available on TCV.

"Kinetic" LIUQE reconstructions using an ion heat transport model for the evaluation of the T_i contribution to the p_i profiles (section 8.3.2) have been performed in the particular case of L-mode discharges with $<n_e>_L \geq 4.0 \cdot 10^{19} m^{-3}$ and moderate $Z_{eff} \leq 2.7$. The computed T_i profiles are in agreement with the requirements of electron-ion power balance and together with the estimated ion density contributions, lead to estimates of W_t which exceed those obtained from the simpler model. The use of averaged T_i profiles is, however, restricted to steady-state discharge conditions, in which sawtooth effects on the measured T_e profiles are simultaneously reduced. Since the T_e and n_e profiles are obtained only from TS measurements with a time resolution of 50ms (≈20ms in 97), the necessary averaging remains a major obstacle in the path of a time-resolved power balance.

At this preliminary stage, estimates of W_t depend on assumptions which cannot be verified experimentally. Values of W_t or related parameters such as β_{pol} or β_{tor} obtained from any kinetic equilibrium solution should be used with care in connection with scaling laws. An extension of the existing DIOP database may allow a relationship between Z_{eff} and $<n_e>_L$ and the ratio W_i/W_e to be established. A constant model factor, M depending on Z_{eff} and $<n_e>_L$ would appear to be an intermediate solution in the problem of modelling the kinetic pressure profiles.

9 Final Conclusions

9.1 Experimental Arrangement

A considerable fraction of the research effort comprising this thesis has been devoted to the implementation of the TCV tokamak vertical Thomson scattering (TS) system. Installation of the diagnostic has been accomplished in two separate phases, finally yielding a configuration permitting routine measurements of T_e and n_e profiles at a sampling frequency of 20 Hz and with a spatial resolution better than 40mm for all possible plasma configurations. The present system can resolve electron temperatures and densities as low as 50eV and $5 \cdot 10^{18} m^{-3}$ respectively.

The initial system constituted a single Nd:YAG laser and was limited to 10 observation points along a vertical chord (R=0.9m). This limitation was due simply to the number of available filter polychromators which, aside from minor modifications to the signal amplifying electronics, had been recovered from the TS system installed on the TCA tokamak. Using three spectral channels, the upper limit for T_e measurements was approximately 2.5keV and was thus sufficient for ohmic discharges. For most effective use of the limited number of observation volumes, an arrangement was chosen allowing good coverage of approximately half of the poloidal plasma cross-section for plasmas in the upper half of the highly elongated TCV vacuum vessel.

Whilst the first version of the diagnostic operated successfully during a period encompassing some 4000 TCV discharges, improvements in machine performance, notably in the form of increased plasma elongation and the recent injection of the first ECRH power, mean that satisfactory TS measurements are only possible with the upgraded system. The extended 25 observation volume diagnostic with a new polychromator design in which 4 spectral channels are available, now permits measurements to be made in any plasma and for electron temperatures up to 5keV.

Further system upgrades, planned but beyond the timescale of this thesis, will address, in the first instance, the addition of further three lasers, the combination of which will permit flexible trigger sequences for measurements with sub-millisecond time resolution. The increased effective laser pulse energy in the case of synchronized triggering will also be useful in certain operation regimes (e.g. low density ECR heated discharges). A second proposal, currently under study, would allow for a second simultaneous vertical observation chord shifted to smaller major radius (R=0.75m). This new chord would provide the opportunity to make TS measurements of electron temperature and density in the cold, high-density plasmas characteristic of the divertor region in SNL discharges.

9.2 Data Analysis and Results

Due to the variety of equilibria possible on TCV, an algorithm based on cubic B-splines has been developed with which TS profiles can be fitted in the normalized poloidal flux coordinate system used by many other TCV diagnostics. Free from any preliminary assumptions regarding the profile shape, the algorithm requires little or no user intervention and is sufficiently fast that profile fits can be available after each discharge.

An interesting result arising from the systematic application of the fitting algorithm, has been the observation that the phenomenon of profile consistency remains valid in highly shaped limited discharges. Scaling expressions for the peaking factors of T_e and n_e demonstrate that the profile shapes are mainly influenced by the edge safety factor and only weakly by shape parameters (eqns. 6.5 and 6.6).

A thorough analysis of T_e profiles has been an essential component leading to an understanding of the relationship between electron energy confinement and plasma shape in L-mode limited discharges. The latter formed part of a confinement study in which plasma elongation and triangularity were systematically varied and in which electron energy confinement was found to increase slightly with elongation but to decrease markedly with increasing (positive) triangularity. A non-linear dependence of the ohmic heat flux on the T_e gradient measured in a restricted region inside the last closed flux surface but near the plasma edge, is a clear sign of heat flux degradation leading to a reduction in electron energy confinement. An increase in the effective ion charge is also observed as confinement degrades. This behaviour also indicates changes in ion transport properties, since neoclassical theory of ion transport predicts a linear increase of the ion heat diffusivity with the effective ion charge. Unfortunately, experimental data are insufficient for such speculation to be confirmed. The observed heat flux degradation and the influence of flux surface geometry on the electron temperature gradients are sufficient to explain the dependence of the electron energy confinement on plasma shape without the need to assume a direct effect of the shape on transport coefficients.

Clear inconsistencies between the measured TS electron pressure profiles and the total plasma pressure profiles computed from the TCV magnetic equilibrium reconstruction code, LIUQE, stimulated an investigation of the extent to which kinetic pressure profiles as code input could be used to constrain the reconstruction. Since measurements of ion temperature and density profiles are not yet available on TCV, two different models have been employed to compute the ion contribution to the total pressure profile on the basis of measured electron pressure profiles. The first imposes a linear scaling (M=1.4) between the electron and total pressure profiles and can be used, bearing in mind the simplicity of the model, for all discharge types. In contrast, the second, more elaborate model derives the ion temperature profile from a stationary ion power balance equation based on neoclassical transport model and may thus only be applied to steady-state conditions.

In both cases, "kinetic" reconstructions ("magnetic" reconstructions plus the additional constraints) yield total pressure profiles in agreement with the model assumptions and remove the inconsistency in the computed plasma energy (without the kinetic constraints, the total energy obtained from a reconstruction based solely on magnetic measurements can, in some cases, be smaller than the measured electron energy). Since the value of the computed plasma energy is strongly coupled to the chosen model, absolute estimates remain rather difficult. In predicting ion contributions to the total energy of up to 80% of the electron contribution, the transport model would seem, however, to be more realistic than the simple scaling model.

The quality of the pressure profile fits employed by LIUQE for interpolation of the discrete set of pressure profile data and, of course, for computation of the total plasma energy, depends strongly on the edge pressure profile gradient. Two different sets of interpolating base functions have therefore been tested for the case of the simple scaling model. The first corresponds to the familiar set and is appropriate for smooth edge pressure gradients (e.g. in L-mode discharges), whilst the second is better adapted to the steep gradients observed, for example, in H-mode discharges.

Qualitative improvements in H-mode total pressure profile fits are, however, accompanied by a significant decrease in the overall quality of the equilibrium reconstruction, and by inconsistencies in the calculated value of the central safety factor as a consequence of changes in the computed current density profiles. This effect is probably due to a problem in the model for the ion contribution - "real" total pressure profiles may be different from those being imposed. The clear dependence of the equilibrium solution on the chosen set of base functions should encourage the search for a more suitable set when measured ion temperature profiles become available on TCV.

References

[1] M. Anton et al, Plasma Phys. Contr. Fusion **38** (1996), 1849

[2] V. Arunasalam, Nuclear Fusion, Vol. **30** (1988), 2111

[3] R. Behn et al., Physical Review Letters **62** (1989), 2833

[4] P. R. Bevington, "Data Reduction and Error Analysis for the Physical Sciences", McGraw-Hill (1992)

[5] M. Born, Diplomarbeit, Düsseldorf, 1991

[6] A. Blondel, Travail de Diplome en Physique, EPFL (CRPP), 1993

[7] T.N. Carlstrom et al., Rev. Sci. Instrum. **63** (10), 4901

[8] P.J. McCarthy, Nuclear Fusion, Vol. **31** (1991), 1595

[9] A. de Chambrier et al., Plasma Phys. Contr. Fusion **31** (1989), 527

[10] C.S. Chang, F.L. Hinton, Phys. Fluids **29** (10), 1986, 3314

[11] C.C. Chu, Europhysics Conference Abstracts, 21st EPS Conference on Controlled Fusion and Plasma Physics, Montpellier, France, June-July 1994, ECA, Vol. **18B**, part III, 1248

[12] B. Coppi, Comments Pl. Phys. Cont. Fusion, Vol. **5** (1980), 261

[13] P. Dierckx, "Curve and Surface Fitting with Splines", Clarendon Press, Oxford (1993)

[14] G. Flor, 8th APS Topical Conference on High-Temperature Plasma Diagnostics, Hyannis, US, 1990, appeared in Rev. Sci. Instrum. **61** (10), 3289

[15] F. Flora et al., Applied Optics **26** (18), 1987, 4001

[16] S. Franke et al., 7th International Symposium on Laser Aided Plasma Diagnostics, Fukuoka, Japan, December 1995

[17] P.E. Gill, "Numerical Linear Algebra and Optimization", Addison-Wesley, Redwood City (1991)

[18] F. Hofmann et al., Plasma Phys. Contr. Fusion **36** (1994), B 277

[19] F. Hofmann, G. Tonetti, Nuclear Fusion, Vol. **28** (1988), 1871

[20] F. Hofmann et al., 24th EPS Conference on Plasma Physics and Controlled Fusion, Berchtesgaden, Bavaria, June 1997 (to be published)

[21] F. Hofmann et al., CRPP - Report, LRP 562/96, December 1996 (submitted for publication in Nuclear Fusion)

[22] I.H. Hutchinson, "Principles of Plasma Diagnostics", Cambridge University Press, Cambridge, 1987

[23] J.D. Jackson, "Classical Electrodynamics", John Wiley & Sons, New York, 1975

[24] JET Team, Plasma Phys. Control. Fusion **37** (1995), A3

[25] B. Kadomtsev, Fiz. of Plasmy **5**, 1975, 710

[26] B. Kadomtsev, Proc. Int. Conf. on Plasma Physics, Kiev, **6-12.4** (1987), 1273, World Scientific

[27] S. M. Kaye, Phys. Fluids **28** (1985) 2327

[28] J. D. Lawson, Proceedings of the Physical Society **B70**,1957, 6

[29] J.B. Lister, Proceedings of the 16th Symposium on Fusion Technology, London, UK, 1990, 1268

[30] J. B. Lister et al., Nuclear Fusion, Vol. **30** (1990), 2349

[31] D.A. Long, Raman Spectroscopy, McGraw-Hill, London,1977

[32] K.V. Mardia et al., "Multivariate Analysis", Academy Press, London , 1979

[33] D.M. Meade et al., Plasma Physics and Controlled Fusion Research, IAEA,

Vienna, Vol. **1** (1990)

[34] K. Miyamoto, "Plasma Physics for Nuclear Fusion", MIT Press, 1976

[35] J.M. Moret, H. Weisen, S. Franke et al., 16th Int. Conf. on Plasma Physics and Controlled Fusion Research, IAEA, Montréal, Canada, October 1996

[36] J.M. Moret, H. Weisen, S. Franke et al., Europhysics Conference Abstracts, 23rd EPS Conference on Plasma Physics and Controlled Fusion, Kiev, Ukraine, June 1996, ECA, Vol. **20C**, part I, 27

[37] J.M. Moret, S. Franke, H. Weisen et al., LRP 560/96, Nov. 1996 (submitted for publication in Physical Review Letters)

[38] H. Murmann et al., Rev. Sci. Instrum. **63** (10), Oct. 1992, 4941

[39] P. Nielsen et al., JET - Report, JET-P(93)62

[40] F. Orsitto et al., Applied Optics, Vol. **34** (1995), 2712

[41] R.R. Parker et al., Nuclear Fusion, Vol. **25** (1985), 1127

[42] N.J. Peacock et al., Nature, Vol. **224**, (1969), 488

[43] C.M. Penney et al., Journal Opt. Soc. Am., **64** (5), 1974, 712

[44] Z.A. Pietrzyk, R. Behn, S. Franke et al., Europhysics Conference Abstracts, 23rd EPS Conference on Controlled Fusion and Plasma Physics, Kiev, Ukraine, June 1996, ECA, Vol. **20C**, part I, 115

[45] P.M. Prenter, "Splines and Variational Methos", John Wiley & Sons, New York, 1989

[46] A.A. Radzig, B.M. Smirnov, "Reference Data on Atoms, Molecules and Ions", Springer Verlag, Berlin, 1985

[47] E. Rebhan, "Heisser als das Sonnenfeuer", Piper Verlag, München, 1992

[48] H.Röhr, Physics Letters, **81A** (8), 1981, 451

[49] H.Röhr, Physics Letters, **60A** (3), 1977, 185

[50] J. Rommers, PhD-Thesis, University of Utrecht, 1996

[51] RBH Optics, Lens Assembly TOM 5A5, Burgess Hill, West Sussex

[52] Saidel, Prokofjev, "Spektraltabellen", VEB Verlag Technik Berlin, 1955

[53] U. Schuhmacher, "Fusionsforschung", Wissenschafliche Buchgesellschaft, Darmstadt, 1993.

[54] B. Schunke, Nuclear Fusion, Vol. **37** (1997), 101

[55] H. R. Schwarz, "Numerical Analysis - A comprehensive Introduction", Wiley & Sons, 1989

[56] A.C. Selden, Physics Letters, **79**A (5,6), 1980, 405

[57] A. C. Selden, Culham Report CLM-R220, January 1982

[58] V.D. Shafranov, Plasma Physics **13** (1971), 757

[59] J. Sheffield, "Plasma Scattering of Electromagnetic Radiation", Academic Press, London , 1975

[60] E.E. Simmet et al., IPP - Report III/215, October 1996

[61] L. Spitzer, "Physics of Fully Ionized Gases", Interscience Publishers Inc., New York, 1956

[62] W.M. Tang, Nuclear Fusion, Vol. **26** (1986), 1605

[63] W. van Toledo, 23rd EPS Conference on Controlled Fusion and Plasma Physics, Kiev, Ukraine, June 1996

[64] N. A. Uckan, J. Sheffield, 7th Course of the Int. School of Fusion Reactor Technology, Erice, Italy, July 1985

[65] F. Wagner et al., Phys. Rev. Letters **49** (1982), 1408

[66] R.E. Waltz et al., Nuclear Fusion, Vol. **26** (1986), 1729

[67] A.A. Ware, Nuclear Fusion, Vol. **21** (1981), 623

[68] P.P. Webb et al, RCA Review, Vol. **35** , 234

[69] H. Weisen et al., H-mode Workshop Princeton, 1995, appeared in Plasma

Phys. Contr. Fusion **38** (1996), 1137

[70] H. Weisen, A. Weller et al., Rev. Sci. Instrum. **62** (6), June 1991

[71] H. Weisen, W. Piffl et al., Europhysics Conference Abstracts, 22nd EPS Conference on Controlled Fusion and Plasma Physics, Bournemouth, UK, July 1995, ECA, Vol. **19C**, part II, 393

[72] H. Weisen et al., Europhysics Conference Abstracts, 23rd EPS Conference on Controlled Fusion and Plasma Physics, Kiev, Ukraine, June 1996, ECA, Vol. **20C**, part I, 111

[73] H. Weisen, J.-M. Moret, S. Franke et al., LRP 571/97, April 1997 (submitted for publication in Nucler Fusion)

[74] J. Wesson, "Tokamaks", Clarendon Press", Oxford, 1987

[75] T. Yamauchi et al., Applied Optics **24** (5), 1985, 700

Appendix A) Rotational Raman Scattering

Raman scattering is an inelastic scattering process which involves energy levels of the scattering atom or molecule. Although the incident photon cannot be directly absorbed, since it is not in resonance with an atomic or molecular transition, a change in excitation is induced. When the spectrum of the scattered radiation is analysed, a shift by $\pm\Delta\lambda$ is observed which corresponds to a difference ΔE between energy levels of the atom or molecule. In pure rotational Raman scattering, the occupancy of the vibrational levels remains unchanged.

Since, at room temperature, excited vibrational states are almost unoccupied, to a good approximation the gases H_2, D_2 and N_2 generally employed for the calibration of the TS system permit only transitions between sublevels of the vibrational ground state [5]. The linear molecule arrangement in these gases imposes the selection rule, $\Delta J = \pm 2$, where J denotes the quantum number of the rotational level. The condition $\Delta J = 2$ is known as Stokes branch of the rotational Raman scattering and corresponds to the case in which the incident photon transfers energy to the molecule. When $\Delta J = -2$, corresponding to the anti-Stokes branch, the molecule transfers energy to the photon and the scattered radiation is shifted to shorter wavelengths. Since the spectral channels of the TCV Thomson scattering filter polychromators lie on the short wavelength side of the laser line, only anti-Stokes RRS lines will be observed. The selection rules of RRS correspond to those of electric quadrupole scattering so that linearly polarized incident light wave will be depolarized. The differential cross-section in the anti-Stokes branch may be written [43]:

$$\left(\frac{d\sigma}{d\Omega}\right)(J \to J' = J-2) = \sigma^{JJ'} = \frac{64\pi^4}{45\lambda^4_{JJ'}} f(J) b(J \to J') \gamma^2 [(1-\rho^{(s)})\cos^2\varphi + \rho^{(s)}] \tag{A.1}$$

where the following abbreviations have been used:

$\lambda_{JJ'}$	Wavelength of the scattered radiation
$f(J)$	Canonical distribution of the rotational states of an ensemble of molecules
$b(J \to J-2)$	Placzek-Teller coefficient
γ	Anisotropic polarizability of the molecules

$\rho^{(s)}$	Depolarization of the scattered radiation, $\rho^{(s)}=0.75$
φ	Angle between polarizations of the incident and the scattered wave

The Placzek-Teller coefficient for the anti-Stokes branch depends on the initial rotational state of the molecule:

$$b(J \to J-2) = \frac{3J(J-1)}{2(2J+1)(2J-1)} \tag{A.2}$$

For the canonical distribution $f(J)$, the following expression holds:

$$f(J) = \frac{g_I(J)(J+1)\exp\left[-\frac{E_0(J)}{k_BT}\right]}{\sum_J g_I(J)(J+1)\exp\left[-\frac{E_0(J)}{k_BT}\right]} \tag{A.3}$$

where the factor $g_I(J)(J+1)$ describes the degeneracy of the rotational state, J. The statistical weight factor g_I depends on the nuclear spin of the single atoms (Table A-1). The quantity $E_0(J)$ denotes the energy of the rotational levels with respect to the vibrational state:

$$E_0(J) = hcB_0J(J+1) - D_0[J(J+1)]^2 + H_0[J(J+1)]^3 \tag{A.4}$$

in which B_0, D_0 and H_0 are constants (Table A-1):

B_0	Rotational constant for the vibrational ground state (v=0) of a rigid rotator
D_0, H_0	Centrifugal distortion constant (v=0)

Table A-1: N_2-Molecule Parameters

	N2	References
B_0 (m^{-1})	198.9	[5], [46]
D_0 (m^{-1})	$<10^{-4}$	[5], [46]
H_0 (m^{-1})		[5], [46]
γ (m-3)	$6.6 \cdot 10^{-31}$	[5], [31], [43]
g (odd)	3	
g (even)	6	

Once E_0 is known, $\lambda_{JJ'}$ may be calculated using the expression:

$$\lambda_{JJ'} = \frac{c}{E_0 + \Delta E(J)} \tag{A.5}$$

where the energy gain of the incident radiation is given by

$$\Delta E(J) = hc\left[\left(4B_0 - 6D_0 + \frac{27}{4}H_0\right)\left(J + \frac{3}{2}\right) - (8D_0 - 34H_0)\left(J + \frac{3}{2}\right)^3 + 12H_0\left(J + \frac{3}{2}\right)^5\right] \tag{A.6}$$

According to eqn. A.1 the differential cross-section $\sigma^{JJ'}$ depends on the polarization angle φ. Since the TCV TS detection system has no preferred polarization direction and since the wave vector of the scattered radiation is perpendicular to the incident polarization direction, the scattered radiation can be detected in orthogonal polarization directions(φ=0° and φ=90°). For $\sigma^{JJ'}$ we may therefore write:

$$\sigma^{JJ'}_{G,RAM} = \frac{7}{4} \cdot \frac{64\pi^4}{45\lambda^4_{G,JJ'}} f(J) b(J \rightarrow J-2)\gamma_G^2 = \frac{7}{4}\sigma_G^{RAM}(\lambda_{JJ'}) \tag{A.7}$$

Table A-2 lists the calculated scattering cross-sections for $\sigma^{JJ'}_{G,RAM} \geq 10^{-38} m^2$.

Table A-2: RRS lines and cross-sections for N_2

Rotational Level J	$\lambda_{N_1}^{JJ'}$ (nm)	$\sigma_{N_2, RAM}^{JJ'}$ ($10^{-38}m^2$)
2	1062.8	57.85
3	1061.9	49.28
4	1061.0	130.71
5	1060.1	77.13
6	1059.2	169.03
7	1058.3	87.67
8	1057.4	174.01
9	1056.5	83.13
10	1055.6	153.61
11	1054.8	68.81
12	1053.9	119.79
13	1053.0	50.75
14	1052.1	83.79
15	1051.2	33.73
16	1050.3	53.02
17	1049.5	20.35
18	1048.6	30.52
19	1047.7	11.19
20	1046.8	16.04
21	1046.0	5.62
22	1045.1	7.71
23	1044.2	2.59
24	1043.4	3.40
25	1042.5	1.09

Appendix B) Distribution of Spectral Channels

The measured signal (eqn. 3.3) from a given spectral channel is a function both of a number of optical and geometric parameters associated with the experimental configuration (incident laser power, dimension of the scattering volumes, scattering angle, etc.) and of the diode characteristics (current response). The basic design specifications of the TCV TS system are a minimum detectable electron density of the order of $5 \cdot 10^{18} m^{-3}$ for electron temperatures in the range 50→2000eV and scattering angles of 60→120°. Even when the radiation source, dispersive elements (filter polychromators) and the detectors are selected, the choice of spectral channel bandwidth and, in particular, interference filters, still remains.

When choosing the spectral channel bandwidths, for the TCV TS system, it was intended that the following criteria be satisfied:

a) The signal-to-noise (S/N) ratio of the detection system should not fall below 10. Here we define the S/N ratio as the ratio between the signal and the noise currents (often power ratios are used).

b) The relative error in $T_{e,q}$ computed from of the conversion functions should be smaller than 10% assuming that the relative uncertainty in the measured signal ratios, dR_q/R_q remains below 5% (section 3.3.1). We obtain therefore the following criterion:

$$\frac{dT_e}{dR_q} \le 2\frac{T_e}{R_q} \tag{B.1}$$

In order to verify these criteria for various interference filter combinations and plasma parameter settings (T_e, n_e, Θ), we consider the case of a circular tokamak equilibrium with parabolic T_e and n_e profiles, $T_e[n_e](r) = T_{e,0}[n_{e,0}](1 - r^2/a^2)$, where $T_{e,0}[n_{e,0}]$ denote the electron temperature and density on the magnetic axis. According to [68], the S/N ratio for an avalanche photodiode detection circuit including the preamplifier noise can be written:

$$\frac{S}{N} = \frac{\rho P_{S,j}}{[2e\Delta f\Gamma\{\rho(P_{S,j} + P_{BG,j}) + I_d^*\}]^{1/2}}$$

(B.2)

where I_d^* denotes the effective dark current including both the surface and bulk generated dark currents and the RMS noise current of the amplifier circuit, Δf the noise bandwidth, Γ the excess noise factor due to the avalanche process and ρ the diode current response. The quantities $P_{S,j}$ (eqn. 3.1) and $P_{BG,j}$ are respectively the collected power due to scattered and background plasma radiation.

The background radiation power is computed assuming only contributions from Bremsstrahlung radiation, including possible line radiation in a rather high value selected for the effective ion charge (Z_{eff}=10)[22, pg. 254]:

$$P_{BG} = A\Delta\Omega Z_{eff} Ce\int\frac{\tau_j(\lambda)}{\lambda^2}\left(\int_{-a}^{a}\frac{n_e^2(r)}{T_e^{1/2}}dr\right)d\lambda$$

(B.3)

where $C=4.3\cdot10^{-35}eV^{3/2}m^4s^{-1}$, and A denotes the projection of the scattering volume on a plane perpendicular to the line-of-sight. Fig. shows two examples of a scattering experiment simulation and Table B-1 compiles the corresponding parameter set. The configuration of spectral channels presented corresponds, in fact, to that which has been chosen for the TCV filter polychromators. This arrangement is particularly favourable, when the observation volumes are located in the upper part of the vacuum vessel, since large scattering angles are clearly preferable for measurements at low T_e.

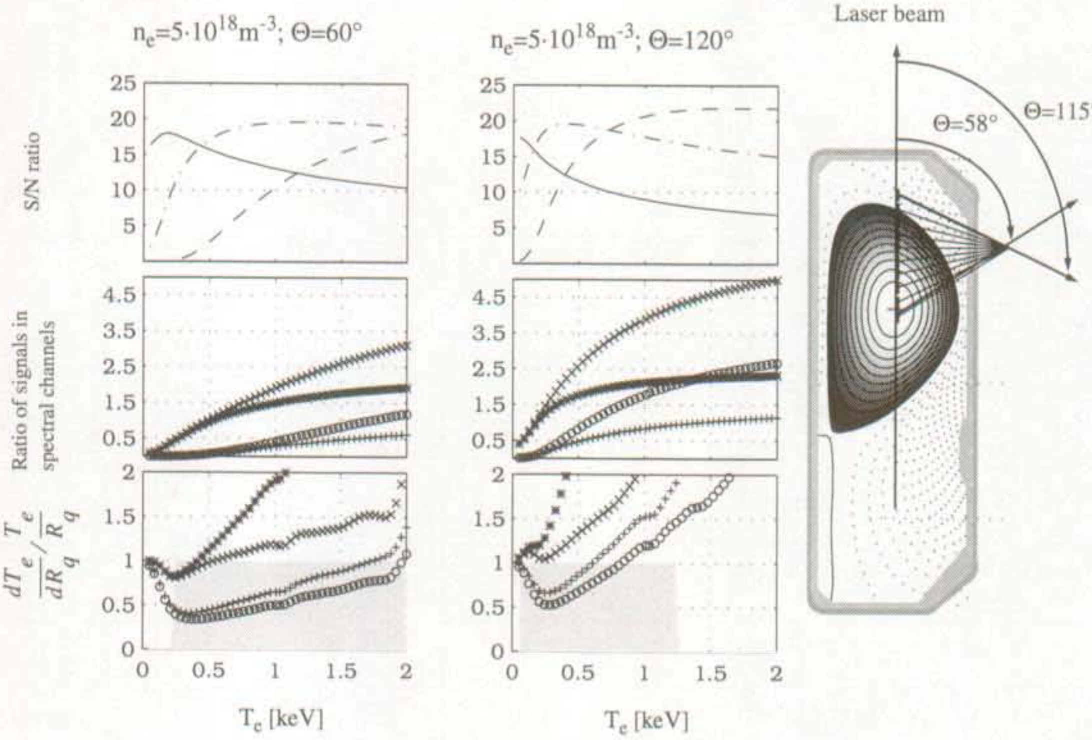

Figure B.1: *The three curves in each column show, from top to bottom, the S/N-ratio of the detector response current in three spectral channels (solid line→j=1, dashed line→j=2, dash-dotted line→j=3), the ratio of signals,* R_q *('*' symbols→*$R_1=P_{s,2}/P_{s,1}$*; 'o' symbols→*$R_2=P_{s,3}/P_{s,1}$*; '*' symbols→*$R_3=(P_{s,3}+P_{s,2})/P_{s,1}$*; 'o' symbols→*$R_4=P_{s,3}/P_{s,2}$*) and the ratio of relative errors in* T_e *and* R_q*. The shaded areas in the lower curves illustrate in which domains* T_e *can be measured for the selected simulation parameters and in accordance with the given criteria. On the right: Scheme of the scattering configuration.*

Table B-1: Simulation Parameters

Quantity	Variable	Spectral Channel	Value	Units
Laser energy	E_L		.8	J
FWHM of laser pulse	t_L		10	ns
Laser wavelength	λ_L		1.064	μm
Electron density on magnetic axis	$n_{e,0}$		variable	m^{-3}
Electron temperature on magnetic axis	$T_{e,0}$		variable	eV
Scattering angle	Θ		variable	°
Length of scattering volume	L		30	mm
Cross-section of scattering volume	A		90	mm^2
Solid angle	$\Delta\Omega$		$5 \cdot 10^{-3}$	sr
Plasma radius	a		0.25	m
Absolute optical transmission	τ		0.3	
Bandwidth of spectral transmission		F1	1035→1055	
		F2	990→1035	nm
		F 3	930→990	
Detector response	ρ	F 1	0.25	
		F 2	0.3	A/W
		F 3	0.45	
Excess noise factor	Γ		2	
Noise bandwidth	Δf		30	MHz
Effective dark current	I_d^*		500	nA

Appendix C) Parameters for the Neoclassical Calculation of the Ion Heat Diffusivity

The formula for the evaluation of the neoclassical heat diffusivity, χ_i^C can be found in reference [10]. When evaluating the constant effective heat diffusivity employed in the solution of the ion heat diffusion equation (eqn. 8.16), the effects of the Shafranov shift are neglected. The table below shows the set of parameters used for the calculation.

Table C-1: Parameter set for the evaluation of χ_i^C

Physical Quantity	Symbol	Value
Plasma major radius	R	0.9 m
Plasma radius	r	0.12 m
Safety factor	q	1
Toroidal Magnetic Field	B_0	1.4 T
Effective ion charge	Z_{eff}	1.5
Ion concentration	c_i	90%
Electron density	n_e	$5\cdot 10^{19} m^{-3}$
Electron temperature	T_e	600 eV
Ion temperature	T_i	500 eV

For this parameter set, we obtain the following results:

$$\chi_i^C = 1.1 \text{ m}^2/\text{s}$$

$$\tau_{ii} = 15\text{ms}$$

$$\nu_i^* = 1$$

$$\rho_{i,\Theta} \approx 20 \text{ mm}$$

Appendix D) Summary of Symbols and Expressions

Quantity	Symbol	Expression
Poloidal Ion Larmor radius	$\rho_{i,\Theta}$	$\frac{v_\perp \cdot m}{e \cdot B_{pol}}$
Ion-Ion Collision Time for Momentum Transfer	τ_{ii}	$\frac{3^{1/2} \cdot 6\pi \cdot \varepsilon_0^2 \cdot m_i^{1/2} \cdot T_i^{3/2}}{Z^4 \cdot n_i \cdot e^4 \cdot \ln\Lambda}$
Ion-Ion Collision Frequency	ν_{ii}	$1/\tau_{ii}$
Ion Transit frequency	ω_{ti}	$\frac{v_{th,i}}{q \cdot R}$
Bounce frequency of Trapped Ions	ω_{bi}	$\varepsilon^{1/2} \cdot \frac{v_{th,i}}{q \cdot R}$
Effective Ion Collisionality	υ_i^*	$\frac{\nu_{ii}}{\varepsilon \cdot \omega_{bi}}$
Poloidal Beta	β_{pol}	$\frac{\langle p \rangle_S}{B_{\Theta,a}^2/(2 \cdot \mu_0)}$
Toroidal Beta	β_{tor}	$\frac{\langle p \rangle_S}{B_0^2/(2 \cdot \mu_0)}$
Line averaged electron density	$\langle n_e \rangle_L$	
Volume averaged electron density	$\langle n_e \rangle_V$	

La pierre n'a point d'espoir d'être autre
chose que pierre. Mais, de collaborer,
elle s'assemble et devient temple.

Antoine de Saint-Exupéry

Acknowledgements

The introductory epigram is an appropriate expression of my years of personal endeavour at the CRPP. Doctoral research is rarely completed successfully without the support of many people; supervisors, colleagues, friends and family. To all of mine, I would like to express my gratitude for their assistance and encouragement over the years and particularly towards the end of this thesis. To some of them I owe especial thanks.

For providing the unique opportunity of a research programme at the CRPP and for their outstanding commitment to and enthusiasm for their institute, I am grateful to Prof. F. Troyon, CRPP Director and Prof. M.Q. Tran, Vice Director.

I sincerely appreciated the patient, encouraging and stimulating supervision of Dr. R. Behn, my "Directeur de these" and captain of the Thomson scattering project on the TCV tokamak. Never once did he hesitate to supply helpful navigational hints when his mate's ship sailed into troubled waters.

My thanks are due to Dr. Z. A. Pietrzyk and F. Hofmann; the former for his maintenance and continuous improvement of the basic Thomson scattering analysis software and the latter for the inclusion of the kinetic constraints into his equilibrium reconstruction code, LIUQE. From both I have learned much during my years at CRPP.

In revealing to me the secrets of cubic B-spline interpolation, Dr. J.M. Moret has made a much appreciated contribution to the content of this thesis. The TCV shape confinement experiments and subsequent transport analysis performed by Dr. Moret, together with Dr. H. Weisen, also constitute important elements of my work. My appreciation of their stimulating comments may best be measured by the number of hours I have spent pondering over them.

A special thank you goes to Dr. R.A. Pitts for his intense linguistic correction of this thesis. Writing it himself would most likely have been easier for him. Helpful discussions with Dr.'s B.P. Duval, Dr. J. Rommers and Dr. Ch. Nieswand are also gratefully acknowledged. The qualities of the latter as a partner for scientific discussion, as a patient listener and as a close friend have been, and continue to be, enormously appreciated.

The practical realization of a physicist's brainwaves depends principally on competent and efficient technical support. It is a great pleasure to acknowledge the provision of such support from the CRPP design draftsmen and the mechanical, electrical and electronic workshops. I would like to extend special thanks to B. Marletaz for his design of the upgraded filter polychromator electronics and for his readiness to assist, whenever solicited, in the solution of even the most minor electronic problems.

For kindly accepting the invitation to participate as members of the thesis examination committee, I would like to thank Prof. Dr. H.F. Doebele (Institut für Laser- und Plasmaphysik, Universität-GH Essen), Dr. P. Morgan (JET Joint Undertaking, Abingdon) and Dr.'s M. Siegrist and H. Weisen of CRPP.

A "Grand Merci" is extended to all the CRPP secretaries, E. Braham, E. Grueter, P. Halter and R. Vincent for their administrative skills, efficiency and support over the years.

The patience and the tolerance with which my girlfriend Angela and my daughter Christina have borne the often difficult times imposed by this thesis are in a large part responsible for its success and will constitute the best possible starting point for a common future.

From the cradle to the doctor's hat, Mum and Dad have given more than words can adequately express. Thanks.

To conclude these words of gratitude, I would like to thank the women, children and all those close to anyone involved in this thesis. The benefit to me was at their expense.

Curriculum vitae

Born on march 3, 1965, in Augsburg (Germany), I attended the primary and secondary school in Kempten (Germany) where I also obtained, in 1984, the university entrance qualification, the so-called 'Abitur', from the 'Carl-von-Linde-Gymnasium'. After military service, I began studying physics at the technical university 'Fridericiana' in Karlsruhe. From 1989 to 1990, I spent 18 months as an exchange student at the 'Laboratoire de Spectrométrie Physique' of the university 'Joseph-Fourier' in Grenoble where I performed the experimental work for the diploma. Returning to Karlsruhe, I received, in June 1991, the degree of qualified physicist ('Diplom-Physiker'). Since November 1991, I have been working as assistant at the 'Centre de Recherche en Physique des Plasmas' in Lausanne.